Characterizing the non-equilibrium quark-gluon plasma with photons and hadrons

Jean-François Paquet
Department of Physics
McGill University, Montréal

September 2015

A thesis submitted to McGill University in partial fulfillment of the requirements of the degree of Doctor of Philosophy

Contents

List of Figures

Résumé

Les collisions d'ions lourds peuvent être utilisées pour étudier les propiétés de la matière nucléaire soumise à des conditions extrêmes. Ces collisions concentrent suffisament d'énergie à l'intérieur d'un volume réduit pour faire fondre les noyaux qui entrent en collision, produisant ainsi un plasma de quarks et de gluons. Ce plasma semble atteindre rapidement un équilibre thermique local, permettant d'étudier ses propriétés à l'aide d'une approche hydrodynamique. Dans cette thèse, la production de hadrons et de photons dans les collisions d'ions lourds est étudiée à l'aide d'un modèle hydrodynamique sophistiqué qui inclut des conditions initiales réalistes, des équations hydrodynamiques complètes avec viscosités de cisaillement et de volume, ainsi qu'un traitement approprié des interactions finales des hadrons. Ce modèle est comparé avec succès à plusieurs observables hadroniques mesurées au "Relativistic Heavy Ion Collider" (RHIC) et au Grand collisionneur de hadrons (LHC), et il est montré que la viscosité de volume est essentielle à ce succès. À l'aide de ce même modèle hydrodynamique, la production de photons directs dans les collisions d'ions lourds est étudiée. L'effet de la viscosité sur le taux de production des photons est étudié, et la méthode pour calculer l'anisotropie en quantité de mouvement des photons directs est clarifiée. Il est montré que le calcul du spectre et de l'anisotropie des photons directs est à l'intérieur de l'incertitude des mesures expérimentales ou légèrement inférieurs à celles-ci.

Abstract

Heavy ion collisions can be used to study the properties of nuclear matter in extreme conditions. These events concentrate enough energy in a small volume to melt the colliding nuclei into a plasma of quarks and gluons. This plasma appears to achieve near local thermal equilibrium during its very short lifetime, allowing for its long scale properties to be investigated with hydrodynamics. In this thesis, the production of hadrons and photons in heavy ion collisions is studied using a sophisticated hydrodynamical model that includes realistic initial conditions, hydrodynamical equations with both shear and bulk viscosities, along with an appropriate treatment of final state hadronic rescatterings. A wide range of hadronic observables, measured at the Relativistic Heavy Ion Collider (RHIC) and the Large Hadron Collider (LHC), are shown to be described well by this model, and bulk viscosity is found to be essential to this level of agreement with data. Building on this successful model, direct photon production in heavy ion collisions is studied. The effect on photon emission of the emitting medium's viscosity is investigated, and the method for evaluating direct photon momentum anisotropies for comparisons with experimental measurements is clarified. Both the direct photon spectrum and momentum anisotropy are shown to be within or slightly below the uncertainties of available experimental measurements.

Acknowledgments

Research is done by building on the work of predecessors, and by combining the thousand ideas, suggestions and comments made to you over the years by authorities and colleagues alike. The work presented in this thesis would not have been possible without the crucial input of many.

I am indebted to my supervisor Charles Gale for the unfaltering patience he showed as academic mentor, and for his guidance in navigating the world of academia. The numerous opportunities he provided me to attend workshops, conferences and summer schools — both to share my work and further my education — equaled the invaluable help he provided me with the work that led to this thesis.

A significant part of my PhD was shaped by the endless stream of ideas and research project suggestions from Gabriel Denicol. His constant help, and willingness to take time, day after day, to answer my countless questions about hydrodynamics, kinetic theory, heavy ion physics et al made the work presented in this thesis possible.

Many thanks to Chun Shen for his close collaboration over the past years on numerous photon-related calculations that, directly and indirectly, led to many of the results presented in this thesis.

I am indebted to Friederike Bock, Maxime Dion, Thomas Epelbaum, Jacopo Ghiglieri, Ulrich Heinz, Sangyong Jeon, Igor Kozlov, Aleksi Kurkela, Matt Luzum, Larry McLerran, Guy Moore, Sangwook Ryu, Björn Schenke, Gojko Vujanovic and Clint Young for their help, for numerous interesting discussions and for their collaboration in various projects over the past years. Special thanks to Thomas for reading this thesis from cover to cover and providing feedback that made it clearer.

I must acknowledge the "EMMI Rapid Reaction Task Force on the direct-photon flow puzzle" at GSI, "Doctoral Training Program on Heavy Ion Collisions" at ECT*, the "Thermal Photons and Dileptons in Heavy-Ion Collisions Workshop" at BNL and the "2013 National Nuclear Physics Summer School" held at Stony Brook, for the great opportunities they provided to exchange and learn with the leading experts in the field.

My deepest thanks to the "Fonds de recherche du Québec - Nature et technologies",

Hydro-Québec and my supervisor Charles Gale for their financial support during my PhD.

The calculations presented in this thesis required a significant amount of CPU power, which was provided in large part by the supercomputer Guillimin. The operation of this supercomputer, managed by Calcul Québec and Compute Canada, is funded by the Canada Foundation for Innovation (CFI), Ministère de l'Économie, de l'Innovation et des Exportations du Québec (MEIE), RMGA and the Fonds de recherche du Québec - Nature et technologies (FRQ-NT). I am indebted to Sangyong Jeon for procuring the heavy ion group a very large amount of CPU time on Guillimin. This computing power was essential to make the calculations presented in this thesis. I also thank Paul Mercure and Juan Gallego for their help with the local computer infrastructure in the physics department.

I thank Kevin Dusling and Ismail Zahed for providing a tabulation of their photon emission rate, which is used in this thesis.

Finally, my warmest thanks to my present and past officemates from 349, for all the good times, the laughs, cookies, chocolate and random discussions we had over the years, which brightened even the most demanding working days.

Statement of originality

The calculations presented in this thesis are original work, with the following exceptions.

The hydrodynamical modeling of heavy ion collisions shown in Chapter 4 is my own work, with the exception of the post-particlisation dynamics simulated with the transport model UrQMD. Beside making these hydrodynamical calculations, I did extended preliminary investigations that allowed to determine the exact hydrodynamical model that was used for this project. I also did the groundwork on constraining the parameter space of the model. The results presented in Chapter 4 have been submitted [1] to Physical Review Letter and are currently undergoing peer-review.

Chapter 6, along with Appendices B and C, cover my own contributions to a work on the effect of shear viscosity on photon production which was published in Ref. [2] with coauthors.

The calculation of photon production in heavy ion collisions presented in Chapter 7 is original and is in the process of being published. The clarification on the proper evaluation of momentum anisotropies in Section 7.2 is unpublished, although preliminary and peripheral investigations on the matter were published previously with collaborators in conference proceedings [3, 4].

Investigations on perturbative QCD at low transverse momentum presented in Appendix A is my original work.

Part I

Introduction

Chapter 1

Studying nuclear matter under extreme conditions

Four decades ago the establishment of the Standard Model inaugurated a new era for particle physics. All interactions known to be important for subatomic physics had been incorporated into a single quantum field theory framework. Although open questions do remain about the Standard Model [5, Chapter 11], its status as a solid effective description of the subatomic world is uncontested.

This remarkable understanding of the underlying interactions of elementary particles is by no means the end of the story. An equally interesting part of the work remains: using this knowledge to understand complex systems of elementary particles. This thesis is built around this idea, for systems of particles interacting through the strong nuclear force.

The strong nuclear force is one of the three elementary forces described by the Standard Model, the other ones being the weak nuclear force and the electromagnetic interaction. Quantum chromodynamics (QCD) is the quantum field theory within the Standard Model that describes strong nuclear interactions. Its fundamental degrees of freedom are quarks and gluons, which carry a charge called "colour". One of the most interesting property of QCD is that such charged, or "coloured", objects have never been observed directly: quarks and gluons are always found in composite colour-neutral objects called hadrons. Protons and neutrons are the best known examples of hadrons.

This neutralisation of the colour charge is called "confinement". It is a phenomenon that has yet to be fully understood from first principles. It is nevertheless closely related to another distinctive feature of QCD: asymptotic freedom, the weakening of the interaction between coloured objects as the interaction energy increases. Asymptotic coupling is illustrated on Figure 1.1 by plotting the strength of the strong nuclear force, as given by the value of the strong coupling constant α_s, in a variety of processes at different energy

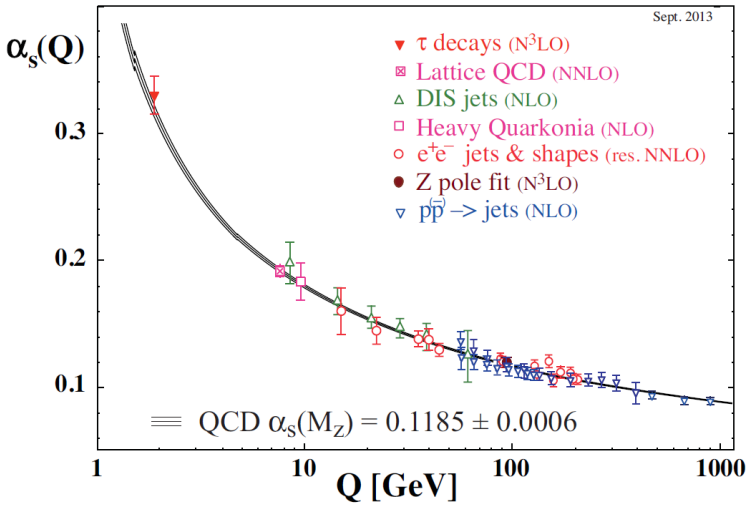

Figure 1.1: Running of the strong coupling constant α_s with the energy scale Q (Figure from [6, Section 9.3.12])

scales Q. Since the value of α_s is fairly small at those high energies, it is possible to use perturbative techniques to evaluate its evolution in Q directly from QCD. This calculation is shown on Figure 1.1 to be in very good agreement will all measurements.

Quantum chromodynamics is now a well-established theory which provides an accurate description of strong interactions in a number of very different measurements, from the traditional hadron spectroscopy to the successful parton model picture of high energy collisions. With this solid theory in hand, one can begin asking more complex questions about the strong nuclear interaction. One area of particular interest is the collective behaviour of systems dominated by the strong interaction.

1.1 Hot nuclear matter

Asymptotic freedom leads to a straightforward conclusion about the collective behaviour of nuclear matter: when a system of hadrons is heated to high temperatures, the force that binds the quarks and gluons within hadrons will weaken as the interaction energy of the constituents increases. Eventually quarks and gluons will be freed from hadrons and will form a plasma of colour-charged particles. This latter state of matter was given the name "quark-gluon plasma" (QGP) [7].

The transition from a *thermally equilibrated* system of interacting hadrons to a quark-gluon plasma — a process referred to as "deconfinement" — is well-studied theoretically. The thermodynamic properties of the gas of hadrons can be calculated with effective models of hadronic interactions, while perturbative QCD techniques can be used at very high

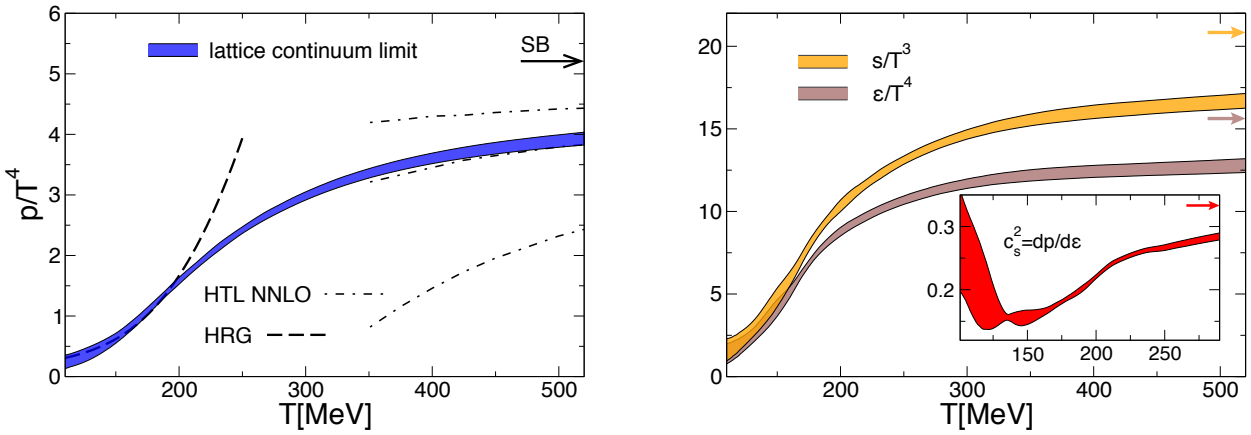

(a) (b)

Figure 1.2: (a) Recent lattice calculation of the pressure of a thermalised QCD medium for temperatures between 100 and 500 MeV. Below 200 MeV, the lattice calculation matches well the pressure computed from an effective hadronic model (hadron resonance gas — HRG). At high temperature, perturbative calculations of the QGP pressure are shown. The three different perturbative calculation illustrate the uncertainty in such calculations. The Stefan-Boltzmann limit of the pressure, which corresponds to an ideal gas of free quarks and gluons, is indicated by an arrow on the right axis (b) Energy density, entropy density and speed of sounds for the same lattice calculation (both figures from [8])

temperatures where $\alpha_s(Q \sim T)$ is small. Neither approaches works in the interesting region where hadronic degrees of freedom give way to quark and gluon ones. This gap was nevertheless narrowed down, over the past two decades, by numerical simulations of lattice QCD.

The pressure of hot QCD matter from a recent lattice calculation [8] is shown on Figure 1.2a. The change in the degrees of freedom dominating the thermodynamics can be better seen in Figure 1.2b, where the rapid change in the temperature-scaled energy density ϵ/T^4 occurring between 100 and 200 MeV[1] is followed by a slow growth of the energy density toward the Stefan-Boltzmann limit, which is the value for an ideal gas of quarks and gluons. Deconfinement of QCD matter is thus expected at energy densities of $\epsilon \sim 1$ GeV/fm^3, which is close to 10 times the normal density of nuclear matter.

Ultrarelativistic collisions of heavy ions were suggested early (see Ref. [9, Section 1.2] and references therein) as a controlled way of reaching the energy densities required to create

[1]For reference, 1 MeV$\approx 1.2 \times 10^{10}$ K.

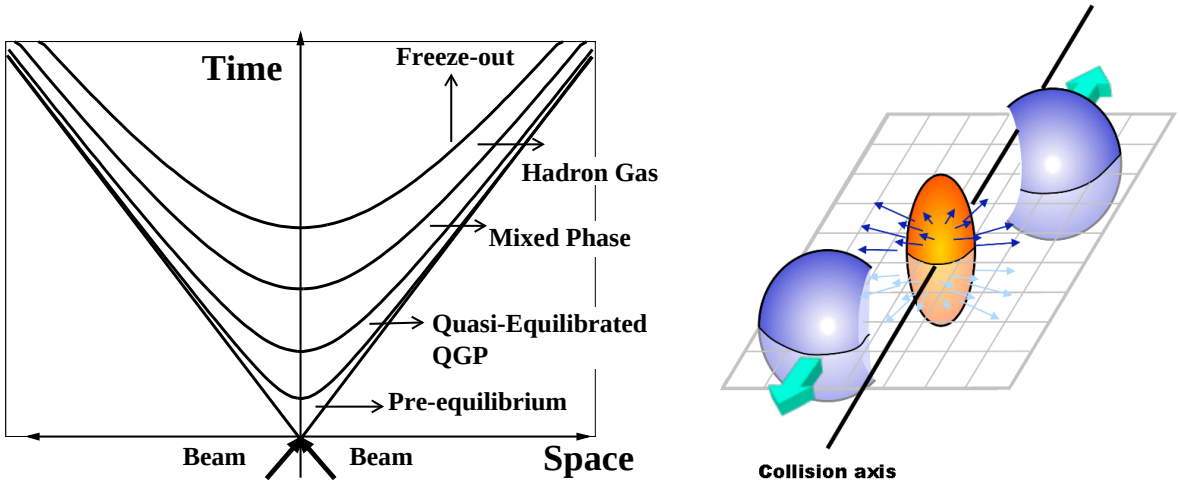

(a) (b)

Figure 1.3: (a) Illustration of the spacetime evolution of a heavy ion collision (adapted from [11]) (b) Illustration of the energy deposition occurring in heavy ion collisions (adapted from [12])

and study the quark-gluon plasma[2]. This aim was achieved slightly more than a decade ago with the commissioning of the Relativistic Heavy Ion Collider at the Brookhaven National Laboratory.

1.2 Ultrarelativistic heavy ion collisions

The Relativistic Heavy Ion Collider (RHIC) is generally considered to be the first hadron collider to bring the experimental study of deconfined nuclear matter to a quantitative level. Evidence for the production of deconfined nuclear matter in heavy ion collisions had been accumulated at previous nucleus colliders, but RHIC was the first to claim unambiguous observation of a new state of nuclear matter, the quark-gluon plasma [9].

In 2010 the European Organization for Nuclear Research's (CERN) Large Hadron Collider (LHC) joined the fray. Better known for its proton collision program, which boosts among other successes the discovery of the Higgs boson, the LHC also has a comprehensive program of nucleus-nucleus collisions. A higher energy collider than RHIC, the LHC

[2] Deconfined nuclear matter and quark-gluon plasma (QGP) are used as synonyms in this thesis, as is common in the field of heavy ion physics. It is important to note that there is no sharp transition (at least at small baryon number density) between a thermal system of hadronic degrees of freedom and one with quark and gluon degrees of freedom [10, Section 2.4]. The point at which hot nuclear matter should be referred to as a QGP is thus ambiguous. Moreover the properties of hot nuclear matter are expected to change significantly between the temperatures typically achieved in modern heavy ion colliders ($T \sim 300-600$ MeV), where deconfined matter is strongly coupled, and asymptotically high temperatures where a gas of weakly interacting quarks and gluons is expected.

confirmed and complemented the numerous observations and findings made at RHIC [13].

A great discovery of RHIC was that the QGP behaves as a strongly interacting fluid, and not a weakly interacting gas of quarks and gluons as previously expected . Although the dynamics of heavy ion collisions is complex, many features of the collisions at RHIC and the LHC are dominated by the creation and expansion of the quark-gluon plasma, with suggestive evidence that the QGP is close to local thermal equilibrium. That near thermal equilibrium could be achieved, locally, in a plasma of quarks and gluons on scales smaller than the size of a nucleus was a striking discovery.

A sketch of the present understanding of the spacetime evolution of heavy ion collisions is shown on Figure 1.3a. At first, two nuclei moving in opposite directions at nearly the speed of light undergo a collision. Upon collision, a deposition of excited coloured matter occurs in the region of overlap of the nuclei (Figure 1.3b). This excited matter appears to go through a rapid process of thermalisation that is not yet fully understood. This pre-equilibrium dynamics leads to the establishment of near local thermal equilibrium in the regions where a sufficiently high energy density was deposited. This all happens on a timescale of approximately 1 fm ($\sim 10^{-24}$ s).

Once local equilibrium is established, a rapid hydrodynamical expansion of the medium follows, which progressively reduces the energy density of the medium. Hydrodynamics expansion is thought to continue after the quark-gluon plasma goes through confinement into hadronic degrees of freedom [13, Section 2]. Eventually the medium becomes too rarefied to maintain local equilibrium, and on a timescale of around 10 fm its expansion changes in nature to become closer to the expansion of a weakly interacting gas than that of a fluid. Interactions among hadrons become less and less frequent as hadrons fly out of the collision region, toward the detectors.

This picture is in large part based on the great success of hydrodynamical models in describing hadronic measurements made at RHIC and the LHC. There are however multiple evidence for the formation of a quark-gluon plasma in heavy ion collisions. One of the most compelling is the suppression of hadron production [13, Section 2], which is the topic of the next section.

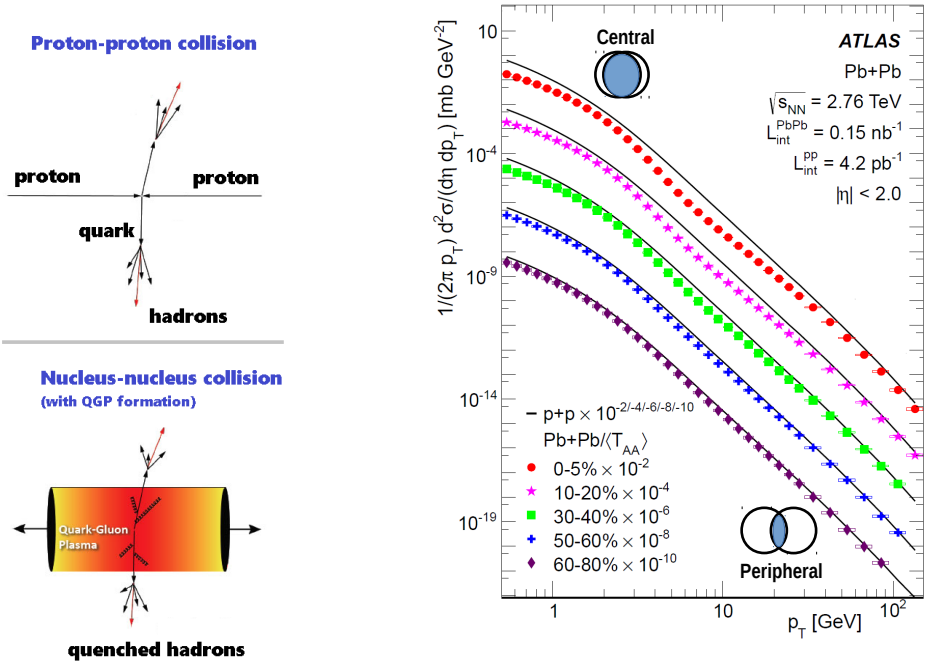

(a) (b)

Figure 1.4: (a) Illustration of hard hadron production in proton-proton collisions (Equation 1.1) compared to heavy ion collisions. Hard hadrons produced in heavy ion collisions carry less energy than the same process in proton-proton collisions, due to energy loss of their father parton to the quark-gluon plasma. (figure adapted from [14]) (b) Suppression of the charged hadron spectra measured at the LHC. See text for explanations of the different curves. (figure adapted from [15])

1.3 Hard probes and energy loss

The production of hard[3] hadrons in proton-proton collisions is very well understood, to the point that they can be used as "probes" of the dynamics of heavy ion collisions. Their production mechanism is illustrated at the top of Figure 1.4a. A parton (a quark or a gluon) from each proton undergoes a hard scattering. The scattered partons then go through a non-perturbative color neutralisation process, called fragmentation, which results in final

[3]A "hard" scattering in QCD is a collision in which the participant undergo a momentum exchange much larger than the scale of QCD, $\Lambda_{QCD} \sim 200$ MeV. In collider experiments, particles produced with transverse momentum larger than ~ 5 GeV are considered hard.

state partons to be converted into hadrons. This process can be written schematically as[4]

$$E\frac{d^3\sigma_{pp}}{d\mathbf{p}} = \sum_{a,b,c,d} f_{a/p}(x_a) \otimes f_{b/p}(x_b) \otimes d\hat{\sigma} \otimes D_{h/c}(z_c) \tag{1.1}$$

where

- $f_{a/p}(x_a)$ is the parton distribution function, representing the probability of finding a parton of type[5] "a" and momentum $p_a = x_a P$ in a proton of momentum P
- $d\hat{\sigma}$ is a differential parton-parton cross-section that can be evaluated perturbatively from first principles in QCD
- $D_{h/c}(z_c)$ is the fragmentation function, representing the probability for a parton of type "c" to fragment into a hadron "h" carrying a fraction z_c of the parton's momentum

and $\otimes$ represents integration over $x_{a/b}$ and z_c with the appropriate integration measure and kinematic cuts.

Parton distribution functions can be measured with dilepton production in proton-proton collisions (commonly referred to as Drell-Yan processes), and fragmentation functions can be measured in electron-position annihilation into hadrons.

Equation 1.1 has been shown to be in very good agreement with hard hadron production in proton-proton collisions [16]. Essentially the same approach can be used to compute the production of hard photon, dilepton and weak boson ($Z/W^{\pm}$) in proton-proton collisions, with a similar good agreement with data being observed [17, 18].

Equation 1.1 has not formally been shown to be applicable to nucleus-nucleus collisions. Nevertheless, hard photon, dilepton and weak boson production is still very well described [19, 20, 21] by approximating the nucleus-nucleus collisions as an incoherent superposition of proton-proton collisions:

$$E\frac{d^3N_{AA}}{d\mathbf{p}} \approx \frac{N_{bin}}{\sigma_{pp}^{inel}} E\frac{d^3\sigma_{pp}}{d\mathbf{p}} \tag{1.2}$$

where N_{bin} is the number of nucleon-nucleon collisions in the nucleus-nucleus collision, which can be computed in models of nucleon interactions such as the Glauber model [22]. The inelastic nucleon-nucleon cross-section σ_{pp}^{inel} is used to relate the differential particle *cross-section* in proton-proton collisions from the right-hand-side of Equation 1.2 to the *number* of particles produced in nucleus-nucleus collisions on the left-hand-side.

[4] The theoretical basis of Equation 1.1 will be reviewed later in this thesis (Section 5.2.1).

[5] Gluons and the different flavours of quarks and antiquarks all have different probability distributions.

Deviations from binary scaling (Equation 1.2) have been observed for hadron production in heavy ion collisions (e.g. [15]). This departure from binary scaling in fact provided one of the most solid evidence that a quark-gluon plasma is formed in such collisions. This is illustrated on Figure 1.4b, which shows the momentum distribution of hadrons in Pb-Pb collisions at the LHC. The bottom data points are for peripheral collisions — collisions where the two lead nuclei collide with a small overlap, depositing a limited amount of energy in the almond-shaped region (as illustrated on Figure 1.3b). The upper data points are for central collisions in which the two nuclei collide nearly head-on and deposit a large amount of energy in the interaction region. The solid black line above each data set is the prediction of Equation 1.2 for different levels of overlap of the colliding nuclei.

Equation 1.2 works reasonably well for peripheral collisions, but overestimates significantly hadron production in central collisions. This deviation is understood to be attributable to parton energy loss [23], illustrated at the *bottom* of Figure 1.4a. The first part of the reaction described by Equations 1.1/1.2 still actually holds: a parton from each nuclei undergo a hard interaction. However, between the hard parton-parton scattering and fragmentation into hadrons, the final state parton interacts with the quark-gluon plasma that is formed around it in the heavy ion collision, as illustrated at the bottom of Figure 1.4a. These interactions lead to a loss of energy for the parton, which is reflected into an energy loss for the final hadrons. Since central heavy ion collisions deposit more energy and create a larger quark-gluon plasma, the parton interacts more with the medium and lose more energy. On the other hand, peripheral collisions create a smaller and shorter lived QGP, translating into a much more limited parton and hadron energy loss. Neither electromagnetic or weak probes are affected: they do not interact significantly through the strong interaction and the QGP is essentially transparent to them.

Hadron energy loss is one of a number of observations that support the conclusion that a QGP is created for an extended spacetime region in heavy ion collisions at RHIC and the LHC. The success of hydrodynamical models in describing a range of measurements is an additional, and possibly stronger, evidence.

1.4 Hydrodynamical simulation of heavy ion collisions

Hydrodynamics provides an effective description of the long scale properties of any system that achieves near local thermal equilibrium [24]. Examples of its success are numerous, ranging from water [25, 26] to ultracold quantum gases and exotic liquid crystals [24].

Whether local equilibrium is achieved in a medium can be inferred from the success of hydrodynamics in describing its dynamics. The effectiveness of hydrodynamical models in

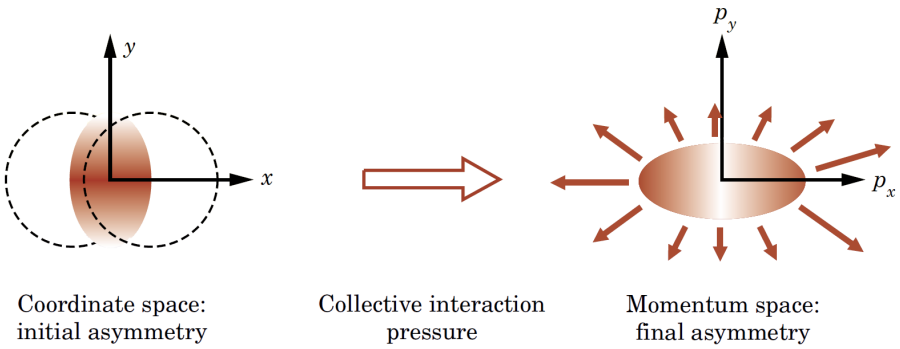

Figure 1.5: Relation between the initial energy spatial anisotropy and the final momentum anisotropy of produced particles (Figure adapted from [27])

describing a wide range of hadronic observables measured in heavy ion collisions is interpreted as strong evidence that the quark-gluon plasma does achieve local thermal equilibrium during its short lifetime.

Of all hadronic observables, the angular distribution of hadrons in the plane transverse to the collision axis is perhaps the most convincing in its support of hydrodynamics. This owes to the straightforward explanation that hydrodynamics provides for the presence of large angular anisotropies in the momentum distribution of hadrons, as observed in heavy ion collisions at both RHIC and the LHC.

The picture that hydrodynamics paints of the quark-gluon plasma's expansion in the transverse direction is shown on Figure 1.5. A peripheral heavy ion collision deposits energy in a highly eccentric shape, as represented on the left-hand-side of Figure 1.5. If local equilibrium is quickly established in this distribution of matter, its subsequent spacetime evolution is described by hydrodynamics. This evolution is driven by pressure gradients, which are much larger along the short axis of the energy deposition. The medium thus expands faster along the x-axis. At the end of the hydrodynamical evolution, when the expanding medium is converted to hadronic degrees of freedom, this expansion anisotropy is imprinted in hadrons, giving them a large momentum anisotropy.

This momentum anisotropy is typically expressed in terms of Fourier coefficients, by writing the differential momentum distribution of hadrons as

$$\frac{1}{2\pi p_T}\frac{dN}{dp_T d\phi} = \left(\frac{1}{2\pi p_T}\frac{dN}{dp_T}\right)\left[1 + 2\sum_{n=1}^{\infty} v_n \cos(n(\phi - \Psi_n))\right] \tag{1.3}$$

where the momentum in the plane transverse to the collision axis is described by the azimuthal angle ϕ and the transverse momentum p_T.

The second Fourier coefficient v_2 and its event-plane Ψ_2 are easiest to understand in

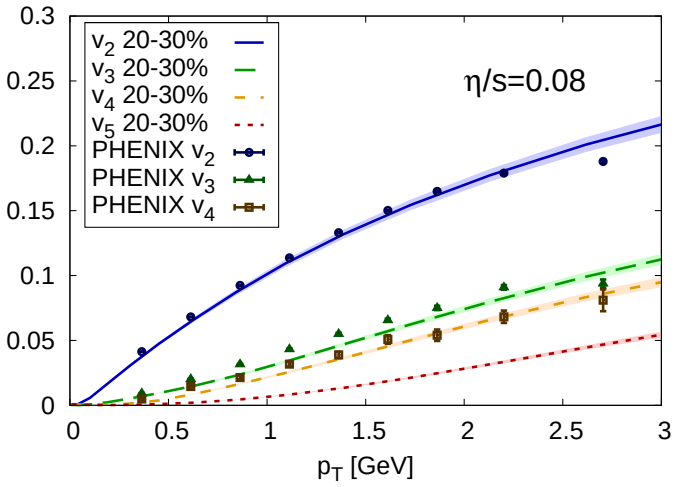

Figure 1.6: Charged hadron momentum anisotropy compared with a hydrodynamical model's calculation (figure from [28])

terms of the picture shown on Figure 1.5. Assuming an idealised collision with an energy deposition profile as symmetric[6] as shown on the left-hand-side of Figure 1.5, the momentum distribution is well-described by a single Fourier coefficient, v_2:

$$\frac{1}{2\pi p_T}\frac{dN}{dp_T d\phi} = \left(\frac{1}{2\pi p_T}\frac{dN}{dp_T}\right)\left[1 + 2v_2\cos(n(\phi - \Psi_2))\right] \tag{1.4}$$

The angle Ψ_2 is the direction where hadrons are dominantly produced in this picture, which from the right-hand-side of Figure 1.5 can be read to be the x-axis. This angle is thus perpendicular to the long axis of the initial energy deposition.

A hydrodynamical description of the dynamics of heavy ion collisions thus predict a specific direction (Ψ_n) and magnitude (v_n) for the azimuthal distribution of hadrons. A very good quantitative agreement is found between v_n measurements[7] and hydrodynamical model predictions, as shown on Figure 1.6.

The success of hydrodynamical models in understanding the azimuthal anisotropy of

[6] While the two nuclei depositing the energy are identical and an approximate almond-shape geometry is expected in peripheral collisions, their energy deposition will never be perfectly symmetric due to quantum fluctuations and pre-equilibrium dynamics. The energy deposition plotted on Figure 1.5 is thus highly idealised.

[7] Neither v_n nor Ψ_n of a single collision can be measured in heavy ion collisions. The possibility of measuring Ψ_n itself would imply that there exists a reference axis from which ϕ can be measured, which is not the case. The value of a single event's v_n is not available either, due to the small number of particle measured in each event. What is measured in heavy ion collisions is rather angular correlations between particles, averaged over multiple collisions, which can be related to the values of v_n or Ψ_n computed in hydrodynamical simulations. The closest thing to v_n that can be measured is its root-mean-square value averaged over multiple events.

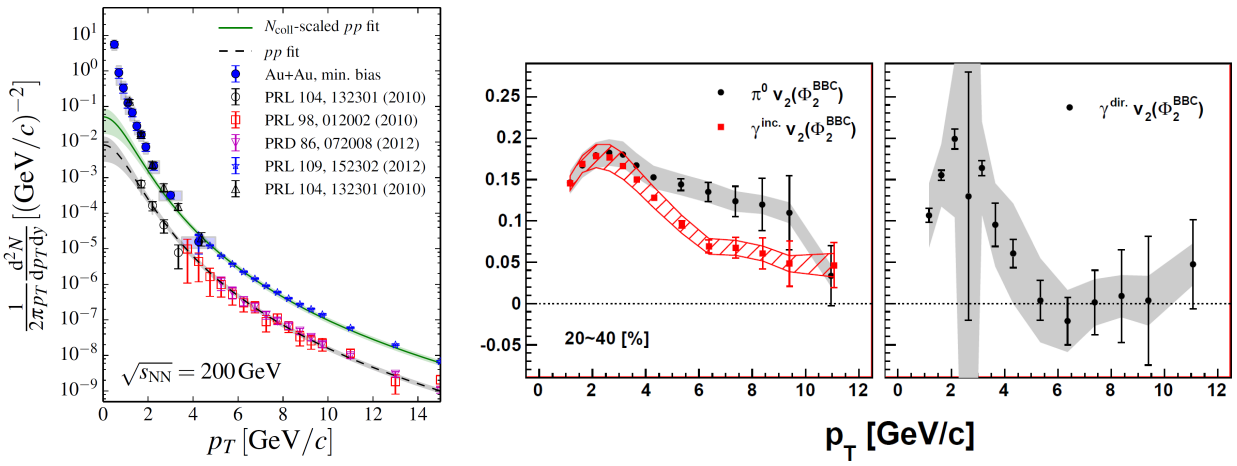

(a) (b)

Figure 1.7: (a) Direct photons measured at RHIC in p+p and Au+Au collisions (Figure from [29]) (b) π^0, inclusive photon and direct photon momentum anisotropy measured at RHIC in Au+Au collisions (Figure adapted from [30]). In both cases, the center-of-mass energy is $\sqrt{s_{NN}} = 200$ GeV

hadrons is considered a major accomplishment of the model, supporting the (near) local thermalisation hypothesis. Yet hadrons are not the only particles produced and measured in heavy ion collisions. Measurements of photon production at both RHIC and the LHC provided a new opportunity to put to the test hydrodynamical models of heavy ion collisions.

1.5 Electromagnetic probes: a complementary window into heavy ion collisions

In the hydrodynamical picture of heavy ion collisions presented above, hadrons are produced in the late stage of the medium's expansion, or at the system's edge, in both case because of the low local energy density in these regions of spacetime. The information carried by hadrons is consequently dominated by the properties of the periphery and of the later phase of the medium evolution. This is a limitation of hadronic observables, since they can only be indirect probes of the quark-gluon plasma.

Photons do not share this limitation, since their mean-free-path in the quark-gluon plasma is significantly larger than the medium produced in current heavy ion collisions[8]. Consequently photons produced at the very center of the QGP, shortly after its formation, can reach the detectors without significant interactions with the medium surrounding it.

[8] The transverse size of the QGP is roughly 10−20 fm. A much larger medium extent, around 300−500 fm, is necessary for photon interactions with the medium to become significant [31, Introduction].

They can thus provide information about every spacetime region of the medium, making them valuable probes of the QGP's properties.

There are many different sources of photons in heavy ion collisions. There are *hadronic decay photons*, which are produced in decays of unstable hadrons through channels such as $\pi^0 \to \gamma\gamma$ or $\eta \to \gamma\gamma$. There are also photons produced through hard parton interactions, the mechanism described in Section 1.3, which produces photons essentially in the same way as it produces hadrons. These photons are referred to as *prompt photons*. Photons emitted by the quark-gluon plasma during its expansion are called *thermal photons*. The term *inclusive photons* is used to describe the total photon signal, without regard on the photon's production mechanism.

Most photons produced in heavy ion collisions are decay photons. While hydrodynamical models predict that a significant amount of thermal photons is emitted throughout the QGP's lifetime, decay photons completely drown their signal. To remedy this problem, experimental collaborations subtract a large part of this decay photon background by modelling them in Monte Carlo simulations constrained from hadronic data. The resulting observable is called *direct photons*.

Thermal photons are thus accessible through comparisons with direct photons. Prompt photons are also a significant source of direct photons. Actually prompt photons are essentially the only source of photons in proton-proton collisions, such that photon measurements from such collisions are used to estimate prompt photons in heavy ion collisions. This method can be used to show that prompt photons are also the dominant source of photons at high transverse momentum in heavy ion collisions. This is illustrated on Figure 1.7a, where the photon spectrum in Au-Au collisions is very well described above $p_T \sim 4$ GeV by simply scaling up the spectrum measured in proton-proton collisions. This is an example of support for binary scaling that was mentioned in Section 1.3.

At low transverse momentum ($p_T \lesssim 4$) the direct photon spectrum from Au-Au collisions shows a large excess of measured photons above the prompt photons baseline. This excess of photons at low p_T was interpreted early as a possible thermal photon signal [32].

The measurement of a large momentum anisotropy of direct photons [30], shown on Figure 1.7b, made the picture more complicated. The left-hand-side of Figure 1.7b shows the v_2 of pions — which are the main source of decay photons — along with the v_2 of inclusive photons, which is the raw measurements of photons that is dominated by hadronic decay photons. Since decay photons carry the momentum anisotropy of their parent hadron, it is expected for inclusive photons to have a v_2 similar to that of pions. On the other hand, it was totally unexpected that *direct* photons, shown on the right-hand-side of Figure 1.7b, would also have a v_2 of the same magnitude as that of pions. This was one of the most

striking discovery made at RHIC.

The large direct photon v_2 came a surprise because early calculations from hydrodynamical models [33, 34] predicted a fairly small direct photon v_2. This discrepancy became known informally as the "direct photon puzzle" (see Ref. [35] and references therein).

1.6 This thesis

The purpose of this thesis is to provide a state-of-the art calculation of direct photon production in heavy ion collisions in order to clarify the status of the direct photon puzzle, which was the subject of numerous investigations [36, 37, 38, 39, 40] over the past years, and to determine if the label "puzzle" is still necessary.

This aim is first achieved by using a sophisticated hydrodynamical model of heavy ion collisions. This model improves upon previous work by including

- a more realistic description of the pre-equilibrium dynamics of the collisions
- a more complete set of hydrodynamical equations to describe the evolution of the locally thermalised QGP
- a more realistic treatment of the hadronic degrees of freedom in the final stage of the collisions

A description of this hydrodynamical model is provided in Chapter 3. It is preceded by an overview of the phenomenology of heavy ion collisions (Chapter 2).

The quality of this hydrodynamical model is shown in Chapter 4 by comparing it with a wide range of hadronic observables measured at both RHIC and the LHC. Hadronic observables are used simultaneously to constrain the parameters of the hydrodynamical model and to verify that, given this choice of parameters, a large set of hadronic measurements can be well-described. The point is to provide confidence in the hydrodynamical model, which can then be used to study direct photon production in heavy ion collisions.

Many different ingredients are necessary to compute photon production in heavy ion collisions. The full description of the formalism used to evaluate prompt and thermal photons in heavy ion collisions is covered in Chapter 5.

For a complete evaluation of thermal photons, the effect on photon emission of deviation from local thermal equilibrium of the quark-gluon plasma must be included. Work on this is presented in Chapter 6.

Comparisons with direct photon measurements from both RHIC and the LHC are shown in Chapter 7, along with a complete discussion of the results.

One important topic in this last chapter is the quantification of uncertainties in the direct photon calculation. This is important both for a proper comparison between the calculations and the measurements, but also to understand the origin of possible tension with data and to point toward solutions. This represents the second aim of this thesis: identifying the sources of uncertainties in the model, to understand to which extent direct photons can currently be used as probes of the properties of the quark-gluon plasma.

Notation

- The "mostly-minus" metric is used: $g^{\mu\nu} = diag(1, -1, -1, -1)$
- Natural units are used: $\hbar = c = k_B = 1$. Consequently, both spatial and temporal values are usually given in fermi (1 fm=10^{-15} m), while energies and momentum are given in MeV or GeV. The value $\hbar c = 0.1973$ GeV fm is used to relate the two units.
- Although there are some exceptions, 4-vectors are usually written in capital letters (X^μ), with their spatial part in bold minuscule ($\mathbf{x}$) and the norm of their spatial part in normal minuscule ($x \equiv |\mathbf{x}|$).

Part II

Phenomenology and theory of heavy ion collisions

In this part of the thesis, the general phenomenology of heavy ion collisions is described. The aim is to provide a brief overview of the available measurements with as little model-dependence as possible. This first chapter on phenomenology is followed in Chapter 3 by a description of the hydrodynamical model of heavy ion collisions used in this thesis. Although emphasis is put on the model used for the present work, general comments positioning the model with respect to the rest of the field are provided.

Chapter 2

Phenomenology of ultrarelativistic heavy ion collisions

The aim of the present chapter is to provide an overview of the important observations made in ultrarelativistic heavy ion collisions at RHIC and the LHC. Measurements of hadronic observables are abundant, in particular for unidentified charged hadrons. Most of what is known about the quark-gluon plasma formed in heavy ion collisions comes from analysis of hadronic data. Electromagnetic observables, on the other hand, are an important complementary probe to hadrons. An overview of the main hadronic and electromagnetic observables is given in the second and third sections of this chapter, respectively.

The coordinate system used to analyse heavy ion measurements, along with the use of centrality to classify collisions, are two important features of heavy ion measurements. They are briefly reviewed in the first section of this chapter.

2.1 Coordinates and centralities

The coordinate system used to report momentum measurements in heavy ion collisions is the same as traditionally employed in proton-proton collisions. Using the nuclei's collision axis as reference, a plane orthogonal to it, the "transverse plane", is defined. This plane is illustrated on Figure 2.1. In this plane, momenta are reported by a 2D vector whose magnitude is the transverse momentum p_T with a direction given by the azimuthal angle ϕ. As previously mentioned, measurements in ϕ are not made with respect to any clear geometrical reference axis, but rather by correlating the azimuthal angle of different sets of

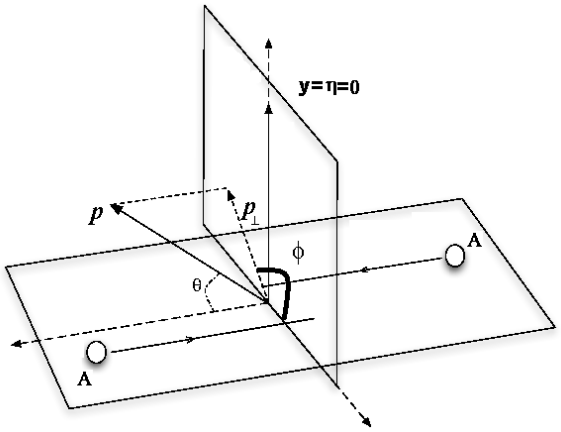

Figure 2.1: Coordinate system used in relativistic nuclear collisions (adapted from [41])

particles[1]. Along the collision axis, rapidity y or pseudorapidity η are used as coordinates, with the collision vertex of the two nuclei serving ($y = \eta = 0$) as origin. They are defined as [42, Appendix B]

$$y = \frac{1}{2} \ln \frac{P^0 + P^3}{P^0 - P^3} \tag{2.1}$$

$$\eta = -\ln \tan \frac{\theta}{2} \tag{2.2}$$

where P^0 is the particle's energy, P^3 its momentum along the collision axis, and θ is the angle with respect to this same axis. For symmetric collisions with identical nuclei of opposite momenta, the term "midrapidity" is used to refer to the region around $y = 0$.

Heavy ion collisions are systematically classified by "centralities", which characterises how much the two nuclei overlapped in the collision. The most central collisions are head-on collisions which are expected to have a roughly circular energy deposition region[2]. Peripheral collisions produce a smaller, ellipsoidal energy deposition region. The different shapes of the energy deposition region have a large effect on the subsequent evolution of the QCD medium, which makes centralities an important tool to classify collisions.

As the geometric overlap of nuclei cannot be measured experimentally, the number of particles produced in each collision is used as a proxy for centrality. The argument is that head-on collisions result in larger energy depositions, which produce a larger number of

[1] Models of nucleus collisions, such as the Glauber model [22], can be used to define a geometrical reference axis. While such definitions are useful to picture heavy ion collisions and understanding some of their properties, it does not represent information that is accessible experimentally.

[2] Central collisions result in an approximately circular energy deposition as long as the nuclei themselves are roughly spherical, which is the case for gold and lead nuclei studied in this thesis. Nuclei such as uranium, which have an ellipsoid shape, are a different story [43].

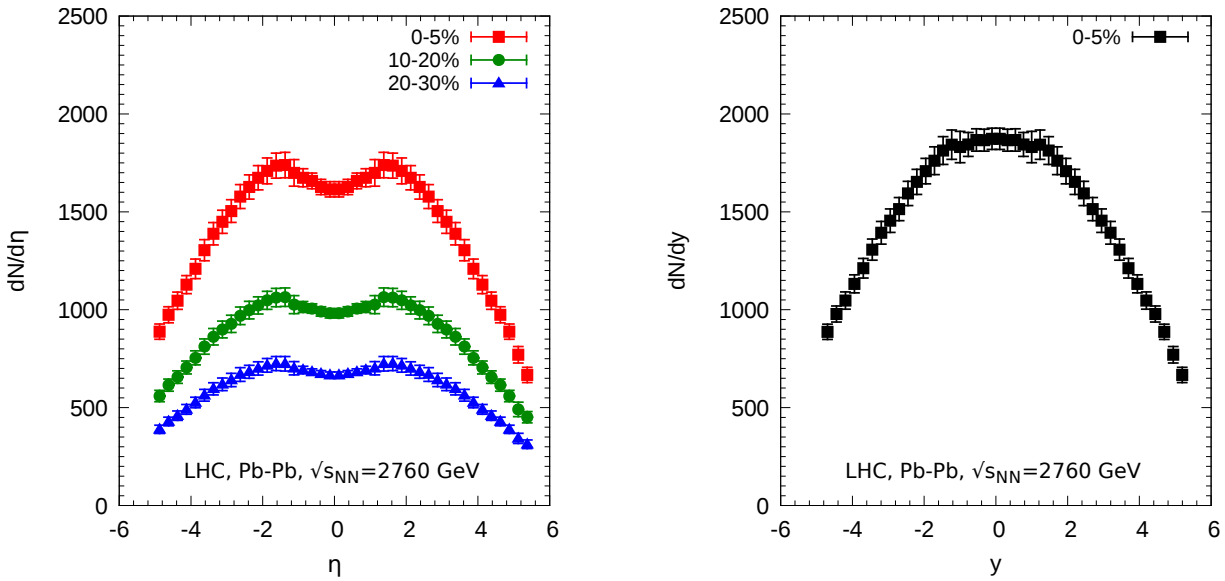

Figure 2.2: (a) Charged hadron multiplicity as a function of pseudorapidity for three centralities and (b) charged hadron multiplicity as a function of rapidity for 0-5% centrality, as measured at the LHC by the ALICE collaboration in Pb-Pb collisions at $\sqrt{s_{NN}} = 2.76$ TeV [44]

particles. The use of this proxy for centrality does not introduce any theoretical ambiguity as long as centralities are defined with multiplicity in theoretical models as well.

Centralities are quoted as fraction of measured collisions that have the largest particle production. For example, $0-5\%$ centrality refers to the subset of 5% of the collisions that produced the most particles.

2.2 Hadronic observables

The first interesting property of heavy ion collisions is the distribution of particles along the collision axis. The charged hadron multiplicity with respect to pseudorapidity, as measured at the LHC, is shown on Figure 2.2a for three different centralities. The multiplicity shows a double-peak structure around midrapidity, for all centralities. This structure can be best understood by looking at the multiplicity with respect to *rapidity*, rather than pseudorapidity. This is shown on Figure 2.2b for $0-5\%$ centrality, which corresponds to the top data points of Figure 2.2a. In rapidity the multiplicity is actually flat around midrapidity, for approximately 1-1.5 unit in rapidity. The structure observed in pseudorapidity is understood to originate from the Jacobian between rapidity and pseudorapidity.

Rapidity invariance has also been observed at RHIC [45]. It is referred to as "boost in-

variance"[3], and it is an important observation in heavy ion collisions: there is a small region around midrapidity where the mechanism of soft particle production appears to be independent of rapidity. The importance of this invariance on hydrodynamical models of heavy ion collisions was recognized early [46], since analytical solutions of relativistic hydrodynamics equations can be derived for systems exhibiting boost invariance [46, 47, 48].

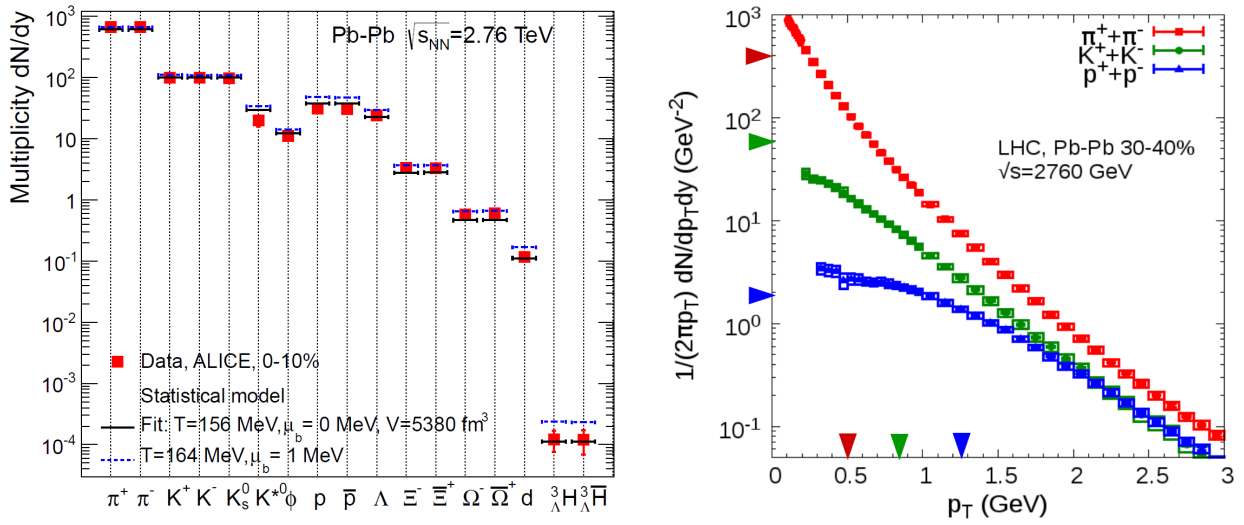

(a) (b)

Figure 2.3: (a) Multiplicity of different species of hadrons measured at the LHC, compared to a thermal model of hadron production (Figure from [49]) (b) Pions, kaons and protons spectra at the LHC with their multiplicity and mean p_T indicated by arrows on the vertical and horizontal axes, respectively (Data from [50])

The majority of hadrons produced in this central plateau are soft pions. This is shown on Figure 2.3a, along with the multiplicity of many other hadrons measured in 0-10% centrality Pb-Pb collisions at the LHC. The different hadronic abundances are described very well by a simple thermal model, with a temperature of the order of that expected for confinement ($T \sim 160$ MeV) along with a vanishingly small baryon chemical potential. This value for the baryon chemical potential is a simple consequence of baryons all having approximately the same multiplicity as their antibaryon.

Hadrons have a non-trivial transverse momentum distribution, shown on Figure 2.3b for pions, kaons and protons in 30-40% centrality Pb-Pb collisions at the LHC. The multiplicity and average transverse momentum of each species of hadrons is indicated by arrows on the vertical and horizontal axes, respectively. While the multiplicity is an important observable, this transverse momentum distribution provides much stronger constraints on the

[3] A Lorentz boost is equivalent to a simple shift in rapidity.

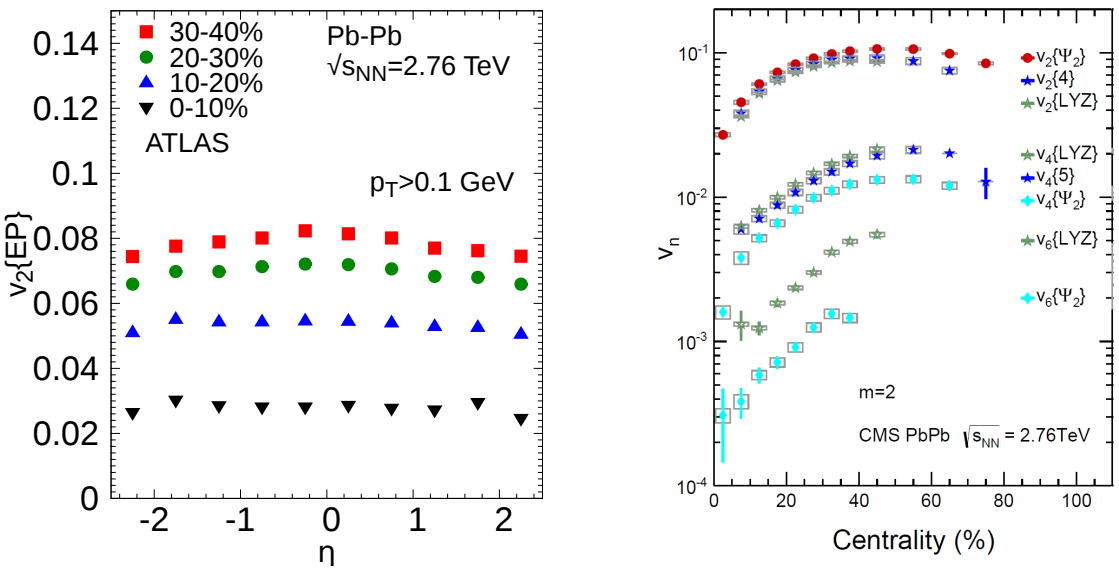

(a) (b)

Figure 2.4: (a) v_2 of charged hadrons with respect to pseudorapidity, measured at the LHC (Data from [51]) (b) Different definitions of v_2, v_4 and v_6 of charged hadrons measured at the LHC (Figure adapted from [52])

mechanisms of hadron production in heavy ion collisions.

The azimuthal anisotropy of hadrons, as introduced in Section 1.4, constitutes another major observable in heavy ion physics. The pseudorapidity and centrality dependence of the p_T-integrated v_2 of charged hadrons is shown on Figure 2.4a. The relative invariance of v_2 in pseudorapidity supports the conclusion reached from Figure 2.2 regarding the existence of a central plateau for particle production in rapidity[4]. Moreover, the centrality dependence of v_2 is clear: the more central the collision, the smaller the v_2. This is consistent with the explanation for the origin of v_2 given in Section 1.4 in terms of pressure gradients developed from an anisotropic energy deposition.

Higher order v_n have also been measured at RHIC and the LHC. Measurements of v_2, v_4 and v_6 at the LHC are shown on Figure 2.4b. For almost every particle species and centrality class, the values of v_n are ordered such that $v_n > v_{n+1}$. This is clear from Figure 2.4b where there is almost an order of magnitude between v_2, v_4 and v_6.

Each anisotropy coefficient $v_n\{\ldots\}$ on Figure 2.4b are shown for two or three different definitions of the momentum anisotropy. These multiple definitions of $v_n\{\ldots\}$ are a consequence of the impossibility of measuring directly the v_n of a single event, which was defined in Equation 1.3. Each definition of $v_n\{\ldots\}$ has a different mapping to event-averages of the

[4] Since v_2 is a ratio, the effect of the Jacobian between the rapidity and pseudorapidity seen in the spectrum largely cancels out.

single-event Fourier coefficient v_n from Equation 1.3. However, unless exotic definitions of $v_n\{\ldots\}$ are used, they all give similar values, typically differing by 10-20%.

In this thesis, charged hadron anisotropies measured with the two-particle cumulant $v_n\{2\}$ are used as far as possible, to avoid confusion. This definition of $v_n\{\ldots\}$ is measured experimentally as [53, 54]

$$v_n^{exp}\{2\} = \sqrt{\left\langle \left\langle e^{in(\phi_1-\phi_2)} \right\rangle_{\text{particles}} \right\rangle_{\text{events}}} \tag{2.3}$$

where the inner brackets represent an average over all particles of interests (e.g. charged hadrons) within an event, and the outer brackets are an average over events in a given centrality class. The two-particle cumulant is also called the "scalar product (SP) method"; $v_n^{exp}\{2\}$ and $v_n^{exp}\{\text{SP}\}$ are used interchangeably in this thesis.

For charged hadrons, $v_n\{2\}$ can be computed theoretically from the single-event v_n given by Equation 1.3 as [54]

$$v_n^{th}\{2\} = \sqrt{\langle (v_n)^2 \rangle_{\text{events}}} \tag{2.4}$$

where the average over events is made in the appropriate centrality class.

This closes this short overview of hadronic observables in heavy ion collisions. Photonic observables are reviewed in the next section.

2.3 Photons

Most photons measured in heavy ion collisions originate from hadronic decays. These photons carry essentially the same information as hadrons themselves. Since the latter are often easier to measure, hadronic decay photons are not of primary interest to investigate the properties of the quark-gluon plasma. Direct photons, which is the photon signal remaining after subtracting the dominant hadronic decays, are much more interesting.

As seen in the introduction, two major contributions to direct photons are thermal and prompt photons. Thermal photons are of interest for the information they provide about the local state of the QGP at the moment of their emission. Prompt photons carry less information about the medium than thermal ones, but are not insensitive to it either, as explained below.

A short summary of prompt, thermal and other possible sources of direct photons is provided in what follows.

2.3.1 Prompt photons

As explained in the introduction, photons can be produced by the hard scattering of partons from each colliding nuclei. This process can be calculated in perturbative QCD from Equation 1.1. More precisely, photons can be produced by two different channels in such reactions[5]. The first one is through fragmentation, just like hadrons:

$$E\frac{d^3\sigma_{pp}}{d\mathbf{p}} = \sum_{a,b,c,d} f_{a/p}(x_a) \otimes f_{b/p}(x_b) \otimes d\hat{\sigma} \otimes D_{\gamma/c}(z_c) \tag{2.5}$$

where parton "c" has a probability of producing a photon of momentum $p_T^\gamma = z_c p_c$ as it fragments. This probability is given by the non-perturbative fragmentation function $D_{\gamma/c}(z_c)$.

Photons can also be produced without going through a fragmentation process, a channel that will be referred to as "isolated photons" in this thesis[6]:

$$E\frac{d^3\sigma_{pp}}{d\mathbf{p}} = \sum_{a,b,d} f_{a/p}(x_a) \otimes f_{b/p}(x_b) \otimes d\hat{\sigma} \tag{2.6}$$

where parton "c" is replaced by a photon. Consequently $d\hat{\sigma}$ describes the process $ab \to \gamma d$ where a, b and d are partons. The leading processes are Compton scattering $gq \to \gamma q$ and quark-antiquark annihilation $q\bar{q} \to \gamma g$.

Isolated photons dominate the prompt photon signal at high p_T, while fragmentation photons are dominant at low p_T. This is shown on Figure 2.5a for proton-proton collisions at RHIC. Isolated photons are the largest contribution to prompt photons above $p_T \sim$ 4 GeV, with fragmentation photons taking over below that. Since low p_T direct photon measurements are not available yet for proton-proton collisions at the LHC, the contribution of isolated and fragmentation photons is shown for Pb-Pb collisions instead. For such nucleus-nucleus collisions, perturbative QCD needs to be supplemented with binary scaling — the assumption that as far as prompt photon production is concerned, nucleus-nucleus collisions

[5]Once final states with more than two particles are taken into account, the division of prompt photons into two fully distinct production channels becomes ambiguous. This subtlety is not of primary importance for the discussion presented in this section, but will be addressed again in Section 5.2.1 when perturbative QCD is explained in greater details.

[6] The nomenclature used to describe the different photon production channels in heavy ion collisions is far from uniform and can bring its share of confusion. The term "isolated photons" suggested in Ref. [55] for processes such as Compton scattering and quark-antiquark annihilation is used in this thesis. It is not a perfect choice since it can be confused with isolated photon measurements, which are photon measurements that suppress background photons through an isolation criteria. Since such isolated photon measurements are not used in this thesis outside of this section, there should not be any confusion on the meaning of "isolated".

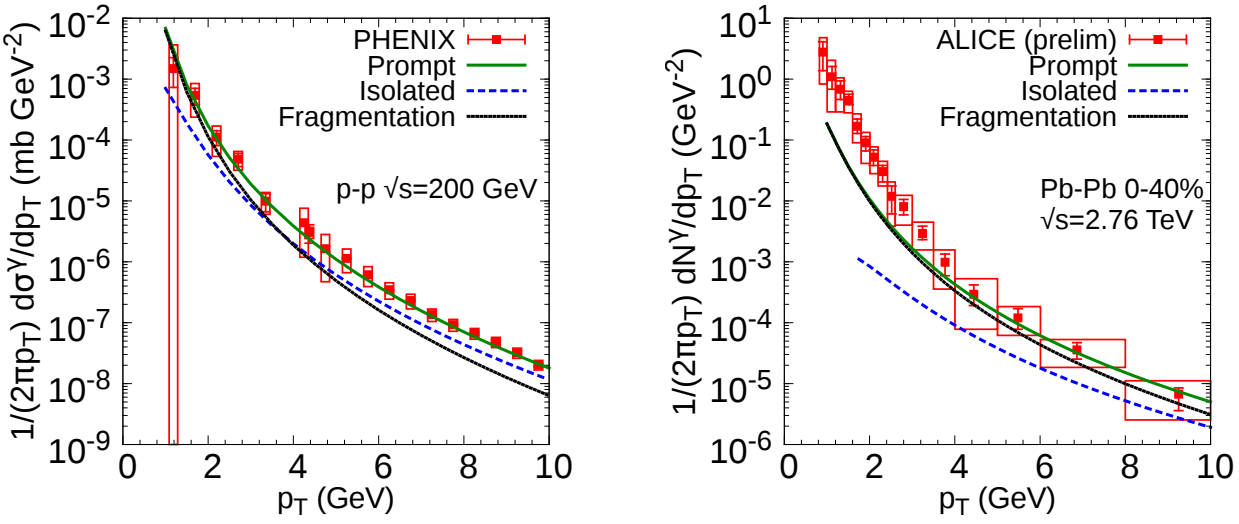

(a) (b)

Figure 2.5: (a) Contribution of the isolated and fragmentation channels to prompt photons, as computed with next-to-leading order perturbative QCD in p-p collisions at $\sqrt{s_{NN}} = 200$ GeV, compared with direct photon measurements from the PHENIX collaboration (data from [20]) (b) perturbative QCD calculations of prompt photons in Pb-Pb collisions at $\sqrt{s_{NN}} = 2.76$ TeV, scaled by the number of binary collisions and compared with preliminary measurements of direct photons from the ALICE collaboration (data from [17])

behave as an incoherent sum of proton-proton collisions. Using binary scaling[7], prompt photons and their contribution from isolated and fragmentation photons can be evaluated and compared with Pb-Pb measurements, shown on Figure 2.5b. At low p_T, fragmentation photons are by far the largest contribution to prompt photons at the LHC, dominating over the entire range of p_T shown. Only at $p_T \sim 15$ GeV does the isolated photon component overtake the fragmentation one.

It is clear from Figure 2.5b that binary scaling and perturbative QCD can describe direct photon measurements in heavy ion collisions very well above $p_T \sim 4$ GeV. Below $p_T \sim 4$ GeV the large excess of photons that is the main topic of this thesis is clearly visible.

There is much support for the validity of binary scaling in proton-nucleus and nucleus-nucleus collisions, independent of the validity of perturbative QCD calculations. A good example is the measurement of direct photons in deuteron-gold collisions at RHIC, shown on Figure 2.6 together with direct photons from proton-proton collisions. As can be seen on the figure, direct photons from deuteron-gold collisions are very well described by normalizing

[7] The normalisation factor used here is $12.8\,\mathrm{mb}^{-1}$, as computed in the Glauber model using an inelastic nucleon-nucleon cross-section of 64 mb. This corresponds to a superposition of $\sim$ 819 nucleon-nucleon collisions.

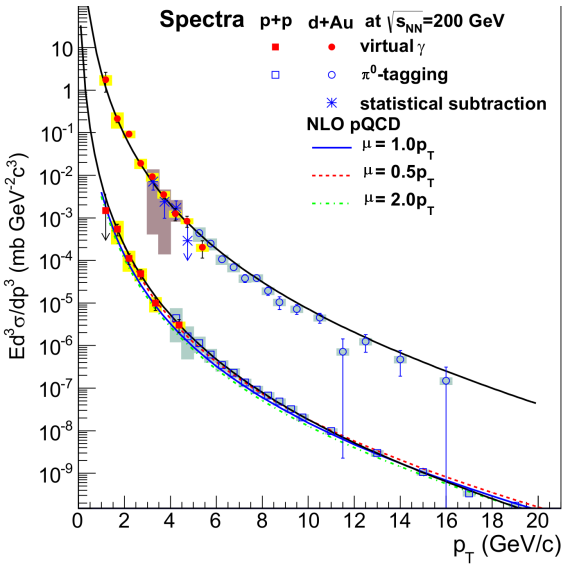

Figure 2.6: Direct photon production in proton-proton and deuteron-gold collisions at RHIC (adapted from [20])

a fit of the proton-proton measurement with the number of binary collisions evaluated from the Glauber model [22]. There are thus no signs of any deviation from binary scaling, nor of any significant source of photons beside prompt ones in deuteron-gold collisions[8].

One possibility that has not yet been widely investigated is that prompt photons could be considerably affected by parton energy loss due to interactions with the quark-gluon plasma. This effect was explained in the introduction (Section 1.3) in the context of hadronic energy loss in central heavy ion collisions. While isolated photons are not expected to suffer any significant energy loss, fragmentation photons should be affected by partonic energy loss to a level similar to hadrons (see e.g. [57, 58, 59]). Remembering that fragmentation photons are the dominant source of prompt photons at low p_T (Figure 2.5), this could change considerably the contribution of prompt photons at low p_T in heavy ion collisions.

Moreover partonic interactions with the QGP do not only result in an energy loss for partons, but also in the production of additional photons. These photons are called "jet-medium photons", and are expected to partially counterbalance for the reduction in photons due to parton energy loss. The actual level of compensation can only be accurately determined by simulations including both effects consistently. Preliminary work in this direction was made in Refs. [57, 58].

Both jet-medium photons and fragmentation photons affected by energy loss are ex-

[8] A small thermal signal was predicted in Ref. [56] for deuteron-gold collisions. Considerably smaller uncertainties are still required on the direct photon spectrum in deuteron-gold collisions before this prediction can be confirmed or refuted.

pected to have a momentum anisotropy. Each source's anisotropy is expected to be of opposite sign: the more medium is encountered in a given direction, the larger the energy loss of fragmentation photons, and the more jet-medium photons produced as well. The momentum anisotropies of the two sources have been found to largely cancel out in previous calculations [58]. More work will be necessary to determine if this finding can be confirmed from other approaches. Low p_T measurements of direct photons in heavy ion collisions using isolation techniques to reduce the contribution of fragmentation and jet-medium photons could also provide useful complementary experimental constraints on the prompt photon contribution [60].

2.3.2 Thermal photons

Thermal photons are photons emitted by the quark-gluon plasma during its short lifetime. Two significant observations make them prime candidates for the direct photon excess observed in heavy ion collisions. The first one is the shape of the direct photon spectrum at low p_T, which is exponential, in agreement with a signal dominated by thermal photons. This is a consequence of photon emission rates from the quark-gluon plasma being approximately exponential in p_T as well.

Another important lead on the origin of the direct photon excess is the large momentum anisotropy of low p_T direct photons. This momentum anisotropy is of the same magnitude as that of pions, which suggests that this direct photon v_2 is produced by a mechanism similar to that producing the hadronic anisotropy: the imprint of the anisotropic hydrodynamical flow on the produced particles, hadrons or photons.

Both observations hint that the direct photon excess originates from thermal photons, which is the reason behind the significant efforts put into quantifying precisely their contribution.

2.3.3 Other sources

Other sources of direct photons have been suggested in heavy ion collisions over the years. Two prominent examples are the production of photons from the strong magnetic fields generated in heavy ion collisions, suggested as a significant source of momentum anisotropy [61], and the possibility of significant photon production from the pre-thermal phase of the collisions [62].

Photons originating from such sources can have very clear signatures. For example, the photon source proposed in Ref. [61] predicts a large contribution to v_2 but a much smaller one to v_3. Seeing such a signature (e.g. a large v_2/v_3 ratio) directly from measurements

would require this specific source of direct photons to be the dominant one, much larger than e.g. thermal photons.

A more likely scenario is that alternative photon sources contribute to direct photons alongside more traditional sources (thermal and prompt). In this case, comparisons with measurements must be made by evaluating these new photon sources in frameworks where prompt, thermal and new photon sources can be investigated concurrently and consistently. This has not been done yet.

Chapter 3

Hydrodynamical modelling of heavy ion collisions

Hydrodynamics is at the core of the present understanding of the quark-gluon plasma formed in heavy ion collisions. While it is the central element of hydrodynamical models, it cannot describe the entire spacetime evolution of heavy ion collisions, and must thus be complemented by other models. As seen in Section 1.2 and illustrated on Figure 1.3a, the hydrodynamical evolution of the QGP is preceded by a thermalisation phase. From a theoretical point of view, the result of this thermalisation process determines the boundary conditions of the hydrodynamics equations.

Similarly, as the hydrodynamical evolution proceeds, the medium's temperature and energy decrease. This rarefication of the medium eventually makes it impossible for local thermal equilibrium to be maintained, leading to a breakdown of the hydrodynamical description of the medium. At this point the medium must be described by a different framework, such as kinetic theory.

These transitions to and from hydrodynamics are major components of hydrodynamical models of heavy ion collisions. The aim of this chapter is to present each component and describe how they are related to each other. The first step is to present relativistic hydrodynamics itself.

3.1 Relativistic hydrodynamics

The symmetries of a complex microscopic system remain valid at macroscopic scales, and form the basis of any attempt at understanding the system's long-scale properties. Poincaré invariance implies the conservation of energy and momentum, which can be written as an

equation of motion for the energy-momentum tensor $T^{\mu\nu}$ of the system [63]:

$$\partial_\mu T^{\mu\nu}(X) = 0 \tag{3.1}$$

where X is the position 4-vector and $\partial_\mu \equiv \partial/\partial X^\mu$.

Other symmetries such as the baryon number, electric charge and strangeness conservation are written as

$$\partial_\mu j^\mu(X) = 0 \tag{3.2}$$

where j^μ is the current associated with the conserved charge.

As seen in Section 2.2, the net baryon density is negligible at the LHC, implying the trivial solution $j^\mu_B \approx 0$ for the baryon current. The same conclusion can be reached for $\sqrt{s_{NN}} = 200$ GeV collisions at RHIC[1] from the observation that baryons and antibaryons have essentially identical multiplicity, spectrum, ... For the same reasons, electric charge and strangeness conservation are not considered either. For the present work, it is thus not necessary to solve the equation of motion given by Equation 3.2.

Equation 3.1 is of limited use if no further assumptions can be made about the underlying microscopic system. A common assumption in physics is global thermal equilibrium, in which case thermodynamics can be used to describe the system's macroscopic properties. In this case, the properties of the system are quantified with its temperature, pressure, entropy, ...

When dynamical systems are under consideration, a more realistic assumption than global equilibrium is "local thermal equilibrium". It is the hypothesis that every part of the system can be approximated to be, locally, in a state of thermodynamic equilibrium, with the assumption that this local equilibrium can be maintained for a certain time as the system evolves. This assumption forms the basis of hydrodynamics.

A hierarchy of scales is needed in a system for local thermal equilibrium to be a realistic assumption:

- A microscopic scale at which the relevant microscopic dynamics (e.g. QCD) is at play
- An intermediate scale which is large enough compared to the microscopic one for thermodynamics to be applicable at this scale
- A macroscopic scale large enough for the intermediate scale to be treated in the continuous limit

In a system where such a hierarchy exists, and where sufficient separation exists between the different scales, local thermal equilibrium can be achieved as long as the timescale for

[1] For lower energy collisions at RHIC, baryon number conservation can become important. Such collisions are not investigated in this thesis.

microscopic interactions is small compared to the timescale over which the macroscopic system evolves [64, Section 2].

If a system is strictly in local thermal equilibrium, it is described by ideal hydrodynamics. When local equilibrium is not exact and a medium exhibits small deviations from it, a generalisation of ideal hydrodynamics must be used: viscous hydrodynamics.

Since most of the intuition about hydrodynamics originates from the ideal case, it is preferable to present it first.

3.1.1 Ideal relativistic hydrodynamics

The energy momentum tensor of a system in global thermal equilibrium, at rest, is given by $T^{\mu\nu} = diag(\epsilon, \mathcal{P}, \mathcal{P}, \mathcal{P})$ where ϵ is the energy density and $\mathcal{P}$ is the pressure. Boosted in a frame where the fluid has a 4-velocity[2] $u^\mu = (u^0, \mathbf{u})$, $T^{\mu\nu}$ takes the form [63]

$$T^{\mu\nu} = (\epsilon + \mathcal{P})u^\mu u^\nu - \mathcal{P}g^{\mu\nu} \tag{3.3}$$

where $u^\mu u_\mu = 1$.

The energy-momentum tensor of a continuous extended system in local thermal equilibrium is simply

$$T^{\mu\nu}(X) = [\epsilon(X) + \mathcal{P}(X)]\, u^\mu(X)u^\nu(X) - \mathcal{P}(X)g^{\mu\nu}(X) \tag{3.4}$$

where $\epsilon(X)$ and $\mathcal{P}(X)$ are the energy density and pressure of the system at point X, in the local rest frame of the fluid, and $u^\mu(X)$ is the velocity of the fluid element at point X. Since the energy density and the pressure are related by thermodynamics relations, only one of them is a degree of freedom. Moreover the flow velocity $u^\mu(X)$ has three degrees of freedom, since it is a unit vector. The energy-momentum tensor $T^{\mu\nu}(X)$ thus have four degrees of freedom.

The conservation equation 3.1 provides four independent equations that fully constrain the spacetime evolution of $T^{\mu\nu}(X)$. Ideal hydrodynamics can thus be summarized by Equation 3.1 and 3.4, along with an equation of state relating the pressure to the energy density.

Exact local thermal equilibrium is a strong assumption that closely constrains the spacetime evolution of a system. If the system is close but not fully in local thermal equilibrium, ideal hydrodynamics is not sufficient to describe its long-scale dynamics. It is nevertheless possible to extend hydrodynamics to describe such systems, which is the topic of the next section.

[2] A more familiar way of writing the 4-velocity is $u^\mu = (u^0, \mathbf{u}) = (\gamma, \gamma\mathbf{v})$, where γ is the Lorentz factor and $\mathbf{v}$ the velocity.

3.1.2 Viscous hydrodynamics

Viscous hydrodynamics is the generalisation of ideal hydrodynamics to systems which deviate from local equilibrium. For such systems, much of the clarity of the ideal case vanishes. It is nevertheless possible to formulate hydrodynamical equations to describe systems that are near but not exactly in local thermal equilibrium, partly based on generalisation of ideal hydrodynamics, and partly based on other approaches such as kinetic theory.

The first requirement is to define a local rest frame for the different parts of the system, a frame where thermodynamical relations are well-defined locally. The most common choice is to select the rest frame with the energy [64, Section 2]:

$$T^{\mu}{}_{\nu}(X)u^{\nu}(X) \equiv \epsilon(X)u^{\mu}(X);\ u^{\mu}u_{\mu} = 1 \tag{3.5}$$

where $T^{\mu\nu}(X)$ is the energy-momentum tensor, $\epsilon(X)$ is the energy density and $u^{\mu}(X)$ is the unit flow velocity. The rest frame of a fluid element is obtained by boosting it to a frame where $u^{\mu}(X) = (1, 0, 0, 0)$.

Tensor decomposition can be used to write a generalised version of $T^{\mu\nu}$ as [64, Section 2]

$$T^{\mu\nu}(X) = \epsilon(X)u^{\mu}(X)u^{\nu}(X) + \frac{1}{3}\left[T^{\alpha}{}_{\alpha}(X) - \epsilon(X)\right]\Delta^{\mu\nu}(X) + \pi^{\mu\nu}(X) \tag{3.6}$$

where $\Delta^{\mu\nu}(X) \equiv g^{\mu\nu} - u^{\mu}(X)u^{\nu}(X)$. At this point, $\pi^{\mu\nu}(X)$ is still an arbitrary tensor defined so as to possess the following symmetries:

$$\begin{aligned} \pi^{\mu\nu}(X) &\equiv \pi^{\nu\mu}(X) \\ \pi^{\mu\nu}(X)u_{\nu}(X) &\equiv 0 \\ \pi^{\mu}{}_{\mu}(X) &\equiv 0 \end{aligned} \tag{3.7}$$

The trace $T^{\alpha}{}_{\alpha}(X)$ can be rewritten in a more meaningful way by exploiting the knowledge that, in an equilibrium system at rest

$$T^{\alpha}{}_{\alpha\ (\mathrm{eq})}(X) = \epsilon(X) - 3\mathcal{P}(X) \tag{3.8}$$

where $\mathcal{P}(X)$ is the pressure. One can define a scalar $\Pi(X)$ such that, in general, $T^{\alpha}{}_{\alpha}$ can be written

$$T^{\alpha}{}_{\alpha}(X) \equiv \epsilon(X) - 3\left[\mathcal{P}(X) + \Pi(X)\right] \tag{3.9}$$

With this definition for $\Pi(X)$, the energy-momentum tensor can be written:

$$T^{\mu\nu}(X) = \epsilon(X)u^{\mu}(X)u^{\nu}(X) - \left[\mathcal{P}(X) + \Pi(X)\right]\Delta^{\mu\nu}(X) + \pi^{\mu\nu}(X) \tag{3.10}$$

By comparison with the ideal $T^{\mu\nu}$ (Eq. 3.4), it is clear that $\Pi(X)$ and $\pi^{\mu\nu}(X)$ are related to the deviation of the system from equilibrium. There is however no constraints on their spacetime evolution at the moment.

Kinetic theory can be used to derive equations of motion for $\Pi(X)$ and $\pi^{\mu\nu}(X)$. The rationale is that there exists regimes where both viscous hydrodynamics and kinetic theory are valid[3] [64, Section 4.1]. Once equations for $\Pi(X)$ and $\pi^{\mu\nu}(X)$ are derived from kinetic theory, it can be expected that they will hold even when a kinetic theory description of the medium becomes impossible.

The starting point is the relativistic Boltzmann equation [65]

$$K^{\mu}\partial_{\mu}f(X,K) = C[f(X,K)] \tag{3.11}$$

where $f(X,K)$ is the single particle distribution function and $C[f(X,K)]$ is the collision term.

For a system in thermal equilibrium, $f(X,K) = f^{(0)}(K)$, the Fermi-Dirac or Bose-Einstein distribution, and both sides of the equation vanish by definition. For a system close yet not exactly in equilibrium, $f(X,K)$ can be written

$$f(X,K) = f^{(0)}(K) + \delta f(X,K) \tag{3.12}$$

The equilibrium pressure and energy density can be given precise kinetic theory definitions in function of $f^{(0)}(K)$ [65, Section 3], while the Π and $\pi^{\mu\nu}$ can be related to $f^{(0)}(K)$ and $\delta f(X,K)$. Given a choice of collision term $C[f(X,K)]$, Equation 3.11 can then be used to derive equations of motion for $\Pi(X)$ and $\pi^{\mu\nu}(X)$ in a given approximation scheme.

Kinetic theory has the benefit of allowing for systematic expansion parameters to be used. The expansion in Knudsen and inverse Reynolds numbers from Ref. [66] forms the basis of the hydrodynamical model used in this work. The Knudsen number $Kn = \lambda/L$ quantifies the ratio of the microscopic mean-free-path λ and a macroscopic length scale L of the medium, while the inverse Reynolds number compares the contribution of the viscous part of the energy-momentum tensor to the ideal one through the ratios $R_{\Pi}^{-1} = |\Pi|/\mathcal{P}$ and $R_{\pi}^{-1} = |\pi^{\mu\nu}|/\mathcal{P}$ [66]. With these definitions, it is possible to find equations of motion for $\Pi(X)$ and $\pi^{\mu\nu}(X)$ with contributions up to second order in the Knudsen and inverse Reynolds

[3] An example provided in Ref [64, Section 4.1] is that of a weakly-coupled and slowly expanding system: weak coupling makes a kinetic theory description possible, while the slow expansion allows for local thermal equilibrium to be maintained despite the weak coupling. The medium produced in heavy ion collisions appears to be the exact opposite: strong coupling and fast expansion.

number:

$$\tau_\Pi \dot{\Pi} + \Pi = -\zeta\theta + \mathcal{K} + \mathcal{R} + \mathcal{J} \tag{3.13}$$

$$\tau_\pi \Delta^{\mu\nu}_{\alpha\beta} \pi^{\alpha\beta} + \pi^{\mu\nu} = 2\eta\sigma^{\mu\nu} + \mathcal{K}^{\mu\nu} + \mathcal{R}^{\mu\nu} + \mathcal{J}^{\mu\nu} \tag{3.14}$$

where $-\zeta\theta$ and $2\eta\sigma^{\mu\nu}$ are the only first order terms. The term $\mathcal{K}$ represents contributions that are second order in the Knudsen number, while $\mathcal{R}$ contains second order contributions in the inverse Reynolds number. Mixed Knudsen/Reynolds terms are in $\mathcal{J}$.

The following definitions were used in Equations 3.13 and 3.14:

$$\theta \equiv \partial_\mu u^\mu \tag{3.15}$$

$$\Delta^{\mu\nu}_{\alpha\beta} \equiv \frac{1}{2}\left(\Delta^\mu_\alpha \Delta^\nu_\beta + \Delta^\mu_\beta \Delta^\nu_\alpha\right) - \frac{1}{3}\Delta^{\mu\nu}\Delta_{\alpha\beta} \tag{3.16}$$

$$\sigma_{\mu\nu} \equiv \Delta^{\mu\nu}_{\alpha\beta} \partial^\alpha u^\beta \tag{3.17}$$

The (relativistic) Navier-Stokes equations can be recovered from Equations 3.13 and 3.14 by dropping second order terms ($\mathcal{K}$, $\mathcal{R}$ and $\mathcal{J}$, plus the $\dot{\Pi}$ and $\dot{\pi}^{\alpha\beta}$ terms on the left-hand-side). While they are much simpler, the relativistic Navier-Stokes equations are acausal and prone to numerical instabilities [67] , which is why second order equations are typically used to describe relativistic systems.

The only first-order transport coefficients are the bulk viscosity ζ and the shear viscosity η. The $\mathcal{K}$, $\mathcal{R}$ and $\mathcal{J}$ terms of Equations 3.13 and 3.14 contain a total of 17 terms with the same number of second order transport coefficients.

All these transport coefficients can in theory be evaluated from kinetic theory, given a collision kernel $C[f(X,K)]$. However, the aim of deriving equations for Π and $\pi^{\mu\nu}$ is that they should hold beyond the regimes of applicability of kinetic theory. In such regimes, the relation between transport coefficients and $C[f(X,K)]$ does not hold anymore.

Instead, efforts were made to identify the dominant second order terms [68], and to find relation between the second and first order transport coefficients [69]. This information was used, along with consideration of numerical stability[4] , to restrict the second order terms included in the hydrodynamical equations used in this thesis to:

$$\mathcal{R}^{\mu\nu} = \varphi_7 \pi^{\lambda\langle\mu}\pi^{\nu\rangle}_\lambda \tag{3.18}$$

[4] For example, the term $2\tau_\pi \Delta^{\mu\nu}_{\alpha\beta}\pi^\alpha_\lambda \omega^{\beta\lambda}$, with $\omega^{\mu\nu} \equiv \frac{1}{2}\left(\nabla^\mu u^\nu - \nabla^\nu u^\mu\right)$ and $\nabla^\mu \equiv \Delta^{\mu\nu}\partial_\nu$, contributes to $\mathcal{J}^{\mu\nu}$. However it has been found to have a small effect on the hydrodynamical simulation, but also to introduce numerical instabilities in certain cases (the hydrodynamical evolution varies considerably from event to event due to the fluctuations present in the initial conditions). Consequently it was omitted from the hydrodynamics equations.

$$\mathcal{J} = -\delta_{\Pi\Pi}\Pi\theta + \lambda_{\Pi\pi}\pi^{\mu\nu}\sigma_{\mu\nu} \tag{3.19}$$

$$\mathcal{J}^{\mu\nu} = -\delta_{\pi\pi}\pi^{\mu\nu}\theta - \tau_{\pi\pi}\pi^{\lambda\langle\mu}\sigma_{\lambda}^{\ \nu\rangle} + \lambda_{\pi\Pi}\Pi\sigma^{\mu\nu} \tag{3.20}$$

Coefficients τ_Π, $\delta_{\Pi\Pi}$, $\lambda_{\Pi\pi}$, τ_π, $\delta_{\pi\pi}$, $\tau_{\pi\pi}$ and $\lambda_{\pi\Pi}$ are all second-order transport coefficients. Using relations derived from kinetic theory in [68, 69], they are all related to first order coefficients:

$$\phi_7 = \frac{9}{70\mathcal{P}} \tag{3.21}$$

$$\tau_\Pi = \frac{\zeta}{15\left(\frac{1}{3} - c_s^2\right)^2(\epsilon + \mathcal{P})} \tag{3.22}$$

$$\delta_{\Pi\Pi} = \frac{2}{3}\tau_\Pi \tag{3.23}$$

$$\lambda_{\Pi\pi} = \frac{8}{5}\left(\frac{1}{3} - c_s^2\right)\tau_\Pi \tag{3.24}$$

$$\tau_\pi = \frac{5\eta}{(\epsilon + \mathcal{P})} \tag{3.25}$$

$$\delta_{\pi\pi} = \frac{4}{3}\tau_\pi \tag{3.26}$$

$$\tau_{\pi\pi} = \frac{10}{7}\tau_\pi \tag{3.27}$$

$$\lambda_{\pi\Pi} = \frac{6}{5} \tag{3.28}$$

$$\tag{3.29}$$

where c_s is the speed of sound, available through the equation of state.

Owing to their basis in kinetic theory, it is fully understood that these relations may not hold exactly when the medium being described is a strongly coupled quark-gluon plasma, which is not expected to have a quasi-particle description necessary for the use of kinetic theory. On the other hand, it is reasonable to assume that these relations capture the main dependence of the second order coefficients in terms of first order transport coefficients and thermodynamical properties.

The hydrodynamical equations used in this work can thus be summarized as

$$\tau_\Pi\dot{\Pi} + \Pi = -\zeta\theta - \delta_{\Pi\Pi}\Pi\theta + \lambda_{\Pi\pi}\pi^{\mu\nu}\sigma_{\mu\nu} \tag{3.30}$$

$$\tau_\pi\Delta^{\mu\nu}_{\alpha\beta}\pi^{\alpha\beta} + \pi^{\mu\nu} = 2\eta\sigma^{\mu\nu} - \delta_{\pi\pi}\pi^{\mu\nu}\theta - \tau_{\pi\pi}\Delta^{\mu\nu}_{\alpha\beta}\pi^{\lambda\alpha}\sigma^{\beta}_{\lambda} + \lambda_{\pi\Pi}\Pi\sigma^{\mu\nu} + \varphi_7\Delta^{\mu\nu}_{\alpha\beta}\pi^{\lambda\alpha}\pi^{\beta}_{\lambda} \tag{3.31}$$

where ζ and η are the only "free" transport coefficients. Hydrodynamical models of heavy ion collisions are used precisely to investigate ζ and η by comparison with measurements.

Effectively, this requires a parametrization for $\zeta(T)$ and $\eta(T)$ with a finite number of degrees of freedom that can be fixed by comparison with data. The parametrizations used in this work are specified in Chapter 4.

3.1.3 Coordinate system

As seen in Section 2.2, the momentum rapidity distribution of hadrons is approximately flat around midrapidity, forming an extended plateau. This is interpreted as a consequence of an approximately uniform energy deposition in spatial rapidity η around the collision vertex ($\eta = z = 0$). It is thus advantageous to use coordinates for which this symmetry can be made explicit. These coordinates are hyperbolic coordinates (τ, x, y, η):

$$\tau \equiv \sqrt{t^2 - z^2} \tag{3.32}$$

$$\tanh(\eta) \equiv \frac{z}{t} \tag{3.33}$$

and x and y are regular Cartesian coordinates in the transverse plane.

Particles produced at midrapidity originate mainly from the region $z = \eta \approx 0$ of the medium. If midrapidity observables are the only ones investigated with the model, it is often enough to assume an infinite plateau in η and forget about the fall-off of the plateau at larger η. In this case the hydrodynamical equations can be reduced from $3+1$D $[(\tau, x, y, \eta)]$ to $2+1$D $[(\tau, x, y)]$, which allows for a considerable gain of computational efficiency.

Since the observables investigated in this thesis are indeed limited to midrapidity observables, $2+1$D hydrodynamics is used in this work.

3.1.4 Solving viscous hydrodynamics

Solving viscous hydrodynamics implies solving Equations 3.1, 3.5, 3.30 and 3.31 given an equation of state that relates the different thermodynamic quantities of the medium. Viscous hydrodynamics must be solved numerically using a scheme robust enough to handle the large gradients found in heavy ion collisions.

For this thesis, the code MUSIC [70, 28] is used to solve Equations 3.1, 3.5, 3.30 and 3.31 using the Kurganov-Tadmor algorithm [71]. While it can solve the full $3+1$D equations in (τ, x, y, η) coordinates, the code is used in $2+1$D in the present work, as discussed above.

The code MUSIC includes routines to initialize the hydrodynamics equation with realistic initial conditions for heavy ion collisions. These initial conditions are the subject of the next section.

3.2 Initial state

It is understood that an "early time" or "pre-equilibrium" phase precedes the establishment of near local thermal equilibrium in the quark-gluon plasma produced in heavy ion collisions. Understanding the early time dynamics of heavy ion collisions is a challenge, in particular the mechanisms through which rapid thermalisation of colored matter is achieved. Although much progress has been made over the past decades [72] the initial conditions of hydrodynamical simulations of heavy ion collisions cannot yet be determined from first principles. This makes initial conditions one of the biggest source of uncertainty in hydrodynamical models.

Various approaches have been used historically to model the state of the quark-gluon plasma at the moment that thermalisation is achieved, without attempting to describe the thermalisation process itself. These attempts focused on the energy distribution in the transverse plane only, since the first hydrodynamical models were ideal and $2+1$D. The Glauber model [22], which describes the distribution of nucleon-nucleon collisions in a nucleus-nucleus collision, is still widely used. Energy is deposited in the transverse plane at the position of the nucleon-nucleon collisions, providing an energy density profile to initialise the hydrodynamics equations. The Glauber model does not provide information about $u^\mu(X_0)$, $\Pi(X_0)$ and $\pi^{\mu\nu}(X_0)$, which must be modelled otherwise. Here X_0 is the coordinate on the 3D hypersurface where the initial conditions of the hydrodynamics equations are specified. This hypersurface is usually chosen to be the "time" $\tau = \tau_0$, with $\tau_0 \sim 0.1 - 1$ fm.

No two heavy ion collisions are identical, and the Glauber model partially take this physics into account through fluctuations in the positions of the nucleon-nucleon collisions. These fluctuations are important in determining the geometry of the initial conditions of hydrodynamics.

An important consequence of these fluctuations is that a full hydrodynamical simulation of *each* sample of initial conditions is necessary. This approach is called "event-by-event hydrodynamics". For many years, event-by-event hydrodynamics was not used, due to both its numerical cost and the incomplete understanding of the importance of fluctuations in the initial conditions. Instead, averaged initial conditions were used: numerous samples of the initial conditions were averaged over, and a single hydrodynamical simulation of the collision would be made with this averaged initial condition.

It is now understood that hydrodynamical models using averaged initial conditions can provide a reasonable approximation of event-by-event hydrodynamics for a subset of observables, in particular observables that are not very dependent on the smaller features of initial conditions. The multiplicity is a good example of such observables. The momentum

anisotropies, on the other hand, are highly sensitive to fluctuations and cannot be described well with averaged hydrodynamics. Since the momentum anisotropy of hadrons and photons are of primary interest in this thesis, event-by-event hydrodynamics is used throughout the present work.

Hydrodynamical models using initial conditions based on the Glauber model were shown (e.g. [28]) to be quite successful in describing measurements from RHIC and the LHC. On the other hand, they contain free parameters that weaken the predictive power of hydrodynamical models. This is a consequence of the limited information provided by the Glauber model, which only models the position of nucleon-nucleon collisions in the heavy ion collisions. The amount of energy deposited at each site and the shape of this energy deposition are parameters of the model which must be tuned to data. Moreover the Glauber model does not provide any information about the initial conditions of $u^\mu(X_0)$, $\Pi(X_0)$ and $\pi^{\mu\nu}(X_0)$, which must be fixed from other models. This is an even larger source of uncertainties in the initial conditions.

These limitations provided strong incentives for the development of new models of initial conditions that include more information from quantum chromodynamics and less free parameters. A major contribution to this effort came from the Color Glass Condensate model. This model is based on the idea that large nuclei accelerated at nearly the velocity of light have a very large density of soft gluons. Because of this high gluon density, a classical description of the gluon field is possible, allowing for the gluon distribution to be estimated from first principles [73]. The model of initial conditions used in the present thesis is based on this approach.

The source of this high density of soft gluons are large momentum colour charge carriers, such as hard gluons and valence quarks, that act as static colour sources in each nucleus [72]. Different models can be used to constrain the distribution of colour sources, which fluctuates not only at the level of the nucleus but at sub-nucleonic scales. Once the colour sources are constrained, the distribution of gluons and its evolution in space and time is described with the classical Yang-Mills equation:

$$[D_\mu, F^{\mu\nu}] = J^\nu \tag{3.34}$$

where D_μ is the covariant derivative, $F^{\mu\nu}$ the gluon field strength tensor and J^ν the colour current given by the colour sources.

This model is called the IP-Glasma model [74, 75], and it is the specific model of heavy ion initial conditions used for all results presented in this thesis. It takes its name from the "impact parameter dependent saturation model" (IP-Sat), which is a version of the Color Glass Condensate model that constrains the distribution of initial colour sources from electron-proton and electron-nucleus collisions. An example of colour source distribution is

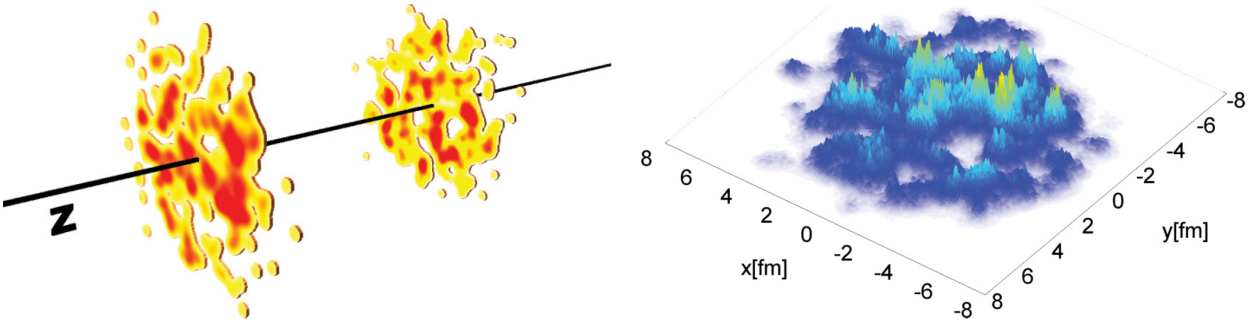

(a) (b)

Figure 3.1: (a) Illustration of the density of colour charges in each nucleus before the collision, with red representing higher colour charge densities (b) Example of energy density profile in the transverse plane from the IP-Glasma model (Figures from [75])

shown on Figure 3.1a.

The best possible scenario when initial condition models such as IP-Glasma are used is for the evolution described by Equation 3.34 to show signs of thermalisation. This would make possible a smooth transition to hydrodynamics. Unfortunately the framework described above does not show signs of thermalisation. There are nevertheless indications that a more complete treatment of the initial colour sources and of the Yang-Mills evolution do lead to certain features associated with thermalisation [76]. The use of IP-Glasma initial conditions does appear to be a first step toward more realistic initial conditions.

While the full energy-momentum tensor of the Yang-Mills evolution is known, the major consequence of the absence of thermalisation is that this energy-momentum tensor is too far out-of-equilibrium to be matched directly to the hydrodynamical model. For example, the value of $\Pi^{\mu\nu}$ will not necessarily be small compared to the energy density itself. Rather than matching this out-of-equilibrium energy-momentum tensor to hydrodynamics, only the energy density and the flow velocities from the Yang-Mills evolution are matched. This is achieved by solving:

$$u_\mu(X_0)T^{\mu\nu}_{CYM}(X_0) = \epsilon(X_0)u^\nu(X_0) \tag{3.35}$$

where $T^{\mu\nu}_{CYM}$ is the classical Yang-Mills energy-momentum tensor. In the present work, $X_0 = \tau_0 = 0.4$ fm.

Since the energy and momentum are not fully conserved in this transition, the final exact normalisation of $\epsilon(\tau_0)$ is considered an adjustable parameter, with the assumption that this normalisation should nevertheless not deviate too much from unity. Normalisations around 1.2 are used in this thesis.

While the IP-Glasma model cannot yet constrain the full initial conditions, it can constrain the two quantities that are the most important for the subsequent evolution, $\epsilon(\tau_0)$ and

$u^\mu(\tau_0)$, with very few parameters. This is a major step forward in reducing the uncertainties associated with initial conditions.

Once the initial conditions of the hydrodynamics equations are fixed, hydrodynamics evolution follows its course. An important input to the hydrodynamical equation is the equation of state, which is presented next.

3.3 Equation of state

The equation of state is used to relate the various thermodynamical quantities entering the hydrodynamical equations. The energy density ϵ, the pressure $\mathcal{P}$ and the entropy density s typically appear as thermodynamical variables in the viscous hydrodynamics equations or in relations between the transport coefficients, while the temperature T enters the Fermi-Dirac or Bose-Einstein distribution when particle production from the medium is evaluated.

As mentioned in the introduction, the equation of state of QCD matter at zero baryon density is known to a quantitative level, to the point that it is probably the best constrained part of the model. This understanding of thermal QCD was made possible by lattice QCD simulations. After years of progress, lattice QCD predictions are now understood to provide an accurate prediction for the thermodynamical properties of QCD matter, for temperatures as low as 125 MeV and as high as 1 GeV [10].

Moreover lattice results have been shown to agree well, at low temperature, with the thermodynamical properties of a non-interacting gas of hadrons and hadronic resonances — referred to as a "hadron resonance gas" — which is understood to be an effective model for an interacting gas of hadrons. This was illustrated on Figure 1.2a. This agreement between lattice calculations and the hadron resonance gas is not only numerical: it can actually be shown from first principles that the pressure of a thermalised QCD medium can be written, at low temperature, in terms of the pressure of a free gas of hadronic degrees of freedom [10, Section 3.12]. The equation of state is thus not only quantified accurately, but its connections to effective descriptions of QCD matter at low temperature are increasingly well understood.

The equation of state used in the present thesis is from Ref. [77]. It is based on lattice QCD calculations at high temperature matched to a hadron resonance gas at low temperature. The matching is important for two reasons. First it allows to extend the equation of state to temperatures lower than that available from lattice QCD.

The second reason is that it permits the conversion of a thermal QCD medium into hadronic degrees of freedom without loss of energy. This conversion needs to be done in hydrodynamical modelling of heavy ion collisions when the medium becomes too diluted for a hydrodynamical description to be valid anymore. The medium must then be converted to

hadrons and a different model must be used for their evolution. This process is explained in the next section.

3.4 Particlisation and afterburners

Hydrodynamics will describe the spacetime evolution of a medium as long as the latter can maintain near local thermal equilibrium. The conditions under which local equilibrium can be preserved depend on the microscopic properties of the medium being described. For a system that allows for a quasi-particle description, this condition is typically that the quasi-particle's mean free path is much smaller than any of the macroscopic length scales of the medium.

In the region of spacetime where hydrodynamics is not valid, typically at the edge of the medium or after expansion has sufficiently rarefied it, a different approach should be used to model the medium, with the appropriate matching to the hydrodynamical simulation [78, Section 5]. This very complex approach is still not mature enough to be used practically in heavy ion collisions. The scheme used in essentially all hydrodynamical models at the moment is a more pragmatic one, which can be divided in three steps:

Particlisation criterion First, a criterion is chosen to determine when the hydrodynamics description should be stopped for a given spacetime region of the medium, based on the local properties of this part of the medium. This process is referred to as "particlisation" [79].

The medium's local temperature is commonly used as a criterion. The idea behind this choice is that the local mean-free-path is expected to be a monotonic function of the temperature (the higher the temperature, the smaller the mean-free-path). It implies that the temperature can be used as proxy for the mean-free-path, which determines if local thermal equilibrium can be maintained in the medium. In this case, the particlisation criterion is simply $T = T_{sw}$, where T_{sw} is a parameter of the hydrodynamical model that is fitted to data.

Viscous hydrodynamical models allow for more realistic particlisation criteria to judge the validity of the hydrodynamical description, by comparing microscopic length scales given by transport coefficients with macroscopic scales. While such criteria are increasingly being investigated [80, 81], they are not yet common in the field. Temperature is used in the present work.

PARTICLISATION The second step relies on the fact that the thermodynamical properties of QCD matter at low temperature can be described in terms of a hadron resonance gas, as seen for the equation of state in the previous section. Once it is established that a hydrodynamical description is no longer applicable in a given spacetime region, the energy of this part of the medium is converted into hadrons and resonances. This requires the assumption that T_{sw} is below the confinement limit of QCD matter, which is one of the reasons why it is simpler to use temperature directly as particlisation criterion. Since there is no precise temperature delimiting confined and deconfined QCD matter, the point from which the thermodynamical properties of the hadron resonance gas matches that of lattice QCD can be used. From Figure 1.2a, this temperature can be read to be around 180 MeV.

The 3D spacetime surface that meets the particlisation criterion at any given point in the hydrodynamical evolution is called the "particlisation hypersurface"[5]. Particlisation is accomplished by evaluating the number of hadrons of each species that cross this hypersurface. The particlisation process is done locally and hadrons are given a (quasi-)thermal distribution of energy and momentum according to the temperature T_{sw} and boosted given to the local flow velocity of the medium. This is referred to as the Cooper-Frye procedure [82], and its mathematical formulation is [83, Section 3.2.4]

$$E\frac{d^3N}{d\mathbf{p}} = \int_\Sigma d\Sigma_\mu P^\mu f(P\cdot u, X) \tag{3.36}$$

where $d\Sigma_0 = d^3r$ and $d\mathbf{\Sigma} = d\tau d^2s\mathbf{n}$ with $\mathbf{n}$ a unit vector normal to the hypersurface and d^2s the local area of the hypersurface. Energy is conserved in this process if all hadrons and resonances entering in the equation of state are produced through Equation 3.36.

Since viscous hydrodynamics is used, the medium is not exactly thermal, which implies that $f_{B/F}(P,X)$ is not the Fermi-Dirac ($f_F^{(0)}$) or Bose-Einstein ($f_B^{(0)}$) distribution, but includes corrections related to the bulk pressure Π and the shear stress tensor $\pi^{\mu\nu}$. The exact expression for f is determined in kinetic theory, in the same way that the equations of motions for Π and $\pi^{\mu\nu}$ were derived [64, Section 5.3].

In the present work, $f_{B/F}(P,X)$ is given by

$$f_{B/F}(P,X) = f^{(0)}_{B/F}(P) + \delta f^{shear}_{B/F}(P,X) + \delta f^{bulk}_{B/F}(P,X) \tag{3.37}$$

where

$$\delta f^{shear}_{B/F}(P,X) = f^{(0)}_{B/F}(P)(1+\sigma_{B/F}f^{(0)}(P))\frac{\pi^{\mu\nu}P^\mu P^\nu}{2T^2(\epsilon+\mathcal{P})} \tag{3.38}$$

[5] When boost-invariant 2+1D hydrodynamical models are used, this particlisation hypersurface is effectively two-dimensional. The rapidity direction is infinite but trivial: the hypersurface is uniform in rapidity.

and [84]

$$\delta f^{bulk}_{B/F}(P,X) = -f^{(0)}_{B/F}(P)(1+\sigma_{B/F}f^{(0)}(P))\left[\frac{1}{3}\frac{m^2}{T^2}\frac{1}{P^0/T} - \frac{P^0}{T}\left(\frac{1}{3}-c_s^2\right)\right]\Pi\frac{\tau_\Pi}{\zeta} \qquad (3.39)$$

with $\sigma_B = 1$ for fermions and $\sigma_F = -1$ for fermions.

Rather than using the approximate relation given by Equation 3.22 to evaluate the ratio τ_Π/ζ in Equation 3.39, it is evaluated directly — as a function of temperature — using a kinetic theory model of the hadron resonance gas [84]. The speed of sound c_s is taken from the equation of state.

The hydrodynamical simulation of the medium and the conversion to hadrons through Cooper-Frye continues until the whole medium has been converted to hadrons.

Afterburner: post-particlisation dynamics By definition, particlisation converts the medium into a gas of interacting hadrons. Although the hadronic interactions could not maintain local thermal equilibrium, they can still affect the distribution of final state hadrons significantly. Elastic collisions modify the hadron's energy-momentum distribution, while inelastic collisions change the relative abundances of each hadron species. Both interactions can be modelled using kinetic theory. In the context of heavy ion collisions, a model that describes such interactions is usually referred to as an afterburner.

Since most produced hadrons and resonances are unstable, they decay into daughter hadrons before reaching the detectors that surround the collision region. Once again this modifies the species and momentum distribution of hadrons. This must also be taken into account before the final distribution of hadrons can be compared with measurements.

In the present work, the transport model UrQMD (Ultra-relativistic Quantum Molecular Dynamics) [85, 86, 87] is used as afterburner. UrQMD is a microscopic model that solves the Boltzmann equation with hadronic degrees of freedom. Hadrons and resonances up to 2.25 GeV in mass are included in the model, with their cross-sections being parametrized from measurements when possible. Hadronic cross-section models are used to estimate those that have not been measured [86].

While UrQMD describes interactions between hadrons in 3+1 dimensions, it is effectively possible to use it in $2+1$ dimensions for boost-invariant systems by initialising it with a wide plateau in rapidity.

In the next chapter, hadronic observables are computed with the hydrodynamical model of heavy ion collisions described in the present chapter. The relative importance of rescattering and decays on the various observables is briefly investigated.

Part III

Hadrons

Hadronic measurements are the most diverse and precise of any measurements made in heavy ion collisions. They are consequently the first used to constrain hydrodynamical models of heavy ion and extract information on the transport properties of the quark-gluon plasma.

In this section, the hydrodynamical model of heavy ion collisions described in Chapter 3 is used to compute hadronic observables measured at RHIC and the LHC. The purpose of this chapter is to show that the state-of-the-art hydrodynamical model used in this thesis can describe very well the major hadronic measurements at RHIC and the LHC. The role of bulk viscosity is highlighted, and along with the importance of final state hadronic rescattering.

This comparison with hadronic observables is the first step in this thesis. Calculations of photons from the same hydrodynamical model are presented in the final part of this thesis.

Chapter 4

Hadron production in a comprehensive hydrodynamical model of heavy ion collisions

Calculations of hadronic observables for collisions of lead ions (Pb-Pb) at a center-of-mass energy of $\sqrt{s_{NN}} = 2.76$ TeV are presented first in this Chapter. After a systematic comparison with measurements from the LHC, these calculations are used to understand the effect of bulk viscosity and of post-particlisation hadronic rescattering on hadronic observables, and the consequence for the hydrodynamical model.

Comparisons with data from RHIC are deferred to the final part of this chapter. To open the chapter, a summary of the hydrodynamical model of heavy ion collisions described in Chapter 3 is provided, with additional information specific to the results presented in this work.

4.1 Summary of the model

The hydrodynamical model of heavy ion collisions used in this work is made of three main parts: initial conditions, hydrodynamical equations for the spacetime evolution, and a particlisation procedure coupled with post-particlisation dynamics.

The IP-Glasma initial condition model described in Section 3.2 is used for all calculations. It provides an initial energy density profile, as well as an initial profile for the flow velocity. As explained in Section 3.2, the energy density normalisation of the IP-Glasma initial conditions is not fully constrained, and small modifications to the normalisation are possible. This normalisation factor is one of the parameters of the model.

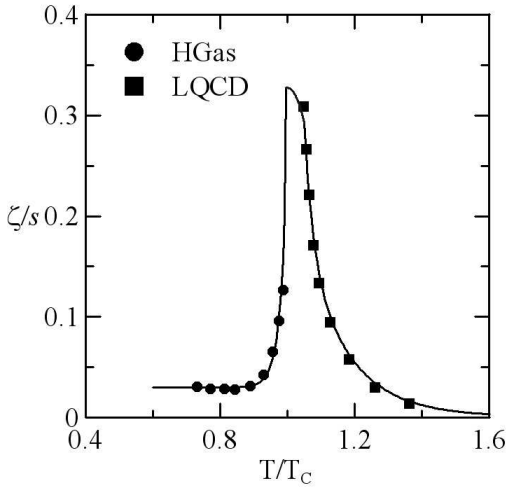

Figure 4.1: Parametrization of bulk viscosity $\zeta(T)$ used in this work (parametrization and figure from [88])

Since initialisation for the shear stress tensor $\pi^{\mu\nu}$ or for the bulk pressure Π are not currently available from IP-Glasma initial conditions, a choice must be made to fix them. They are set to zero in the present work.

This thesis focuses on midrapidity hadronic measurements. In consequence $2+1$D hydrodynamical equations are used.

Event-by-event hydrodynamics is used in order to include the fluctuations necessary to describe the azimuthal anisotropy of hadrons. As described in Section 3.1, second order hydrodynamics is used, with all transport coefficients related to the shear and bulk viscosities using relations derived from kinetic theory (see Section 3.1).

Shear viscosity η is assumed to be proportional to the entropy density s, $\eta/s = h$ with the constant h being a parameter of the hydrodynamical model that is extracted from data.

For bulk viscosity, the temperature-dependent parametrization proposed in Ref. [88] is used. This parametrization, plotted on Figure 4.1 as a ratio of bulk viscosity and entropy density, has a peak in ζ/s at temperature $T = 180$ MeV. Below 180 MeV, the temperature dependence of ζ/s is estimated from the bulk viscosity of a hadron resonance gas with Hagedorn states [89], while values of the bulk viscosity estimated [90] from lattice QCD simulations are used to constrain ζ/s above 180 MeV.

At temperature T_{sw}, the particlisation procedure described in Section 3.4 is used. The kinetic model UrQMD is then used to describe hadronic interactions. The parameter T_{sw} is the third parameter of the hydrodynamical model, which is fixed by comparison with data.

Before turning to comparisons with LHC measurements, a short summary of the hadronic observables studied in this work is presented.

4.2 Hadronic observables

The following observables are computed and compared with data in this chapter:

- Centrality dependence of pion, kaon and proton *multiplicity*
- Centrality dependence of pion, kaon and proton *average transverse momentum*
- Centrality dependence of v_2, v_3 and v_4 for unidentified charged hadrons
- Transverse momentum differential spectra of pions, kaons and protons
- Transverse momentum differential v_2, v_3 and v_4 of unidentified charged hadrons

The centrality dependence is shown using four different centralities: 0-5%, 10-20%, 20-30% and 30-40%. Transverse momentum differential spectra and anisotropies are shown for the first and last of these centralities.

A slightly different set of observables and centralities are shown for RHIC measurements, due to the unavailability of certain data sets.

4.3 Comparisons with LHC measurements: Pb-Pb collisions at $\sqrt{s_{NN}} = 2760$ GeV

Comparison of the hydrodynamical model summarized in Section 4.1 with the hadronic observables listed in the previous section is shown on Figure 4.2. The centrality dependence of the multiplicity, average p_T and p_T-integrated v_n are shown on Figures 4.2a, 4.2b and 4.2c respectively. Data are taken from Ref. [50] for the multiplicity and average p_T, and from Ref. [91] for the integrated v_n.

All three measurements can be described well by the hydrodynamical model's prediction, once the model's parameters are fixed. The energy normalisation of the initial conditions is fixed with the pion multiplicity. The centrality dependence of the multiplicy, which is a prediction of the model, is in very good agreement with the data.

The temperature hypersurface at which hydrodynamics stops and hadronic rescatterings start is fixed at $T_{sw} = 145$ MeV, as it provides the best description of the proton multiplicity and average p_T. While the centrality dependence of the kaon and proton average p_T deviates slightly from measurements, their description by the hydrodynamical model remains reasonable.

Unlike the multiplicity and average p_T, the integrated v_n shown on Figure 4.2c are highly sensitive to the shear viscosity η, and are used to extract the shear viscosity of the model,

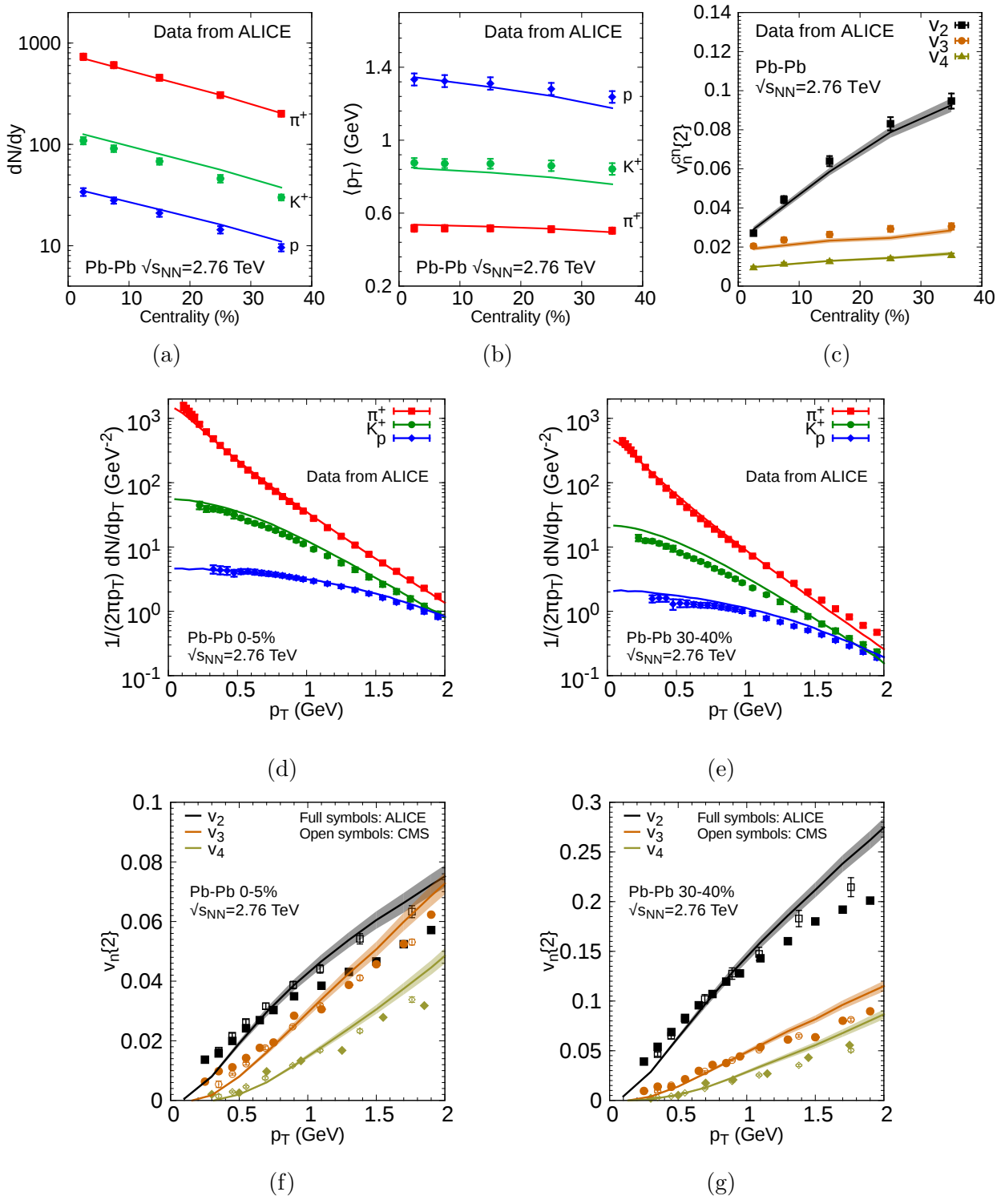

Figure 4.2: Comparison of hydrodynamical model with hadronic (a) multiplicity, (b) average-p_T and (c) p_T-integrated v_n with respect to centrality; p_T-differential hadron spectra for (d) 0-5% centraliy and (e) 30-40% centrality; and charged hadrons p_T-differential v_2, v_3 and v_4 for (f) 0-5% centraliy and (g) 30-40% centrality, all for Pb-Pb collisions at $\sqrt{s_{NN}} = 2.76$ TeV. The shaded band around the hydrodynamical calculation are statistical uncertainty of the average over events.

$\eta/s = 0.095$. This value provides a fairly good description of the v_2, v_3 and v_4 for all centralities.

The differential spectra shown on Figures 4.2d and 4.2e confirm that, as hinted by the good agreement of the multiplicity and average p_T, the momentum distribution of hadrons is very well described by the hydrodynamical model, in particular for 0-5% centrality. Measurements were taken from Ref. [50].

The transverse momentum dependence of the charged hadron's v_n, Figures 4.2f and 4.2g, is compared with measurements from both ALICE [91] and CMS [92]. This differential v_n definitively shows tension between the calculation and measurements, both at low and high p_T. For v_2, however, it is not clear how serious this tension is at high p_T, since ALICE and CMS measurements disagree in this region. The origin of the disagreement between the hydrodynamical model and the measurements at low p_T is not understood yet. The pion spectra also exhibit a small disagreement with measurements at very low p_T (see Figures 4.2d and 4.2e), and both effects might be related.

Like the p_T-integrated v_n, the differential v_n also has a strong dependence on the shear viscosity η. The tension observed on Figures 4.2f and 4.2g could be reduced by modifying the value of η/s. On the other hand, integrated observables are more robust observables than differential ones — much less dependent on $\delta f_{B/F}$ (Equation 3.37) for example — and the value of η/s extracted from p_T-integrated v_n is considered more reliable.

The overall agreement of the hydrodynamical model with measurements from the LHC is good, in particular considering the limited number of free parameters in the model and the large number of observables described. This degree of agreement would not have been possible without two important ingredients of this model: the introduction of bulk viscosity, and the improved description of final state dynamics provided by the UrQMD afterburner. The importance of each is shown separately in the next two sections.

4.3.1 Effect of bulk viscosity

The introduction of bulk viscosity is essential to achieve the description of hadronic observables presented above. This is shown in the present section by turning off bulk viscosity altogether, i.e. setting $\zeta = 0$. Such a value of bulk viscosity is not wholly unphysical: in a nearly conformal system such as a high temperature QGP, ζ should indeed be very small. However the quark-gluon plasma produced in heavy ion collisions is not a very high temperature one, and conformal invariance is certainly broken by confinement. As seen in Section 4.1, there are currently good evidence for a peak of bulk viscosity near deconfinement [89, 90], evidence that were used to constrain the temperature-dependence of the bulk

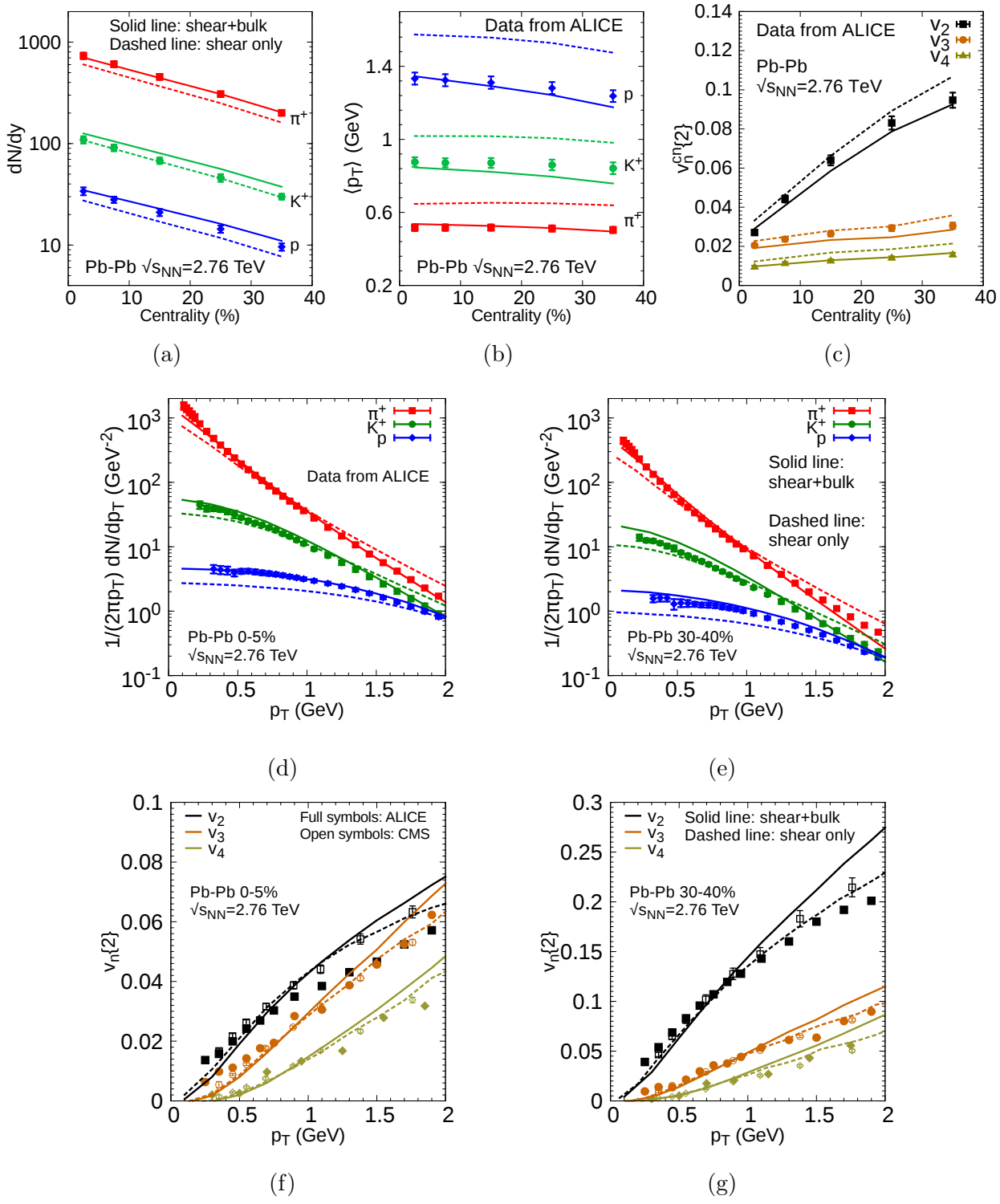

(a) (b) (c)

(d) (e)

(f) (g)

Figure 4.3: Effect of bulk viscosity on the same observables as Figure 4.2. Solid line is with both shear and bulk, dashed line is without bulk.

viscosity used in the present work (Figure 4.1).

The effect of setting $\zeta = 0$ on the same observables as presented in the previous section is shown on Figure 4.3. The solid lines are the same calculation as shown in the previous section on Figure 4.2, and the dashed lines are the results of the hydrodynamical model with $\zeta = 0$ instead of the parametrization of Figure 4.1. Data is also shown for reference.

The effect of bulk viscosity on the multiplicity (Figure 4.3a) is visible but moderate. From a phenomenological point of view, this could be corrected by readjusting the energy normalisation of the initial conditions to a larger value.

On the other hand, the average p_T is shown on Figure 4.3b to have a strong dependence on bulk viscosity. The introduction of bulk viscosity decreases significantly the average p_T of pions, kaons and protons, and is essential in describing the measurements. The same conclusion can be reached from the p_T differential spectra, Figures 4.3d and 4.3e, which have an incorrect momentum dependence without bulk viscosity.

The hadronic v_n also shows a dependence on bulk viscosity, as seen on Figure 4.3c. It is nevertheless possible to describe the charged hadron v_n measurements without bulk viscosity by increasing the value of the *shear* viscosity. This is shown on Figure 4.4: the p_T-integrated v_n for a hydrodynamical model with bulk viscosity given by Figure 4.1 and $\eta/s = 0.095$ is almost the same as for a hydrodynamical models with $\zeta = 0$ and $\eta/s = 0.16$. Since the shear viscosity of the quark-gluon plasma is primarily extracted from hadronic v_n measurements, the presence of bulk viscosity has a significant effect on its determination. The latter conclusion is important, because studying and quantifying the transport properties of QCD is one of the important goals pursued in heavy ion physics.

It is thus clear that for the hydrodynamical model used in this work, the inclusion of bulk viscosity allows for a better description of LHC data. Considering that the present hydrodynamical model, with IP-Glasma initial conditions and final state hadronic dynamics, is among the most realistic ever used to study heavy ion collisions, it provides strong support for a finite value of the bulk viscosity of QCD around deconfinement.

4.3.2 Post-particlisation dynamics

The transition from hydrodynamics to hadrons was described in Section 3.4. One important feature of this part of the model is the inclusion of a dynamical model of hadronic rescatterings (UrQMD) after particlisation. This section focuses on the effect of hadronic rescatterings, and not of post-particlisation hadronic decays. The distinction is made because hadronic decays do not actually need a complex model of hadronic interaction to be included. There are actually analytic formulae for most hadronic decays, and their implementation are

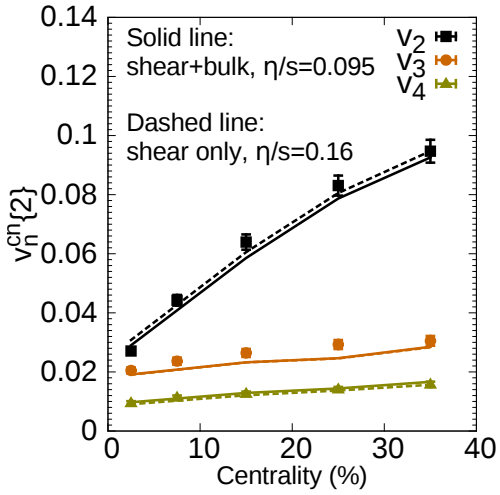

Figure 4.4: Charged hadron v_n from a hydrodynamical model with both shear and bulk viscosity, and $\eta/s = 0.095$, compared with the same calculation without bulk viscosity, and with $\eta/s = 0.16$

relatively fast and are consequently used almost universally in the field.

Hadronic rescatterings, on the other hand, require the use of a model of hadronic interactions such as UrQMD. It brings an additional degree of complexity to the hydrodynamical model, and an additional numerical cost, which makes their inclusion more difficult. There are thus strong incentives to identify the observables for which the inclusion of hadronic rescatterings is important.

The results are shown on Figure 4.5. As in the previous section, the comparisons is made with the same observables as previously shown on Figure 4.2. The solid line is the calculation with post-particlisation hadronic interactions and hadronic decays (the same calculation as shown on Figure 4.2). The dashed line includes decays but no collisions.

The first conclusion from Figure 4.5 is that pions and unidentified charged hadrons (which are dominated by pions) are mostly unaffected by hadronic rescatterings in the final state of the collision. The exception is the differential v_n at high p_T (Figures 4.5f and 4.5g), where the momentum distribution of the v_n are clearly modified by rescatterings.

For kaons and protons, hadronic collisions produce an important change in the momentum distribution. This can be seen clearly in the average transverse momentum (Figure 4.5b) and in the spectra (Figures 4.5d and 4.5e)

For both high p_T differential v_n and kaons and proton spectra, it is also clear that most central events ($0 - 5\%$) are more affected than peripheral ones ($30 - 40\%$). This is in line with the expectation that most central events produce more hadrons, which makes them more likely to undergo interactions.

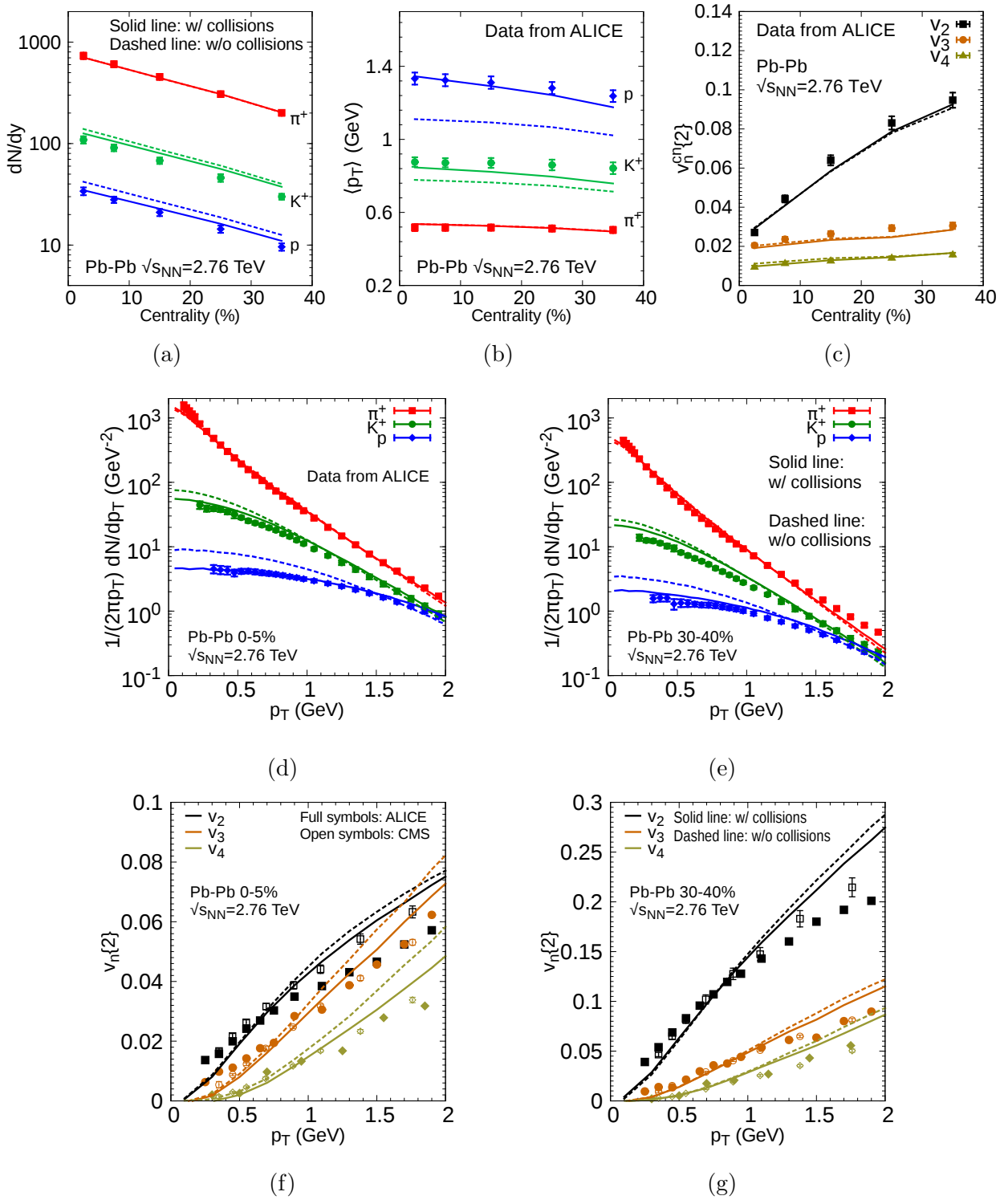

Figure 4.5: Effect of hadronic rescattering on the same observables as Figure 4.2. Solid line is with hadronic rescattering, dashed line is without.

The observation that charged hadrons and pions are mostly insensitive to hadronic rescatterings is important. It implies that two of the three parameters in this model, the energy normalisation and the shear viscosity, do not depend significantly on the details of hadronic rescatterings. On the other hand, since the particlisation temperature is fixed with the proton multiplicity and average p_T, it is clearly dependent on hadronic rescattering. As will be seen later, the particlisation temperature is an important parameter for photons. The issue of hadronic rescattering will thus be raised again in the context of photon production.

4.4 Comparisons with RHIC measurements: Au-Au collisions at $\sqrt{s_{NN}} = 200$ GeV

After the detailed comparison with hadronic measurements at the LHC made in the previous chapter, the same hydrodynamical model is compared with measurements from RHIC. The parameters of the model are fixed to data as in the previous section:

- The normalisation of the IP-Glasma initial conditions is adjusted to obtain a good pion multiplicity
- The temperature at which the hydrodynamical evolution is stopped is fixed at $T_{sw} = 165$ MeV so as to provide the best global description of hadronic measurements, in particular of the proton and kaon spectra.
- The value of η is fixed to $\eta/s = 0.06$ by comparison with the integrated v_n of charged hadrons

The result is shown on Figure 4.6. Data is from Ref. [93] for the multiplicity and average p_T, from Refs [94] and [95] for the integrated $v_2\{2\}$ and $v_3\{2\}$, and from Refs [96] and [97] for the hadron spectra.

There are some differences on Figure 4.6 compared to the figures shown in the previous section. First, only the v_2 and v_3 is shown on Figure 4.6c due to the unavailability of v_4. Since no p_T-differential charged hadron two-cumulant $v_n\{2\}$ are available at RHIC (see Section 2.2), only the integrated v_n is shown.

Moreover, unlike in the preceding section, the proton multiplicity [93] shown on Figure 4.6a includes protons from weak decays such as $\Lambda \to p\pi^-$ and $\Sigma^+ \to p\pi^0$, which are considered stable in the hydrodynamical model. The proton average p_T measurements from STAR [93] also contain the effect of these weak decays. Multiplicity calculations from the hydrodynamical model can be and are corrected to include weak decays, but the same is

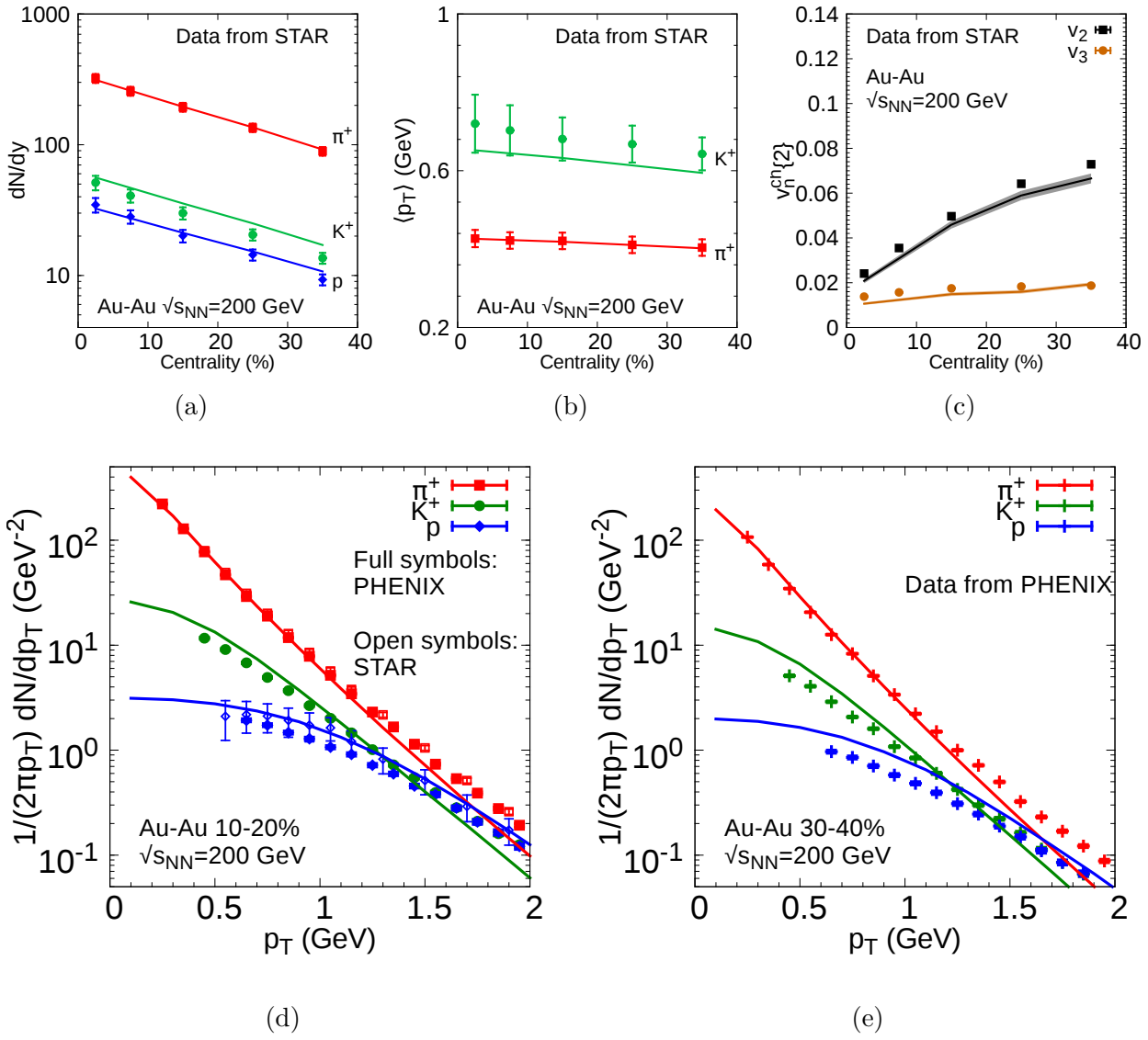

Figure 4.6: Comparison of hydrodynamical model with hadronic (a) multiplicity, (b) average-p_T and (c) p_T-integrated v_n with respect to centrality, p_T-differential hadron spectra for (d) 10-20% centraliy and (e) 30-40% centrality, for Au-Au collisions at $\sqrt{s_{NN}} = 200$ GeV. The shaded band around the hydrodynamical calculation are statistical uncertainties.

not possible for the average p_T without making complex modifications to the afterburner UrQMD. Consequently the model's prediction for the proton average p_T is not compared to measurements.

Differential spectra for which weak decays were subtracted were published by both the PHENIX [96] and STAR [97] collaboration. To compare them, the differential spectra (Figure 4.6d) is shown for $10-20\%$ instead of $0-5\%$, since PHENIX and STAR proton data are only both available for this centrality. It is clear from Figure 4.6d that the hydrodynamical prediction for the proton spectra deviates significantly from the PHENIX data, but agrees well with STAR measurements. The agreement with the STAR data is in fact consistent with the agreements found for the multiplicity on Figure 4.6a. The origin of this discrepancy between the two data sets has not been identified at the moment.

Beside this subtleties in the proton spectra, the agreement is quite similar to that seen with LHC data, with very good pion spectra and good p_T-integrated v_n, but some tension with the kaons. The overall agreement of the hydrodynamical model is thus also good at RHIC.

4.5 Hydrodynamical model and hadronic data: summary

The hydrodynamical model used in this thesis was compared with hadronic measurements from both RHIC and the LHC. In both case, the model was found to be in good agreement with data, although some tension is apparent for kaons as well as for the p_T-differential v_n. Considering the small number of parameters in the model, the general agreement with data of its predictions indicates that the hydrodynamical model provides a solid description of the dynamics of heavy ion collisions.

With this successful hydrodynamical model of heavy ion collisions in hand, the production of photons is investigated next.

Part IV

Photons

Direct photon measurements in heavy ion collisions show a large excess of photons over the expected prompt photon signal. These photons have also been measured to have a large momentum anisotropy. Photons emitted by the quark-gluon plasma during its expansion are prime candidates for this excess of photons.

In this part of the thesis, the hydrodynamical model described in Chapter 3, and compared successfully to hadronic data in the preceding chapter, is used to evaluate thermal photons and to compare with direct photon measurements from both RHIC and the LHC.

Chapter 5

Photon sources

As outlined in Section 2.3, photons can be produced through a variety of mechanisms in heavy ion collisions. This thesis focuses on two of these production mechanisms: thermal photons and prompt photons. A third source of photons, those from hadronic decays that are not subtracted in direct photon measurements, is also investigated briefly.

This chapter is meant to explain how each of these sources is evaluated in this thesis.

5.1 Non-cocktail photons

"Non-cocktail photons" are hadronic decays into photons that are not subtracted from inclusive photons in the definition of direct photons. The list of decays that are *subtracted* in direct photons are taken from Ref. [98, Section 10.1] for LHC measurements and from Ref.[99, Section 3.5] for RHIC measurements. At both RHIC and the LHC, the dominant non-cocktail channels are $\Sigma^0 \to \Lambda\gamma$, $f_1(1285) \to \rho^0\gamma$ and $K^*(892) \to K\gamma$. The channel $\pi^0 \to e^+e^-\gamma$ is also an important non-cocktail contribution at RHIC, since unlike in the LHC analysis, it is not subtracted.

The production of hadrons from the hydrodynamical model was described in Section 3.4 as well as in Chapter 4. With the knowledge of the momentum distributions of each hadron species, decay photons are evaluated using the appropriate branching ratio for each decay channel [6].

5.2 Prompt photons

When two relativistic hadrons collide, most of the momenta of their quarks and gluons is along the collision axis. If two such energetic partons q_1 and q_2 undergo a $2 \to 2$ collisions

$q_1 q_2 \to q_3 q_4$, there is a finite probability that particle q_3 will be produced with a significant momentum p_T in the plane transverse to the collision axis, with q_4 carrying an opposite transverse momentum by conservation.

Since q_1 and q_2 did not have any significant initial *transverse* momentum, the momentum exchange between the initial state particles q_1 and q_2 must have been at least of order p_T. This momentum p_T sets the scale at which the strong coupling constant $\alpha_s(Q)$ is evaluated in this process. Because of asymptotic freedom in quantum chromodynamics (Figure 1.1), the larger p_T, the smaller α_s.

A small value of α_s implies that the cross-section $q_1 q_2 \to q_3 q_4$ can be computed perturbatively from QCD. This is the essence of perturbative QCD, and it is the basis for the great interest of the nuclear and heavy ion physicists with high-p_T particles. This mechanism of photon production is referred to as prompt photons in this thesis.

5.2.1 A review of perturbative QCD in proton-proton collisions

Schematic formulae for the mathematical formulation of perturbative QCD were given previously in this thesis (see Sections 1.3 and 2.3.1). A more precise formulation is

$$E\frac{d^3\sigma_{pp}}{d\mathbf{p}} = \sum_{a,b,c,d} f_{a/p}(x_a, Q_{fact}) \otimes f_{b/p}(x_b, Q_{fact}) \otimes d\hat{\sigma}(Q_{ren}) \otimes D_{\gamma/c}(z_c, Q_{frag}) \tag{5.1}$$

where Q_{fact}, Q_{ren} and Q_{frag} are energy scales entering respectively the parton distribution function $f_{a/p}(x_a, Q_{fact})$, the partonic cross-section $d\hat{\sigma}(Q_{ren})$ and the fragmentation function $D_{h/c}(z_c, Q_{frag})$. The cross-section of the partonic scattering described in the previous section is $d\hat{\sigma}(Q_{ren})$, and Q_{ren} is the scale at which the strong coupling constant $\alpha_s(Q)$ is evaluated. As explained above, this scale should be of the order of the transverse momentum of final state partons.

The factorisation and fragmentation scales can be better understood by remembering that the parton distribution function and fragmentation function encode non-perturbative information about the collision. The parton distribution function, for example, can be thought of as representing the probability of a parton "a" with momentum $x_a P$ to be found in a proton of momentum P. However, this probability depends on the scale at which the proton is probed: the parton content of the proton is dynamic.

This dynamics can be understood with perturbative QCD. Say $f_{a/p}(x_a, Q_0)$ gives the parton distribution of a proton at an energy scale Q_0. The parton distribution at another energy scale Q can be evaluated in perturbative QCD[1], as long as both Q_0 and Q are large

[1] This is accomplished with the DGLAP equations. See e.g. [6, Chapter 9 & 19].

enough for perturbative QCD to be applicable. Assuming that Q_0 is the lowest scale at which this perturbative QCD evolution can trusted, then $f_{a/p}(x_a, Q_0)$ can be thought of as the actual function that needs to be extracted from data, since the information it contains is no longer perturbative. It can be used as a reference parton distribution function, and it can be related to any $f_{a/p}(x_a, Q)$ with scale $Q > Q_0$. The same logic applies to fragmentation functions.

All the scales, Q_{fact}, Q_{ren} and Q_{frag}, should be of the order of the large energy scale in the problem, the scale that allows perturbative QCD to be used in the first place. In the example given in the previous section, this scale was the transverse momentum.

Computing photon production in proton-proton collisions from the formalism described above implies having access to a proton parton distribution function $f_{a/p}(x_a, Q_{fact})$, a parton to photon fragmentation function $D_{\gamma/c}(z_c, Q_{frag})$ and the partonic matrix element $d\hat{\sigma}(Q_{ren})$. The latter is currently known at next-to-leading order in the strong coupling constant for both isolated photons [100] and fragmentation photons[2] [101]. Combined with next-to-leading order parton distribution and fragmentation functions, this perturbative QCD calculation has been shown repeatedly to agree very well with direct photon measurements in proton-proton collisions at RHIC[3] , the LHC [21] and previous colliders [102].

The perturbative QCD framework used in this work is essentially the next-to-leading order calculation described in the preceding paragraph. The code INCNLO [103], from the research group that made the original calculation [101, 100], is used[4]. The proton parton distribution function and photon fragmentation function used are respectively CTEQ61m [105] and BFG-2 [106].

The factorisation, renormalisation and fragmentation scales are all set equal: $Q_{fact} = Q_{ren} = Q_{frag} = Q$. The transverse momentum of the produced photon is used to set the scale, with a normalisation constant: $Q = Np_T^\gamma$. The constant N is fixed to $1/2$ so as to provide the best description of the available proton-proton measurements.

The scale Q_0, described above as the lowest scale for which perturbative QCD is considered reliable, is usually $Q_0 \sim 1.5$ GeV in parametrizations of parton distribution functions and fragmentation functions. With $Q = p_T^\gamma/2$, this implies that the lowest p_T^γ that can be

[2] At next-to-leading order, there is no absolute division between isolated and fragmentation photons. This is a consequence of the three-particle phase space of isolated photons at next-to-leading order, which allows for e.g. a final state photon to be produced arbitrarily close to a final state parton, mimicking a fragmentation photon. A careful treatment of the isolated and fragmentation photon's phase space is thus necessary to avoid double-counting, which partially blurs the distinction between the two processes.

[3] This can be seen on the bottom curves of Figure 2.6, where a perturbative QCD calculation is compared to direct photon measurements from the PHENIX collaboration.

[4] The code was slightly modified to allow for the use of recent parton distribution functions through the LHAPDF library [104].

computed is $p_T^\gamma \sim 3$ GeV.

Since the direct photon excess in heavy ion collisions is mostly observed below 3 GeV, it is very important to be able to compute prompt photons in that region of p_T. Using a larger N in $Q = Np_T^\gamma$ would allow to extend the perturbative QCD calculation to lower transverse momentum, with the caveat that it would not describe proton-proton measurements as well at high p_T.

The approach used in this thesis exploits the observation that a change in N (in the equality $Q = Np_T^\gamma$) mostly results in a change in the normalisation of the perturbative calculation. Thus, using a larger N and adjusting the normalisation to that of $N = 1/2$ (i.e. that of high p_T data) allows to evaluate prompt photons at low p_T. This method is described in more details in Appendix A.

The reliability of perturbative QCD at low p_T is difficult to judge, since the assumption that the transverse momentum is large is essential to the derivation of Equation 5.1. The transverse momentum p_T must be large compared the other energy scales in the problem, in particular $\Lambda_{QCD} \sim 200$ MeV.

On the other hand, comparisons of perturbative QCD calculations with low p_T measurements of photons and pions shows a good agreement, as discussed in Appendix A. This suggests that perturbative QCD still provides a reasonable estimate of prompt photons at p_T as low as $1 - 1.5$ GeV.

5.2.2 Prompt photons in heavy ion collisions: Cold nuclear effects and binary scaling

Perturbative QCD is one of the two ingredients necessary to evaluate prompt photons in heavy ion collisions, the other one being binary scaling.

Two small modifications to perturbative QCD are necessary in order to account for differences between proton-proton collisions and nucleus-nucleus collisions. First, a nucleus-nucleus collision is not only a superposition of proton-proton collisions, but also of proton-neutron and neutron-neutron collisions. The parton distribution of neutrons can be related to that of protons through the isospin symmetry, e.g. $f_{u/n}(x_a, Q) = f_{d/p}(x_a, Q)$. This effect is called the "isospin effect" and it is included in the evaluation of prompt photons in this work.

The second effect is the modification of the proton parton distribution function inside a nucleus: the parton content of a proton inside of a nucleus is known to be slightly different from that of a free proton. This effect can be taken into account by using nuclear parton distribution functions. For the present work, the EPS09 nuclear parton distribution

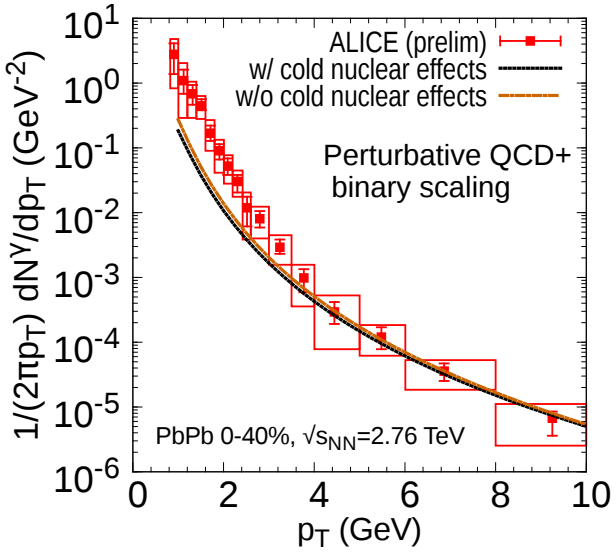

Figure 5.1: Effect of nuclear parton distribution functions and the isospin effect on prompt photons computed at the LHC

function [107] is used.

The two effects described above are termed "cold nuclear matter effects", since they are modifications to the production of hard particles that are not related to the formation of a hot medium in nucleus-nucleus collisions. Their effect on prompt photons is shown on Figure 5.1 for Pb-Pb collisions at $\sqrt{s_{NN}} = 2.76$ TeV. It is a modest effect.

It should be noted that there are still significant uncertainties in the parametrization of cold nuclear matter effects, and that different approaches do not fully agree [108]. The modern nuclear parton distribution function from Ref. [107] is nevertheless expected to provide a reasonable estimate of cold nuclear effects on prompt photons.

On top of cold nuclear matter effect, "*hot* nuclear matter effects" are also expected on prompt photon production in heavy ion collisions, as discussed in Section 2.3.1. These would take the form of suppressed fragmentation photons due to parton energy loss, along with jet-medium photon production. While the inclusion of these effects will certainly be an important step forward in understanding direct photon measurements in heavy ion collisions, they are much more difficult to include than cold nuclear effects, since they depend on the dynamical properties of the quark-gluon plasma. Their inclusion was beyond the scope of the present work.

Binary scaling is the last ingredient necessary to complete the prompt photon calculations. As stated many time already, the number of binary collisions is computed from the Glauber model [22].

5.3 Thermal photon production

Hydrodynamical models of heavy ion collisions describe the expansion of the quark-gluon plasma. This hot QCD medium has a complex spacetime distribution of local temperatures and expansion rates, and its degrees of freedom change considerably during its lifetime. As such, computing photons produced by this medium — so called thermal photons — is not a simple task.

The first ingredient is the photon production rate of static, thermalised QCD matter. This much simpler question, by itself, is not easy and has mostly been answered for limiting cases where the medium has well-defined degrees of freedom: a gas of hadrons, or a plasma of free quarks and gluons. An overview of the different calculations of photon emission from hot QCD matter is presented in the next section.

5.3.1 Thermal photon rates

Photon production from a high temperature quark-gluon plasma is known at next-to-leading order in the strong coupling constant [109]. The calculation assumes $g_s \ll 1$, a value that is understood only to be attained in a quark-gluon plasma at very high temperatures, much larger than the temperatures of a few hundreds of MeV reached in current heavy ion collisions. Nevertheless it is hoped that such a perturbative calculation captures the main physics of photon production by quark and gluon degrees of freedom, and can provide a reasonable estimate of photon production even for much larger values of g_s[5].

This next-to-leading order calculation of photon emission from the QGP was found [109] to be very similar to the leading order calculation [31]. In view of the similarity between the leading order rate and the much more complicated next-to-leading order one, the leading order calculation is used in this work. It is referred in what follows as the "QGP LO" photon rate.

Attempts were made to study the effect of confinement on photon production from systems with quark and gluon degree of freedom. It was found in Ref. [111] that photons emission at temperatures not significantly above confinement ($T \sim 200 - 500$ MeV) appeared to be considerably smaller than expected from perturbative calculations that do not include the effect of confinement, such as the QGP LO rate. The model in Ref. [111] —

[5] Calculations of the photon emission rate for a strongly-coupled quark-gluon plasma — with $g_s \gg 1$ — are not currently available. It is worth mentioning, however, that photon emission in the strongly-coupled regime has been computed [110] for a supersymmetric Yang-Mills plasma, using the AdS/CFT correspondence.

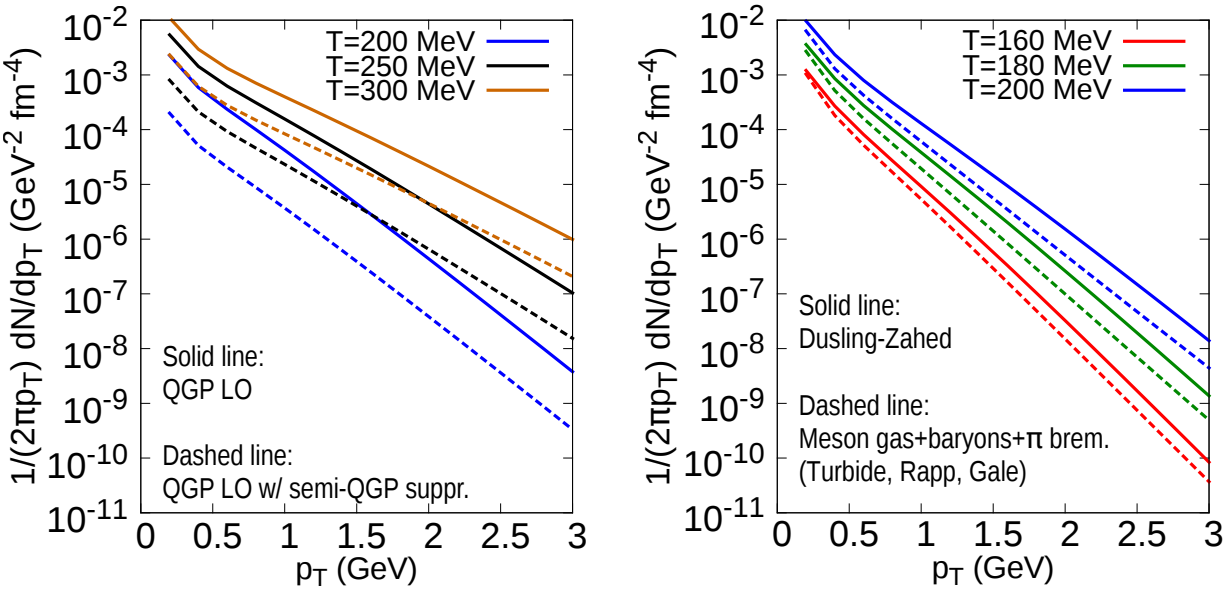

(a) (b)

Figure 5.2: (a) Comparison of the QGP LO photon emission rate from Ref. [31] and the semi-QGP rate from Ref. [111] at temperatures 200, 250 and 300 MeV (b) Comparison the hadronic photon emission rate from Refs. [112, 113, 114] ("Turbide, Rapp, Gale") and the hadronic rate from Ref. [115] ("Dusling-Zahed") at temperatures 160, 180 and 200 MeV.

referred to as the "semi-QGP" — is compared[6] to the QGP LO rate on Figure 5.2a. The suppression is very large, close to a factor of 10 in the $T \sim 200 - 300$ MeV region.

At lower temperatures, QCD matter can be described by hadronic degrees of freedom. Two notable calculations of the thermal photon production rate in this range of temperatures are Refs. [112, 113, 114] and Ref. [115].

The two calculations use different approaches. In Refs. [112, 113, 114], the emission of photons from light mesons (π, K, ρ, K^* and a_1) is evaluated by describing the mesons with a massive Yang-Mills Lagrangian. Moreover the contribution of baryons and additional mesonic sources to photon emission is included by evaluating the in-medium self-energy of the rho meson and relating it to the photon self-energy by through the vector dominance model [112]. Contributions from pion bremsstrahlung, $\pi\pi \to \pi\pi\gamma$ are also included [113, 114].

On the other hand, Ref. [115] uses a technique called chiral reduction to evaluate the production of photons. This approach is not straightforward to compare to the previous

[6] In Ref. [111], the effect of confinement is found to be a suppression factor that multiplies the thermal rate computed without confinement effects, like the QGP LO rate. However, the calculation is not made at full leading order in α_s, but only at "leading log" order. In the present work, the suppression factor is applied to the full QGP LO rate, which is an approximation. The same approximation was made in the numerical calculations of QGP photons shown in Ref. [111].

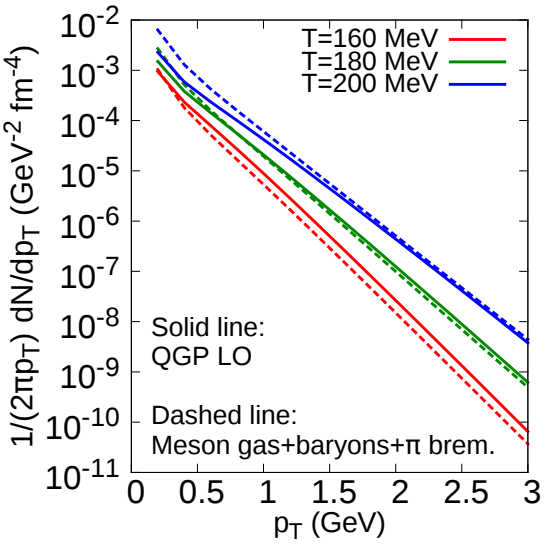

Figure 5.3: Comparison of the QGP LO photon emission rate from Ref. [31] and the hadronic rate from Refs. [112, 113, 114] at temperature 160, 180 and 200 MeV.

one, although certain specific reactions such as $\pi\rho \to \pi\gamma$ and $\pi\pi \to \pi\pi\gamma$ can be approximately compared, and were found to be in qualitative agreement [115, Section II-A]. While acceptable qualitative agreement was found for these channels, the total rates are significantly different, as shown on Figure 5.2b. The rate from Ref. [115] is much larger than that from Refs. [112, 113, 114], by as much as a factor of 2 or 3. The two approaches of evaluating photon emission are significantly different, and a systematic comparison of the two calculations to identify the origin of this discrepancy is not straightforward and has not yet been undertaken.

In summary, some uncertainties remain in the thermal photon emission rate of hot QCD matter. In this thesis, the QGP LO rate from Ref. [31] and the hadronic rate from Refs. [112, 113, 114] are used as reference thermal rates. The QGP rate is used for temperatures above $T_{tr} = 180$ MeV and the hadron gas rate below. As shown on Figure 5.3, the two rates are actually similar in magnitude around $T_{tr} = 180$ MeV. This would be different if another choice of hadronic or QGP rate had been made. The effect on direct photon calculations of changing the value of T_{tr} and of using different thermal rates is investigated in Chapter 7.

Once a choice of thermal photon emission rate has been made, thermal photons can be evaluated by folding the rate with the medium description provided by the hydrodynamical model.

5.3.2 Convoluting spacetime and rates

Denoting the thermal photon production rate

$$E\frac{d^3\Gamma}{d\mathbf{k}}(\mathbf{k}, T) \tag{5.2}$$

the photon emission in a frame boosted with 4-velocity u is

$$E\frac{d^3\Gamma}{d\mathbf{k}}(K \cdot u, T) \tag{5.3}$$

For a medium described by *ideal* hydrodynamics, photon emission is given by convoluting the medium description with the thermal photon rate

$$E\frac{d^3N}{d\mathbf{k}} = \int d^4X E\frac{d^3\Gamma}{d\mathbf{k}}(K \cdot u(X), T(X)) \tag{5.4}$$

If the medium is described by viscous hydrodynamics, the photon emission rate must be modified accordingly. This was also the case for hadrons, as described in Section 3.4.

For photons, emission is then given by

$$E\frac{d^3N}{d\mathbf{k}} = \int d^4X E\frac{d^3\Gamma}{d\mathbf{k}}(K^\mu, u^\mu(X), T(X), \pi^{\mu\nu}(X), \Pi(X)) \tag{5.5}$$

Evaluating the effect on photon production of the deviation from thermal equilibrium encoded in $\pi^{\mu\nu}(X)$ and $\Pi(X)$ is not straightforward. It is the subject of the next chapter.

Chapter 6

Thermal photon emission and viscosity

Ideal hydrodynamics describes a medium in perfect local thermal equilibrium. Deviations from local thermal equilibrium translate into the appearance of viscosity in the hydrodynamical equations. Photon emission from a medium described by viscous hydrodynamics must thus take these deviations from equilibrium into account.

For a medium with a quasiparticle description, viscosity implies a deviation of the quasiparticle's momentum distribution from the thermal Bose-Einstein and Fermi-Dirac distribution: shear and bulk viscosity are related to an anisotropy in the momentum distribution. The effect of this momentum anisotropy on photon production is investigated in this chapter.

Photon production from a hot QCD medium has been evaluated from many different approaches (c.f. Section 5.3.1); introducing the effect of viscosity in each approach presents its own intricacies. The present chapter focuses on the effect of viscosity on two channels of photon production by the QGP: Compton scattering ($gq \to \gamma q$) and quark-antiquark annihilation ($q\bar{q} \to g\gamma$), where q stands for a quark, $\bar{q}$ for an antiquark and g for a gluon. These two channels, which will be referred to as "$2 \to 2$ channels", represent approximately half of the full leading order (in α_s) photon production rate by the QGP [31].

There is an additional production channel, photon produced through soft bremsstrahlung ($2 \to n$ channels), that contributes to the same order in α_s and needs to be included for a full leading order evaluation of photon production by the QGP [31]. Introducing the effect of viscosity to this latter production channel presents significant new challenges, and is not addressed in this work.

At low temperatures, the contribution of light mesons (π, K, ρ, K^* and a_1) to the hadronic rates presented in Refs. [112, 113, 114] also represents approximately half of the total hadronic photon rate. Since photon production from these mesons is computed in a

kinetic theory approach, the effect of viscosity is straightforward to include. This is discussed briefly in the last section of this chapter. Taking into account the effect of viscosity on the other hadronic rates is more challenging; no attempts are made in the present work.

Before turning to the effect of viscosity in the QGP "$2 \to 2$" photon production channels, an general overview of photon production by a hot QCD medium is provided, followed by the derivation of general expressions for writing viscous corrections to photon production rates.

6.1 General

At leading order in the electromagnetic coupling constant, the production of photons of energy k and momentum $\mathbf{k}$ by a static[1] medium is given by [117]:

$$k\frac{d^3\Gamma}{d\mathbf{k}} = \frac{i}{2(2\pi)^3}\Pi^{12\mu}{}_{\mu}(k,\mathbf{k}) \tag{6.1}$$

where $\Pi^{12\mu}{}_{\mu}$ is the in-medium photon polarization tensor in the Schwinger-Keldish formalism.

Equation 6.1 can also be given a kinetic theory formulation, which for $2 \to 2$ scattering processes is [118]:

$$\begin{aligned} k\frac{d^3\Gamma_\gamma}{d\mathbf{k}} &= \frac{1}{2(2\pi)^3}\int \frac{d^3p_1}{2P_1^0(2\pi)^3}\frac{d^3p_2}{2P_2^0(2\pi)^3}\frac{d^3p_3}{2P_3^0(2\pi)^3}(2\pi)^4\delta^4(P_1+P_2-P_3-K)|\mathcal{M}|^2 \\ &\quad \times f_{B/F}(P_1)f_{B/F}(P_2)(1+\sigma_{B/F}f_{B/F}(P_3)) \end{aligned} \tag{6.2}$$

where $|\mathcal{M}|^2$ is the squared matrix element corresponding to the $2 \to 2$ scattering and $f_{B/F}$ is the particle momentum distribution for bosons ($\sigma_B = 1$) or fermions ($\sigma_F = -1$). Photon absorption by the medium is neglected in Equation 6.2.

For photon production by the QGP, $\bar{\Pi}^{<\mu}{}_{\mu}(k,\mathbf{k})$ or $|\mathcal{M}|^2$ are computed directly from quantum chromodynamics as perturbative series in the strong coupling constant. The same cannot be done for photon emission from hadronic degrees of freedom; other approaches such as effective models of hadronic and photonic interactions are used instead.

At both low and high temperatures, corrections to the photon rate due to viscosity enter in Equations 6.1 and 6.2 through the particle momentum distribution $f_{B/F}(P)$. More

[1] In this section as in this whole thesis, photons are assumed to be produced on timescales much smaller than any macroscopic timescale of the emitting medium. As a consequence the medium is considered static during the photon emission. The theoretical framework for photon emission from an evolving medium is discussed in [116, Section 4.2].

precisely, they enter in $f_{B/F}(P)$ as a correction to the thermal distribution function $f^{(0)}_{B/F}(P)$:

$$f_{B/F}(P,X) = f^{(0)}_{B/F}(P) + \delta f_{B/F}(P,X) \tag{6.3}$$

Since deviations from thermal equilibrium should be small, linearising the photon emission rate $kd^3\Gamma_\gamma/d\mathbf{k}$ in $\delta f_{B/F}(P,X)$ is expected to be a reasonable approximation. This linearisation can be used to write general expressions for the viscous corrections to photon production, which is shown in the next section.

6.1.1 Viscosity and generalised tensor decomposition

General formulae for the correction to photon production due to viscosity can be derived for Equation 6.2, since the momentum distribution $f_{B/F}(P,X)$ are explicit. Linearising in $\delta f_{B/F}(P,X)$,

$$\begin{aligned}
k\frac{d^3\Gamma_\gamma}{d\mathbf{k}} &\approx \frac{1}{2(2\pi)^3}\int \frac{d^3p_1}{2P_1^0(2\pi)^3}\frac{d^3p_2}{2P_2^0(2\pi)^3}\frac{d^3p_3}{2P_3^0(2\pi)^3}(2\pi)^4\delta^4(P_1+P_2-P_3-K)|\mathcal{M}|^2 \\
&\quad\times\Big[f^{(0)}_{B/F}(P_1)f^{(0)}_{B/F}(P_2)(1+\sigma_{B/F}f^{(0)}_{B/F}(P_3)) \\
&\qquad+\delta f_{B/F}(P_1)f^{(0)}_{B/F}(P_2)(1+\sigma_{B/F}f^{(0)}_{B/F}(P_3)) \\
&\qquad\quad+f^{(0)}_{B/F}(P_1)\delta f_{B/F}(P_2)(1+\sigma_{B/F}f^{(0)}_{B/F}(P_3)) \\
&\qquad\qquad+f^{(0)}_{B/F}(P_1)f^{(0)}_{B/F}(P_2)(\sigma_{B/F}\delta f_{B/F}(P_3))\Big] \\
&= k\frac{d^3\Gamma^{(0)}_\gamma}{d\mathbf{k}} + k\frac{d^3\Gamma^{(visc)}_\gamma}{d\mathbf{k}}
\end{aligned} \tag{6.4}$$

where $kd^3\Gamma^{(0)}_\gamma/d\mathbf{k}$ is the ideal emission rate and its correction due to viscosity is

$$\begin{aligned}
k\frac{d^3\Gamma^{(visc)}_\gamma}{d\mathbf{k}} &= \frac{1}{2(2\pi)^3}\int \frac{d^3p_1}{2P_1^0(2\pi)^3}\frac{d^3p_2}{2P_2^0(2\pi)^3}\frac{d^3p_3}{2P_3^0(2\pi)^3}(2\pi)^4\delta^4(P_1+P_2-P_3-K)|\mathcal{M}|^2 \\
&\quad\times\Big[\delta f_{B/F}(P_1)f^{(0)}_{B/F}(P_2)(1+\sigma_{B/F}f^{(0)}_{B/F}(P_3)) \\
&\qquad+f^{(0)}_{B/F}(P_1)\delta f_{B/F}(P_2)(1+\sigma_{B/F}f^{(0)}_{B/F}(P_3)) \\
&\qquad\quad+f^{(0)}_{B/F}(P_1)f^{(0)}_{B/F}(P_2)(\sigma_{B/F}\delta f_{B/F}(P_3))\Big]
\end{aligned} \tag{6.5}$$

To proceed further, assumptions need to be made about the form of $\delta f_{B/F}(P,X)$. A first assumption is that $\delta f_{B/F}(P,X)$ is linear in the shear stress tensor $\pi^{\mu\nu}$ and the bulk

pressure Π. In this case:

$$\delta f_{B/F}(P,X) = \pi_{\mu\nu}(X)P^\mu P^\nu S(P,X) + \Pi(X)B(P,X) \tag{6.6}$$

where two properties of $\pi_{\mu\nu}(X)$, $\pi_{\mu\nu}(X)g^{\mu\nu} = 0$ and $\pi_{\mu\nu}(X)u^\mu = 0$, were used to constrain the expansion of $\delta f_{B/F}(P,X)$ in $\pi_{\mu\nu}(X)$.

The arbitrary functions $S(P,X)$ and $B(P,X)$ can depend on the spacetime position X through e.g. the local value of the temperature $T(X)$, the energy density $\epsilon(X)$, the entropy density $s(X)$, etc. All these implicit functions of X are thermodynamical quantities that are related through the equation of state of the medium. For practical reasons, it is better if corrections to photon emission do not have an explicit dependence on the equation of state. This can be achieved if the momentum dependence of $S(P,X)$ and $B(P,X)$ can be factorised from the rest such as:

$$\delta f_{B/F}(P,X) = \pi_{\mu\nu}(X)P^\mu P^\nu \sum_j S_X^{(j)}(X)S_M^{(j)}(P,T) + \Pi(X)\sum_j B_X^{(j)}(X)B_M^{(j)}(P,T) \tag{6.7}$$

where it was assumed that the momentum-dependent factor $S/B_M^{(j)}(P,T)$ could also depend on the temperature, but no other thermodynamical quantities. The subscript X was used to identify the spatial part of S and B, while the subscript M is used for the momentum dependent term. The sum over j is necessary if e.g. $B(P,X)$ cannot be factorised as $B_S(X)B_M(P)$ but is factorisable as a sum of such terms $(B_S^{(1)}(X)B_M^{(1)}(P) + B_S^{(2)}(X)B_M^{(2)}(P))$. It will be shown shortly that such a general form is necessary for the $\delta f_{B/F}(P,X)$ used in this thesis. In general, expressions for $\delta f_{B/F}(P,X)$ derived from the Boltzmann equation can be written without loss of generality as Equation 6.7 (see e.g. Ref. [65, Chapter 4]).

Using Equation 6.7, the effect of viscosity on photon production (Equation 6.5) can be written

$$k\frac{d^3\Gamma_\gamma^{(visc)}}{d\mathbf{k}} = \pi_{\mu\nu}(X)K^\mu K^\nu \sum_j S_X^{(j)}(X)\tilde{S}_M^{(j)}(K,T) + \Pi(X)\sum_j B_X^{(j)}(X)\tilde{B}_M^{(j)}(K,T) \tag{6.8}$$

where $\pi_{\mu\nu}(X)g^{\mu\nu} = 0$ and $\pi_{\mu\nu}(X)u^\mu = 0$ were used again to constrain the coefficient multiplying $\pi_{\mu\nu}(X)$.

The coefficient $\tilde{S}_M^{(j)}(K,T)$ is given by

$$\begin{aligned}\tilde{S}_M^{(j)}(K,T) &= \frac{1}{2(K\cdot u)^2}\left[g_{\mu\nu}+2u_\mu u_\nu+3\left(\frac{K_\mu K_\nu}{(K\cdot u)^2}-\frac{(K_\mu u_\nu+u_\mu K_\nu)}{(K\cdot u)}\right)\right]\\ &\times\frac{1}{2(2\pi)^3}\int\frac{d^3p_1}{2P_1^0(2\pi)^3}\frac{d^3p_2}{2P_2^0(2\pi)^3}\frac{d^3p_3}{2P_3^0(2\pi)^3}(2\pi)^4\delta^4(P_1+P_2-P_3-K)|\mathcal{M}|^2\\ &\times\Big[\Big(P_1^\mu P_1^\nu S_M^{(j)}(P_1)\Big)f_{B/F}^{(0)}(P_2)(1+\sigma_{B/F}f_{B/F}^{(0)}(P_3))\\ &\quad+f_{B/F}^{(0)}(P_1)\Big(P_2^\mu P_2^\nu S_M^{(j)}(P_2)\Big)(1+\sigma_{B/F}f_{B/F}^{(0)}(P_3))\\ &\quad+f_{B/F}^{(0)}(P_1)f_{B/F}^{(0)}(P_2)\Big(\sigma_{B/F}P_3^\mu P_3^\nu S_M^{(j)}(P_3)\Big)\Big]\end{aligned} \tag{6.9}$$

while $\tilde{B}_M^{(j)}(K,T)$ is given by the simpler expression

$$\begin{aligned}\tilde{B}_M^{(j)}(K,T) &= \frac{1}{2(2\pi)^3}\int\frac{d^3p_1}{2P_1^0(2\pi)^3}\frac{d^3p_2}{2P_2^0(2\pi)^3}\frac{d^3p_3}{2P_3^0(2\pi)^3}(2\pi)^4\delta^4(P_1+P_2-P_3-K)|\mathcal{M}|^2\\ &\times\Big[\Big(B_M^{(j)}(P_1)\Big)f_{B/F}^{(0)}(P_2)(1+\sigma_{B/F}f_{B/F}^{(0)}(P_3))\\ &\quad+f_{B/F}^{(0)}(P_1)\Big(B_M^{(j)}(P_2)\Big)(1+\sigma_{B/F}f_{B/F}^{(0)}(P_3))\\ &\quad+f_{B/F}^{(0)}(P_1)f_{B/F}^{(0)}(P_2)\Big(\sigma_{B/F}B_M^{(j)}(P_3)\Big)\Big]\end{aligned} \tag{6.10}$$

Since $\tilde{S}_M^{(j)}(K,T)$ and $\tilde{B}_M^{(j)}(K,T)$ are scalars, they can only depend on K through the combination $K\cdot u$. In the rest frame of the fluid, $K\cdot u = K^0 = k$, which means that $\tilde{S}_M^{(j)}(K,T)$ and $\tilde{B}_M^{(j)}(K,T)$ only depend on the energy of the photon, along with the temperature. Although $\tilde{S}_M^{(j)}(K,T)$ and $\tilde{B}_M^{(j)}(K,T)$ cannot generally be reduced to an analytical expression, it is nevertheless possible to tabulate them as functions of the photon energy k and the medium's local temperature T.

All the above derivations were made possible by the linearisation in $\delta f_{B/F}(P,X)$ of Equation 6.5, as well as the assumption that $\delta f_{B/F}(P,X)$ can be written as Equation 6.7. With these assumptions, the final expression for the photon emission rate is

$$k\frac{d^3\Gamma_\gamma}{d\mathbf{k}} = k\frac{d^3\Gamma_\gamma^{(0)}}{d\mathbf{k}}+\pi_{\mu\nu}(X)K^\mu K^\nu\sum_j S_X^{(j)}(X)\tilde{S}_M^{(j)}(K,T)+\Pi(X)\sum_j B_X^{(j)}(X)\tilde{B}_M^{(j)}(K,T) \tag{6.11}$$

If photon production is computed in the diagrammatic method from Equation 6.1 instead of the kinetic theory approach, linearisation in $\delta f_{B/F}(P,X)$ can still be used to write the photon rate as Equation 6.11, although with different expressions for $\tilde{S}_M^{(j)}(K)$ and $\tilde{B}_M^{(j)}(K)$.

There is no general formula for $\tilde{S}_M^{(j)}(K)$ and $\tilde{B}_M^{(j)}(K)$ in this case; it depends on the exact expression for $\Pi^{12\mu}{}_{\mu}(k, \mathbf{k})$.

Having formulated general expressions for the effect of viscosity on photon emission, the exact form of momentum anisotropy $\delta f_{B/F}(P, X)$ used in this work is specified in the next section.

6.1.2 Momentum anisotropy $\delta f_{B/F}(P, X)$

The momentum anisotropy $\delta f_{B/F}(P, X)$ affects the production of photons and hadrons alike (see Section 3.4). The form for $\delta f_{B/F}(P, X)$ used in this thesis for the momentum distribution of hadron was given at Equations 3.37, 3.38 and 3.39.

For photons produced at low temperatures, it is also appropriate to use Equations 3.37, 3.38 and 3.39 as momentum anisotropy.

On the other hand, at high temperature, the momentum anisotropy of bulk viscosity takes a different form. This is a consequence of quarks and gluons not having fixed masses like hadrons, but effective masses that depend on the temperature. In this case, δf_{bulk} is given by [84]

$$\delta f_{B/F}^{bulk,QGP} = -f_{B/F}^{(0)} \left(1 + \sigma_{B/F} f_{B/F}^{(0)}\right) \left[\frac{m^2}{T^2} \frac{1}{P^0/T} - \frac{P^0}{T}\right] \frac{\Pi}{15\left(\frac{1}{3} - c_s^2\right)(\epsilon + \mathcal{P})} \tag{6.12}$$

The mass entering Equation 6.12 is taken to be the thermal mass of quarks, $m_\infty^2 = g_s^2 T^2/3$.

The relation between τ_Π and ζ given by Equation 3.22 was used in Equation 6.12. For hadrons, τ_Π/ζ was computed from a hadron resonance gas, but this would not be appropriate for quarks and gluons.

For shear viscosity, the same expression for the momentum anisotropy is used for quarks and gluons as for hadronic degrees of freedom, i.e. Equation 3.38, since the relation between mass and temperature does not affect it.

Using the notation of Equation 6.7, the momentum anisotropy at high temperatures is given by

$$\delta f_{B/F}^{QGP}(P, X) \;=\; \pi_{\mu\nu}(X) P^\mu P^\nu S_X S_M(P, T) + \Pi(X) B_X^{QGP} B_M^{QGP}(P, T) \tag{6.13}$$

with

$$S_X = \frac{1}{2(\epsilon+\mathcal{P})}; \qquad S_M = \frac{f^{(0)}_{B/F}\left(1+\sigma_{B/F}f^{(0)}_{B/F}\right)}{T^2}$$
$$B_X^{QGP} = -\frac{1}{15\left(\frac{1}{3}-c_s^2\right)(\epsilon+\mathcal{P})}; \qquad B_M^{QGP} = f^{(0)}_{B/F}(P)\left(1+\sigma_{B/F}f^{(0)}_{B/F}(P)\right)\left[\frac{m^2}{T^2}\frac{1}{P^0/T}-\frac{P^0}{T}\right] \tag{6.14}$$

For hadronic degrees of freedom, it is given by

$$\begin{aligned}\delta f^{HG}_{B/F}(P,X) &= \pi_{\mu\nu}(X)P^\mu P^\nu S_X S_M(P,T) \\ &\quad +\Pi(X)\left[B_X^{HG,1}(X)B_M^{HG,1}(P,T)+B_X^{HG,2}(X)B_M^{HG,2}(P,T)\right]\end{aligned} \tag{6.15}$$

with

$$B_X^{HG,1} = -\frac{\tau_\Pi}{\zeta}; \qquad B_M^{HG,1} = f^{(0)}_{B/F}(P)\left(1+\sigma_{B/F}f^{(0)}_{B/F}(P)\right)\frac{1}{3}\frac{m^2}{T^2}\frac{1}{P^0/T}$$
$$B_X^{HG,2} = -\frac{\tau_\Pi}{\zeta}\left(\frac{1}{3}-c_s^2\right); \qquad B_M^{HG,2} = f^{(0)}_{B/F}(P)\left(1+\sigma_{B/F}f^{(0)}_{B/F}(P)\right)\left(-\frac{P^0}{T}\right) \tag{6.16}$$

The above decompositions are not uniquely defined, since temperature factors and constants can be in either coefficients. This is not a problem as long as the above definitions are used consistently.

With the expressions for $\delta f_{B/F}(P,X)$ fixed, the next section of this chapter is dedicated to evaluating $\tilde{S}_M^{(j)}(K,T)$ and $\tilde{B}_M^{(j)}(K,T)$ for photon produced through $2\to 2$ scattering in the QGP.

6.2 QGP photon rates for $2 \to 2$ channels

Photon production through $2 \to 2$ scattering contributes at leading order in the strong coupling constant to photon production by a hot quark-gluon plasma.

The evaluation of these channels of photon production is made in two steps, corresponding to two kinematic regions that need to be treated differently. These kinematic regions are referred to as the "hard" and "soft" parts of the $2 \to 2$ processes. This division of the calculation can be understood from the diagrams that contribute to the photon self-energy $\Pi^{12\mu}{}_{\mu}(k,\mathbf{k})$ in Equation 6.1. These diagrams are shown on Figure 6.1.

The hard and soft division of the kinematics is due to the quark self-energy delimited by the quark propagators with momentum Q in the first two diagrams of Figure 6.1. In these two diagrams, the quark self-energy is evaluated with one gluon loop, which results

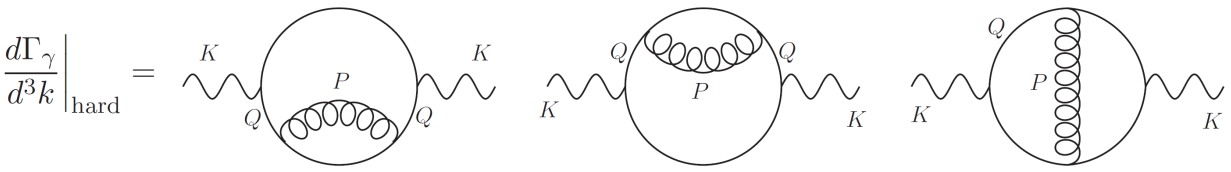

Figure 6.1: Photon self-energies contributing at leading order in α_s to photon production from the QGP (Figure adapted from [109])

in a leading order contribution to $\Pi^{12\mu}{}_{\mu}(k,\mathbf{k})$ when the momentum Q is of order T. The temperature T is referred to as the "hard" scale.

There is also a soft scale, g_sT, with the assumption $g_s \ll 1$. When $Q \sim gT$ the quark self-energy cannot be evaluated with a single gluon loop, due to subtleties in power counting in finite temperature quantum chromodynamics. An infinite number of diagrams must be resummed. This approach is called the "hard thermal loop" resummation [119]. The soft part of the calculation corresponds to evaluating the first two diagrams of Figure 6.1 with this resummed quark self-energy.

The spatial part of Q, $q = |\mathbf{q}|$, is used to separate the hard and soft part of the calculation. The hard part corresponds to $q > q_*$ and the soft part to $q < q_*$. The cut-off q^* is chosen such that $g_sT \ll q^* \ll T$. The dependence of the photon rate on this cut-off is investigated later in this section.

Following the definitions given in Sections 6.1.1 and 6.1.2, the rate is written

$$\begin{aligned} k\frac{d^3\Gamma_\gamma^{QGP}}{d\mathbf{k}} &= k\frac{d^3\Gamma_\gamma^{(0)QGP}}{d\mathbf{k}} + \frac{\pi_{\mu\nu}(X)K^\mu K^\nu}{2(\epsilon+\mathcal{P})}\tilde{S}_M^{QGP}(K,T) \\ &\quad + \left(-\frac{\Pi(X)}{15\left(\frac{1}{3}-c_s^2\right)(\epsilon+\mathcal{P})}\right)\tilde{B}_M^{QGP}(K,T) \end{aligned} \tag{6.17}$$

As a consequence of the division in two kinematic regions of photon production from QGP $2 \to 2$ channels, the effect of viscosity must be evaluated separately for each part of the calculation. As a first step, the effect of *shear* viscosity on QGP $2 \to 2$ processes is investigated, starting with the hard part followed by the soft part. This forms the first part (Section 6.2.1) of this section. The result is $\tilde{S}_M^{QGP}(K,T,q_*)$.

The calculation of the effect of shear viscosity is then repeated using the "forward scattering approximation", which simplifies considerably the evaluation of the effect of viscosity on QGP $2 \to 2$ processes. The validity of the forward scattering approximation is established by comparison with the full calculation.

Finally the forward scattering approximation is used in Section 6.2.2 to evaluate the effect

of bulk viscosity on QGP $2 \to 2$ photon production, yielding an estimate of $\tilde{B}_M^{QGP}(K,T)$.

6.2.1 Shear viscosity correction: full calculation

The function $\tilde{S}_M^{QGP}(K,T,q_*)$ from Equation 6.17 is divided in two:

$$\tilde{S}_M^{QGP}(K,T,q_*) = \tilde{S}_M^{hard}(K,T,q_*) + \tilde{S}_M^{soft}(K,T,q_*) \tag{6.18}$$

The effect on QGP $2 \to 2$ photon production of an anisotropy in the momentum distribution of quarks and gluons was investigated in Ref. [120] for a momentum anisotropy of the form $f_{B/F}(\mathbf{p}) \propto f_{B/F}^{(0)}(\sqrt{\mathbf{p}^2 + \xi(\mathbf{p}\cdot\hat{\mathbf{n}})^2})$ with $\hat{\mathbf{n}}$ the direction of the assumed momentum anisotropy. This specific form of momentum anisotropy allows for a fairly straightforward inclusion of the effect of momentum anisotropy in the photon production rates. On the other hand, it does not correspond to the $\delta f_{B/F}(P,X)$ ansatz typically used in hydrodynamical models of heavy ion collisions. In particular, the expression for $\delta f_{B/F}(P,X)$ used in the present work (Section 6.1.2) cannot be written as $f_{B/F}^{(0)}(\sqrt{\mathbf{p}^2 + \xi(\mathbf{p}\cdot\hat{\mathbf{n}})^2})$.

In what follows, the approach presented in Ref. [120] is extended to the momentum anisotropy ansatz $\delta f_{B/F}^{shear}(P,X)$ used in this thesis. The "hard" kinematic region is treated first.

6.2.1.1 Hard $2 \to 2$ kinematic region

The diagrams that represent the $2 \to 2$ scattering contribution to $\Pi^{12\mu}{}_{\mu}(k,\mathbf{k})$ at leading order in α_s are shown on Figure 6.1. These diagrams can be written in terms of matrix elements, to be used with Equation 6.2. The squared matrix element for Compton scattering and quark-antiquark annihilation are explicitely given by [31]

$$|\mathcal{M}_C|^2 = N_M \left[\frac{-s}{t} + \frac{-t}{s}\right] \tag{6.19}$$

$$|\mathcal{M}_A|^2 = N_M \left[\frac{u}{t}\right] \tag{6.20}$$

with

$$N_M \equiv 64\pi\alpha_{EM} \left[N_c \sum_s q_s^2\right] C_F g_s^2 \tag{6.21}$$

where $N_c = 3$ and $C_F = 4/3$ for QCD, and $\alpha_{EM} \approx 1/137$ is the electromagnetic coupling constant. The sum over s is a sum over the quark flavours, with q_s being the quark's electric charge in units of the proton's charge. The variable $g_s = \sqrt{4\pi\alpha_s}$ is the strong coupling

constant (the name is used for both g_s and α_s). The Mandelstam variables are defined as:

$$s = (P_1 + P_2)^2;\ t = (P_1 - K)^2;\ u = (P_1 - P_3)^2 \tag{6.22}$$

where P_1 and P_2 are the 4-momenta of the initial state quarks/gluons, P_3 that of the final state quark/gluon and K that of the photon.

Photon production is thus given by

$$\begin{aligned} k\frac{d^3\Gamma_\gamma^{hard}}{d\mathbf{k}} &= \frac{1}{2(2\pi)^3}\int \frac{d^3p_1}{2P_1^0(2\pi)^3}\frac{d^3p_2}{2P_2^0(2\pi)^3}\frac{d^3p_3}{2P_3^0(2\pi)^3}(2\pi)^4\delta^4(P_1+P_2-P_3-K) \\ &\times\left[f_F(P_1)f_B(P_2)(1-f_F(P_3))|\mathcal{M}_C|^2 + f_F(P_1)f_F(P_2)(1+f_B(P_3))|\mathcal{M}_A|^2\right] \end{aligned} \tag{6.23}$$

The division of the kinematic in soft and hard parts only affects terms with $1/t$ dependence in the matrix elements [31, Section 5]. Separating the $1/t$ terms from the rest, photon emission can be written:

$$k\frac{d^3\Gamma_\gamma^{hard}}{d\mathbf{k}} = k\frac{d^3\Gamma_\gamma^{[u/t]}}{d\mathbf{k}} + k\frac{d^3\Gamma_\gamma^{[-s/t]}}{d\mathbf{k}} + k\frac{d^3\Gamma_\gamma^{[-t/s]}}{d\mathbf{k}} \tag{6.24}$$

with

$$\begin{aligned} k\frac{d^3\Gamma_\gamma^{[u/t]}}{d\mathbf{k}} &= \frac{N_M}{2(2\pi)^3}\int \frac{d^3p_1}{2P_1^0(2\pi)^3}\frac{d^3p_2}{2P_2^0(2\pi)^3}\frac{d^3p_3}{2P_3^0(2\pi)^3}(2\pi)^4\delta^4(P_1+P_2-P_3-K) \\ &\times\left[f_F(P_1)f_F(P_2)(1+f_B(P_3))\left(\frac{u}{t}\right)\right] \end{aligned} \tag{6.25}$$

$$\begin{aligned} k\frac{d^3\Gamma_\gamma^{[-s/t]}}{d\mathbf{k}} &= \frac{N_M}{2(2\pi)^3}\int \frac{d^3p_1}{2P_1^0(2\pi)^3}\frac{d^3p_2}{2P_2^0(2\pi)^3}\frac{d^3p_3}{2P_3^0(2\pi)^3}(2\pi)^4\delta^4(P_1+P_2-P_3-K) \\ &\times\left[f_F(P_1)f_B(P_2)(1-f_F(P_3))\left(\frac{-s}{t}\right)\right] \end{aligned} \tag{6.26}$$

and

$$\begin{aligned} k\frac{d^3\Gamma_\gamma^{[-t/s]}}{d\mathbf{k}} &= \frac{N_M}{2(2\pi)^3}\int \frac{d^3p_1}{2P_1^0(2\pi)^3}\frac{d^3p_2}{2P_2^0(2\pi)^3}\frac{d^3p_3}{2P_3^0(2\pi)^3}(2\pi)^4\delta^4(P_1+P_2-P_3-K) \\ &\times f_F(P_1)f_B(P_2)(1-f_F(P_3))\left(\frac{-t}{s}\right) \end{aligned} \tag{6.27}$$

The same notation as Ref. [31] is used for convenience.

The phase space of Equations 6.25 and 6.26 is restricted to $q > q_*$, with $q \equiv |\mathbf{k} - \mathbf{p}_1|$. The region $q < q_*$ is the soft part of the calculation, treated in the next section. The cut-off q_* is assumed to be $g_s T \ll q_* \ll T$. Equation 6.27 does not have any kinematic restriction, and integration is over the full phase space.

Equations 6.25, 6.26 and 6.27 all correspond to separate terms in the viscous correction $\tilde{S}_M^{hard}(K,T)$:

$$\tilde{S}_M^{hard}(K,T) = \tilde{S}_M^{hard}(K,T,q_*)[u/t] + \tilde{S}_M^{hard}(K,T,q_*)[s/t] + \tilde{S}_M^{hard}(K,T)[t/s] \tag{6.28}$$

The general decomposition from Section 6.1.1 can be used to evaluate $\tilde{S}_M^{hard}(K,T)$. Following Equation 6.9, the term $\tilde{S}_M^{hard}(K,T)[u/t]$ is given by

$$\begin{aligned}
\tilde{S}_M^{hard}(K,T)[u/t] &= \frac{1}{2(K\cdot u)^2}\left[g_{\mu\nu} + 2u_\mu u_\nu + 3\left(\frac{K_\mu K_\nu}{(K\cdot u)^2} - \frac{(K_\mu u_\nu + u_\mu K_\nu)}{(K\cdot u)}\right)\right] \\
&\quad \times \frac{N_M}{2(2\pi)^3}\int \frac{d^3p_1}{2P_1^0(2\pi)^3}\frac{d^3p_2}{2P_2^0(2\pi)^3}\frac{d^3p_3}{2P_3^0(2\pi)^3}(2\pi)^4\delta^4(P_1+P_2-P_3-K)\left(\frac{u}{t}\right) \\
&\quad \times \left[P_1^\mu P_1^\nu\left(\frac{f_F^{(0)}(P_1)\left(1-f_F^{(0)}(P_1)\right)}{T^2}\right) f_F^{(0)}(P_2)(1+f_B^{(0)}(P_3))\right. \\
&\qquad + f_F^{(0)}(P_1)P_2^\mu P_2^\nu\left(\frac{f_F^{(0)}(P_2)\left(1-f_F^{(0)}(P_2)\right)}{T^2}\right)(1+f_B^{(0)}(P_3)) \\
&\qquad \left. + f_F^{(0)}(P_1)f_F^{(0)}(P_2)P_3^\mu P_3^\nu\left(\frac{f_B^{(0)}(P_3)\left(1+f_B^{(0)}(P_3)\right)}{T^2}\right)\right]
\end{aligned} \tag{6.29}$$

Quarks are considered massless in this part of the calculation, and there are no other energy scales than P_i, K and T. It is thus convenient to scale all momenta by the temperature, $\tilde{P}_i = P_i/T$ and $\tilde{K}_i = K/T$, to get a unitless integral:

$$\begin{aligned}
\tilde{S}_M^{hard}(\tilde{K})[u/t] &= \frac{1}{2(\tilde{K}\cdot u)^2}\left[g_{\mu\nu} + 2u_\mu u_\nu + 3\left(\frac{\tilde{K}_\mu \tilde{K}_\nu}{(\tilde{K}\cdot u)^2} - \frac{(\tilde{K}_\mu u_\nu + u_\mu \tilde{K}_\nu)}{(\tilde{K}\cdot u)}\right)\right] \\
&\quad \times \frac{N_M}{2^4(2\pi)^8} Y^{\mu\nu}[u/t]
\end{aligned} \tag{6.30}$$

with

$$\begin{aligned}
Y^{\mu\nu}[u/t] &\equiv \int \frac{d^3\tilde{p}_1}{\tilde{P}_1^0}\frac{d^3\tilde{p}_2}{\tilde{P}_2^0}\frac{d^3\tilde{p}_3}{\tilde{P}_3^0}\delta^4(\tilde{P}_1+\tilde{P}_2-\tilde{P}_3-\tilde{K})\left(\frac{u}{t}\right) \\
&\quad f_F^{(0)}(\tilde{p}_1)f_F^{(0)}(\tilde{p}_2)(1+f_B^{(0)}(\tilde{p}_3)) \\
&\quad \times \left[\tilde{P}_1^\mu \tilde{P}_1^\nu\left(1-f_F^{(0)}(\tilde{p}_1)\right) + \tilde{P}_2^\mu \tilde{P}_2^\nu\left(1-f_F^{(0)}(\tilde{p}_2)\right) + \tilde{P}_3^\mu \tilde{P}_3^\nu f_B^{(0)}(\tilde{p}_3)\right]
\end{aligned} \tag{6.31}$$

Applying the projector on $Y^{\mu\nu}[u/t]$, $\tilde{S}_M^{hard}(\tilde{K})[u/t]$ reduces to

$$\tilde{S}_M^{hard}(\tilde{K})[u/t] = \frac{1}{2(\tilde{K}\cdot u)^2}\frac{N_M}{2^4(2\pi)^8}\left[-Y^{00}[u/t] + \frac{\tilde{\mathbf{k}}_i\tilde{\mathbf{k}}_j Y^{ij}[u/t]}{\tilde{k}^2}\right] \tag{6.32}$$

where i and j run over the spatial index only.

Similar expression are found for $\tilde{S}_M^{hard}(\tilde{K})[-s/t]$ and $\tilde{S}_M^{hard}(\tilde{K})[-t/s]$ by replacing the matrix element u/t by $-s/t$ and $-t/s$.

No simple expressions were found for Y^{00} and Y^{ij}. Their complete calculation is shown in Appendix B.

Both $\tilde{S}_M^{hard}(\tilde{K})[u/t]$ and $\tilde{S}_M^{hard}(\tilde{K})[-s/t]$ depend on the cut-off q_*. This cut-off dependence should be canceled by the soft part of the calculation, which is computed in the next section.

6.2.1.2 Soft $2 \to 2$ kinematic region

Soft photons are evaluated with Equation 6.1. Using the hard thermal loop prescription described in the beginning of this chapter, $\bar{\Pi}^{12\mu}{}_{\mu}(k,\mathbf{k})$ is given by [120]

$$\begin{aligned}\Pi^{12\mu}{}_{\mu}(K) &= ie^2\sum_s q_s^2 N_c\int_{q<q_*}\frac{d^4Q}{(2\pi)^4}\mathrm{Tr}[S_{12}^D(Q)\gamma^\mu S_{21}(Q-K)\gamma_\mu \\ &\quad + S_{21}^D(Q)\gamma^\mu S_{12}(Q+K)\gamma_\mu]\end{aligned} \tag{6.33}$$

where S^D refers to dressed (HTL) quark propagators and γ^μ are the Dirac gamma matrices. The momentum Q is defined in the same way as in the previous section (see also Figure 6.1), such that the integral over Q must be limited to $q < q_*$.

The free fermion and boson propagators are given, respectively, by

$$S_{12/21}(K) = \not{K}2\pi i\delta(K^2)[-\theta(-\sigma K^0) + f_F(K)] \tag{6.34}$$

$$\Delta_{12/21}(K) = -2\pi i\delta(K^2)[\theta(-\sigma K^0) + f_B(K)] \tag{6.35}$$

while the dressed propagators are given by

$$S_{12/21}^D(P) = S_R^D(P)\Sigma_{12/21}(P)S_A^D(P) \tag{6.36}$$

where

$$\Sigma_{12/21}(P) = 2ig_s^2 C_F\int\frac{d^4V}{(2\pi)^4}S_{12/21}(V)\Delta_{12/21}(P-V) \tag{6.37}$$

and

$$S_R^D(P) = \frac{(\not{P} - \Sigma_R(P))}{(P-\Sigma_R(P))^2};\quad \Sigma_R(P) = \Sigma_R^\mu(P)\gamma_\mu \tag{6.38}$$

with

$$\Sigma_R^\mu(K) = m_\infty^2 \int \frac{d^3\mathbf{v}}{(2\pi)^3} \frac{4(f_F(V) + f_B(V))}{v} \frac{V^\mu}{V \cdot K + i\epsilon}; \;\; m_\infty^2 = \frac{C_F g_s^2 T^2}{4} \tag{6.39}$$

The advanced fermion propagator and fermion self-energy are given by the complex conjugate of the retarded ones.

All these relations hold for momentum distributions $f_{F/B}(P)$ with arbitrary momentum anisotropy [121, 122, 123], as long as the medium is static.

Equation 6.33 can be simplified considerably if the distribution function $f_{F/B}(P)$ is assumed to be reflection-symmetric:

$$f_{F/B}(-P) = f_{F/B}(P) \tag{6.40}$$

This assumption is valid for the thermal distribution $f_{F/B}^{(0)}(P) = 1/(e^{|P^0|/T} \pm 1)$.

Since $\delta f_{F/B}^{shear}$ only depends on P through $f_{F/B}^{(0)}(P)$, and through $P^\mu P^\nu \pi_{\mu\nu}$, which is trivially even in P, $\delta f_{F/B}^{shear}$ also respects Equation 6.40.

Using Equation 6.40, Equation 6.33 can be shown to reduce to

$$-i\Pi_{12}{}^\mu{}_\mu(K) \;\; = \;\; \frac{8e^2 \sum_q q_s^2 N_c}{(2\pi)^3} f_F(K) \int_{q<q_*} d^4Q \delta(K \cdot Q) \mathrm{Im}\left[K \cdot S_R^D(Q)\right] \tag{6.41}$$

The complete derivation is shown in Appendix C.1.

The soft contribution to the photon production rate is thus given by

$$k\frac{d^3\Gamma_\gamma^{soft}}{d\mathbf{k}} = \frac{-4e^2 \sum_q q_s^2 N_c}{(2\pi)^6} f_F(K) \int_{q<q_*} d^4Q \delta(K \cdot Q) \mathrm{Im}\left[K \cdot S_R^D(Q)\right] \tag{6.42}$$

Two terms linear in $\delta f_{F/B}^{shear}$ are possible. The first one has δf_F^{shear} in the prefactor $f_F(K)$, and the retarded self-energy $S_R^D(Q)$ evaluted with thermal distributions $f_{B/F}^{(0)}$. The second one has the prefactor $f_F^{(0)}(K)$, and one factor of $\delta f_{F/B}^{shear}$ in $S_R^D(Q)$, which implies linearising the self-energy $S_R^D(Q)$ in $\delta f_{F/B}^{shear}$.

Defining

$$A(k) \equiv \frac{1}{2\pi k} e^2 N_c \sum_s q_s^2 m_\infty^2 f_F^{(0)}(k) \tag{6.43}$$

to follow the notation of Ref. [31], and

$$J(K) \equiv \frac{1}{m_\infty^2} \int d^4Q \delta(K \cdot Q) K_\mu Im[S_R^{D\mu}(Q)] \tag{6.44}$$

it follows that Equation 6.42 can be written

$$E\frac{d\Gamma_\gamma^{soft}}{dk^3} = \frac{-4k}{(2\pi)^5}A(k)\frac{f_F(K)}{f_F^{(0)}(K)}J(K) \tag{6.45}$$

By scaling Q by m_∞ ($Q = m_\infty X$), $J(K)$ can be shown to be unitless

$$J(K) = \int d^4X\delta(K\cdot X)K_\mu Im\left[\frac{-\tilde{\Sigma}_R^\mu(X)}{(X-\tilde{\Sigma}_R(X))^2}\right] \tag{6.46}$$

where

$$\tilde{\Sigma}_R^\mu(X) = \int \frac{d^3\mathbf{v}}{(2\pi)^3}\frac{f(V)}{v}\frac{V^\mu}{V\cdot X + i\epsilon} \tag{6.47}$$

Defining $J(K) \equiv \sum_l J_l(K)$ where $J_l(K)$ has "l" powers of $\delta f_{F/B}^{shear}$, the soft part of the photon rate can be written, at leading order in $\delta f_{F/B}^{shear}$, as

$$\begin{aligned} E\frac{d\Gamma_\gamma^{soft}}{dk^3} &\approx \frac{-4k}{(2\pi)^5}A(k)\left[\frac{f_F(K)}{f_F^{(0)}(K)}J_0(K) + J_1(K)\right] \\ &= E\frac{d\Gamma_\gamma^{(0)soft}}{dk^3} + \frac{-4k}{(2\pi)^5}A(k)\left[\frac{\delta f_F(K)}{f_F^{(0)}(K)}J_0(K) + J_1(K)\right] \end{aligned} \tag{6.48}$$

To write the above equation in the form of Equation 6.17, the expression of $\delta f_F^{shear}(K)$ used in this thesis is inserted, and the definition

$$J_1 \equiv \frac{\pi_{\mu\nu}K^\mu K^\nu}{2(\epsilon+\mathcal{P})}\frac{J_1'}{k^2} \tag{6.49}$$

is used to define J_1'. The rate can then be written as

$$E\frac{d\Gamma_\gamma^{soft}}{dk^3} = E\frac{d\Gamma_\gamma^{soft(0)}}{dk^3} + \frac{\pi_{\mu\nu}K^\mu K^\nu}{2(\epsilon+\mathcal{P})}\tilde{S}_M^{soft}(K/T, q_*) \tag{6.50}$$

with

$$\tilde{S}_M^{soft}(K/T, q_*) = \frac{-4k}{(2\pi)^5}A(k)\left[\left(1-f_F^{(0)}\right)\frac{J_0(K)}{T^2} + \frac{J_1'(K)}{k^2}\right] \tag{6.51}$$

Functions $J_0(K)$ and $J_1'(K)$ do not have simple expressions. Full expression for each function is given in Appendix C.2.

6.2.1.3 Discussion

The final formula for the effect of shear viscosity on QGP $2 \to 2$ photon production is

$$E\frac{d\Gamma_\gamma}{dk^3} = E\frac{d\Gamma_\gamma^{(0)}}{dk^3} + \frac{\pi_{\mu\nu}K^\mu K^\nu}{2(\epsilon+\mathcal{P})}\tilde{S}_M^{QGP}(K/T, q_*) \tag{6.52}$$

with

$$\begin{aligned}\tilde{S}_M^{QGP}(K/T, q_*) = \frac{kA(k)}{(2\pi)^3k^2}\Bigg(&\frac{-4}{(2\pi)^2}\left[\tilde{k}^2\left(1-f_F^{(0)}\right)J_0(K) + J_1'(K)\right] + \\ &\frac{2}{f_F^{(0)}(k)(2\pi)^4}\Bigg[-\left(Y^{00}[u/t](q_*) + Y^{00}[-s/t](q_*) + Y^{00}[-t/s]\right) \\ &+ \frac{\mathbf{k}_i\mathbf{k}_j Y^{ij}[u/t] + \mathbf{k}_i\mathbf{k}_j Y^{ij}[-s/t] + \mathbf{k}_i\mathbf{k}_j Y^{ij}[-t/s]}{k^2}\Bigg]\Bigg)\end{aligned} \tag{6.53}$$

To ease comparisons between the correction to the rate due to viscosity and the ideal rate, $\tilde{S}_M^{QGP}(K/T, q_*)$ is written

$$\tilde{S}_M^{QGP}(K/T, q_*) \equiv \frac{kA(k)}{(2\pi)^3k^2}R_{shear}(K/T, q_*) \tag{6.54}$$

and the ideal rate is written as

$$E\frac{d\Gamma_\gamma^{(0)}}{dk^3} \equiv \frac{kA(k)}{(2\pi)^3}R_{ideal}(K/T, q_*) \tag{6.55}$$

such that

$$E\frac{d\Gamma_\gamma^{(0)}}{dk^3} = \frac{kA(k)}{(2\pi)^3}\left[R_{ideal}(K/T, q_*) + \frac{\pi_{\mu\nu}}{2(\epsilon+\mathcal{P})}\frac{K^\mu K^\nu}{k^2}R_{shear}(K/T, q_*)\right] \tag{6.56}$$

Both $R_{ideal}(K/T, q_*)$ and $R_{shear}(K/T, q_*)$ are dimensionless quantities whose q_* dependence is shown on Figure 6.2, at $k/T = 2$. Results are shown for a small and a large value of g_s: $g_s = 0.01$ (left) and $g_s = 2$ (right).

When a small value of g_s is used, there is a clear separation of scale between g_sT and T, which is necessary for the hard thermal loop resummation to work. In this case, the photon rate calculation is expected to be largely independent of the cut-off q_* between g_sT and T. This is the observed behaviour on Figure 6.2a for both the ideal and the viscous part of the rate. The q_*/T axis is logarithmic, and both $R_{ideal}(K/T, q_*)$ and $R_{shear}(K/T, q_*)$ show a large plateau between $q_*/T = g_s = 0.01$ and $q_*/T = 1$.

Figure 6.2b is shown to highlight that this plateau cannot be maintained when $g_s \gtrsim 1$, due to the loss of scale separation between g_sT and T. The fact that the calculation breaks

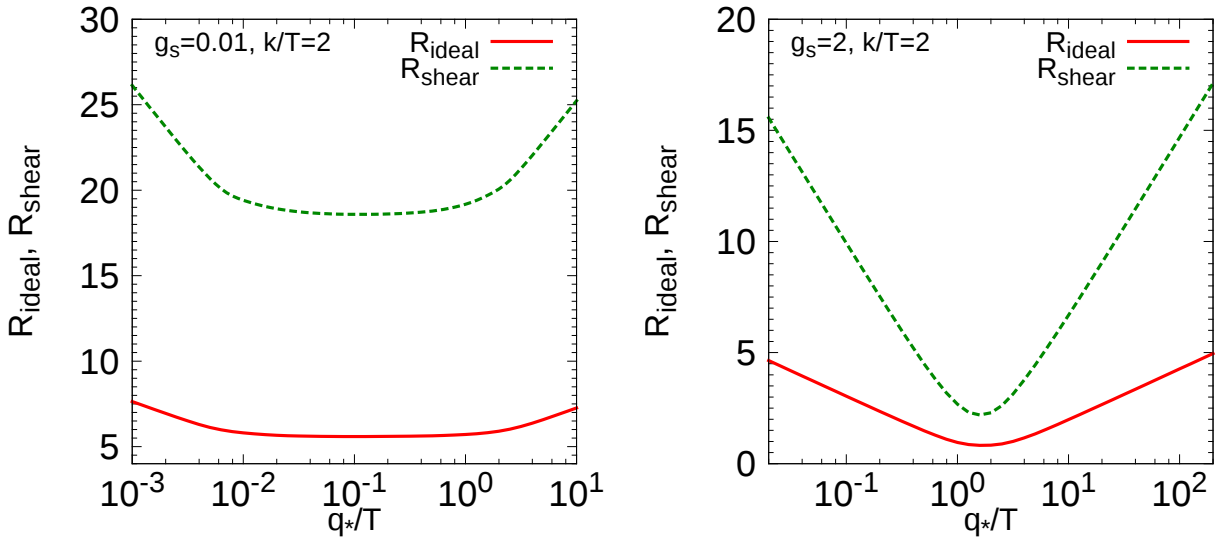

(a) (b)

Figure 6.2: Coefficient $R_{ideal}(K/T, q_*)$ and $R_{shear}(K/T, q_*)$, as defined in Equations 6.55 and 6.54, with respect to cut-off q_*/T, at k/T=2 for (a) $g_s = 0.01$ and (b) $g_s = 2$

down at $g_s \gtrsim 1$ is not surprising, since such values of g_s break the underlying assumptions of the derivation.

On the other hand it is still relevant to understand how the calculation behave in this limit, since the values of g_s typically used in heavy ion collisions are larger than one. This evaluation of the effect of shear viscosity on photon production will thus be used for large value of g_s. Since the minimum of both $R_{ideal}(K/T, q_*)$ and $R_{shear}(K/T, q_*)$ is still around $q_*/T = \sqrt{g_s}$, despite the absence of plateau around it, choosing $q_*/T \sim \sqrt{g_s}$ minimises the dependence of the rate on the unphysical parameter q_*. This choice of q_* appears to be the best possible one if this calculation is pushed outside its region of applicability in g_s.

Dependence of $\frac{R_{shear}(K/T)}{R_{ideal}(K/T)}$ on g_s and $\frac{k}{T}$ Fixing $q_*/T = \sqrt{g_s}$, interesting properties of the ratio $R_{shear}(K/T)/R_{ideal}(K/T)$ can be observed by plotting it with respect to g_s (Figure 6.3a) and k/T (Figure 6.3b).

The first figure indicates that for any realistic value of g_s, the ratio R_{shear}/R_{ideal} is essentially independent of g_s. This means that the ideal calculation and its correction due to shear viscosity have the same dependence on g_s, which is a non-trivial result.

Moreover Figure 6.3b indicates that the k/T dependence of the ratio is roughly quadratic in (k/T). This is not necessarily surprising since the momentum dependence of δf^{shear} is also quadratic. At low values of the strong coupling, the dependence on k/T is more accurately

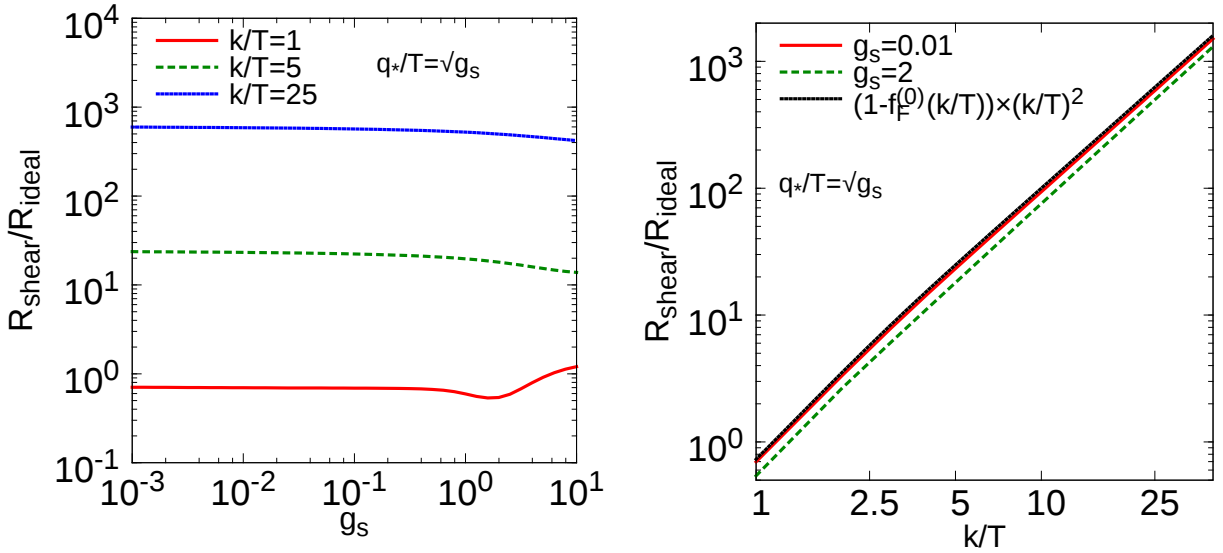

(a) (b)

Figure 6.3: (a) Ratio $R_{shear}(K/T)/R_{ideal}(K/T)$ with respect to the strong coupling constant g_s (b) Ratio $R_{shear}(K/T)/R_{ideal}(K/T)$ with respect k/T. In both cases, $q_*/T = \sqrt{g_s}$.

given by:

$$\frac{R_{shear}(K/T)}{R_{ideal}(K/T)} \approx \left(\frac{k}{T}\right)^2 (1 - f_F^{(0)}(k)) \tag{6.57}$$

This is shown on Figure 6.3b, compared with the k/T dependence of R_{shear}/R_{ideal} for $g_s = 0.01$. The k/T dependence is also shown for $g_s = 2$, for reference.

The origin of Equation 6.57 can be understood in the forward scattering approximation [124, Chapter 16], which is an approximation for the matrix elements of QGP $2 \to 2$ processes that was used in Ref. [125] as a straightforward approach to evaluate viscous corrections on photon production rates.

Forward scattering approximation The idea behind the forward scattering approximation is that most photons produced in Compton scattering and quark-antiquark annihilation originate from a restricted region of phase space, specifically the region where the momentum of the produced photon is approximately collinear with one of the initial state quarks. It implies that Equation 6.24 can be approximated by

$$\begin{aligned} k\frac{d^3\Gamma_\gamma^{hard}}{d\mathbf{k}} \approx & \frac{f_F(K)}{2(2\pi)^3} \int \frac{d^3p_1}{2P_1^0(2\pi)^3} \frac{d^3p_2}{2P_2^0(2\pi)^3} \frac{d^3p_3}{2P_3^0(2\pi)^3} (2\pi)^4 \delta^4(P_1 + P_2 - P_3 - K) \\ & \times \left[f_B(P_2)(1 - f_F(P_3))|\mathcal{M}_C|^2 + f_F(P_2)(1 + f_B(P_3))|\mathcal{M}_A|^2 \right] \end{aligned} \tag{6.58}$$

by using $f_F(P_1) \approx f_F(K)$.

Assuming that the dominant contributions to viscous effects originate from the $f_F(K)$ pre-factor, and not the momentum distributions that are integrated over inside the integral, it means that

$$k\frac{d^3\Gamma_\gamma^{hard}}{d\mathbf{k}} \approx \frac{f_F(K)}{f_F^{(0)}(K)}\left[k\frac{d^3\Gamma_\gamma^{(0)hard}}{d\mathbf{k}}\right] \tag{6.59}$$

For the soft part, Equation 6.42 can also be written as

$$k\frac{d^3\Gamma_\gamma^{soft}}{d\mathbf{k}} \approx \frac{f_F(K)}{f_F^{(0)}(K)}\left[k\frac{d^3\Gamma_\gamma^{(0)soft}}{d\mathbf{k}}\right] \tag{6.60}$$

under the reasonable assumption that the dominant viscous effects originate from the $f_F(K)$ pre-factor, and not from the effect of $f_{F/B}$ in the retarded self energy (see text after Equation 6.42).

Since

$$\frac{f_F(K)}{f_F^{(0)}(K)} = \frac{\pi^{\mu\nu}K^\mu K^\nu}{k^2}\left(\frac{k}{T}\right)^2\left(1 - f_F^{(0)}(k)\right) \tag{6.61}$$

it is straightforward to see that Equations 6.59 and 6.60 lead to Equation 6.57.

Equation 6.57 can thus be used to provide a simple estimate of the effect of viscosity on QGP $2 \to 2$ photon production rates. It is used in the next section to evaluate the effect of bulk viscosity on photon production.

6.2.2 Bulk viscosity correction

Following the previous section, the effect of bulk viscosity on QGP $2 \to 2$ photon production can be approximated by

$$k\frac{d^3\Gamma_\gamma^{bulk}}{d\mathbf{k}} \approx \frac{\delta f_F^{bulk}(K)}{f_F^{(0)}(K)}\left[k\frac{d^3\Gamma_\gamma^{(0)}}{d\mathbf{k}}\right] \tag{6.62}$$

where $kd^3\Gamma_\gamma^{(0)}/d\mathbf{k}$ is the ideal QGP $2 \to 2$ emission rate.

Inserting the value of $\delta f_F^{bulk}(K)$ used in this thesis, the rate correction becomes

$$k\frac{d^3\Gamma_\gamma^{bulk}}{d\mathbf{k}} \approx -\frac{\Pi}{15\left(\frac{1}{3} - c_s^2\right)(\epsilon + \mathcal{P})}\left(1 - f_F^{(0)}(K)\right)\left[\frac{m^2}{T^2}\frac{1}{k/T} - \frac{k}{T}\right]\left[k\frac{d^3\Gamma_\gamma^{(0)}}{d\mathbf{k}}\right] \tag{6.63}$$

implying that the value of $\tilde{B}_M^{QGP}(K,T)$ as defined in Equation 6.17 is given by

$$\tilde{B}_M^{QGP}(K,T) \approx \left(1 - f_F^{(0)}(K)\right)\left[\frac{m^2}{T^2}\frac{1}{k/T} - \frac{k}{T}\right]\left[k\frac{d^3\Gamma_\gamma^{(0)}}{d\mathbf{k}}\right] \tag{6.64}$$

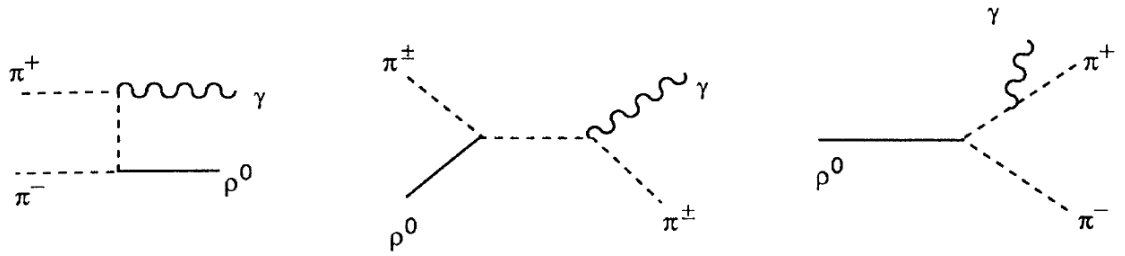

Figure 6.4: Examples of photon production channels for mesons (Figure adapted from [126])

The mass m is taken to be the asymptotic thermal quark mass, $m_\infty = g_s T/\sqrt{3}$.

This concludes this section on the correction due to viscosity on photon production through Compton scattering and quark-antiquark annihilation in a hot quark-gluon plasma. In the next section, a brief overview of viscous effect on photon production from light mesons is provided.

6.3 Mesonic photon rate

Photon produced by mesonic interactions involving π, K, ρ, K^* and a_1 are included in this thesis using the effective Lagrangian approach described in Ref. [112]. Example of production channels are shown on Figure 6.4.

Photon production is evaluated in a kinetic approach with Equation 6.2. Consequently the general derivations from Section 6.1.1 can be used to compute viscous corrections to the rate.

Evaluating the viscous corrections — or the ideal rate itself for that matter — is not straightforward because of the number and complexity of the matrix elements. The full matrix elements are available in Refs. [127, Appendix C] and [128, Appendix D].

The effect of shear viscosity on this channel of photon production were first investigated in Ref. [36], and were also used in Ref. [38]. The numerical evaluation of the effect of bulk viscosity on photon emission from mesons is evaluated in the same way as in these two publications [129].

Chapter 7

An up-to-date hydrodynamical calculation of photon production in heavy ion collisions

In this chapter, direct photon production at RHIC and the LHC is computed for the same hydrodynamical model used to evaluate hadron production in Chapter 4. The formalism used to compute thermal, prompt and non-cocktail photons was described in Chapter 5. The effect of viscosity on photon production was discussed in Chapter 6. A summary of these previous chapters is provided in the first section of the present chapter.

The rest of the chapter is divided as follows. The proper way of evaluating the photon momentum anisotropy is explained in Section 7.2. Comparison with preliminary measurements from the LHC are made in Section 7.3. A discussion of certain features and uncertainties of the photon calculations is made in the same section. Comparisons with RHIC measurements close this chapter.

7.1 Summary of the model

Prompt photons are computed as described in Section 5.2. In the present work, they depend only on the type of nuclei and center-of-mass energy of the heavy ion collisions, and not on the dynamics of the QGP created in the collisions. They are thus completely independent of any features of the hydrodynamical model.

Thermal photons are computed by folding the hydrodynamical description of the medium used in Chapter 4 together with photon production rates. The equilibrium rates used in this work were described in Section 5.3. Viscous corrections evaluated in Chapter 6 are included.

Rate	Ideal?	Shear correction?	Bulk correction?
QGP $2 \to 2$ [31]	Yes	Yes	Partial (Forward Scattering)
QGP bremsstrahlung [31]	Yes	No	No
HG light mesons [112]	Yes	Yes	Yes
HG ρ spectral function [112]	Yes	No	No
HG $\pi + \pi$ bremsstrahlung [113]	Yes	No	No

Table 7.1: Photon rates used in the evaluation of thermal photons in this chapter

A summary of the photon rates and viscous corrections used in this work is given in Table 7.1.

The strong coupling constant is set to $g_s = 2$, corresponding to $\alpha_s \approx 0.3$, which is in line with values of α_s extracted from analyses of jet energy loss in heavy ion collisions [130].

The particlisation temperatures extracted from comparisons with hadronic data were $T_{sw} = 145$ MeV at the LHC (Section 4.3) and $T_{sw} = 165$ MeV at RHIC (Section 4.4). For hadrons, the dynamics of the medium from this point on was modelled with UrQMD, a microscopic model of hadronic interactions. The same model cannot be used to investigate the production of photons in this post-particlisation phase, since UrQMD does not handle photon production through inelastic hadron collisions.

An alternative approach would be to extract a temperature, flow velocity and volume distribution from UrQMD by coarse-graining, and to combine this spacetime profile with thermal rates using Equation 5.4. Dilepton production in low energy nucleus collisions has been studied previously with this technique [131, 132]. While this method of evaluating photons produced after particlisation is interesting, it presents significant technical challenges that are beyond the scope of this work. On the other hand, a previous study found that the temperature, flow and volume profiles obtained from this UrQMD coarse-graining procedure are not too different from that of a hydrodynamical model, down to $100 - 110$ MeV [133]. Since the temperature, flow and volume distributions are the main factors controlling the production of thermal photons, evaluating post-particlisation photons by stopping the hydrodynamics at lower temperatures should provide a reasonable first-order estimate.

Based on the above, the hydrodynamics is stopped at 105 GeV, with thermal photons emitted between T_{sw} and this lower temperature being considered an estimate of post-particlisation photons. The importance on the final direct photon calculations of post-particlisation photons is quantified in Section 7.3.1.

Many features of the direct photon calculation presented in this chapter are considerable improvements over previous calculations. Photons have never been computed with a hydrodynamical model that include IP-Glasma initial conditions and second order hydrodynamical equations with bulk viscosity. Previous calculations either used ideal hydrodynamics [134, 39] or simpler initial conditions and hydrodynamical equations [38].

Viscous corrections to the photon emission rates were previously included in Ref. [38], but this previous calculation used a less complete rate for hadronic photons.

A further improvement of the present calculation is the evaluation of photon momentum anisotropies following more closely the details of the experimental measurements. Many features of the measurements of photon anisotropies have been overlooked in the past, leading to confusion in the evaluation of photon anisotropies from hydrodynamical simulations. This is the topic of the next section.

7.2 Evaluation of the direct photon v_n for comparison with data

Two direct photon observables have been measured at RHIC and the LHC: the p_T differential spectrum and anisotropic flow coefficients v_2, both at midrapidity.

The direct photon spectrum has a simple experimental definition and is straightforward to evaluate from hydrodynamical calculations. This is not true for the v_n coefficients, which is not a simple measurements and which in consequence must be evaluated theoretically with care.

The anisotropy coefficient v_n of a single event is defined in Equation 1.3. It can also be written in complex notation as

$$v_n^s e^{in\Psi_n^s} = \frac{\int dp_T dy d\phi p_T \left[E\frac{d^3N^s}{d^3p}\right] e^{in\phi}}{\int dp_T dy d\phi p_T \left[E\frac{d^3N^s}{d^3p}\right]} \tag{7.1}$$

where s denote the particle species. While Equation 1.3 assumed that v_n was defined for a narrow bin in p_T and y, such that $v_n = v_n(p_T, y)$, it is also possible to define v_n integrated over a bin in transverse momentum and rapidity. Equation 7.1 provides a general definition for v_n in such cases.

As explained previously in this thesis (Section 2.2), the hadron v_n of a single event cannot be measured, but measurements of azimuthal correlations between hadrons, averaged over multiple events, can be related to the hadronic v_n and Ψ_n . This applies to photons as well.

Due to the low number of measured photons, the photon momentum anisotropy is not measured as a photon-photon correlation, but rather as a photon-hadron correlation. For the photon v_n measurements currently available, the event-plane method was used to measure this photon-hadron correlation. This method can be understood as using hadrons to define an effective plane in the transverse direction, based on their azimuthal distribution, with photons then measured with respect to this hadronic plane. However, depending on the

number of hadrons being measured and on the size of their azimuthal momentum anisotropy, the hadronic event-plane cannot necessarily be reconstructed accurately. Because of this, it is not possible to provide an unambiguous mapping of event-plane method measurement to the v_n and Ψ_n of photons and hadrons [54, Section 2].

There are however two known limits, the low and high resolution limits, which typically do not differ by more than 10% [54, Section 2]. In the low resolution limit, the event-plane anisotropy reduces to the two-particle cumulant (also called the scalar product $v_2\{SP\}$) anisotropy [54, Section 2]:

$$v_n\{EP\} \approx v_n\{2\} = \frac{\langle v_n^\gamma v_n^h \cos(n(\Psi_n^\gamma - \Psi_n^h))\rangle}{\sqrt{\langle (v_n^h)^2\rangle}} \tag{7.2}$$

The other limit is the high resolution limit:

$$v_n\{EP\} \approx \langle v_n^\gamma \cos(n(\Psi_n^\gamma - \Psi_n^h))\rangle \tag{7.3}$$

The "resolution correction", which quantifies the accuracy of the event-plane reconstruction, is used to determine which limit is closer to event-plane measurements. The resolution corrections for both RHIC and LHC measurements are shown respectively in Refs. [99, Section 4.2.2] and [98, Section 9.1.2]. The value of the resolution correction changes with the centrality and methods used to determine the event-plane, and for $n = 2$ ($v_2\{EP\}$), is neither clearly in the high nor low resolution limit. On the other hand, higher harmonics ($n > 2$) have systematically lower resolution corrections, and are closer to the low resolution limit. The low resolution limit, $v_n\{EP\} \approx v_n\{2\} \equiv v_n\{SP\}$, is thus used in this work. It is verified at the end of this section that the low and high resolution limits indeed only differ by approximately 10%. The uncertainty associated with this ambiguity in $v_n\{EP\}$ is thus not a significant issue.

The event-plane method has been superseded by other methods for hadronic anisotropy measurements, methods such as the two-particle cumulants $v_2\{2\}$ mentioned at the end of Section 2.2. It is likely that future photon measurements will also be measured with the two-particle cumulant method, which is an additional incentive to use the limit $v_n\{EP\} \approx v_n\{2\}$. In the meantime, the uncertainty intrinsic to the current measurements is treated as a theoretical uncertainty.

The experimental measurements correlate hadrons from a wide bin in p_T to photons measured in a small p_T bin, effectively resulting in a $v_n^\gamma\{EP\}$ differential in the photon transverse momentum:

$$v_n^\gamma\{EP\}(p_T^\gamma) \approx \frac{\langle v_n^\gamma(p_T^\gamma) v_n^h \cos(n(\Psi_n^\gamma(p_T^\gamma) - \Psi_n^h))\rangle}{\sqrt{\langle (v_n^h)^2\rangle}} \tag{7.4}$$

Equation 7.4 assumes that the events that are averaged over have small multiplicity fluctuations. That is, all events are assumed to produce a similar number of photons and hadrons. If large multiplicity fluctuations are present, Equation 7.4 will take a different form depending of the details of the measurement, for example whether all events are treated equally, or if events with more hadrons and photons are given a larger weight in the event-average.

To reduce the importance of multiplicity fluctuations, experimental collaborations first measure Equation 7.4 in small centrality bins [98, Chapter 9]. The anisotropy measurements from these smaller centrality bins are then recombined into a larger centrality to reduce the statistical uncertainty of the measurement. When the small centrality bins are recombined, each centrality is weighted by the number of photons measured in the centrality [98, Chapter 9]:

$$v_n^\gamma\{EP\}[c_{min}, c_{max}] = \frac{\sum_{c\in[c_{min},c_{max}]} v_n^\gamma\{EP\}[c]N[c]}{\sum_{c\in[c_{min},c_{max}]} N[c]} \tag{7.5}$$

where $N[c]$ is the number of photons measured in centrality c, $v_n^\gamma\{EP\}[c]$ is the momentum anisotropy measured in c and $[c_{min}, c_{max}]$ is the final (large) centrality class in which the measurement is reported. At the LHC the sub-bins are [98, Chapter 9] $0-5\%$, $5-10\%$, $10-20\%$, $20-30\%$ and $30-40\%$, while 10% bins are used at RHIC [99].

The quantity $v_n^\gamma\{EP\}[c_{min}, c_{max}]$ (Equation 7.5) is the one that should be compared to PHENIX and ALICE measurements.

7.2.1 Simplifications

With reasonable approximations, it is possible to simplify Equation 7.5 considerably. Numerical values from hadron and direct photon production computed in the hydrodynamical model presented in this thesis, for Pb-Pb collisions at $\sqrt{s_{NN}} = 2.76$ TeV, are used to support the approximations. The simplifications are restricted to the second order coefficients, $v_2^\gamma\{EP\}[c_{min}, c_{max}]$.

Event-planes The first approximation used is that the event-plane angles of direct photons and hadrons are usually close to each other: $\Psi_2^\gamma(p_T) \approx \Psi_2^h$. This is confirmed very nicely by evaluating $\left\langle\cos(2(\Psi_2^\gamma(p_T^\gamma) - \Psi_2^h))\right\rangle$, shown on Figure 7.1. The value is essentially 1, allowing $v_2^\gamma\{EP\}(p_T^\gamma)$ to be written

$$v_2^\gamma\{EP\}(p_T^\gamma) \approx \frac{\langle v_2^\gamma(p_T^\gamma)v_2^h\rangle}{\sqrt{\langle(v_2^h)^2\rangle}} \tag{7.6}$$

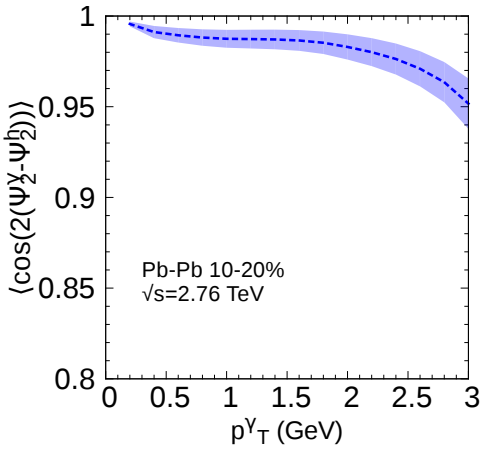

Figure 7.1: Correlation between the hadronic and photonic event-plane Ψ_2 as expressed by $\left\langle \cos(n(\Psi_n^\gamma(p_T^\gamma) - \Psi_n^h)) \right\rangle$ in Pb-Pb collisions at $\sqrt{s_{NN}} = 2.76$ TeV in $10-20\%$ centrality.

Anisotropy correlations A further simplification can be obtained from the observations that the v_2 of photons and hadrons are correlated within each event. As seen in the introduction, the anisotropy of hadrons is a result of the initial anisotropy of the matter deposited in heavy ion collisions (see e.g. Figure 1.5). The same is true for thermal photons, whose momentum anisotropy also results from the flow anisotropies developed in the hydrodynamical expansion. Since thermal photons are the dominant source of momentum anisotropy in direct photons, it is reasonable to expect $v_2^\gamma(p_T^\gamma)$ and v_2^h to be related. This can be verified numerically, which is shown on Figure 7.2 for different values of p_T^γ. It is apparent from Figure 7.2 that $v_2^\gamma(p_T^\gamma) \propto v_2^h$ is a fairly good approximation at lower p_T^γ, although deviations are visible at higher p_T^γ.

Using $v_2^\gamma(p_T^\gamma) \propto v_2^h$, $v_2^\gamma\{EP\}(p_T^\gamma)$ reduces to

$$v_2^\gamma\{EP\}(p_T^\gamma) \approx \sqrt{\langle (v_2^\gamma(p_T^\gamma))^2 \rangle} \tag{7.7}$$

This approximation, together with the previous approximation that $\Psi_2^\gamma(p_T) \approx \Psi_2^h$, thus allows to remove all dependence of $v_2^\gamma\{EP\}(p_T^\gamma)$ on hadronic quantities.

Photon multiplicity weighting Finally, the weighting procedure from Equation 7.5 should be reasonably well-approximated by weighting each event with its own photon multiplicity, rather than the multiplicity of the sub-centrality class c. This assumptions yields:

$$v_n^\gamma\{EP\}[c_{min}, c_{max}](p_T^\gamma) \approx \sqrt{\frac{\left\langle \left(\frac{1}{2\pi p_T}\frac{dN^\gamma}{dp_T}\right)(v_2^\gamma(p_T^\gamma))^2 \right\rangle}{\left\langle \frac{1}{2\pi p_T}\frac{dN^\gamma}{dp_T} \right\rangle}} \tag{7.8}$$

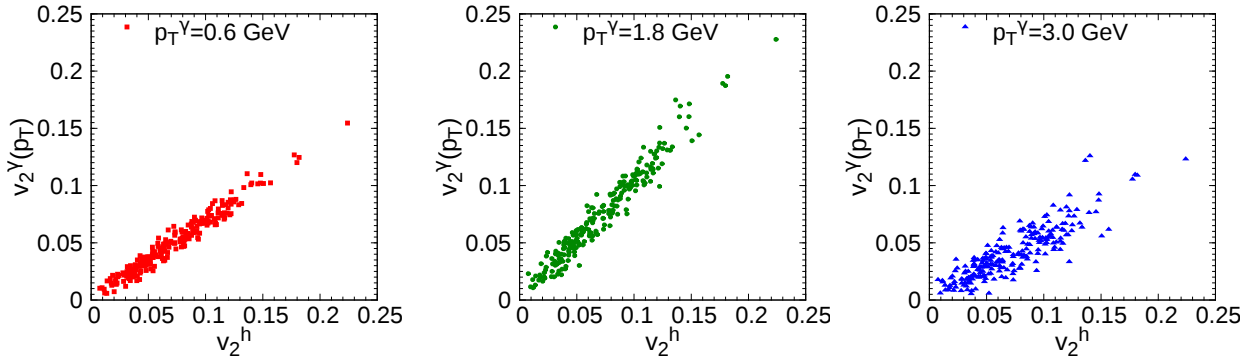

(a) (b) (c)

Figure 7.2: Distribution of photon $v_2^\gamma(p_T)$ and p_T-integrated charged hadrons v_n^h for ~ 240 Pb-Pb collisions at $\sqrt{s_{NN}} = 2.76$ TeV in $0-40\%$ centrality for (a) $p_T^\gamma = 0.6$ GeV (b) $p_T^\gamma = 1.8$ GeV and (c) $p_T^\gamma = 3.0$ GeV.

Equation 7.8 has the considerable benefit of not depending on the details of the sub-binning of the final centrality class.

A comparison of the different simplified $v_n^\gamma\{EP\}[c_{min}, c_{max}](p_T^\gamma)$ proposed in this section is shown on Figure 7.3a. The anisotropy computed from Equation 7.5 is labeled "Exact", while the other curves correspond to

- Equation 7.5 with $v_n^\gamma\{EP\}[c]$ from Equation 7.6 (labelled "$\Psi_2^\gamma \approx \Psi_2^h$")
- Equation 7.5 with $v_n^\gamma\{EP\}[c]$ from Equation 7.7 (labelled "$\Psi_2^\gamma \approx \Psi_2^h$ & $v_2^\gamma \propto v_2^h$")
- Equation 7.8 (labelled "$\Psi_2^\gamma \approx \Psi_2^h$ & $v_2^\gamma \propto v_2^h$ & event multiplicity weight")

It is clear from Figure 7.3a that the only approximation that is not fully justified is to approximate the per-centrality photon multiplicity weight with a per-event one (Equation 7.8), although it remains a reasonable approximation.

It is important to clarify that, although the simplifications made in this section appear justified for the direct photon signal predicted in this thesis, it might not be the case if direct photons are not dominated by thermal photons. For example, if it turns out that some non-thermal photon source is found to contribute significantly to both the direct photon spectrum and the momentum anisotropy, the assumptions that $\Psi_2^\gamma(p_T) \approx \Psi_2^h$ and $v_2^\gamma(p_T^\gamma) \propto v_2^h$ would most likely *not* hold. Then the simplifications made above would break down. This has to be kept in mind when more exotic sources of direct photons are being investigated. For completeness, a comparison of the two limits of $v_2^\gamma\{EP\}$, $v_2^\gamma\{2\}$ and $\langle v_2^\gamma \cos(n(\Psi_2^\gamma - \Psi_2^h))\rangle$, is shown on Figure 7.3b. As expected, the effect is around 10%.

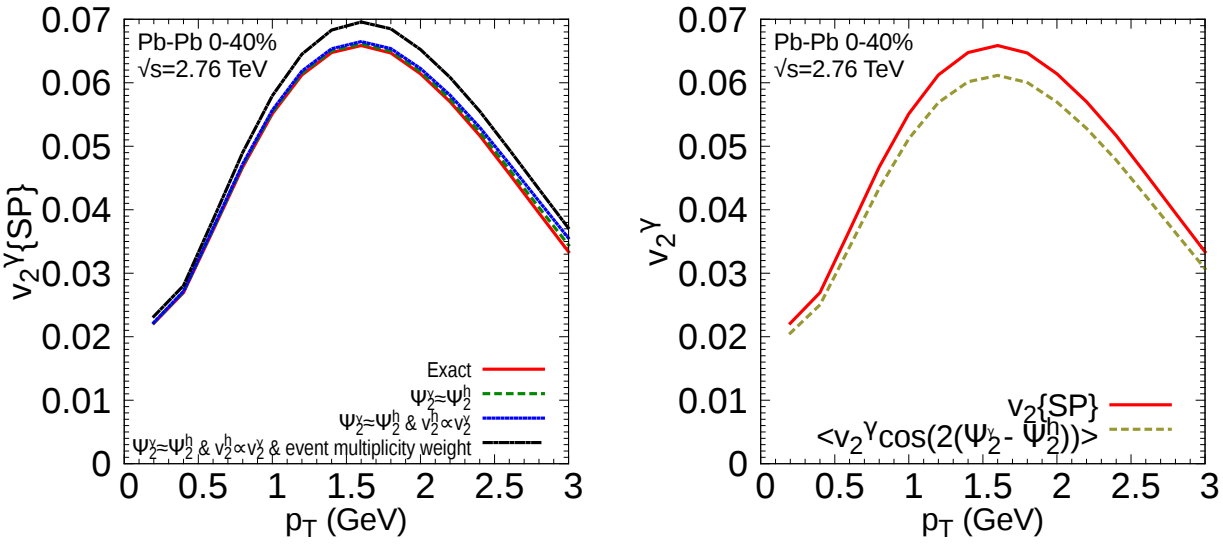

(a) (b)

Figure 7.3: (a) Direct photons anisotropies computed with different methods (see text) (b) Difference between the two limits of the event-plane anisotropy, $v_2\{SP\}$ and $\langle v_2^\gamma \cos(n(\Psi_2^\gamma - \Psi_2^h))\rangle$. For Pb-Pb collisions at $\sqrt{s_{NN}} = 2.76$ TeV in $0-40\%$ centrality.

With the clarifications from this section on the proper way of evaluation the direct photon anisotropy, comparisons with measurements can now be considered. Direct photons calculations at the LHC are presented in the next section.

7.3 LHC

The direct photon spectrum and v_2 in Pb-Pb collisions at $\sqrt{s_{NN}} = 2760$ GeV is presented on Figure 7.4. The photon anisotropy was evaluated with Equation 7.5. The calculations are compared with preliminary measurements from the ALICE collaboration [17, 135, 98].

The three sources of direct photon considered in this work — thermal, prompt and non-cocktail — are shown separately on Figure 7.4a. Their sum is labelled "Direct". Thermal photons are the dominant source of direct photons below $p_T^\gamma = 2.5$ GeV. At very low p_T, thermal and prompt photons are again of the same size, but the unknown reliability of the prompt photon calculation has to be kept in mind at such low momenta (see Appendix A).

A different breakdown of the three photon sources is shown for v_2 on Figure 7.4b, to emphasize that thermal photons carry essentially all the momentum anisotropy. The large thermal photon v_2 is diluted by the prompt photons, which carry no v_2 at all in the present calculation. The addition of non-cocktail contributions to the thermal and the prompt

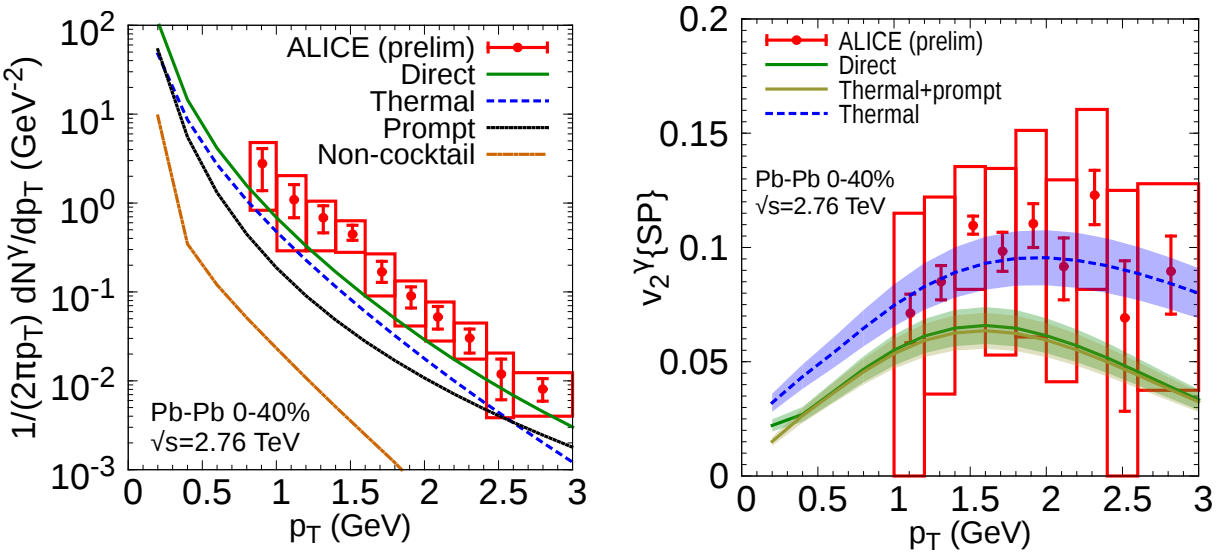

(a) (b)

Figure 7.4: (a) Direct photon spectrum and (b) direct photon v_2 for Pb-Pb collisions at $\sqrt{s_{NN}} = 2.76$ TeV for 0-40% centrality. The shaded bands represent the statistical uncertainty on direct photons. Statistical and systematic uncertainties on the data are represented by bars and boxes, respectively.

photons is a small effect, but is shown for completeness.

Despite the significant contribution of thermal photons, the direct photon spectrum and v_2 are on the lower side of the data. Both calculations are nevertheless within the combined statistical and systematic uncertainties in many p_T bins.

In what follows, various features of the model are investigated to help understand the uncertainties entering the evaluation of thermal photons.

7.3.1 Post-particlisation dynamics

The calculation shown on Figure 7.4 includes photons down to $T_{sw} = 105$ MeV. The particlisation temperature favored by hadronic observables at the LHC is $T_{sw} = 145$ MeV, and past this point, the dynamics of *hadrons* was handled by a kinetic theory simulation (UrQMD). The same post-particlisation model cannot be used to compute photons produced in this phase, and another approach must be used. As explained in Section 7.1, post-particlisation photons are estimated in this work by letting the hydrodynamical model run past $T_{sw} = 145$ MeV, down to $T_{sw} = 105$ MeV. As mentioned previously, in this temperature range, comparisons of temperature and volume profiles of coarse-grained UrQMD simulations and hydrodynamical models were shown to be reasonably similar to each other [133],

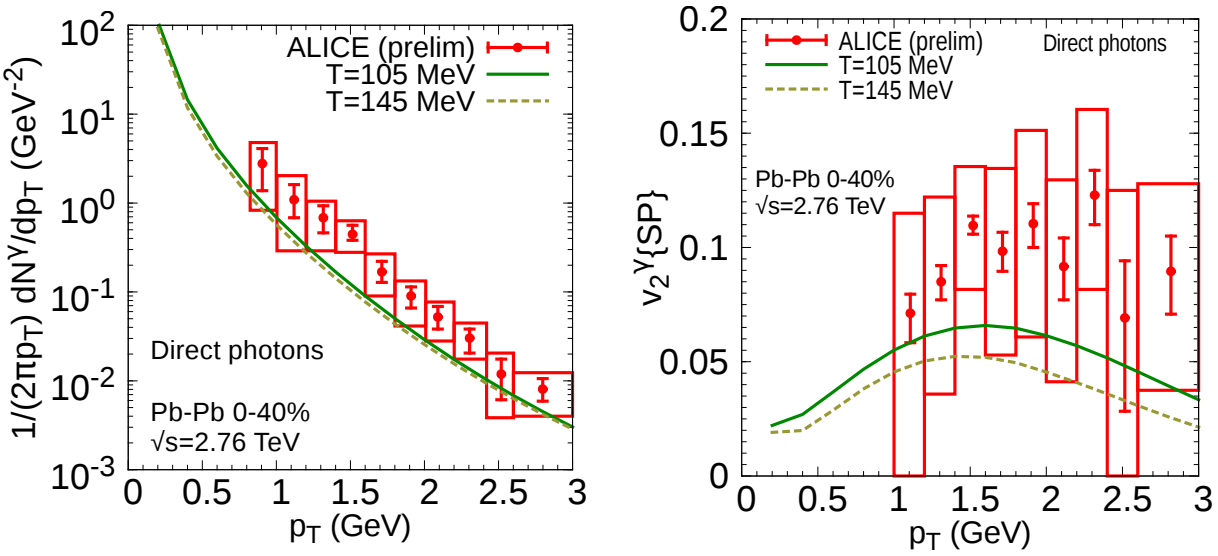

(a) (b)

Figure 7.5: Effect on (a) the direct photon spectrum and (b) the direct photon v_2 of including thermal photons down to $T = 105$ MeV.

supporting the idea that post-particlisation photons can be estimated by extending the hydrodynamical evolution to lower temperatures.

Since photons produced between 145 and 105 MeV are an estimate, it is relevant to quantify their contribution to the final calculations shown on Figure 7.4. This is shown on Figure 7.5. The effect of post-particlisation photons on the spectra, Figure 7.5a, is between 10 and 20%, which is barely visible on the figure. On the other hand, v_2^γ gets a significant contribution from post-particlisation photons, as shown on Figure 7.5b, from a $\sim 30\%$ increase at low p_T to $\sim 50\%$ increase at high p_T. To understand how a $10 - 20\%$ increase in the *direct* photon spectrum can lead to a much larger increase in the v_2, it is necessary to take a closer look at the dynamics of heavy ion collisions, and at the relation between photon production and the spacetime profile of the medium.

Time and temperature Since the QGP created in heavy ion collisions expands in a vacuum, the temperature drops essentially monotonically with "time" τ. While there is a distribution of high and low temperatures even at the earliest time, high temperatures are found at earlier times. Temperature is thus a good proxy for τ: lower average temperatures mean larger τ. Post-particlisation photons are thus mainly produced at late times.

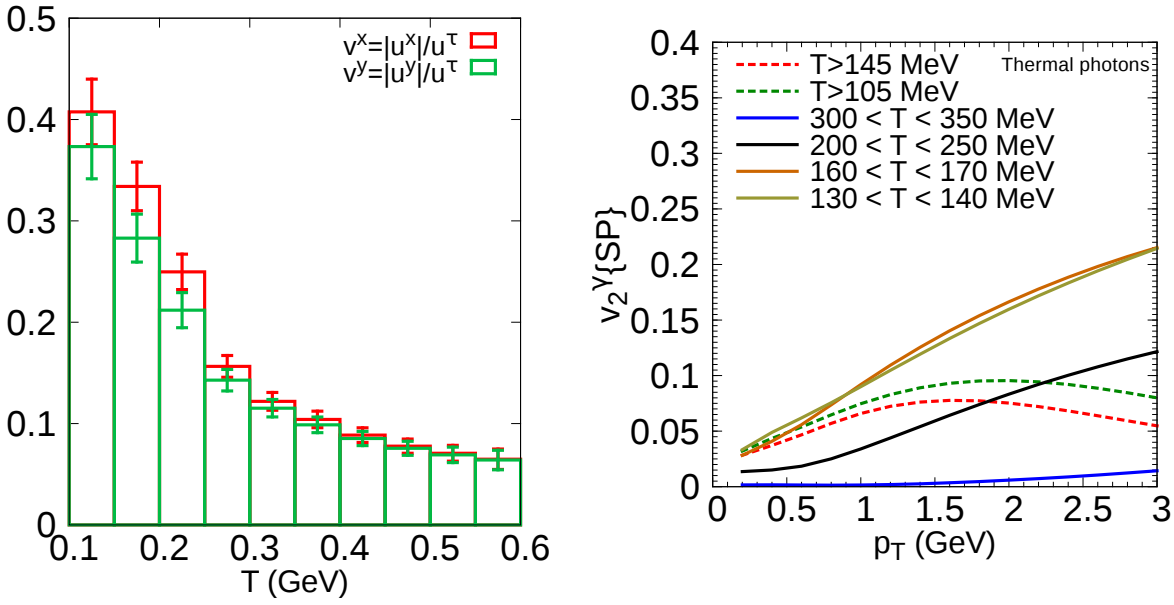

(a) (b)

Figure 7.6: (a) $|u^{x/y}|/u^{\tau}$ averaged over events as a function of temperature (b) *Thermal* photon anisotropy $v_n^{\gamma,th}\{EP\}(T_i)$ as a function of p_T^{γ} for different temperature cuts.

Flow velocity anisotropies Like hadrons, the *thermal* photon v_2 is essentially a reflection of the flow anisotropy that develops in heavy ion collisions due to the anisotropic initial energy deposition. This flow anisotropy grows larger and larger as the hydrodynamical evolution progresses, until lower pressure gradients and viscous effects slowly reduce this anisotropy. This is illustrated on Figure 7.6a by plotting the event-average of $|u^{x/y}|/u^{\tau} = |u^{x/y}|/\sqrt{1+u_x^2+u_y^2}$ for different temperature cuts.

When the hydrodynamical simulation is started, the only flow present is that from the IP-Glasma initial conditions, which is symmetric on average. The $u^{x/y}$ anisotropy grows larger with decreasing temperatures (later times). The eventual saturation and decline of the flow anisotropy is noticeable form the fact that the $u^{x/y}$ asymmetry of the lowest temperature cut ($100-150$ MeV) is visibly smaller than that of the preceding temperature bin ($150-200$ MeV).

Anisotropy of thermal photons emitted from specific temperature regions The magnitude of the v_2 of *thermal* photons originating from different regions of temperature can be investigated by computing the v_2 for different temperature cuts separately. Due to the complicated form of Equation 7.5, this temperature slicing is not trivial. To make the

problem tractable, a simpler definition of $v_n\{EP\}$ is used:

$$v_n^{\gamma,th}\{EP\} \approx \frac{\left\langle \left(\frac{1}{2\pi p_T}\frac{dN}{dp_T}\right) v_n^\gamma v_n^h \right\rangle}{\left\langle \frac{1}{2\pi p_T}\frac{dN}{dp_T} \right\rangle \sqrt{\langle (v_n^h)^2 \rangle}} \tag{7.9}$$

which is similar to Equation 7.8 except that the approximation $v_n^h \propto v_n^\gamma$ was not made. Because of this different definition of $v_n\{EP\}$, the results that follow will differ slightly with those presented before this point.

The fully differential thermal photon spectrum can be divided in contributions coming from different temperature ranges

$$\frac{1}{2\pi p_T}\frac{d^2N}{dp_T d\phi} = \sum_{T_i} \frac{1}{2\pi p_T}\frac{d^2N(T_i)}{dp_T d\phi} \tag{7.10}$$

where T_i stands for a choice of temperature cut.

Defining $v_n^\gamma(T_i)$ as the v_n of $1/(2\pi p_T)d^2N(T_i)/dp_T d\phi$ and assuming that the event-plane Ψ_n^γ is similar for all temperatures, it is straightforward to show that

$$\left(\frac{1}{2\pi p_T}\frac{dN}{dp_T}\right) v_n^\gamma = \sum_{T_i} \left(\frac{1}{2\pi p_T}\frac{d^2N(T_i)}{dp_T}\right) v_n^\gamma(T_i) \tag{7.11}$$

This can be used to rewrite Equation 7.9 as

$$v_n^{\gamma,th}\{EP\} \approx \sum_{T_i} \frac{\left\langle \frac{1}{2\pi p_T}\frac{d^2N(T_i)}{dp_T} \right\rangle}{\left\langle \frac{1}{2\pi p_T}\frac{dN}{dp_T} \right\rangle} \frac{\left\langle \left(\frac{1}{2\pi p_T}\frac{d^2N(T_i)}{dp_T}\right) v_n^\gamma(T_i) v_n^h \right\rangle}{\left(\frac{1}{2\pi p_T}\frac{d^2N(T_i)}{dp_T}\right) \sqrt{\langle (v_n^h)^2 \rangle}} \tag{7.12}$$

$$\approx \sum_{T_i} \frac{\left\langle \frac{1}{2\pi p_T}\frac{d^2N(T_i)}{dp_T} \right\rangle}{\left\langle \frac{1}{2\pi p_T}\frac{dN}{dp_T} \right\rangle} v_n^{\gamma,th}\{EP\}(T_i) \tag{7.13}$$

The momentum anisotropy of *thermal* photons emitted in a given range of temperature is thus $v_n^{\gamma,th}\{EP\}(T_i)$, and their total momentum anisotropy is a sum of the $v_n^{\gamma,th}\{EP\}(T_i)$ of all temperature slices, weighted by each slice's contribution to the thermal photon spectrum.

Returning to Figure 7.6a, since the flow velocity anisotropy is larger at lower temperature, $v_n^{\gamma,th}\{EP\}(T_i)$ should be as well. The negligible flow anisotropy at high temperature should result in a very small $v_n^{\gamma,th}\{EP\}(T_i)$. This result is illustrated on Figure 7.6b. Indeed, thermal photons produced at low temperature have a very large v_2, while thermal photons produced at high temperature barely have any v_2.

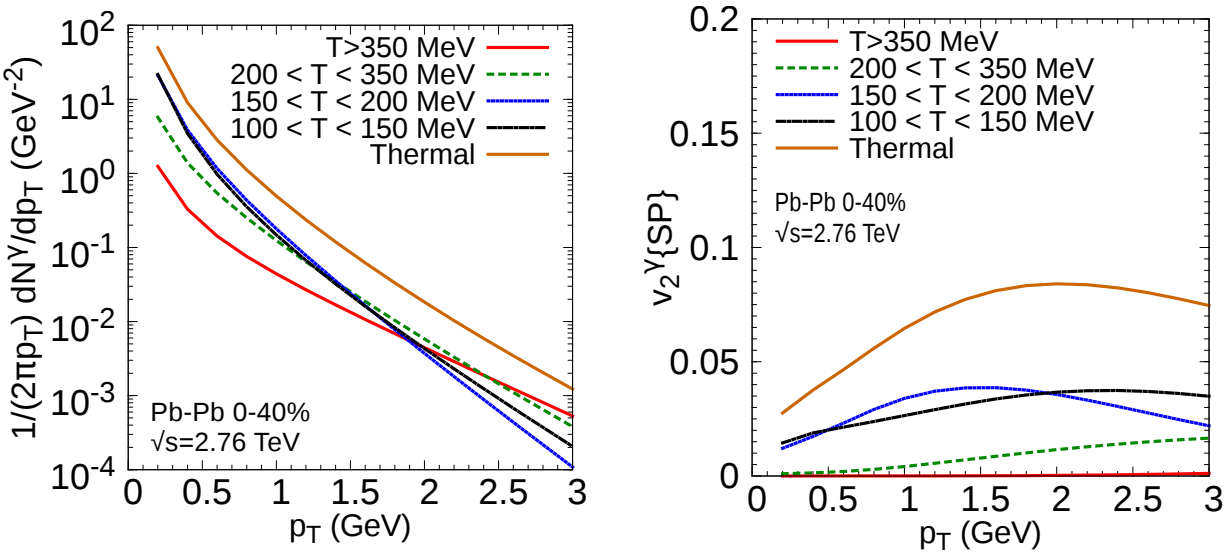

(a) (b)

Figure 7.7: (a) Contribution to the thermal photon spectrum of different ranges of medium temperature (b) Weighted thermal photon v_n for different temperature cuts, as defined in Equations 7.14 and 7.15. On both figures, the curve labeled "Thermal" is the total thermal photon result, obtained by summing up the contribution of the four different temperature cuts.

Weighted thermal photon anisotropies While low temperature photons have a large momentum anisotropy and definitively contribute to raise the total thermal photon $v_2^{\gamma,th}\{EP\}$, it is not possible to tell from Figure 7.6b if they have a large contribution to the total thermal photon v_2: this depends on the amount of photons produced at low temperatures.

To clarify this, Equation 7.13 is rewritten

$$v_n^{\gamma,th}\{EP\} \approx \sum_{T_i} v_n^{\gamma,th,\text{weighted}}\{EP\}(T_i) \tag{7.14}$$

with

$$v_n^{\gamma,th,\text{weighted}}\{EP\}(T_i) = \frac{\left\langle \frac{1}{2\pi p_T}\frac{d^2N(T_i)}{dp_T}\right\rangle}{\left\langle \frac{1}{2\pi p_T}\frac{dN}{dp_T}\right\rangle} v_n^{\gamma,th}\{EP\}(T_i) \tag{7.15}$$

The weighted $v_n^{\gamma,th,\text{weighted}}\{EP\}(T_i)$ is plotted on Figure 7.7b for four temperature cuts that cover the entire temperature profile: $100 < T < 150$ MeV, $150 < T < 200$ MeV, $200 < T < 350$ MeV and $T > 350$ MeV. These temperature cuts were chosen so that the contribution of each one to the thermal photon spectrum were approximately of the same

order, which can be seen on Figure 7.7a, where $1/(2\pi p_T) d^2N(T_i)/dp_T$ is plotted for each temperature cut.

What is clear from Figure 7.7a is that photons produced in the highest temperature regions of the medium contribute significantly to thermal photons at high p_T^γ but are completely sub-dominant at lower p_T. A large portion of low p_T photons are actually produced at temperatures lower than 200 MeV.

Since thermal photons emitted from high temperature regions have a very small $v_n^{\gamma,th}\{EP\}(T_i)$ (c.f. Figure 7.6b), they barely contribute to the total photon anisotropy, as seen on Figure 7.7b.

The important message conveyed by Figure 7.7a and Figure 7.7b is that almost all the momentum anisotropy and a good portion of the spectra of thermal photons originate from the low temperature regions of the medium. It is thus no surprise that post-particlisation thermal photons contribute so much to the direct photon anisotropy.

The overall conclusion of the above is that in view of the large contribution of post-particlisation photons to the direct photon spectrum and v_2, a more sophisticated evaluation of their contribution using e.g. a kinetic theory approach might be necessary. Whether this improved treatment of post-particlisation photons would increase or decrease the photon spectrum or v_2 has yet to be determined.

7.3.2 Photon production rates

Thermal photons are determined by the spacetime description of the medium and the photon emission rates used for this medium. A simple explanation for the underestimated spectrum and v_2 shown on Figure 7.4 is that the thermal rates are too low. For example, a factor of two increase in the thermal rates corresponds directly to a factor of two increase in the contribution of thermal photons to the direct photon spectrum. This doubling of the thermal rate would not change at all the *thermal* photon v_2 shown on Figure 7.4b, but it would pull the *direct* photon v_2 — which is a weighted average of the different photon sources — toward the thermal photon v_2, which is larger.

As seen in Section 5.3, there still are significant uncertainties in the evaluation of thermal photon rates, notwithstanding additional subtleties from viscous corrections to these rates. The effect on direct photons of some of these uncertainties are highlighted in what follows.

QGP TO HADRONIC RATE TRANSITION The first uncertainty that can be quantified is the temperature chosen to switch from the QGP photon rate to the hadronic photon rate. The above results used $T_{tr} = 180$ MeV. As shown on Figure 5.3, the rates used as reference in this thesis — QGP LO at high temperature and hadronic rate from Refs. [112, 113, 114] at low

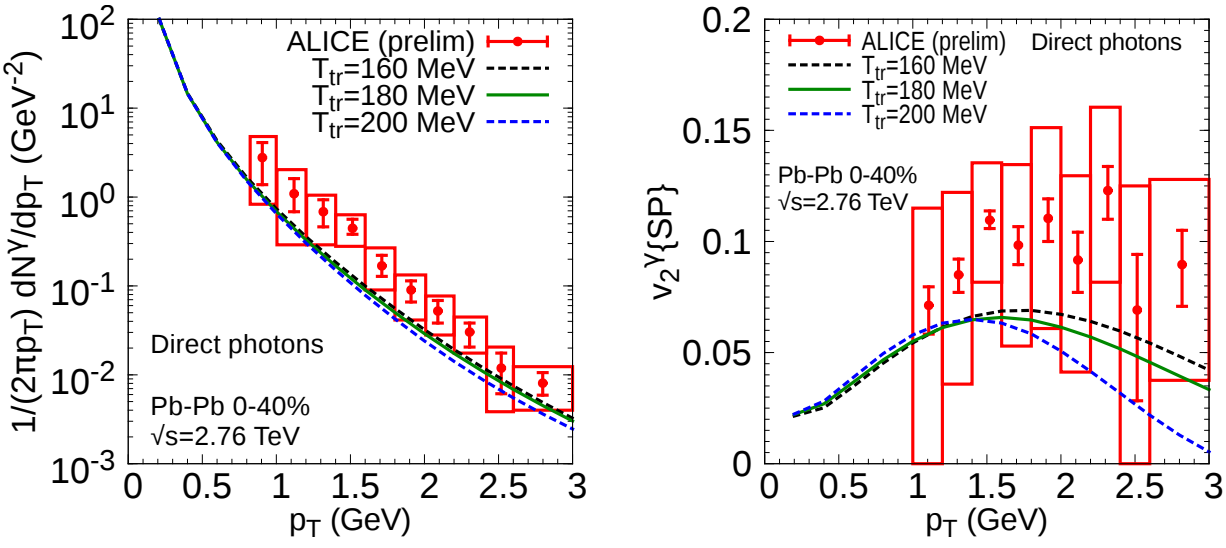

(a) (b)

Figure 7.8: Effect on the direct photon (a) spectrum and (b) v_2 of varying the temperature at which the QGP LO photon rate is switched to the hadronic photon rate from Refs. [112, 113, 114].

T — are fairly similar in the temperature range where one expects quark and gluon degrees of freedom to transition of hadronic ones. It is nevertheless instructive to see the effect of changing T_{tr} from 160 to 200 MeV, which is shown for the spectrum and v_2 on Figure 7.8.

The effect on the direct photon spectrum (Figure 7.8a) is small. The effect of T_{tr} is also small at low p_T on the photon v_2. On the other hand, for $p_T > 1.5$ GeV, varying T_{tr} by 40 MeV has a large effect on v_2. This can be understood from the fact that the QGP rate is in general larger than the hadron gas rate in this range of temperature explored for T_{tr}. The consequence is that using the QGP rate down to lower temperatures produces more photons — photons which were shown in the previous section to have a large momentum anisotropy. A lower T_{tr} thus increases the direct photon v_2, while the opposite happens if T_{tr} goes from 180 to 200 MeV.

Viscous corrections to the emission rates Another uncertainty in the rates is the effect of viscosity on photon emission. As summarized in Table 7.1, the effect of viscosity has only been evaluated for a subset of emission rates. To quantify the uncertainty introduced by this partial correction of the photon emission rates, the effect of bulk and shear viscosity *on the emission rates* is turned off one after the other on Figure 7.9.

From Figure 7.9, the effect of viscosity appears to be fairly modest, except on v_2 at high

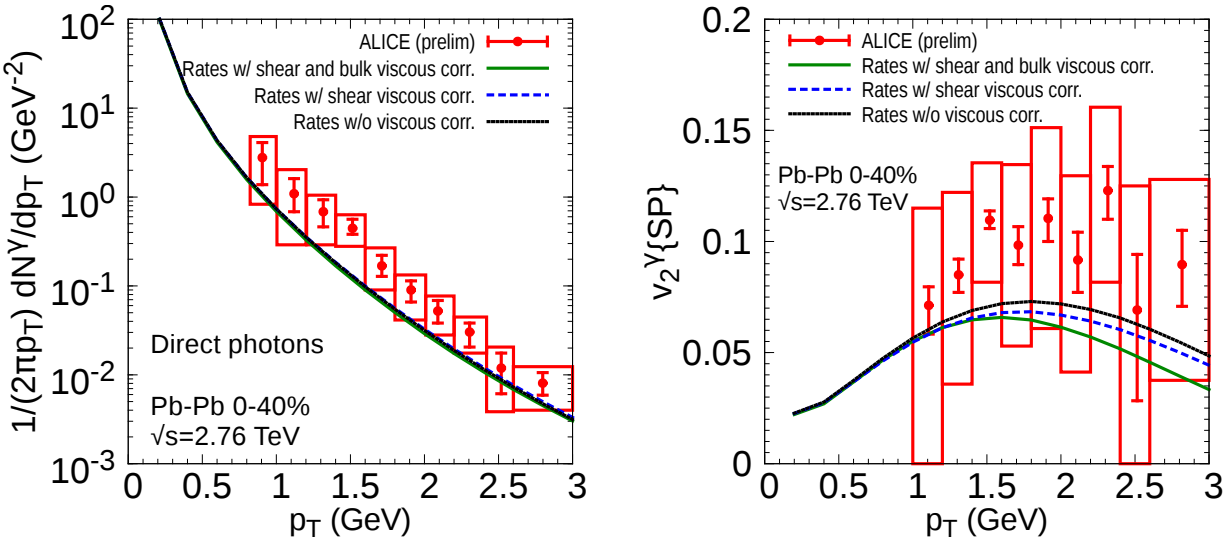

(a) (b)

Figure 7.9: Effect of viscous corrections to the photon emission rates on the direct photon (a) spectrum and (b) v_2.

p_T. The rates for which the viscous corrections are currently included represent approximately half of the total photon emission rate[1]. Assuming that the viscous corrections to the uncorrected rates are of the same order as the corrections currently available, it can be concluded from Figure 7.9 that the missing viscous corrections represent at least a $20-30\%$ uncertainty on the direct photon v_2 at $p_T \gtrsim 2$ GeV.

The effect of viscous corrections to the rates are small for the direct photon spectrum. This can be understood from the fact that viscous corrections are larger at higher p_T, where the thermal photon signal is increasingly eclipsed by prompt photons.

Even with the knowledge that Figure 7.9 is only a partial reflection of the effect of viscosity on photon emission — due to the missing corrections — it is still difficult to fully realise the importance of viscous corrections from that figure. To remedy this, Figure 7.9 is reproduced by using only equilibrium thermal rates for which viscous corrections are available. This restricts the rates to the QGP $2 \to 2$ rates and photons produced by light mesons. The result is shown on Figure 7.10.

Although the spectrum (Figure 7.10a) still shows no significant dependence on viscous corrections, the v_2 (Figure 7.10b) is shown to be suppressed considerably by viscous corrections to the rates. The lesson that must be drawn from Figure 7.10 is that quantitative

[1] The $2 \to 2$ QGP photon rates is approximately of the same order as the QGP bremsstrahlung contribution. Similarly, the photon emission rate from light mesons is roughly half the total hadronic rates.

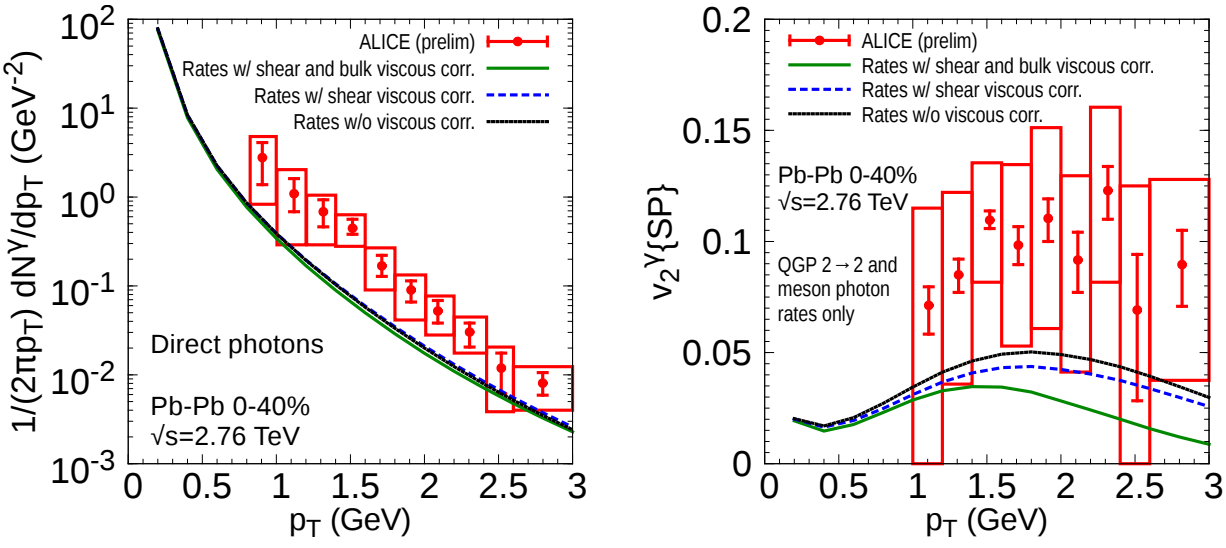

(a) (b)

Figure 7.10: Effect of viscous corrections to the photon emission rates on the direct photons if the only equilibrium rates included are those for which viscous corrections are available (i.e. photons from QGP $2 \to 2$ and from light mesons). The spectrum is (a) and the v_2 is (b).

comparisons with data require not only a good knowledge of photon emission rates from the QGP, but also from the effect of viscosity on these rates.

Other thermal rates A final estimate of the uncertainty in photon rates can be provided by using different thermal photon rates. The fact that there are still considerable uncertainties in the equilibrium photon emission rates from QCD matter was highlighted in Section 5.3. Up to this point in this analysis, the photon rates used were the QGP LO rates for $T > 180$ MeV and the hadronic rates from Refs. [112, 113, 114] below that temperature. However other rates were presented in Section 5.3 and using them instead of the above rates is a simple way of estimating the effect on direct photons of the difference between these rates. Since viscous corrections have not been evaluated for these rates, the comparisons in what follows are made *without viscous corrections to any of the rates.*

The semi-QGP rate from Ref. [111] was shown on Figure 5.2a while the hadron gas rate from Dusling and Zahed (Ref. [115]) was shown on Figure 5.2b. The result of making the direct photon spectrum and v_2 calculation with these rates is shown on Figure 7.11. As it could be expected, using the semi-QGP rate suppresses the direct photon spectrum considerably, while using the hadronic rate from Ref. [115] increases it. Moreover, the hadronic rate

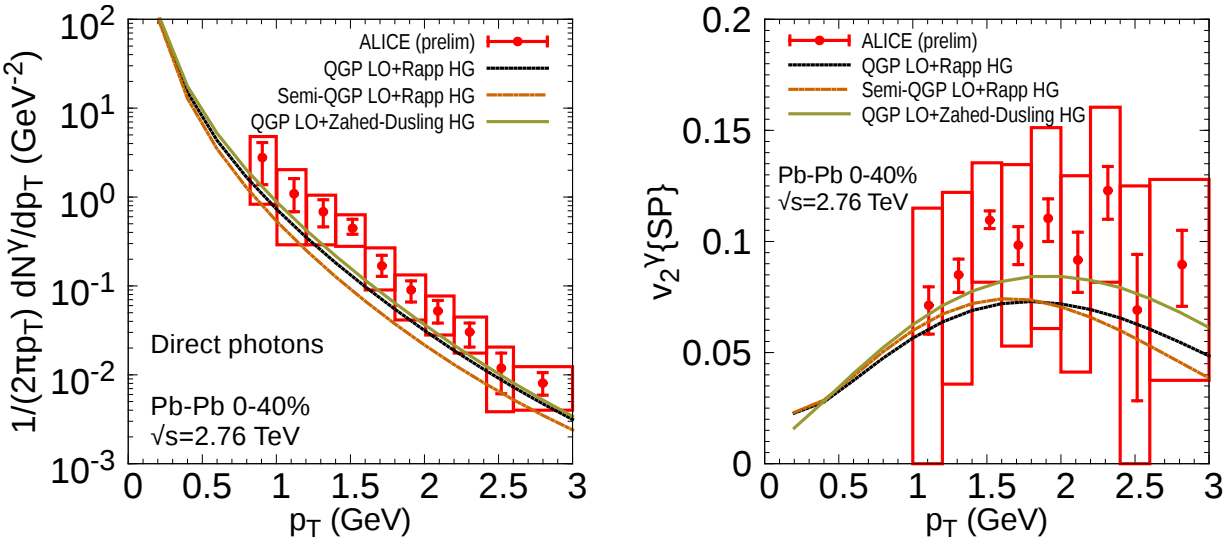

(a) (b)

Figure 7.11: Direct photon (a) spectra and (b) v_2 evaluated with either i) the QGP LO rate and the hadronic rate from Refs. [112, 113, 114] (labeled "Rapp HG") ii) the semi-QGP rate and the hadronic rate from Refs. [112, 113, 114] iii) the QGP LO rate with the hadronic rate from Ref. [115] (labeled "Zahed-Dusling").

from Ref. [115] results in a much larger photon v_2, in better agreement with measurements.

The effect of the semi-QGP rate on the photon v_2 is more subtle, since there is a competition between two effects. On one hand, a lower QGP rate increases the total *thermal* photon v_2, since photons produced at high temperatures have a smaller v_2 than those produced at low temperatures (c.f. Figure 7.6b). On the other hand, while the thermal v_2 is increased by suppressing the QGP rate, the thermal photon spectrum necessarily decreases as well, which is clear from the spectrum (Figure 7.11a). The smaller the thermal photon spectrum is with respect to prompt photons, the smaller is the final *direct* photon v_2, since it pulls the v_2 towards that of the prompt photons, which is zero in the present case.

In the end, the overall effect of the semi-QGP on the direct photon v_2 is fairly small, in particular in view of the large suppression the rate brought to the spectrum. It is due to the two effects just described largely canceling each other. This is a good reminder of the complementarity of the photon spectrum and v_2 as observables.

On a last note, it is important to remember that the dependence on the T_{tr} shown at the beginning of this section would be significantly different for the results shown on Figure 7.11 than what was seen on Figure 7.8. For example, the semi-QGP rate and the hadronic rate from Refs. [112, 113, 114] are very different at $T_{tr} = 180$ MeV, and changing T_{tr} to a lower

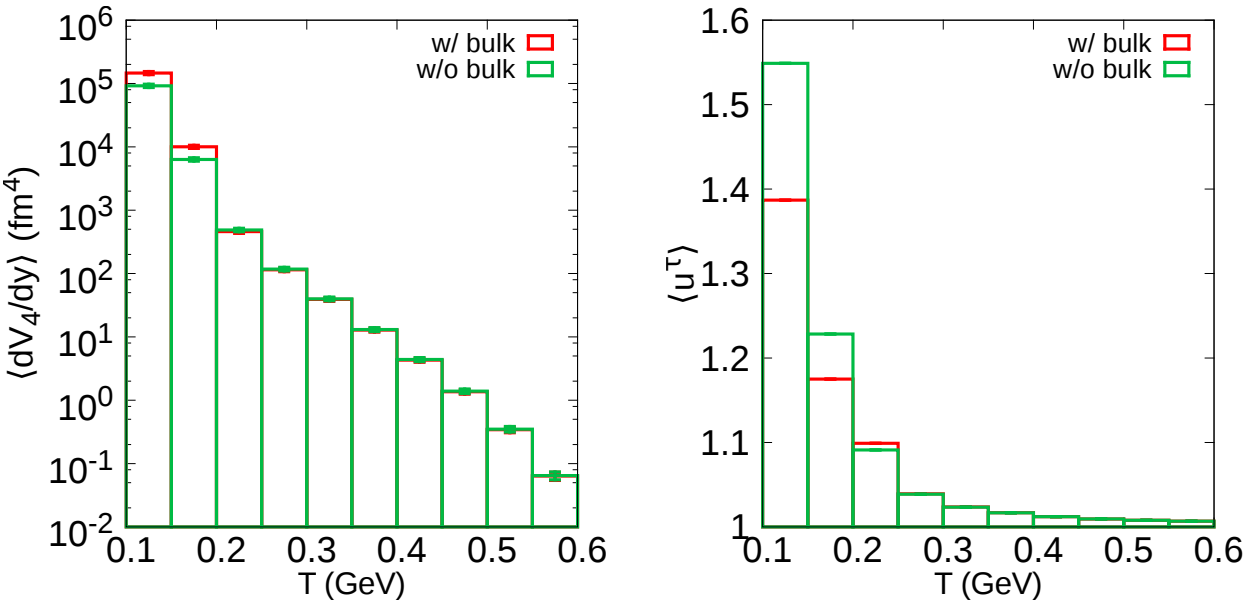

(a) (b)

Figure 7.12: (a) Event-average $\langle dV_4/dy \rangle_T$ as defined by Equation 7.16 (error bars indicate the variance from the event-average) (b) Event-average $\langle u^\tau \rangle_T$ as defined by Equation 7.17 (event-by-event variance not shown for clarity). For hydrodynamical model with and without bulk viscosity.

or higher value would change significantly the results shown on Figure 7.11.

The conclusion of this subsection is that progress in understanding direct photon measurements are significantly dependent on improvements in the understanding of thermal emission rates.

7.3.3 Effect of bulk viscosity

The effect of bulk viscosity on hadronic observables was investigated in Section 4.3.1. It was concluded that the presence of bulk viscosity, with a temperature-dependence given by Figure 4.1, brought a considerable improvement to the description of the average transverse momentum of hadrons. Moreover the introduction of bulk viscosity was found to have a considerable effect on the extraction of the shear viscosity η from hadronic measurements.

As this work is the first to compute direct photons with a hydrodynamical model that includes bulk viscosity, it is important to quantify its effect. This will allow to make connection with previous calculations that do not include bulk viscosity, and also to understand the part played by bulk in thermal photon production.

Spacetime volume and flow profile Photon production is primarily affected by changes in the flow and temperature profile of the modelled quark-gluon plasma. The effect of bulk viscosity on the temperature profile can be quantified by computing the spacetime volume of the medium for different temperature cuts, averaged over events:

$$\left\langle \frac{dV_4}{dy} \right\rangle_T = \frac{1}{N_{\text{events}}} \sum_{\text{events}} \frac{1}{dy} \int d^4x \Theta(T_{min} < T(x) < T_{max}) \tag{7.16}$$

The result is differential in rapidity since the volume is infinite in the longitudinal direction (the hydrodynamical model is $2+1$D). Averaging over events permits to determine if there are significant fluctuations of this quantity between the different events in the centrality class.

Similarly, the event-averaged flow can be quantified with $u^\tau = \sqrt{1 + (u^x)^2 + (u^y)^2}$:

$$\langle u^\tau \rangle_T = \frac{\sum_{\text{events}} \int d^4x u^\tau(x) \Theta(T_{min} < T(x) < T_{max})}{\sum_{\text{events}} \int d^4x \Theta(T_{min} < T(x) < T_{max})} \tag{7.17}$$

The spacetime volume is shown on Figure 7.12a and $\langle u^\tau \rangle$ on Figure 7.12b, for a hydrodynamical evolution with and without bulk viscosity.

Bulk viscosity increases the spacetime volume at low temperature by approximately 50% for $T < 200$ MeV, but does not affect significantly the temperature distribution above 200 MeV. This is in line with the temperature dependence used for the bulk viscosity (Figure 4.1), which is sharply peaked at $T = 180$ MeV but is very small away from this peak.

On the other hand, a significant decrease in the flow velocity (Figure 7.12b) due to the introduction of bulk viscosity is observed for the same temperature range where the spacetime volume increase is observed. Bulk viscosity is understood to act as a resistance to expansion or compression. Since heavy ion collisions are mostly dominated by an expansion phase, the bulk viscous pressure is mostly negative, slowing down the expansion of the medium.

Effect on direct photons A larger spacetime volume is almost invariably associated with a larger number of produced photons. The flow does affect the momentum distribution of the photons, but not their number, up to bulk viscosity effects on the photon rates.

If the effect of viscosity on photon rates is ignored, the number of photons is actually totally invariant under the flow profile. This is shown on Figure 7.13a by plotting the multiplicity *per volume* for the photon computed from the hydrodynamical model with and without bulk viscosity. The multiplicity is obtained by integrating the photon spectrum above $p_T = 0.05$ GeV. As expected, at equal volumes, the change in flow velocity due to the introduction of bulk viscosity does not affect the number of photons produced in heavy ion

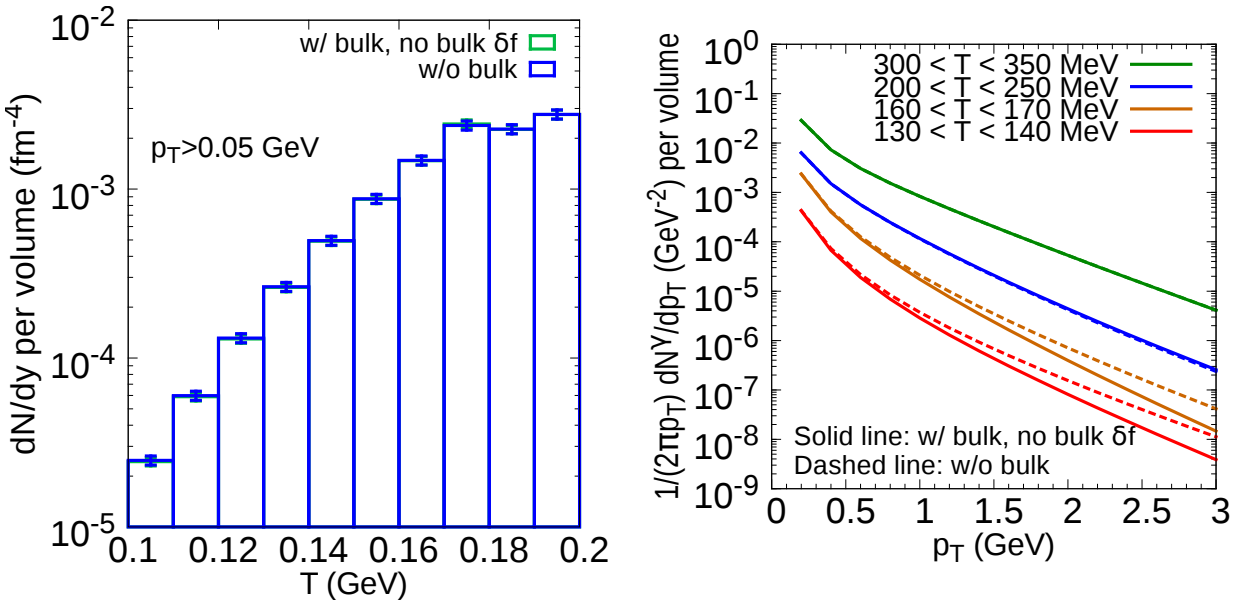

(a) (b)

Figure 7.13: Effect of bulk viscosity on (a) the direct photon multiplicity per spacetime volume (b) the direct photon spectrum per spacetime volume.

collisions.

The effect of the flow velocity on the thermal photon spectrum can be seen from Figure 7.13b. Once again, the effect of the different volumes was removed by considering the photon spectrum *per volume*.

The reduction of the flow velocity induced by bulk viscosity in the low temperature region of the medium translates into a softer thermal photon spectrum at low temperatures: slightly more photons are produced at low p_T and significantly less are produced at high p_T. If the effect of bulk viscosity on photon emission is taken into account, the above conclusions remain the same since the effect of viscosity is to decrease further the thermal photon spectrum at high p_T, an effect previously seen on Figure 7.9b.

Overall effect of bulk viscosity Comparing the overall effect of bulk viscosity on direct photons is not straightforward, since calculations with and without bulk viscosity require different hydrodynamical parameters to describe hadronic observables. Two alternatives are shown on Figure 7.14. In the first case, the hydrodynamical models with and without bulk viscosity uses the same parameters (η/s, T_{sw}, ...) and bulk viscosity is simply turned off in the shear-only case. In the second case, η/s is readjusted after bulk viscosity is turned off so that the integrated hadron v_n are still reproduced by the hydrodynamical model without bulk viscosity (c.f Figure 4.4). In both cases, it can be seen that the overall

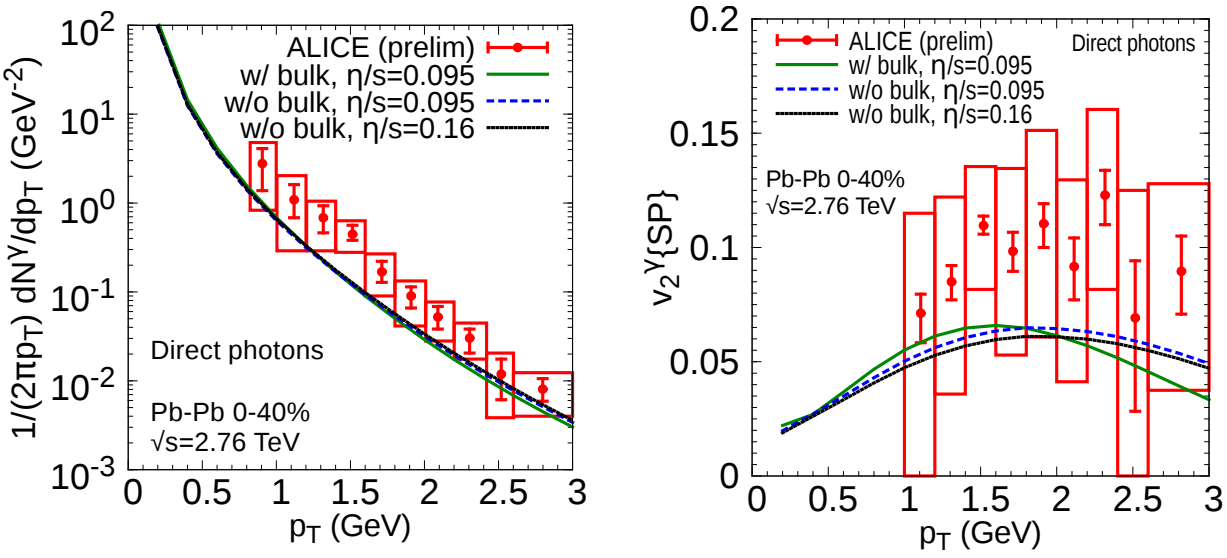

(a) (b)

Figure 7.14: Overall effect of bulk viscosity on the direct photon (a) spectrum and (b) v_2.

effect of bulk viscosity is not very large, in particular compared to the uncertainties related to the photon emission rates explored in the previous section. As expected from the preceding discussion, the combination of larger spacetime volume and softer thermal spectrum results in a net gain in the photon v_2 at low p_T, although the photon v_2 is reduced at higher p_T.

While the overall effect of bulk viscosity on direct photons is modest — a small increase a low p_T and a moderate decrease at high p_T — it does change significantly the shape of the direct photon v_2. This is a very interesting observation. With improved measurements and lower theoretical uncertainties, this finding could be used to provide constraints on the shear and bulk viscosities of the quark-gluon plasma.

With this closing remark on the effect of bulk at the LHC, comparisons of direct photons with RHIC measurements are presented in the next section.

7.4 RHIC

The direct photon spectrum and v_2 were also measured at RHIC by the PHENIX collaboration [29, 30, 136]. These measurements were made in Au-Au collisions at $\sqrt{s_{NN}} = 200$ GeV for centralities 0-20% and 20-40%. Comparison of the hydrodynamical model's prediction for direct photons is shown on Figure 7.15.

The photon anisotropy is compared with the preliminary measurements from Ref. [136]

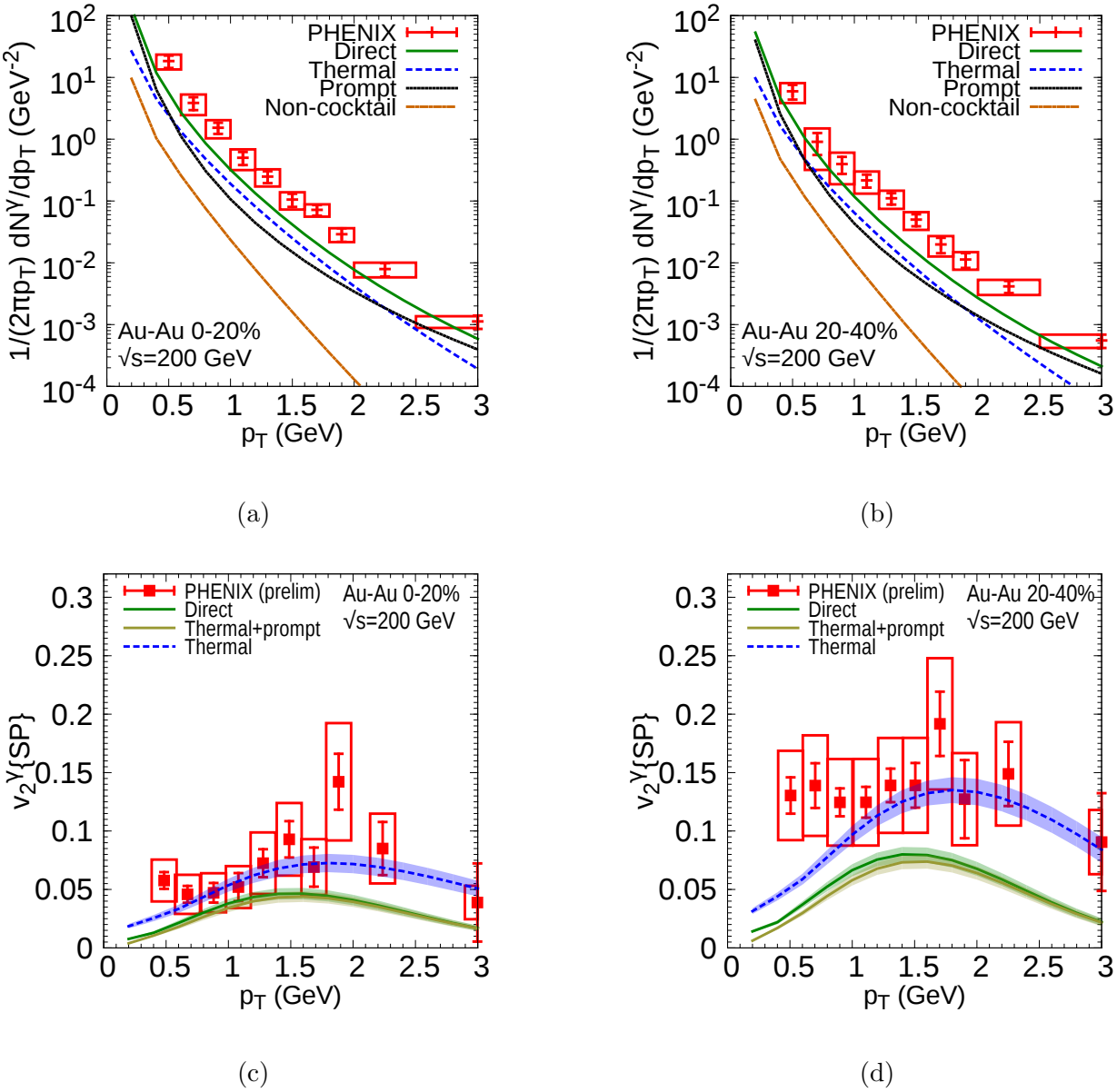

Figure 7.15: Direct photon spectra for (a) $0-20\%$ centrality (b) $20-40\%$ centrality and direct photon v_2 for (c) $0-20\%$ centrality (d) $20-40\%$. For Au-Au collisions at $\sqrt{s_{NN}} = 200$ GeV.

rather than the older measurements from Ref. [30]. The rationale is that the preliminary measurements are consistent with the older ones, but go to much lower transverse momentum and have smaller uncertainties. Showing both would make the figures difficult to read.

Unlike at the LHC, measurements at RHIC are available for p_T smaller than 1 GeV. As explained in Section 5.2 and Appendix A, the perturbative QCD calculation used in this thesis to evaluate prompt photons appears to be reliable for photon transverse momenta larger than $p_T \sim 1 - 1.5$ GeV. In what follows, the direct photon calculations are compared

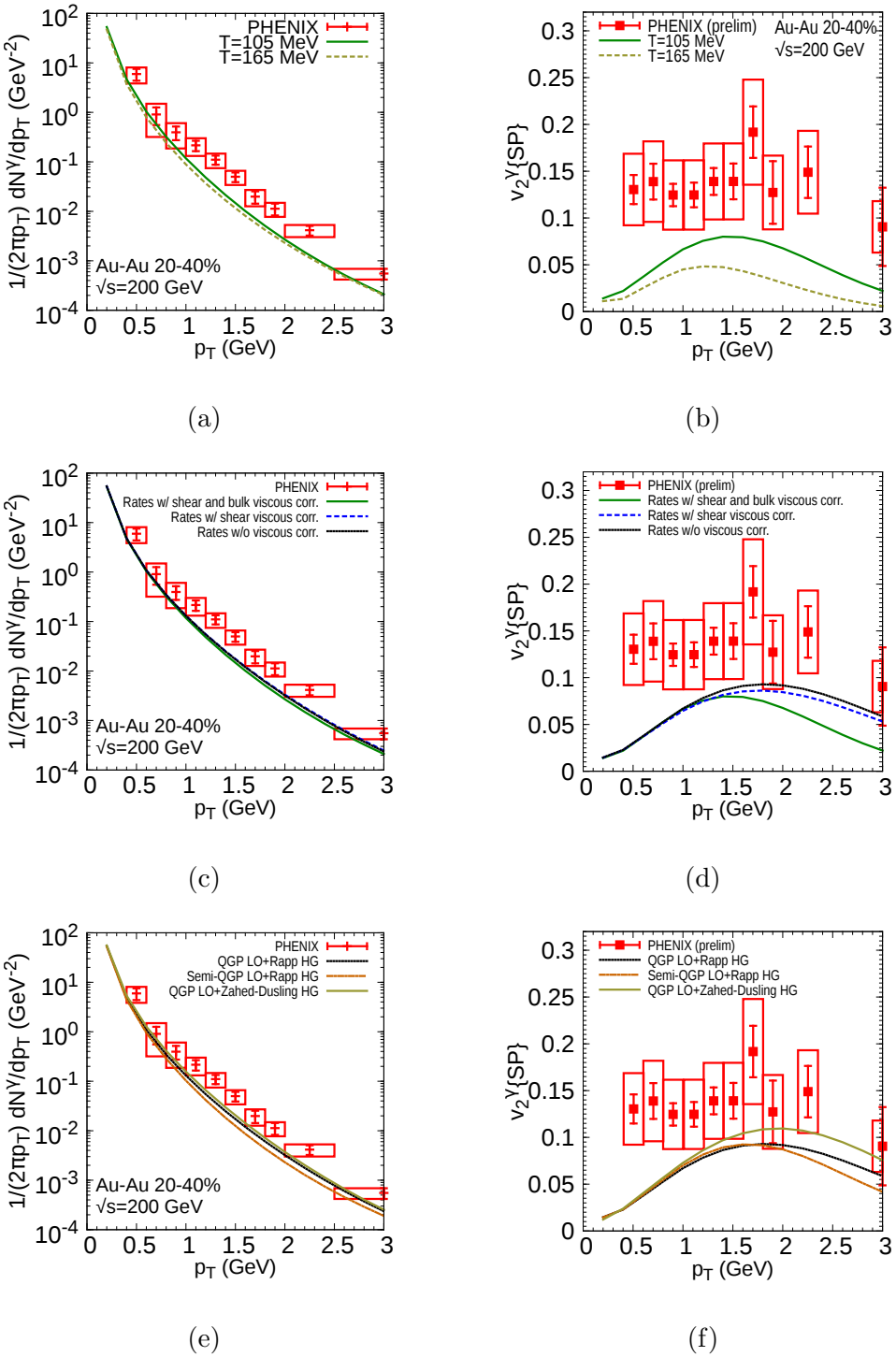

Figure 7.16: Effect on (a) the direct photon spectrum and (b) the direct photon v_2 of including thermal photons down to $T = 105$ MeV as opposed to $T = 165$ MeV; Effect of viscous corrections to the photon emission rates on the direct photon (c) spectrum and (d) v_2; (e) (f) Same as Figure 7.11. For Au-Au collisions at $\sqrt{s_{NN}} = 200$ GeV, $20 - 40\%$ centrality.

with RHIC data over the whole p_T range covered by the measurements. The limited reliability of the prompt photon results — and consequently of the direct photon calculations — in the low p_T region should be kept in mind.

For both centralities, the agreement with the spectrum is similar to what was seen at the LHC: the direct photon calculation tends to underestimate the measured spectrum, but is fairly close to the lower uncertainties. The agreement appears to be slightly better for $0-20\%$ centrality than $20-40\%$. The same is true for the v_2, where the calculation is in general within the combined lower uncertainties in $0-20\%$ but is farther from the measurements for $20-40\%$. Overall, the agreement with measurements at the LHC was slightly better than the current results at RHIC.

It is relevant to verify the effect on direct photon calculations at RHIC of some of the uncertainties investigated in the previous section for LHC calculations. The effect of the post-particlisation photons is shown on Figures 7.16a and 7.16b, while the effect of viscosity corrections to the rates is shown on Figures 7.16c and 7.16d. Finally, the effect of using different thermal photon rates is shown on Figures 7.16e and 7.16f. All of this is shown for $20-40\%$ centrality. In all cases, the effect are in line with what was observed at the LHC.

It is not clear at the moment why agreement with data is better for 0-20% centrality than 20-40% at RHIC, nor why it is better at the LHC than RHIC. Post-particlisation photons could be at the origin of this pattern: post-particlisation dynamics is expected to be more important in lower energy collisions and in more peripheral centralities. It is thus possible that a more sophisticated treatment of photon production in the latter phase of the collisions could explain the differences observed between RHIC centralities, and between RHIC and the LHC.

7.5 Hydrodynamical model and direct photons: summary

The hydrodynamical model presented in Chapter 3 was shown in Chapter 4 to provide a good description of hadronic observables. This same model was used in the present chapter to compute direct photon production at RHIC and the LHC. The result of this direct photon calculation was shown on Figure 7.4 for the LHC and on Figure 7.15 for RHIC. At both colliders, comparisons with measurements showed similar features: calculations tend to be lower than measurements, although often within systematic and statistical uncertainties. Agreement with measurements was found to be better at the LHC than at RHIC.

Thermal photons were found to be considerably larger than prompt photons at the LHC

(Figure 7.4) for transverse momenta between 1 and 2 GeV, with prompt photons becoming the dominant source of direct photons at higher p_T. At RHIC, thermal photons do not show as strong of a dominance over prompt photons for $p_T \sim 1 - 2$ GeV (Figure 7.15), although they remain the largest source of direct photons in this transverse momentum range. The reliability of direct photon calculations below $p_T \sim 1$ GeV is currently limited by the uncertainty in prompt photons at such low transverse momenta (see Appendix A).

Different sources of uncertainties in the thermal photon calculations were quantified both for RHIC and the LHC. The importance of post-particlisation photons was shown on Figures 7.5a and 7.5b for the LHC and Figures 7.16a and 7.16b for RHIC. It was shown in Section 7.3.1 that photons created at temperatures lower than 250 MeV carry most of the momentum anisotropy of thermal photons at the LHC, providing further incentive to improve the treatment of post-particlisation photons in the future.

Uncertainties in the photon emission rates were investigated in Section 7.3.2 for the LHC. The importance of stronger theoretical constraints on the thermal photon emission rate and on the effect of shear and bulk viscosities on the rate were highlighted. The effect of these uncertainties were also shown at RHIC on Figures 7.16c, 7.16d, 7.16e and 7.16f.

Finally, the effect of bulk viscosity on direct photons was investigated at the LHC in Section 7.3.3. The most notable feature is a change in the shape of the direct photon v_2, shown on Figure 7.14b: bulk viscosity increases the direct photon v_2 at low p_T and decreases it at high p_T.

Part V

Conclusion

In this thesis, the production of hadrons and photons in heavy ion collisions was studied at RHIC and the LHC using a modern hydrodynamical model of heavy ion collisions. This comprehensive model included realistic initial conditions (IP-Glasma), second-order hydrodynamics equations with both shear and bulk viscosities, along with post-particlisation dynamics of hadrons.

It was shown in Chapter 4 that a wide range of hadronic observables could be described well by this hydrodynamical model. Bulk viscosity was found to be important to achieve a good description of the hadronic spectra, in particular the average transverse momentum of hadrons. It was also shown to have a large effect on the value of the shear viscosity of the quark-gluon plasma extracted from comparison with measurements.

Future work on hadron production includes determining the level of constraint that hadronic observables provides on bulk viscosity. It will be interesting to see the extent to which the position (in temperature) of the peak in bulk viscosity, along with the peak's magnitude, can be constrained from the average transverse momentum of identified hadrons.

The production of direct photons was computed from the same hydrodynamical model, and compared in Chapter 7 with spectra and v_2 measurements from both RHIC and the LHC. Direct photon calculations were found to be within or slightly below the large systematic and statistical uncertainties of data. A series of uncertainties in the direct photon calculation have been highlighted, indicating that additional theoretical investigations are necessary before direct photon measurements can be said to be described or not by calculations from hydrodynamical models.

A first important improvement will be a better description of the post-particlisation phase of the collisions, where a large number of photons are produced. In this later phase of the collision, an approach based on kinetic theory — which was shown to give good results for hadrons in Chapter 4 — might be necessary for photons as well. Post-particlisation photons contribute significantly to the photon momentum anisotropy, and quantifying them with greater accuracy will strengthen considerably the predictions of the hydrodynamical model.

Calculations shown in Section 7.3.2 also highlighted the importance of increased theoretical constraints on the equilibrium photon rates in reducing the uncertainty on the direct photon calculation. The evaluation of the effect of viscosity on these rates — as presented for a subset of thermal rates in Chapter 6 — will also be necessary.

The presence of bulk viscosity in the hydrodynamical evolution produced a small effect on the photon spectrum at the LHC, and a modest change in the overall magnitude of the photon v_2. On the other hand, it produced a clear change in the shape of v_2, enhancing it at low p_T^γ and reducing it at higher p_T^γ. While theoretical and experimental uncertainties do not currently permit to determine if this change in the shape of v_2 is favored by data, the

reduction of both uncertainties in the future could make direct photons a good probe of the bulk viscosity of quantum chromodynamics.

Important future work that was not addressed in this thesis is a more sophisticated treatment of prompt photon production in heavy ion collisions, including both parton energy loss and jet-medium photon production. The production of photons during the pre-thermalised phase of the collisions will also be a part of the framework needing greater scrutiny.

Until at least preliminary investigations of the above improvements are undertaken, determining if there still is a "direct photon puzzle" is difficult. On the other hand, the calculations presented in this work show a much reduced tension with the available measurements than previous work [36, 37, 38], and constitute a solid basis for future work on the puzzle.

Appendix

Appendix A

Perturbative QCD photons at low p_T

Pertubative QCD is based on the idea that a large momentum exchange occurs in a hadronic collisions, allowing for a part of the cross-section to be computed perturbatively. Photons produced at large transverse momentum can be described by perturbative QCD because the magnitude of their transverse momentum guarantees a large momentum exchange.

It is understood that perturbative QCD eventually breaks down at low transverse momentum, although the exact value of p_T at which this happens is not clear. When global fits of parton distribution functions and fragmentation functions to data are made, this issue has to be considered: data points with scale Q smaller than a chosen minimum scale Q_0 are not used in the fits. The value of Q_0 is typically $1 - 1.5$ GeV. This value provides an estimate for the lowest energy scale at which perturbative QCD should be considered reliable.

For photon production in perturbative QCD, the scales are given by an energy scale of the order of the photon transverse momentum. It is not compulsory to set the scales equal to p_T^γ; there could be a proportionality constant, for example. Even a scale that is related to p_T^γ would do. Such a scale exists for fragmentation photons, where a large transverse momentum parton is produced first, and then produces a photon through fragmentation. In this case, using the energy of the parton as scale would also be justified.

In this thesis, the factorisation, renormalisation and fragmentation scales are all set to $Q = p_T^\gamma/2$. The reason behind this choice can be seen on Figure A.1a, where the perturbative QCD calculation of prompt photons described in Section 5.2.1 is evaluated at different scales $Q = Np_T^\gamma$ and compared to direct photon measurements in proton-proton collisions at $\sqrt{s_{NN}} = 200$ GeV from RHIC [20]. Results are plotted for $Q = Np_T^\gamma$; $N = 1/2$ to $N = 8$, with the calculations going down to $p_T^\gamma = 1.5/N$ GeV due Q_0 being approximately equal to 1.5 GeV in the calculation.

It is apparent from Figure A.1a that a small proportionality constant such as $Q = p_T^\gamma/2$ provides a better description of the available measurements. The choice $Q = p_T^\gamma/2$ in

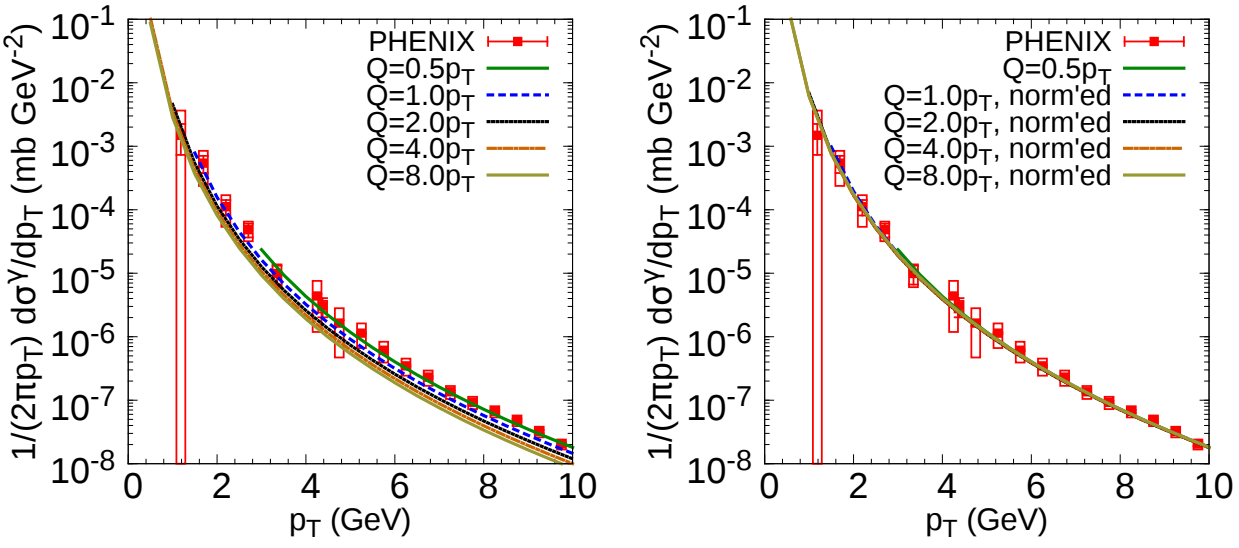

(a) (b)

Figure A.1: Direct photon spectrum measured in $\sqrt{s_{NN}} = 200$ GeV proton-proton collisions at RHIC compared with (a) perturbative QCD calculations made with different scales Q (b) normalised perturbative QCD calculations (Equation A.1)

Section 5.2.1 was made based on this observation.

The lowest p_T^γ available for $Q = p_T^\gamma/2$ is $p_T^\gamma = 3$ GeV, assuming $Q_0 = 1.5$ GeV. Computing photons at a lower p_T^γ would require a smaller Q_0, which would imply using the perturbative scale evolution below Q_0. A different approach is used here, based on the scale dependence of the perturbative QCD calculation.

Figure A.1a hints that the main effect of changing the value of N in $Q = Np_T^\gamma$ is a change of normalization of the photon spectrum, although it is difficult to see if the calculations have a different p_T^γ-dependence. This can be verified by rescaling all the calculations by a constant, so that they have the same normalisation. The following formula is used for the normalisation

$$\frac{1}{2\pi p_T}\frac{d\sigma_{pp}^{renorm}}{dp_T}\bigg|_{Q=Np_T^\gamma} = 1.25N^{0.26}\left[\frac{1}{2\pi p_T}\frac{d\sigma_{pp}}{dp_T}\right] \tag{A.1}$$

so that $Q = p_T^\gamma/2$ is not rescaled, but perturbative QCD calculations made with higher values of Q are normalised up. The result is shown on Figure A.1b. All calculations fall on top of each other, supporting the claim that a change in scale results essentially in a change of normalisation, and not a change in momentum dependence.

The above observation is not trivial. It could very well have been that normalising all the calculations to have the same magnitude at high p_T would have resulted in a different

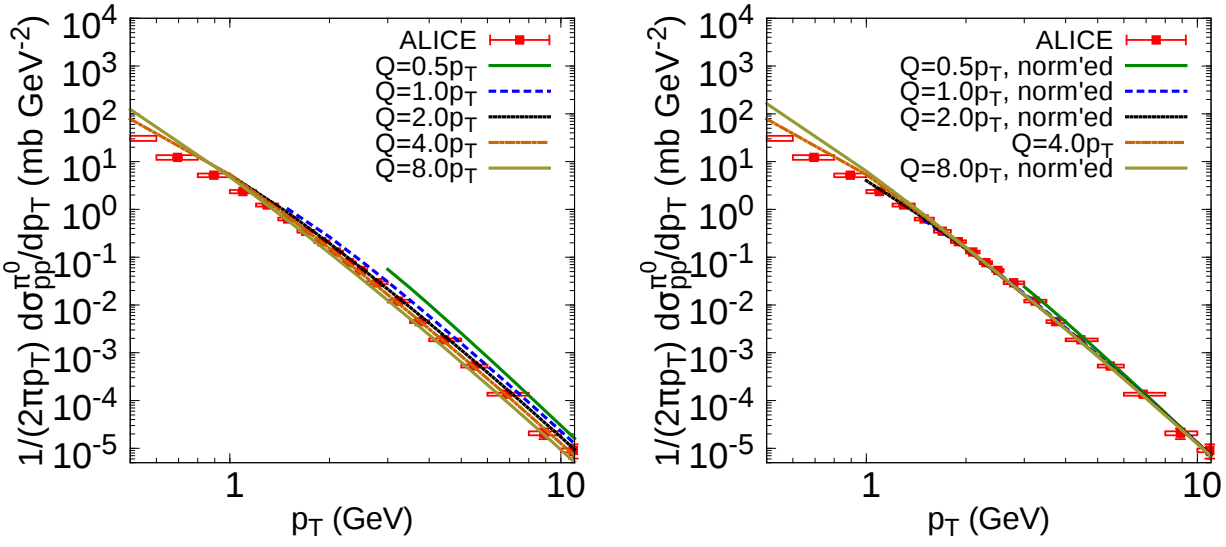

(a) (b)

Figure A.2: Same as Figure A.1 for pions measured in $\sqrt{s_{NN}} = 2.76$ TeV proton-proton collisions at the LHC

low p_T-dependence. Instead, all calculations lined up. This finding can be used to compute prompt photons to low p_T by simply using a large proportionality constant between Q and p_T^γ and modifying the overall normalisation so that high p_T data are fitted, which in this case corresponds to the normalisation of $Q \approx p_T^\gamma/2$.

Figure A.1b indicates that the perturbative QCD calculation of prompt photons is in good agreement with direct photon measurements at low p_T^γ, although it overestimates slightly the very lowest point around 1 GeV. This good agreement with measurements at low p_T^γ supports the idea that perturbative QCD calculations can be relied on even at fairly low transverse momentum. To provide further support for this idea, a similar test is made at the LHC.

While there are no low p_T direct photon measurements in proton-proton collisions at the LHC, there are measurements for e.g. neutral pions. It can thus be verified if the same scaling behaviour is observed for pions at the LHC. The perturbative QCD calculation of π^0 for different scales is shown on Figure A.2a, while the normalised results are shown on Figure A.2b. This time, all results were normalised so as to have the same high p_T magnitude as $Q = 4p_T^{\pi^0}$. Note that both axis are logarithmic, unlike the previous figures.

Once again, the normalised calculations line up well, although arguably not as well as for photons. Nevertheless, the normalised perturbative calculations are in good agreement with π^0 measurements down to $p_T^{\pi^0} \sim 1 - 2$ GeV.

Two conclusions can be drawn from the above. The first one is that any limitation

imposed by the presence of an effective lower scale Q_0 in parton distribution functions and fragmentation functions can be sidestepped by using larger proportionality constant between the factorisation/fragmentation scales and the transverse momentum.

The second conclusion is that perturbative QCD appears to provide a good description of the momentum dependence of hard photons and pions down to $p_T \sim 1 - 1.5$ GeV. On the other hand, the present results suggest that below this momentum, the perturbative QCD calculation overestimates the production of particles. With this warning in mind, it can be said that perturbative QCD can provide an appropriate estimate of prompt photons at low p_T.

It is important to note that the value of for Q should not, in theory, be considered a parameter of the model to be adjusted to provide a better description of measurements. Calculations in perturbative QCD are actual predictions, and their scale dependence are uncertainties of the calculations. The higher the order of the calculation in α_s, the smaller the scale uncertainty.

The pragmatic point of view adopted in this thesis is that prompt photons are needed at low p_T to understand the direct photon excess observed in heavy ion collisions, and the best estimate of prompt photons should be used. If a given choice of scale provides a better description of the available direct photon data in proton-proton collisions, than it is reasonable to assume that using this scale will also provide the best description of low p_T prompt photons in heavy ion collisions.

Appendix B

Effect of shear viscosity on QGP $2 \to 2$ photon emission processes: the "hard" part

In this Appendix, Y^{00} and $\tilde{\mathbf{k}}_i \tilde{\mathbf{k}}_j Y^{ij}$ as defined at the end of Section 6.2.1.1 are evaluated.

B.1 Evaluating Y^{00}

The expression for Y^{00} is straightforward to evaluate using what is already known for the ideal part [31].

$$\begin{aligned} Y^{00}(k/T)[M] &= \int \frac{d^3\tilde{p}_1 d^3\tilde{p}_2 d^3\tilde{p}_3}{\tilde{P}_1^0 \tilde{P}_2^0 \tilde{P}_3^0} \delta^4(\tilde{P}_1 + \tilde{P}_2 - \tilde{P}_3 - \tilde{K}) M n^1 n^2 \left(1 + \sigma_3 n^3\right) \\ &\quad \left[(1 + \sigma_1 n^1)(\tilde{P}_1^0)^2 + (1 + \sigma_2 n^2)(\tilde{P}_2^0)^2 + \sigma_3 n^3 (\tilde{P}_3^0)^2\right] \end{aligned} \tag{B.1}$$

where the following short notations is used:

$$\begin{aligned} n^j &\equiv f_{F/B}^{(0)}(P_j) \\ \sigma_j &\equiv \sigma_{B/F}(P_j) \end{aligned}$$

Moreover, the notation

$$\begin{aligned} f^j &\equiv f_F^{(0)}(P_j) \\ b^j &\equiv f_B^{(0)}(P_j) \end{aligned}$$

is used in everything that follows.

For $M = -t/s$,

$$\begin{aligned} Y^{00}\left[\frac{-t}{s}\right] &= \frac{f(\tilde{k})(2\pi)^2}{2}\int_{\tilde{k}}^{\infty} d\omega \int_{|2\tilde{k}-\omega|}^{\omega} \frac{dq}{q^2}\int_{(\omega-q)/2}^{(\omega+q)/2} d\tilde{p}_1 \frac{f(\tilde{p}_1)b(\omega-\tilde{p}_1)\left[1-f(\omega-\tilde{k})\right]}{\tilde{k}f(\tilde{k})} \\ &\quad \left[q^2-(2\tilde{p}_1-\omega)(2\tilde{k}-\omega)\right] \\ &\quad \left[(1-f(\tilde{p}_1))\tilde{p}_1^2+(1+b(\omega-\tilde{p}_1))(\omega-\tilde{p}_1)^2-f(\omega-\tilde{k})(\omega-\tilde{k})^2\right] \end{aligned} \tag{B.2}$$

For $M = -s/t$ and $M = u/t$,

$$\begin{aligned} Y^{00}_{q>q_*}\left[\frac{-s}{t},\frac{u}{t}\right] &= \frac{f(\tilde{k})(2\pi)^2}{2}\int_{q_*}^{\infty}\frac{dq}{q^2}\int_{-q}^{min(q,2\tilde{k}-q)} d\omega \int_{(\omega+q)/2}^{\infty} d\tilde{p}_2 \\ &\quad \left[\frac{f(\tilde{k}-\omega)b(\tilde{p}_2)\left[1-f(\tilde{p}_2-\omega)\right]}{\tilde{k}f(\tilde{k})}\left[(2\tilde{p}_2-\omega)(2\tilde{k}-\omega)+q^2\right]\right. \\ &\quad \left.\left[(1-f(\tilde{k}-\omega))(\tilde{k}-\omega)^2+(1+b(\tilde{p}_2))(\tilde{p}_2)^2-f(\tilde{p}_2-\omega)(\tilde{p}_2-\omega)^2\right]\right. \\ &\quad +\frac{f(\tilde{k}-\omega)f(\tilde{p}_2)\left[1+b(\tilde{p}_2-\omega)\right]}{\tilde{k}f(\tilde{k})}\left[(2\tilde{p}_2-\omega)(2\tilde{k}-\omega)-q^2\right] \\ &\quad \left.\left[(1-f(\tilde{k}-\omega))(\tilde{k}-\omega)^2+(1-f(\tilde{p}_2))(\tilde{p}_2)^2+b(\tilde{p}_2-\omega)(\tilde{p}_2-\omega)^2\right]\right] \end{aligned} \tag{B.3}$$

B.2 Evaluating $\tilde{\mathbf{k}}_i\tilde{\mathbf{k}}_j Y^{ij}$

The second term to evaluate is:

$$\begin{aligned} \tilde{\mathbf{k}}_i\tilde{\mathbf{k}}_j Y^{ij}[M] &= \int \frac{d^3\tilde{p}_1 d^3\tilde{p}_2 d^3\tilde{p}_3}{\tilde{P}_1^0\tilde{P}_2^0\tilde{P}_3^0}\delta^4(\tilde{P}_1+\tilde{P}_2-\tilde{P}_3-\tilde{K})Mn^1n^2\left(1+\sigma_3 n^3\right) \\ &\quad \left[(1+\sigma_1 n^1)(\tilde{\mathbf{k}}\cdot\tilde{\mathbf{p}}_1)^2+(1+\sigma_2 n^2)(\tilde{\mathbf{k}}\cdot\tilde{\mathbf{p}}_2)^2+\sigma_3 n^3(\tilde{\mathbf{k}}\cdot\tilde{\mathbf{p}}_3)^2\right] \end{aligned} \tag{B.4}$$

Remember that M can be equal to $-t/s$, $-s/t$ and u/t.

B.2.1 First Compton term ($-t/s$)

The starting point is

$$\begin{aligned} \tilde{\mathbf{k}}_i\tilde{\mathbf{k}}_j Y^{ij}\left[\frac{-t}{s}\right] &= \int \frac{d^3\tilde{p}_1 d^3\tilde{p}_2 d^3\tilde{p}_3}{\tilde{P}_1^0\tilde{P}_2^0\tilde{P}_3^0}\delta^4(\tilde{P}_1+\tilde{P}_2-\tilde{P}_3-\tilde{K})\left(\frac{-t}{s}\right)f^1b^2\left(1-f^3\right) \\ &\quad \left[(1-f^1)(\tilde{\mathbf{k}}\cdot\tilde{\mathbf{p}}_1)^2+(1+b^2)(\tilde{\mathbf{k}}\cdot\tilde{\mathbf{p}}_2)^2-f^3(\tilde{\mathbf{k}}\cdot\tilde{\mathbf{p}}_3)^2\right] \end{aligned} \tag{B.5}$$

Introducing the change of variable $\mathbf{q} \equiv \tilde{\mathbf{p}}_1 + \tilde{\mathbf{p}}_2$ and $\omega \equiv \tilde{P}_1^0 + \tilde{P}_2^0$:

$$\begin{aligned}\tilde{\mathbf{k}}_i\tilde{\mathbf{k}}_j Y^{ij}\left[\frac{-t}{s}\right] &= \int d^4Q \int \frac{d^3\tilde{p}_1 d^3\tilde{p}_2 d^3\tilde{p}_3}{\tilde{P}_1^0\tilde{P}_2^0\tilde{P}_3^0}\delta^4(Q-\tilde{P}_3-\tilde{K})\left(\frac{-t}{s}\right) f^1 b^2\left(1-f^3\right) \\ &\quad \left[(1-f^1)(\tilde{\mathbf{k}}\cdot\tilde{\mathbf{p}}_1)^2 + (1+b^2)(\tilde{\mathbf{k}}\cdot\tilde{\mathbf{p}}_2)^2 - f^3(\tilde{\mathbf{k}}\cdot\tilde{\mathbf{p}}_3)^2\right]\delta^4(\tilde{P}_1+\tilde{P}_2-Q)\end{aligned} \tag{B.6}$$

In terms of Q, $\tilde{P}_1$ and $\tilde{K}$,

$$\frac{-t}{s} = \frac{2\tilde{P}_1\cdot\tilde{K}}{Q^2} \tag{B.7}$$

Without integrating, the delta functions can be used to transform the integral. First, expanding the delta functions

$$\begin{aligned}\delta^4(\tilde{P}_1^0+\tilde{P}_2^0-Q) &= \delta(\tilde{p}_1+\tilde{p}_2-\omega)\delta^3(\tilde{\mathbf{p}}_1+\tilde{\mathbf{p}}_2-\mathbf{q}) \\ &= \delta(\tilde{p}_1+|\mathbf{q}-\tilde{\mathbf{p}}_1|-\omega)\delta^3(\tilde{\mathbf{p}}_1+\tilde{\mathbf{p}}_2-\mathbf{q}) \qquad \text{(B.8)} \\ \delta^4(Q-\tilde{P}_3^0-\tilde{K}) &= \delta(\omega-\tilde{p}_3-\tilde{k})\delta^3(\mathbf{q}-\tilde{\mathbf{p}}_3-\tilde{\mathbf{k}}) \\ &= \delta(\omega-|\mathbf{q}-\tilde{\mathbf{k}}|-\tilde{k})\delta^3(\mathbf{q}-\tilde{\mathbf{p}}_3-\tilde{\mathbf{k}}) \qquad \text{(B.9)}\end{aligned}$$

Using these Dirac deltas, b^2 and f^3 can be written

$$b^2 = b(\omega-\tilde{p}_1) \tag{B.10}$$

$$f^3 = f(\omega-\tilde{k}) \tag{B.11}$$

These expressions hold for this entire subsection (and only this subsection; not the next).

Using the $\tilde{\mathbf{p}}_2 \to \mathbf{q}-\tilde{\mathbf{p}}_1$ and $\tilde{\mathbf{p}}_3 \to \mathbf{q}-\tilde{\mathbf{k}}$ replacements permitted by the delta functions, the square bracket becomes:

$$\begin{aligned}&\left[(1-f^1)(\tilde{\mathbf{k}}\cdot\tilde{\mathbf{p}}_1)^2 + (1+b^2)(\tilde{\mathbf{k}}\cdot(\mathbf{q}-\tilde{\mathbf{p}}_1))^2 - f^3(\tilde{\mathbf{k}}\cdot(\mathbf{q}-\tilde{\mathbf{k}}))^2\right] \\ &\qquad = \left[(1-f^1)(\tilde{\mathbf{k}}\cdot\tilde{\mathbf{p}}_1)^2 + (1+b^2)(\tilde{\mathbf{k}}\cdot\mathbf{q}-\tilde{\mathbf{k}}\cdot\tilde{\mathbf{p}}_1)^2 - f^3(\tilde{\mathbf{k}}\cdot\mathbf{q}-\tilde{\mathbf{k}}^2)^2\right]\end{aligned} \tag{B.12}$$

Using the above, the integral can be rewritten, after integration over $\tilde{\mathbf{p}}_2$ and $\tilde{\mathbf{p}}_3$:

$$\begin{aligned}\tilde{\mathbf{k}}_i\tilde{\mathbf{k}}_j Y^{ij}\left[\frac{-t}{s}\right] &= \int d^4Q \int d^3\tilde{p}_1 \frac{\Theta(\omega-\tilde{p}_1\geq 0)\Theta(\omega-\tilde{k}\geq 0)}{\tilde{p}_1(\omega-\tilde{p}_1)(\omega-\tilde{k})}\left(\frac{2\tilde{P}_1\cdot\tilde{K}}{Q^2}\right) f^1 b^2\left(1-f^3\right) \\ &\quad \left[(1-f^1)(\tilde{\mathbf{k}}\cdot\tilde{\mathbf{p}}_1)^2 + (1+b^2)(\tilde{\mathbf{k}}\cdot\mathbf{q}-\tilde{\mathbf{k}}\cdot\tilde{\mathbf{p}}_1)^2 - f^3(\tilde{\mathbf{k}}\cdot\mathbf{q}-\tilde{\mathbf{k}}^2)^2\right] \\ &\quad \delta(\omega-|\mathbf{q}-\tilde{\mathbf{k}}|-\tilde{k})\delta(\tilde{p}_1+|\mathbf{q}-\tilde{\mathbf{p}}_1|-\omega)\end{aligned} \tag{B.13}$$

The last integrals that can be solved analytically are the angular integrals. To do so, the

z-axis of $\tilde{\mathbf{p}}_1$ is aligned along $\mathbf{q}$, and the z-axis of $\mathbf{q}$ along $\tilde{\mathbf{k}}$:

$$\begin{aligned}
\tilde{\mathbf{k}}_i\tilde{\mathbf{k}}_j Y^{ij}\left[\frac{-t}{s}\right] &= \int d\omega dq q^2 \int d\tilde{p}_1 \tilde{p}_1^2 \frac{\Theta(\omega-\tilde{p}_1\geq 0)\Theta(\omega-\tilde{k}\geq 0)}{\tilde{p}_1(\omega-\tilde{p}_1)(\omega-\tilde{k})} \\
&\quad f^1 b^2\left(1-f^3\right)\int_0^{2\pi} d\phi_{qk}\int_0^{\pi} d\theta_{qk}\sin(\theta_{qk})\int_0^{2\pi} d\phi_{qp}\int_0^{\pi} d\theta_{qp}\sin(\theta_{qp}) \\
&\quad \left(\frac{2\tilde{P}_1\cdot\tilde{K}}{Q^2}\right)\delta(\omega-|\mathbf{q}-\tilde{\mathbf{k}}|-\tilde{k})\delta(\tilde{p}_1+|\mathbf{q}-\tilde{\mathbf{p}}_1|-\omega) \\
&\quad \left[(1-f^1)(\tilde{\mathbf{k}}\cdot\tilde{\mathbf{p}}_1)^2+(1+b^2)(\tilde{\mathbf{k}}\cdot\mathbf{q}-\tilde{\mathbf{k}}\cdot\tilde{\mathbf{p}}_1)^2-f^3(\tilde{\mathbf{k}}\cdot\mathbf{q}-\tilde{k}^2)^2\right]
\end{aligned} \tag{B.14}$$

Expanding the remaining delta functions:

$$\begin{aligned}
\delta\left(\omega-|\mathbf{q}-\tilde{\mathbf{k}}|-\tilde{k}\right) &= \delta\left(\omega-\sqrt{q^2-2q\tilde{k}\cos(\theta_{qk})+\tilde{k}^2}-\tilde{k}\right) \\
&= \left|\frac{d}{d\cos(\theta_{qk})}\left(\omega-\sqrt{q^2-2q\tilde{k}\cos(\theta_{qk})+\tilde{k}^2}-\tilde{k}\right)\right|^{-1}_{\cos(\theta_{qk})=\lambda_1} \\
&\quad \times\delta\left(\cos(\theta_{qk})-\lambda_1\right) \\
&= \frac{|\tilde{k}-\omega|}{q\tilde{k}}\delta\left(\cos(\theta_{qk})-\lambda_1\right);\ \lambda_1=\frac{q^2+\tilde{k}^2-(\omega-\tilde{k})^2}{2q\tilde{k}}
\end{aligned} \tag{B.15}$$

Similarly,

$$\delta(\omega-|\mathbf{q}-\tilde{\mathbf{p}}_1|-\tilde{p}_1) = \frac{|\tilde{p}_1-\omega|}{q\tilde{p}_1}\delta(\cos(\theta_{qp})-\lambda_2);\ \lambda_2=\frac{q^2+\tilde{p}_1^2-(\omega-\tilde{p}_1)^2}{2q\tilde{p}_1} \tag{B.16}$$

Using this, every occurrence of $\tilde{\mathbf{k}}\cdot\mathbf{q}$ is replaced by $\tilde{k}q\lambda_1$. Doing this and simplifying further:

$$\begin{aligned}
\tilde{\mathbf{k}}_i\tilde{\mathbf{k}}_j Y^{ij}\left[\frac{-t}{s}\right] &= 2\int d\omega dq\int d\tilde{p}_1\frac{\Theta(\omega-\tilde{p}_1\geq 0)\Theta(\omega-\tilde{k}\geq 0)}{\tilde{k}} \\
&\quad f^1 b^2\left(1-f^3\right)\int_0^{2\pi} d\phi_{qk}\int_0^{\pi} d\theta_{qk}\sin(\theta_{qk})\int_0^{2\pi} d\phi_{qp}\int_0^{\pi} d\theta_{qp}\sin(\theta_{qp}) \\
&\quad \left(\frac{\tilde{p}_1\tilde{k}-\tilde{\mathbf{p}}_1\cdot\tilde{\mathbf{k}}}{Q^2}\right)\delta(\cos(\theta_{qk})-\lambda_1)\delta(\cos(\theta_{qp})-\lambda_2) \\
&\quad \left[(1-f^1)(\tilde{\mathbf{k}}\cdot\tilde{\mathbf{p}}_1)^2+(1+b^2)(\tilde{k}q\lambda_1-\tilde{\mathbf{k}}\cdot\tilde{\mathbf{p}}_1)^2-f^3(\tilde{k}q\lambda_1-\tilde{k}^2)^2\right]
\end{aligned} \tag{B.17}$$

Defining $\tilde{\mathbf{k}} \cdot \tilde{\mathbf{p}}_1 = \tilde{k}\tilde{p}_1 \cos(\theta_{kp})$, the square bracket is written in an expansion in $\cos(\theta_{kp})$:

$$\begin{aligned}(1-f^1)(\tilde{k}\tilde{p}_1\cos(\theta_{kp}))^2 + (1+b^2)(\tilde{k}q\lambda_1 - \tilde{k}\tilde{p}_1\cos(\theta_{kp}))^2 - f^3(\tilde{k}q\lambda_1 - \tilde{k}^2)^2 \\ = (1-f^1)\tilde{k}^2\tilde{p}_1^2\cos(\theta_{kp})^2 + (1+b^2)(\tilde{k}q\lambda_1)^2 - 2(1+b^2)(\tilde{k}^2 q\tilde{p}_1\lambda_1\cos(\theta_{kp})) \\ + (1+b^2)\tilde{k}^2\tilde{p}_1^2\cos(\theta_{kp})^2 - f^3(\tilde{k}q\lambda_1 - \tilde{k}^2)^2 = \sum_{n=0}^{2}\alpha_n\cos(\theta_{kp})^n\end{aligned}$$

where

$$\begin{aligned}\alpha_0 &= (1+b^2)\tilde{k}^2q^2\lambda_1^2 - f^3(\tilde{k}q\lambda_1 - \tilde{k}^2)^2 && \text{(B.18)}\\ \alpha_1 &= -2(1+b^2)(\tilde{k}^2 q\tilde{p}_1\lambda_1) && \text{(B.19)}\\ \alpha_2 &= (1-f^1)\tilde{k}^2\tilde{p}_1^2 + (1+b^2)\tilde{k}^2\tilde{p}_1^2 && \text{(B.20)}\end{aligned}$$

The term $\cos(\theta_{kp})$ can be written

$$\begin{aligned}\cos(\theta_{kp}) &= \sin(\theta_{qp})\sin(\theta_{qk})\cos(\phi_{qp}-\phi_{qk}) + \cos(\theta_{qp})\cos(\theta_{qk}) \\ &= \epsilon_1\sqrt{1-\lambda_1^2}\epsilon_2\sqrt{1-\lambda_2^2}\cos(\phi_{qp}-\phi_{qk}) + \lambda_1\lambda_2 && \text{(B.21)}\end{aligned}$$

where $\epsilon_i = \pm 1$ depending on the argument of the corresponding $\cos(\theta)$.

Replacing the square bracket by $\sum_{n=0}^{2}\alpha_n\cos(\theta_{kp})^n$ and replacing the integral over the delta functions by their values (which is $\Theta(\lambda_i^2 \leq 1)$):

$$\begin{aligned}\tilde{\mathbf{k}}_i\tilde{\mathbf{k}}_j Y^{ij}\left[\frac{-t}{s}\right] &= 2\int d\omega dq \int d\tilde{p}_1 \frac{\Theta(\omega-\tilde{p}_1\geq 0)\Theta(\omega-\tilde{k}\geq 0)}{\tilde{k}} f^1 b^2\left(1-f^3\right)\frac{\tilde{p}_1\tilde{k}}{Q^2} \\ &\quad \Theta(\lambda_1^2\leq 1)\Theta(\lambda_2^2\leq 1) \\ &\quad \int_0^{2\pi}d\phi_{qk}\int_0^{2\pi}d\phi_{qp}\left(\sum_{n=0}^{2}\alpha_n\cos(\theta_{kp})^n - \sum_{n=0}^{2}\alpha_n\cos(\theta_{kp})^{n+1}\right) && \text{(B.22)}\end{aligned}$$

The integrals over $\cos(\theta_{kp})^n$ can be done analytically. Defining I_n as

$$I_n(\lambda_1,\lambda_2) = \int_0^{2\pi}d\phi_{qk}\int_0^{2\pi}d\phi_{qp}\cos(\theta_{kp})^n \qquad \text{(B.23)}$$

$\tilde{\mathbf{k}}_i\tilde{\mathbf{k}}_j Y^{ij}\left[\frac{-t}{s}\right]$ can finally be written

$$\begin{aligned}\tilde{\mathbf{k}}_i\tilde{\mathbf{k}}_j Y^{ij}\left[\frac{-t}{s}\right] &= 2\int d\omega dq \int d\tilde{p}_1 \frac{\Theta(\omega-\tilde{p}_1\geq 0)\Theta(\omega-\tilde{k}\geq 0)}{\tilde{k}} f^1 b^2\left(1-f^3\right)\frac{\tilde{p}_1\tilde{k}}{Q^2} \\ &\quad \Theta(\lambda_1^2\leq 1)\Theta(\lambda_2^2\leq 1)\sum_{n=0}^{2}\alpha_n(I_n - I_{n+1}) && \text{(B.24)}\end{aligned}$$

The Θ functions are the same as in the ideal case, and thus yield the same limits on the integrals:

$$\tilde{\mathbf{k}}_i\tilde{\mathbf{k}}_j Y^{ij}\left[\frac{-t}{s}\right] = 2\int_{\tilde{k}}^{\infty} d\omega \int_{|2\tilde{k}-\omega|}^{\omega} dq \int_{\frac{\omega-q}{2}}^{\frac{\omega+q}{2}} d\tilde{p}_1 \frac{f^1 b^2\,(1-f^3)\,\tilde{p}_1}{(\omega^2-q^2)} \sum_{n=0}^{2} \alpha_n (I_n - I_{n+1}) \tag{B.25}$$

For $n = 0$ to 3, I_n is

$$I_0 = (2\pi)^2 \tag{B.26}$$

$$I_1 = (2\pi)^2 \lambda_1 \lambda_2 \tag{B.27}$$

$$I_2 = \frac{(2\pi)^2}{2}\left(2\lambda_1^2\lambda_2^2 + (\lambda_1^2-1)(\lambda_2^2-1)\right) \tag{B.28}$$

$$I_3 = \frac{(2\pi)^2}{2}\lambda_1\lambda_2\left(2\lambda_1^2\lambda_2^2 + 3(\lambda_1^2-1)(\lambda_2^2-1)\right) \tag{B.29}$$

B.2.2 Second Compton term and annihilation

The two remaining terms ($-s/t$ and u/t) share part of the derivation. Consequently as much as possible of the derivation is made before replacing the value of the squared matrix element M. This time the change of variable used is $\mathbf{q} \equiv \tilde{\mathbf{k}} - \tilde{\mathbf{p}}_1$ and $\omega \equiv \tilde{K}^0 - \tilde{P}_1^0$. The cut-off $q > q_*$ is imposed on the Q integral.

$$\begin{aligned}\tilde{\mathbf{k}}_i\tilde{\mathbf{k}}_j Y^{ij}[M] = &\int d^4Q \frac{d^3\tilde{p}_1 d^3\tilde{p}_2 d^3\tilde{p}_3}{\tilde{P}_1^0\tilde{P}_2^0\tilde{P}_3^0}\delta^4(\tilde{P}_2-\tilde{P}_3-Q) M n^1 n^2\left(1+\sigma_3 n^3\right) \\ &\left[(1+\sigma_1 n^1)(\tilde{\mathbf{k}}\cdot\tilde{\mathbf{p}}_1)^2 + (1+\sigma_2 n^2)(\tilde{\mathbf{k}}\cdot\tilde{\mathbf{p}}_2)^2 + \sigma_3 n^3(\tilde{\mathbf{k}}\cdot\tilde{\mathbf{p}}_3)^2\right]\delta^4(\tilde{K}-\tilde{P}_1-Q)\end{aligned} \tag{B.30}$$

Note that the values of the σ_i's are different for Compton scattering ($-s/t$) and quark-antiquark annihilation (u/t).

The momentum that are integrated over are $\tilde{p}_1$ and $\tilde{p}_3$. Without integrating, these variables are replaced in the integrand using the delta functions:

$$\begin{aligned}\tilde{\mathbf{k}}_i\tilde{\mathbf{k}}_j Y^{ij}[M] = &\int d^4Q \frac{d^3\tilde{p}_1 d^3\tilde{p}_2 d^3\tilde{p}_3}{\tilde{P}_1^0\tilde{P}_2^0\tilde{P}_3^0}\delta^4(\tilde{P}_2-\tilde{P}_3-Q) M n^1 n^2\left(1+\sigma_3 n^3\right) \\ &\left[(1+\sigma_1 n^1)(\tilde{\mathbf{k}}\cdot(\tilde{\mathbf{k}}-\mathbf{q}))^2 + (1+\sigma_2 n^2)(\tilde{\mathbf{k}}\cdot\tilde{\mathbf{p}}_2)^2 + \sigma_3 n^3(\tilde{\mathbf{k}}\cdot(\tilde{\mathbf{p}}_2-\mathbf{q}))^2\right] \\ &\delta^4(\tilde{K}-\tilde{P}_1-Q)\end{aligned} \tag{B.31}$$

with

$$n^1 = n(\tilde{k} - \omega) \tag{B.32}$$
$$n^2 = n(\tilde{p}_2) \tag{B.33}$$
$$n^3 = n(\tilde{p}_2 - \omega) \tag{B.34}$$

In terms of Q and $\tilde{P}_2$, M is either

$$\frac{-s}{t} = \frac{-(\tilde{P}_1 + \tilde{P}_2)^2}{(\tilde{P}_1 - \tilde{K})^2} = \frac{-2\tilde{P}_1 \cdot \tilde{P}_2}{Q^2} = \frac{-2(\tilde{P}_2 \cdot \tilde{K} - \tilde{P}_2 \cdot Q)}{Q^2} \tag{B.35}$$

or

$$\frac{u}{t} = \frac{(\tilde{P}_2 - \tilde{K})^2}{(\tilde{P}_1 - \tilde{K})^2} = \frac{-2\tilde{P}_2 \cdot \tilde{K}}{Q^2} \tag{B.36}$$

Expanding the Dirac deltas:

$$\begin{aligned} \delta^4(\tilde{P}_2 - \tilde{P}_3 - Q) &= \delta(\tilde{p}_2 - \tilde{p}_3 - \omega)\delta^3(\tilde{\mathbf{p}}_2 - \tilde{\mathbf{p}}_3 - \mathbf{q}) \\ &= \delta(\tilde{p}_2 - |\tilde{\mathbf{p}}_2 - \mathbf{q}| - \omega)\delta^3(\tilde{\mathbf{p}}_2 - \tilde{\mathbf{p}}_3 - \mathbf{q}) \end{aligned} \tag{B.37}$$

and

$$\begin{aligned} \delta^4(\tilde{K} - \tilde{P}_1 - Q) &= \delta(\tilde{k} - \tilde{p}_1 - \omega)\delta^3(\tilde{\mathbf{k}} - \tilde{\mathbf{p}}_1 - \mathbf{q}) \\ &= \delta(\tilde{k} - |\tilde{\mathbf{k}} - \mathbf{q}| - \omega)\delta^3(\tilde{\mathbf{k}} - \tilde{\mathbf{p}}_1 - \mathbf{q}) \end{aligned} \tag{B.38}$$

Remembering that

$$\delta(a \pm |\mathbf{b} - \mathbf{c}|) = \frac{|a|}{bc}\delta(\cos(\theta_{bc}) - \lambda);\ \lambda = \frac{b^2 + c^2 - a^2}{2bc} \tag{B.39}$$

for an arbitrary non-zero scalar a and vectors $\mathbf{b}$ and $\mathbf{c}$, θ_{bc} being the angle between those two vectors, the delta functions can be expanded:

$$\delta(\tilde{p}_2 - |\tilde{\mathbf{p}}_2 - \mathbf{q}| - \omega) = \frac{|\tilde{p}_2 - \omega|}{\tilde{p}_2 q}\delta(\cos(\theta_{qp}) - \lambda_1);\ \lambda_1 = \frac{\tilde{p}_2^2 + q^2 - (\tilde{p}_2 - \omega)^2}{2\tilde{p}_2 q} \tag{B.40}$$

and

$$\delta(\tilde{k} - |\tilde{\mathbf{k}} - \mathbf{q}| - \omega) = \frac{|\tilde{k} - \omega|}{\tilde{k} q}\delta(\cos(\theta_{qk}) - \lambda_2);\ \lambda_2 = \frac{\tilde{k}^2 + q^2 - (\tilde{k} - \omega)^2}{2\tilde{k} q} \tag{B.41}$$

The above expressions can be used to write:

$$Q \cdot \tilde{P}_2 = \omega \tilde{p}_2^0 - q\tilde{p}_2 \cos(\theta_{qp}) = \omega\tilde{p}_2 - q\tilde{p}_2\lambda_1 \quad \text{(B.42)}$$

$$\tilde{\mathbf{k}} \cdot \mathbf{q} = \tilde{k}q\cos(\theta_{qk}) = \tilde{k}q\lambda_2 \quad \text{(B.43)}$$

At this point, nothing depends on $\tilde{p}_1$ and $\tilde{p}_3$ anymore, so the integration over these variables is trivial, and yields only two theta functions: $\Theta(\tilde{k} - \omega \geq 0)$ and $\Theta(\tilde{p}_2 - \omega \geq 0)$:

$$\begin{aligned}\tilde{\mathbf{k}}_i\tilde{\mathbf{k}}_j Y^{ij}[M] = & \int d^4Q \frac{d^3\tilde{p}_2}{(\tilde{k}-\omega)\tilde{p}_2(\tilde{p}_2-\omega)} Mn^1n^2\left(1+\sigma_3 n^3\right)\Theta(\tilde{k}-\omega\geq 0)\Theta(\tilde{p}_2-\omega\geq 0) \\ & \left[(1+\sigma_1 n^1)(\tilde{k}^2-\tilde{k}q\lambda_2)^2 + (1+\sigma_2 n^2)(\tilde{\mathbf{k}}\cdot\tilde{\mathbf{p}}_2)^2 + \sigma_3 n^3(\tilde{\mathbf{k}}\cdot\tilde{\mathbf{p}}_2 - \tilde{k}q\lambda_2)^2\right] \\ & \frac{|\tilde{p}_2-\omega|}{\tilde{p}_2 q}\delta(\cos(\theta_{qp})-\lambda_1)\frac{|\tilde{k}-\omega|}{\tilde{k}q}\delta(\cos(\theta_{qk})-\lambda_2) \quad \text{(B.44)}\end{aligned}$$

Writing $\tilde{\mathbf{k}} \cdot \tilde{\mathbf{p}}_2 = \tilde{k}\tilde{p}_2\cos(\theta_{kp})$,

$$\tilde{k}\cdot\tilde{p}_2 = \tilde{k}\tilde{p}_2(1-\cos(\theta_{kp})) \quad \text{(B.45)}$$

In terms of $\cos(\theta_{qp})$ and $\cos(\theta_{qk})$, $\cos(\theta_{kp})$ is

$$\begin{aligned}\cos(\theta_{kp}) &= \sin(\theta_{qp})\sin(\theta_{qk})\left[\sin(\phi_{qp})\sin(\phi_{qk}) + \cos(\phi_{qp})\cos(\phi_{qk})\right] + \cos(\theta_{qp})\cos(\theta_{qk}) \\ &= \epsilon_1\sqrt{1-\lambda_1^2}\epsilon_2\sqrt{1-\lambda_2^2}\left[\sin(\phi_{qp})\sin(\phi_{qk}) + \cos(\phi_{qp})\cos(\phi_{qk})\right] + \lambda_1\lambda_2 \quad \text{(B.46)}\end{aligned}$$

where $\epsilon_i = \pm 1$ depending on value of θ when the relation $\sin(\theta) = \pm\sqrt{1-\cos(\theta)^2}$ is used.

Rewriting M according to the above transformations:

$$\frac{-s}{t} = \frac{2(\omega\tilde{p}_2 - q\tilde{p}_2\lambda_1)}{Q^2} + \frac{u}{t} \quad \text{(B.47)}$$

and

$$\frac{u}{t} = \frac{-2\tilde{k}\tilde{p}_2(1-\cos(\theta_{kp}))}{Q^2} \quad \text{(B.48)}$$

Every θ_{qk} and θ_{qp} dependence have been removed, besides the delta functions. It is thus possible to integrate over these two variables to get rid of the two last delta functions. After these integrations and further simplifications:

$$\begin{aligned}\tilde{\mathbf{k}}_i\tilde{\mathbf{k}}_j Y^{ij}[M] = & \int d\omega dq \frac{d\tilde{p}_2}{\tilde{k}} n^1n^2\left(1+\sigma_3 n^3\right)\Theta(\tilde{k}-\omega\geq 0)\Theta(\tilde{p}_2-\omega\geq 0) \quad \text{(B.49)} \\ & \Theta(\lambda_1^2\leq 1)\Theta(\lambda_2^2\leq 1)\int_0^{2\pi} d\phi_{qp}\int_0^{2\pi} d\phi_{qk} M \\ & \left[(1+\sigma_1 n^1)(\tilde{k}^2-\tilde{k}q\lambda_2)^2 + (1+\sigma_2 n^2)(\tilde{\mathbf{k}}\cdot\tilde{\mathbf{p}}_2)^2 + \sigma_3 n^3(\tilde{\mathbf{k}}\cdot\tilde{\mathbf{p}}_2 - \tilde{k}q\lambda_2)^2\right]\end{aligned}$$

The theta functions are the same as in the ideal case and impose the following limits on the integrals: $-q < \omega < min(q, 2k-q)$ and $(q+\omega)/2 < \tilde{p}_2 < \infty$, meaning that

$$\begin{aligned}\tilde{\mathbf{k}}_i\tilde{\mathbf{k}}_j Y^{ij}[M] &= \int_{q_*}^{\infty} dq \int_q^{min(q,2k-q)} d\omega \int_{(q+\omega)/2}^{\infty} \frac{d\tilde{p}_2}{\tilde{k}} n^1 n^2 \left(1+\sigma_3 n^3\right) \\ &\int_0^{2\pi} d\phi_{qp} \int_0^{2\pi} d\phi_{qk} M \Big[(1+\sigma_1 n^1)(\tilde{k}^2 - \tilde{k}q\lambda_2)^2 \\ &+(1+\sigma_2 n^2)(\tilde{\mathbf{k}}\cdot\tilde{\mathbf{p}}_2)^2 + \sigma_3 n^3(\tilde{\mathbf{k}}\cdot\tilde{\mathbf{p}}_2 - \tilde{k}q\lambda_2)^2\Big] \end{aligned} \tag{B.50}$$

The integrand of the ϕ integrals is written as $\sum_{n=0}^{2}\beta_n\cos(\theta_{kp})$. Expanding the integrand:

$$\begin{aligned}(1+\sigma_1 n^1)(\tilde{k}^2 - \tilde{k}q\lambda_2)^2 + (1+\sigma_2 n^2)(\tilde{k}\tilde{p}_2\cos(\theta_{kp}))^2 + \sigma_3 n^3(\tilde{k}\tilde{p}_2)^2\cos(\theta_{kp})^2 \\ - 2\sigma_3 n^3(\tilde{k}^2\tilde{p}_2 q\lambda_2)\cos(\theta_{kp}) + \sigma_3 n^3(\tilde{k}q\lambda_2)^2 \end{aligned} \tag{B.51}$$

implies that

$$\begin{aligned}\beta_0 &= (1+\sigma_1 n^1)(\tilde{k}^2 - \tilde{k}q\lambda_2)^2 + \sigma_3 n^3(\tilde{k}q\lambda_2)^2 \\ \beta_1 &= -2\sigma_3 n^3(\tilde{k}^2\tilde{p}_2 q\lambda_2) \\ \beta_2 &= (1+\sigma_2 n^2)(\tilde{k}\tilde{p}_2)^2 + \sigma_3 n^3(\tilde{k}\tilde{p}_2)^2\end{aligned}$$

Using again the definition

$$I_n = \int_0^{2\pi} d\phi_{qp} \int_0^{2\pi} d\phi_{qk}\cos(\theta_{kp})^n \tag{B.52}$$

$\tilde{\mathbf{k}}_i\tilde{\mathbf{k}}_j Y^{ij}\left[\frac{-s}{t}\right]$ can be written

$$\begin{aligned}\tilde{\mathbf{k}}_i\tilde{\mathbf{k}}_j Y^{ij}\left[\frac{-s}{t}\right] &= \int_{q_*}^{\infty} dq \int_q^{min(q,2k-q)} d\omega \int_{(q+\omega)/2}^{\infty} \frac{d\tilde{p}_2}{\tilde{k}} n^1 n^2 \left(1+\sigma_3 n^3\right) \\ &\frac{1}{Q^2}\left[2(\omega\tilde{p}_2 - q\tilde{p}_2\lambda_1)\sum_{n=0}^{2}\beta_n^C I_n - 2\tilde{k}\tilde{p}_2\sum_{n=0}^{2}\beta_n^C(I_n - I_{n+1})\right]\end{aligned} \tag{B.53}$$

with

$$\beta_0^C = (1-f^1)(\tilde{k}^2 - \tilde{k}q\lambda_2)^2 - f^3(\tilde{k}q\lambda_2)^2 \tag{B.54}$$

$$\beta_1^C = 2f^3(\tilde{k}^2\tilde{p}_2 q\lambda_2) \tag{B.55}$$

$$\beta_2^C = (1+b^2)(\tilde{k}\tilde{p}_2)^2 - f^3(\tilde{k}\tilde{p}_2)^2 \tag{B.56}$$

and

$$\tilde{\mathbf{k}}_i\tilde{\mathbf{k}}_j Y^{ij}\left[\frac{u}{t}\right] = \int_{q_*}^{\infty} dq \int_{q}^{min(q,2k-q)} d\omega \int_{(q+\omega)/2}^{\infty} \frac{d\tilde{p}_2}{\tilde{k}} n^1 n^2 \left(1+\sigma_3 n^3\right) \left(\frac{-2\tilde{k}\tilde{p}_2}{Q^2}\sum_{n=0}^{2}\beta_n^A (I_n - I_{n+1})\right) \tag{B.57}$$

with

$$\beta_0^A = (1-f^1)(\tilde{k}^2 - \tilde{k}q\lambda_2)^2 + b^3(\tilde{k}q\lambda_2)^2 \tag{B.58}$$

$$\beta_1^A = -2b^3(\tilde{k}^2\tilde{p}_2 q\lambda_2) \tag{B.59}$$

$$\beta_2^A = (1-f^2)(\tilde{k}\tilde{p}_2)^2 + b^3(\tilde{k}\tilde{p}_2)^2 \tag{B.60}$$

Appendix C

Effect of shear viscosity on QGP $2 \to 2$ photon emission processes: the "soft" part

C.1 Simplifying $i\Pi^{\mu}_{12\mu}(K)$

The assumption is made that $f_{F/B}(-K) = f_{F/B}(K)$. The first step in simplifying $i\Pi^{\mu}_{12\mu}(K)$ is to make explicit how the various propagators and self-energies entering the calculations tranform under $K \to -K$.

C.1.1 Useful symmetry properties

First note that

$$S_{12/21}(-K) = -S_{21/12}(K) \tag{C.1}$$

$$\Delta_{12/21}(-K) = \Delta_{21/12}(K) \tag{C.2}$$

Then see that

$$\Sigma_{12/21}(-P) \;\; = \;\; -\Sigma_{21/12}(P) \tag{C.3}$$

Consequently the self-energy transforms as

$$\Sigma^{\mu}_{R}(-P) = -\Sigma^{\mu}_{A}(P) \tag{C.4}$$

which implies that

$$S^{D}_{R}(-P) = -S^{D}_{A}(P) \tag{C.5}$$

Then

$$\begin{aligned} S^D_{12/21}(-P) &= S^D_R(-P)\Sigma_{12/21}(-P)S^D_A(-P) = -S^D_A(P)\Sigma_{21/12}(P)S^D_R(P) \\ &= (S^D_R(P)\Sigma_{21/12}(P)S^D_A(P))^* = (S^D_{21/12}(P))^* \end{aligned} \tag{C.6}$$

where the relation $(\Sigma_{21/12}(P))^* = -\Sigma_{21/12}(P)$ and $(S^D_R(P))^* = S^D_A(P)$ where used.

Since $S_{12/21}(K)$ is proportional to a single gamma matrix,

$$\gamma^\mu S_{12/21}(K)\gamma_\mu = -2S_{12/21}(K) \tag{C.7}$$

C.1.2 KMS-like relations in the hard thermal loop limit

In the following, the KMS-like relation $\Sigma_{12} = -\Sigma_{21} = -i\mathrm{Im}[\Sigma_R]$ is derived for a general ansatz of momentum anisotropy that respects $f_{F/B}(-K) = f_{F/B}(K)$.

The starting point is

$$\Sigma_{12}(P) = 2ig_s^2 C_F \int \frac{d^4W}{(2\pi)^4} S_{12}(W)\Delta_{12}(P-W) \tag{C.8}$$

with the assumption that P is soft ($\sim g_sT$) and W is hard ($\sim T$), the so-called hard-loop limit.

$$\begin{aligned} \Sigma^\mu_{12}(P) &= 2ig_s^2 C_F \int \frac{d^4W}{(2\pi)^4} W^\mu 2\pi i\delta(W^2)[-\theta(-W^0) + f_F(W)] \\ &\quad (-2\pi)i\delta((P-W)^2)[\theta(-(P^0-W^0)) + f_B(P-W)] \\ &\approx 2ig_s^2 C_F \int \frac{d^4W}{(2\pi)^2} W^\mu \delta((W^0)^2 - w^2)[-\theta(-W^0) + f_F(W)] \\ &\quad \delta(2P\cdot W)[\theta(-(P^0-W^0)) + f_B(P-W)] \\ &\approx ig_s^2 C_F \left[\int \frac{d^4W}{(2\pi)^2} W^\mu \delta(W^0 - w) f_F(W)\delta(P^0W^0 - \mathbf{p}\cdot\mathbf{w})[1 + f_B(W)]\right. \\ &\quad \left. + \int \frac{d^4W}{(2\pi)^2} W^\mu \delta(W^0 + w)[-1 + f_F(W)]\delta(P^0W^0 - \mathbf{p}\cdot\mathbf{w}) f_B(W)\right] \end{aligned} \tag{C.9}$$

The following relation was used:

$$\delta((W^0)^2 - w^2) = \frac{\delta(W^0 - w) + \delta(W^0 + w)}{2w} \tag{C.10}$$

The last lines of the above equation do not change under the transformation $P \to -P$. Thus, in the hard loop limit, $\Sigma_{12/21}(P) = \Sigma_{12/21}(-P)$.

It is already known that $\Sigma_{12/21}(-P) = -\Sigma_{21/12}(P)$. Thus, in the hard loop limit

$\Sigma_{12/21}(P) = -\Sigma_{21/12}(P)$ hold for any distribution $f_{F/B}(W)$ that has the property $f_{F/B}(W) = f_{F/B}(-W)$.

The next step is to show that $\Sigma_{12} = -i\text{Im}[\Sigma_R]$. By changing $W \to -W$ in the last term, it can be combined with the first.

$$\begin{aligned}\Sigma^{\mu}_{12}(P) &= \frac{ig_s^2 C_F}{2}\int \frac{d^4W}{(2\pi)^2}\frac{W^\mu}{w}\delta(W^0 - w)\delta(P^0W^0 - \mathbf{p}\cdot\mathbf{w}) \\ &\quad [f_F(W)[1 + f_B(W)] - [-1 + f_F(W)]f_B(W)] \\ &= \frac{ig_s^2 C_F}{2}\int \frac{d^4W}{(2\pi)^2}\frac{W^\mu}{w}\delta(W^0 - w)\delta(P^0W^0 - \mathbf{p}\cdot\mathbf{w})\,[f_F(W) + f_B(W)]\end{aligned}$$

Delta function $\delta(W^0 - w)$ simply means that w is on-shell:

$$\Sigma^{\mu}_{12}(P) = i\pi g_s^2 C_F \int \frac{d^3w}{(2\pi)^3}\frac{W^\mu}{w^2}\delta(P^0 - \mathbf{p}\cdot\hat{\mathbf{w}})\,[f_F(W) + f_B(W)]$$

Extracting a factor of T from W ($W \equiv VT$), $\Sigma^{\mu}_{12}(P)$ becomes

$$\Sigma^{\mu}_{12}(P) = i\pi g_s^2 C_F T^2 \int \frac{d^3v}{(2\pi)^3}\frac{V^\mu}{v^2}\delta(P^0 - \mathbf{p}\cdot\hat{\mathbf{v}})\,[f_F(V) + f_B(V)]$$

On the other hand, $-i\text{Im}[\Sigma_R]$ is given by

$$-i\text{Im}[\Sigma_R](P) = \frac{-iC_F g_s^2 T^2}{4}\int \frac{d^3\mathbf{v}}{(2\pi)^3}\frac{4(f_F(V) + f_B(V))}{v}V^\mu \text{Im}\left[\frac{1}{V\cdot P + i\epsilon}\right] \tag{C.11}$$

Writing $V\cdot P + i\epsilon = v(\hat{V}\cdot P + i\epsilon')$, the imaginary part is then

$$\text{Im}\left[\frac{1}{\hat{V}\cdot P + i\epsilon'}\right] = \frac{-\epsilon'}{(\hat{V}\cdot P)^2 + \epsilon'^2} \tag{C.12}$$

In the limit $\epsilon' \to 0$,

$$\lim_{\epsilon'\to 0}\frac{-\epsilon'}{(\hat{V}\cdot P)^2 + \epsilon'^2} = -\pi\delta(\hat{V}\cdot P) \tag{C.13}$$

Then

$$-i\text{Im}[\Sigma_R(P)] = i\pi C_F g_s^2 T^2 \int \frac{d^3v}{(2\pi)^3}\frac{(f_F(V) + f_B(V))}{v}V^\mu\delta(\hat{V}\cdot P) \tag{C.14}$$

Consequently $\Sigma^{\mu}_{12}(P) = -i\text{Im}[\Sigma_R(P)]$.

C.1.3 Final simplifications

Using the properties of the previous section, $i\Pi_{12}{}^{\mu}{}_{\mu}(K)$ can be rewritten as

$$-i\Pi_{12}{}^{\mu}{}_{\mu}(K) = -2e^2 \sum_q q_s^2 N_c \int \frac{d^4Q}{(2\pi)^4} \mathrm{Tr}[S_{12}^D(Q) S_{21}(Q-K) + S_{21}^D(Q) S_{12}(Q+K)]$$

For convenience, the following definition is made

$$-i\Pi_{12}{}^{\mu}{}_{\mu}(K) \equiv \frac{-2e^2 \sum_q q_s^2 N_c}{(2\pi)^4} I(K) \tag{C.15}$$

with

$$I(K) = \int d^4Q \mathrm{Tr}[S_{12}^D(Q) S_{21}(Q-K) + S_{21}^D(Q) S_{12}(Q+K)]$$

Inverting Q in the last term of the integrand of I(K), we get

$$\begin{aligned} I &= \int d^4Q \mathrm{Tr}[S_{12}^D(Q) S_{21}(Q-K) + S_{21}^D(-Q) S_{12}(-Q+K)] \\ &= \int d^4Q \mathrm{Tr}[S_{12}^D(Q) S_{21}(Q-K) - (S_{12}^D(Q))^* S_{21}(Q-K)] \\ &= \int d^4Q \mathrm{Tr}[2iIm[S_{12}^D(Q)] S_{21}(Q-K)] \\ &= -4\pi \int d^4Q \delta((Q-K)^2)[-\theta((Q^0-K^0)) + f_F(Q-K)] \mathrm{Tr}[Im[S_{12}^D(Q)](\not{Q} - \not{K})] \end{aligned}$$

The argument that $K \sim T \gg Q \sim gT$ was used to get rid of the theta functions and to replace $Q-K$ by $-K$ where possible.

$$I = 2f_F(K)\pi \int d^4Q \delta(K \cdot Q) \mathrm{Tr}[\not{K} Im[S_{12}^D(Q)]] \tag{C.16}$$

Using $\Sigma_{12}(Q) = -iIm[\Sigma_R(Q)]$, then

$$S_{12/21}^D(Q) = -iS_R^D(Q) Im[\Sigma_R(Q)] S_A^D(Q) \tag{C.17}$$

Then I(K) is

$$I(K) = 2\pi f_F(K) \int d^4Q \delta(K \cdot Q) \mathrm{Tr}[\not{K} Im[-iS_R^D(P) Im[\Sigma_R(Q)] S_A^D(P)]]$$

A gamma matrix can be extracted from both $S_R^D(P)$ and $\Sigma_{12}(P)$:

$$\mathrm{Tr}[\gamma^\mu \gamma^\nu \gamma^\sigma \gamma^\lambda] = 4(g^{\mu\nu} g^{\sigma\lambda} - g^{\mu\sigma} g^{\nu\lambda} + g^{\mu\lambda} g^{\nu\sigma}) \tag{C.18}$$

Then I(K) is

$$\begin{aligned} I(K) &= 8\pi f_F(K)\int d^4Q\delta(K\cdot Q)[Im[-iK\cdot S_R^D(Q)Im[\Sigma_R(Q)]\cdot S_A^D(Q)] \\ &\quad +K\cdot Im[\Sigma_R(Q)]S_R^D(Q)\cdot S_A^D(Q)+Im[-iK\cdot S_A^D(Q)S_R^D(Q)\cdot Im[\Sigma_R(Q)]]] \end{aligned}$$

Combining the first and last terms:

$$\begin{aligned} I(K) &= 8\pi f_F(K)\int d^4Q\delta(K\cdot Q)[-2Re[K\cdot S_R^D(Q)Im[\Sigma_R(Q)]\cdot S_A^D(Q)] \\ &\quad +K\cdot Im[\Sigma_R(Q)]S_R^D(Q)\cdot S_A^D(Q)] \end{aligned}$$

By expanding $S_{R/A}^D(Q)$ and using the property that $Q_\mu\Sigma_R^{D\mu}(Q)$ is real, the proof can be completed:

$$\begin{aligned} I(K) &= 8\pi f_F(K)\int d^4Q\delta(K\cdot Q)\left[-2\mathrm{Re}\left[K\cdot\frac{(Q-\Sigma_R(Q))}{(Q-\Sigma_R(Q))^2}\mathrm{Im}\left[\Sigma_R(Q)\right]\cdot\frac{(Q-\Sigma_R^*(Q))}{(Q-\Sigma_R^*(Q))^2}\right]\right. \\ &\quad \left.+K\cdot\mathrm{Im}\left[\Sigma_R(Q)\frac{(Q-\Sigma_R(Q))}{(Q-\Sigma_R(Q))^2}\cdot\frac{(Q-\Sigma_R^*(Q))}{(Q-\Sigma_R^*(Q))^2}\right]\right] \\ &= 8\pi f_F(K)\int d^4Q\delta(K\cdot Q)\left[-2\mathrm{Re}\left[\frac{K\cdot\Sigma_R(Q)}{(Q-\Sigma_R(Q))^2}\frac{[\Sigma_R(Q)-\Sigma_R^*(Q)]}{2i}\cdot\frac{(\Sigma_R^*(Q))}{(Q-\Sigma_R^*(Q))^2}\right]\right. \\ &\quad \left.+\mathrm{Im}\left[\frac{K\cdot\Sigma_R(Q)}{(Q-\Sigma_R(Q))^2}\frac{(Q-\Sigma_R(Q))\cdot(Q-\Sigma_R^*(Q))}{(Q-\Sigma_R^*(Q))^2}\right]\right] \\ &= 8\pi f_F(K)\int d^4Q\delta(K\cdot Q)\left[-\mathrm{Im}\left[-K\cdot S_R^D(Q)\frac{\Sigma_R(Q)\cdot\Sigma_R^*(Q)-\Sigma_R^*(Q)^2}{(Q-\Sigma_R^*(Q))^2}\right]\right. \\ &\quad \left.+\mathrm{Im}\left[-K\cdot S_R^D(Q)\frac{(Q-\Sigma_R(Q))\cdot(Q-\Sigma_R^*(Q))}{(Q-\Sigma_R^*(Q))^2}\right]\right] \end{aligned}$$

Noting that

$$\begin{aligned} &-\Sigma_R(Q)\cdot\Sigma_R^*(Q)+\Sigma_R^*(Q)^2+(Q-\Sigma_R(Q))\cdot(Q-\Sigma_R^*(Q)) \\ &\quad =-\Sigma_R(Q)\cdot\Sigma_R^*(Q)+\Sigma_R^*(Q)^2+Q^2-2Q\cdot\Sigma_R^*(Q)+\Sigma_R(Q)\cdot\Sigma_R^*(Q) \\ &\quad =Q^2-2Q\cdot\Sigma_R^*(Q)+\Sigma_R^*(Q)^2 \\ &\quad =(Q-\Sigma_R^*(Q))^2 \end{aligned} \quad \text{(C.19)}$$

it is finally possible to write

$$I(K) = -8\pi f_F(K)\int d^4Q\delta(K\cdot Q)\mathrm{Im}\left[K\cdot S_R^D(Q)\right]$$

C.2 Evaluating $J_0(K)$ $J_1'(K)$

With the ansatz $f_{F/B}^{shear}(V)$ used for shear viscosity in this thesis, $f(V)$ is given by

$$4(f_F(V)+f_B(V)) = \frac{4}{\sinh(V)} + \frac{4\cosh(V)}{\sinh(V)^2} A_{\mu\nu}V^\mu V^\nu \tag{C.20}$$

where

$$A_{\mu\nu} \equiv \frac{\pi^{\mu\nu}}{2(\epsilon+\mathcal{P})} \tag{C.21}$$

The first term of Equation C.20 is denoted $f_{(0)}(V)$ and the second $f_{(1)}(V)$.

It is clear that $\tilde{\Sigma}^\mu_R(X)$ can thus be split in two terms:

$$\tilde{\Sigma}^\mu_R(X) = \tilde{\Sigma}^\mu_{R(0)}(X) + \tilde{\Sigma}^\mu_{R(1)}(X) \tag{C.22}$$

where $\tilde{\Sigma}^\mu_{R(0)}(X)$ is the equilibrium retarded self-energy and $\tilde{\Sigma}^\mu_{R(1)}(X)$ contains one power of $A_{\mu\nu}$.

Linearising in $A_{\mu\nu}$, $J(K)$ can be written

$$\begin{aligned}
J(K) &= -\int d^4X\delta(K\cdot X)K_\mu \mathrm{Im}\left[\frac{\tilde{\Sigma}^\mu_{R(0)}(X)+\tilde{\Sigma}^\mu_{R(1)}(X)}{(X-\tilde{\Sigma}_{R(0)}(X)-\tilde{\Sigma}_{R(1)}(X))^2}\right] \\
&\approx -\int d^4X\delta(K\cdot X)K_\mu \mathrm{Im}\left[\frac{\tilde{\Sigma}^\mu_{R(0)}(X)+\tilde{\Sigma}^\mu_{R(1)}(X)}{[(X-\tilde{\Sigma}_{R(0)}(X))^2 - 2(X-\tilde{\Sigma}_{R(0)}(X))\cdot\tilde{\Sigma}_{R(1)}(X)]}\right] \\
&\approx -\int d^4X\delta(K\cdot X)K_\mu \\
&\quad \mathrm{Im}\left[\left[\frac{\tilde{\Sigma}^\mu_{R(0)}(X)+\tilde{\Sigma}^\mu_{R(1)}(X)}{(X-\tilde{\Sigma}_{R(0)}(X))^2}\right]\left[1-\frac{2(X-\tilde{\Sigma}_{R(0)}(X))\cdot\tilde{\Sigma}_{R(1)}(X)}{(X-\tilde{\Sigma}_{R(0)}(X))^2}\right]^{-1}\right] \\
&\approx -\int d^4X\delta(K\cdot X)K_\mu \\
&\quad \mathrm{Im}\left[\left[\frac{\tilde{\Sigma}^\mu_{R(0)}(X)+\tilde{\Sigma}^\mu_{R(1)}(X)}{(X-\tilde{\Sigma}_{R(0)}(X))^2}\right]\left[1+\frac{2(X-\tilde{\Sigma}_{R(0)}(X))\cdot\tilde{\Sigma}_{R(1)}(X)}{(X-\tilde{\Sigma}_{R(0)}(X))^2}\right]\right] \\
&\approx -\int d^4X\delta(K\cdot X)K_\mu \left[\mathrm{Im}\left[\frac{\tilde{\Sigma}^\mu_{R(0)}(X)}{(X-\tilde{\Sigma}_{R(0)}(X))^2}\right]\right. \\
&\quad \left. + \mathrm{Im}\left[\frac{\tilde{\Sigma}^\mu_{R(1)}(X)}{(X-\tilde{\Sigma}_{R(0)}(X))^2} + \frac{2\tilde{\Sigma}^\mu_{R(0)}(X)(X-\tilde{\Sigma}_{R(0)}(X))\cdot\tilde{\Sigma}_{R(1)}(X)}{(X-\tilde{\Sigma}_{R(0)}(X))^4}\right]\right]
\end{aligned}$$

The second to last line can be identified the equilibrium result $J_0(K)$, and the last line as the viscous correction $J_1(K)$.

In the equilibrium case, $\tilde{\Sigma}_{R(0)}$ admits simple tensor decomposition:

$$\tilde{\Sigma}_{R(0)}(X) = \tilde{A}X^{\mu} + \tilde{B}u^{\mu} \tag{C.23}$$

which can be used to write out the expression for $J_0(K)$ as:

$$J_0(K) \;=\; -k\int d^4X\delta(K\cdot X)\mathrm{Im}\left[\frac{\tilde{B}}{((1-\tilde{A})^2X^2 - 2(1-\tilde{A})\tilde{B}X^0 + \tilde{B}^2)}\right]$$

Similarly,

$$\begin{aligned} J_1(K) \;&=\; -\int d^4X\delta(K\cdot X) \\ &\qquad \mathrm{Im}\left[\frac{K_{\mu}\tilde{\Sigma}^{\mu}_{R(1)}(X)}{(X-\tilde{\Sigma}_{R(0)}(X))^2} - \frac{2\tilde{B}K\cdot u\tilde{B}u_{\mu}\tilde{\Sigma}^{\mu}_{R(1)}(X)}{(X-\tilde{\Sigma}_{R(0)}(X))^4}\right] \end{aligned} \tag{C.24}$$

Writing $\tilde{\Sigma}^{\mu}_{R(1)}(X)$ as $\tilde{\Sigma}^{\mu}_{R(1)}(X) = A_{\alpha\beta}Y^{\alpha\beta\mu}$ where

$$Y^{\alpha\beta\mu}(X) = \int \frac{d^3\mathbf{v}}{(2\pi)^3}\frac{4\cosh(V)}{\sinh(V)^2}\frac{1}{v}\frac{V^{\alpha}V^{\beta}V^{\mu}}{V\cdot X + i\epsilon} \tag{C.25}$$

then

$$\begin{aligned} J_1(K) \;&=\; -A_{\alpha\beta}\int d^4X\delta(K\cdot X) \\ &\qquad \mathrm{Im}\left[\frac{K_{\mu}Y^{\alpha\beta\mu}}{(X-\tilde{\Sigma}_{R(0)}(X))^2} - \frac{2\tilde{B}K\cdot u\tilde{B}u_{\mu}Y^{\alpha\beta\mu}}{(X-\tilde{\Sigma}_{R(0)}(X))^4}\right] \end{aligned} \tag{C.26}$$

The remaining integral is defined as $Z^{\alpha\beta}$. By tensor decomposition, it is given by

$$Z^{\alpha\beta} = ag^{\alpha\beta} + bu^{\alpha}u^{\beta} + cK^{\alpha}K^{\beta} + d(K^{\alpha}u^{\beta} + K^{\beta}u^{\alpha}) \tag{C.27}$$

After contraction with $A_{\alpha\beta}$, the only term that survives is $cK^{\alpha}K^{\beta}$:

$$J_1(K) \;=\; -A_{\alpha\beta}cK^{\alpha}K^{\beta} \tag{C.28}$$

The coefficient c is given by the projector $P_{(c)\alpha\beta}$:

$$P_{(c)\alpha\beta} = \frac{\left[[(u\cdot K)^2 - K^2]g^{\alpha\beta} + [2(u\cdot K)^2 + K^2]u^{\alpha}u^{\beta} + 3K^{\alpha}K^{\beta} - 6K\cdot uu^{\alpha}K^{\beta}\right]}{2[(u\cdot K)^2 - K^2]^2} \tag{C.29}$$

which can be simplified to

$$P_{(c)\alpha\beta} = \frac{\left[k^2 g^{\alpha\beta} + 2k^2 u^\alpha u^\beta + 3K^\alpha K^\beta - 6k u^\alpha K^\beta\right]}{2k^4} \tag{C.30}$$

since K is on-shell and massless.

The coefficient c is then given by

$$\begin{aligned} c &= \int d^4X \delta(K\cdot X) \\ &\quad \mathrm{Im}\left[\frac{P_{(c)\alpha\beta}K_\mu Y^{\alpha\beta\mu}}{(X-\tilde{\Sigma}_{R(0)}(X))^2} - \frac{2\tilde{B}K\cdot u\tilde{B}P_{(c)\alpha\beta}u_\mu Y^{\alpha\beta\mu}}{(X-\tilde{\Sigma}_{R(0)}(X))^4}\right] \end{aligned} \tag{C.31}$$

The contractions $u_\alpha u_\beta K_\mu Y^{\alpha\beta\mu}$, $K_\alpha K_\beta K_\mu Y^{\alpha\beta\mu}$, $u_\alpha K_\beta K_\mu Y^{\alpha\beta\mu}$, $u_\alpha u_\beta u_\mu Y^{\alpha\beta\mu}$ must be evaluated. To do so, the tensor decomposition of $Y^{\alpha\beta\mu}$ is used:

$$\begin{aligned} Y^{\alpha\beta\mu} &= a(X^\mu g^{\alpha\beta} + X^\alpha g^{\beta\mu} + X^\beta g^{\mu\alpha}) + b(u^\mu g^{\alpha\beta} + u^\alpha g^{\beta\mu} + u^\beta g^{\mu\alpha}) \\ &\quad + c(X^\mu u^\alpha u^\beta + X^\alpha u^\beta u^\mu + X^\beta u^\mu u^\alpha) \\ &\quad + d(X^\mu X^\alpha u^\beta + X^\alpha X^\beta u^\mu + X^\beta X^\mu u^\alpha) \\ &\quad + f(u^\mu u^\alpha u^\beta) + g(X^\mu X^\alpha X^\beta) \end{aligned} \tag{C.32}$$

Using the property $K\cdot X = 0$, $P_{(c)\alpha\beta}K_\mu Y^{\alpha\beta\mu}$ is found to be

$$\begin{aligned} P_{(c)\alpha\beta}K_\mu Y^{\alpha\beta\mu} &= P_{(c)\alpha\beta}K_\mu \left[a(X^\alpha g^{\beta\mu} + X^\beta g^{\mu\alpha}) + b(u^\alpha g^{\beta\mu} + u^\beta g^{\mu\alpha})\right. \\ &\quad \left. + c(X^\alpha u^\beta u^\mu + X^\beta u^\mu u^\alpha) + d(X^\alpha X^\beta u^\mu)\right] \\ &= P_{(c)\alpha\beta}\left[a(X^\alpha K^\beta + X^\beta K^\alpha) + b(u^\alpha K^\beta + u^\beta K^\alpha)\right. \\ &\quad \left. + ck(X^\alpha u^\beta + X^\beta u^\alpha) + dkX^\alpha X^\beta\right] \end{aligned} \tag{C.33}$$

$$\begin{aligned} P_{(c)\alpha\beta}u_\mu Y^{\alpha\beta\mu} &= P_{(c)\alpha\beta}u_\mu \left[a(X^\alpha g^{\beta\mu} + X^\beta g^{\mu\alpha}) + b(u^\alpha g^{\beta\mu} + u^\beta g^{\mu\alpha}) + c(X^\alpha u^\beta u^\mu + X^\beta u^\mu u^\alpha) + \ldots\right. \\ &= P_{(c)\alpha\beta}\left[(a + c + dX^0)(X^\alpha u^\beta + X^\beta u^\alpha) + (d + gX^0)X^\alpha X^\beta\right] \end{aligned} \tag{C.34}$$

$$
\begin{aligned}
P_{(c)\alpha\beta}(X^\alpha K^\beta + X^\beta K^\alpha) &= \frac{2X^0}{k} \\
P_{(c)\alpha\beta}(u^\alpha K^\beta + u^\beta K^\alpha) &= 0 \\
P_{(c)\alpha\beta}(X^\alpha u^\beta + X^\beta u^\alpha) &= 0 \\
P_{(c)\alpha\beta}X^\alpha X^\beta &= \frac{X^2 + 2(X^0)^2}{2k^2}
\end{aligned}
\tag{C.35}
$$

Thus

$$
\begin{aligned}
P_{(c)\alpha\beta}K_\mu Y^{\alpha\beta\mu} &= \left[\frac{2X^0}{k}a + \frac{X^2 + 2(X^0)^2}{2k}d\right] \\
P_{(c)\alpha\beta}u_\mu Y^{\alpha\beta\mu} &= \frac{X^2 + 2(X^0)^2}{2k^2}(d + gX^0)
\end{aligned}
\tag{C.36}
$$

Coefficient a, d and g can be evaluated as

$$
\begin{aligned}
a &= \frac{21\zeta(3)}{\pi^2}\left(-\frac{(X^0)^2 + ((X^0)^2 - x^2)\,(2 - 6X^0\Sigma^0_{(0)}(X))}{6x^4}\right) \\
d &= \frac{21\zeta(3)}{\pi^2}\left(\frac{15(X^0)^3 - 13X^0x^2 - 30(X^0)^4\Sigma^0_{(0)}(X) + 36(X^0)^2x^2\Sigma^0_{(0)}(X) - 6x^4\Sigma^0_{(0)}(X)}{6x^6}\right) \\
g &= \frac{21\zeta(3)}{\pi^2}\left(\frac{-15(X^0)^2 + 4x^2 + 30(X^0)^3\Sigma^0_{(0)}(X) - 18X^0x^2\Sigma^0_{(0)}(X)}{6x^6}\right)
\end{aligned}
\tag{C.37}
$$

Finally, $J_1(K)$ is given by

$$
J_1(K) = A_{\alpha\beta}K^\alpha K^\beta \frac{1}{k^2}J_1'(K) \tag{C.38}
$$

where J_1' is given by

$$
\begin{aligned}
J_1' &= -k^2\int d^4X\delta(K\cdot X) \\
&\quad \mathrm{Im}\left[\left[\frac{2X^0}{k}a + \frac{X^2 + 2(X^0)^2}{2k}d\right]\frac{1}{((1-\tilde{A})^2X^2 - 2(1-\tilde{A})\tilde{B}X^0 + \tilde{B}^2)}\right. \\
&\quad \left. -\frac{X^2 + 2(X^0)^2}{2k}(d + gX^0)\frac{2\tilde{B}^2}{[((1-\tilde{A})^2X^2 - 2(1-\tilde{A})\tilde{B}X^0 + \tilde{B}^2)]^2}\right]
\end{aligned}
\tag{C.39}
$$

C.2.1 Evaluating $\tilde{A}$ and $\tilde{B}$

In this section, $\tilde{A}$ and $\tilde{B}$ as defined in

$$\tilde{\Sigma}_{R(0)}(X) = \tilde{A}X^\mu + \tilde{B}u^\mu \tag{C.40}$$

are evaluated in terms of $\tilde{\Sigma}^0_R(X)$ and $X_\mu\tilde{\Sigma}^\mu_R(X)$.

First

$$\begin{aligned} \tilde{\Sigma}^0_R(X) &= \tilde{A}X^0 + \tilde{B} \\ X_\mu\tilde{\Sigma}^\mu_R(X) &= \tilde{A}X^2 + \tilde{B}X^0 \end{aligned} \tag{C.41}$$

so that

$$\begin{aligned} \tilde{A} &= \frac{X^0\tilde{\Sigma}^0_R(X) - X_\mu\tilde{\Sigma}^\mu_R(X)}{(X^0)^2 - X^2} \\ \tilde{B} &= -\frac{X^2\tilde{\Sigma}^0_R(X) - X^0X_\mu\tilde{\Sigma}^\mu_R(X)}{(X^0)^2 - X^2} \end{aligned} \tag{C.42}$$

Evaluating $\tilde{\Sigma}^0_R(X)$ yields

$$\begin{aligned} \tilde{\Sigma}^0_R(X) &= \int \frac{d^3\mathbf{v}}{(2\pi)^3}\frac{f(V)}{v}\frac{V^0}{V\cdot X + i\epsilon} \\ &= \int \frac{dvv}{(2\pi)^2}f(v)\frac{1}{x}\int_0^\pi d\theta\sin(\theta)\frac{1}{X^0/x - \cos(\theta) + i\epsilon'} \\ &= \frac{1}{4x}\left[\ln\left(\frac{1+X^0/x}{1-X^0/x}\right) - i\pi\right] \end{aligned}$$

if $|X^0/x| < 1$ (the imaginary part drops if $|X^0/x| > 1$).

The second term is simpler:

$$X_\mu\tilde{\Sigma}^\mu_R(X) = \int \frac{d^3\mathbf{v}}{(2\pi)^3}\frac{f(V)}{v} = \frac{1}{2} \tag{C.43}$$

Bibliography

[1] S. Ryu, J.-F. Paquet, C. Shen, G. S. Denicol, B. Schenke, S. Jeon, and C. Gale, "Importance of the bulk viscosity of qcd in ultrarelativistic heavy-ion collisions," *Phys. Rev. Lett.*, vol. 115, p. 132301, 2015.

[2] C. Shen, J.-F. Paquet, U. Heinz, and C. Gale, "Photon Emission from a Momentum Anisotropic Quark-Gluon Plasma," *Phys.Rev.*, vol. C91, no. 1, p. 014908, 2015.

[3] C. Shen, J.-F. Paquet, J. Liu, G. Denicol, U. Heinz, *et al.*, "Event-by-event direct photon anisotropic flow in relativistic heavy-ion collisions," *Nucl.Phys.*, vol. A931, pp. 675–680, 2014.

[4] C. Shen, U. Heinz, J.-F. Paquet, and C. Gale, "Thermal photon anisotropic flow serves as a quark-gluon plasma viscometer," 2014.

[5] C. Burgess and G. Moore, *The Standard Model: A primer*. Cambridge University Press, 2007.

[6] K. Olive *et al.*, "Review of Particle Physics," *Chin.Phys.*, vol. C38, p. 090001, 2014.

[7] E. V. Shuryak, "Quantum Chromodynamics and the Theory of Superdense Matter," *Phys.Rept.*, vol. 61, pp. 71–158, 1980.

[8] S. Borsanyi, Z. Fodor, C. Hoelbling, S. D. Katz, S. Krieg, *et al.*, "Full result for the QCD equation of state with 2+1 flavors," *Phys.Lett.*, vol. B730, pp. 99–104, 2014.

[9] M. Tannenbaum, "Recent results in relativistic heavy ion collisions: From 'a new state of matter' to 'the perfect fluid'," *Rept.Prog.Phys.*, vol. 69, pp. 2005–2060, 2006.

[10] O. Philipsen, "The QCD equation of state from the lattice," *Prog.Part.Nucl.Phys.*, vol. 70, pp. 55–107, 2013.

[11] S. Tiwari and C. Singh, "Particle production in Ultra-relativistic Heavy-Ion Collisions : A Statistical-Thermal Model Review," *Adv.High Energy Phys.*, vol. 2013, p. 805413, 2013.

[12] M. Kaneta, "Event anisotropy of identified π^0, γ and e compared to charged π, K, p, and d in $\sqrt{s_{NN}}$ = 200 GeV Au+Au at PHENIX," Presented at Quark Matter, Oakland, 2004.

[13] B. Muller, J. Schukraft, and B. Wyslouch, "First Results from Pb+Pb collisions at the LHC," *Ann.Rev.Nucl.Part.Sci.*, vol. 62, pp. 361–386, 2012.

[14] A. Mischke, "Research Group QGP-ALICE: Research." `http://www.staff.science.uu.nl/~misch101/research.htm` [Retrieved on April 19, 2015].

[15] G. Aad *et al.*, "Measurement of charged-particle spectra in Pb+Pb collisions at $\sqrt{s_{\mathrm{NN}}}$ = 2.76 TeV with the ATLAS detector at the LHC," 2015.

[16] J. M. Butterworth, G. Dissertori, and G. P. Salam, "Hard Processes in Proton-Proton Collisions at the Large Hadron Collider," *Ann.Rev.Nucl.Part.Sci.*, vol. 62, pp. 387–405, 2012.

[17] M. Wilde, "Measurement of Direct Photons in pp and Pb-Pb Collisions with ALICE," *Nucl.Phys.*, vol. A904-905, pp. 573c–576c, 2013.

[18] S. Chatrchyan *et al.*, "Measurement of inclusive W and Z boson production cross sections in pp collisions at $\sqrt{s}$ = 8 TeV," *Phys.Rev.Lett.*, vol. 112, p. 191802, 2014.

[19] S. Chatrchyan *et al.*, "Study of Z production in PbPb and pp collisions at $\sqrt{s_{\mathrm{NN}}}$ = 2.76 TeV in the dimuon and dielectron decay channels," *JHEP*, vol. 1503, p. 022, 2015.

[20] A. Adare, S. Adler, S. Afanasiev, C. Aidala, N. Ajitanand, *et al.*, "Direct photon production in d+Au collisions at $\sqrt{s_{NN}}$ = 200 GeV," *Phys.Rev.*, vol. C87, p. 054907, 2013.

[21] S. Chatrchyan *et al.*, "Measurement of isolated photon production in *pp* and PbPb collisions at $\sqrt{s_{NN}}$ = 2.76 TeV," *Phys.Lett.*, vol. B710, pp. 256–277, 2012.

[22] M. L. Miller, K. Reygers, S. J. Sanders, and P. Steinberg, "Glauber modeling in high energy nuclear collisions," *Ann.Rev.Nucl.Part.Sci.*, vol. 57, pp. 205–243, 2007.

[23] A. Majumder and M. Van Leeuwen, "The Theory and Phenomenology of Perturbative QCD Based Jet Quenching," *Prog.Part.Nucl.Phys.*, vol. A66, pp. 41–92, 2011.

[24] T. Schäfer, "Fluid dynamics and viscosity in strongly correlated fluids," *Annual Review of Nuclear and Particle Science*, vol. 64, no. 1, pp. 125–148, 2014.

[25] J. L. R. d'Alembert, *Essai d'une nouvelle théorie de la résistance des fluides*. David l'aîné, 1752.

[26] L. Euler, *Principes généraux de l'état d'équilibre des fluides*, vol. 11. Mémoires de l'académie des sciences de Berlin, 1757. `http://eulerarchive.maa.org/pages/E225.html`.

[27] T. Ludlam and L. McLerran, "What have we learned from the Relativistic Heavy Ion Collider?," *Phys.Today*, vol. 56N10, pp. 48–54, 2003.

[28] B. Schenke, S. Jeon, and C. Gale, "Higher flow harmonics from (3+1)D event-by-event viscous hydrodynamics," *Phys.Rev.*, vol. C85, p. 024901, 2012.

[29] A. Adare *et al.*, "Centrality dependence of low-momentum direct-photon production in Au+Au collisions at $\sqrt{s_{NN}} = 200$ GeV," 2014.

[30] A. Adare *et al.*, "Observation of direct-photon collective flow in $\sqrt{s_{NN}} = 200$ GeV Au+Au collisions," *Phys.Rev.Lett.*, vol. 109, p. 122302, 2012.

[31] P. B. Arnold, G. D. Moore, and L. G. Yaffe, "Photon emission from quark gluon plasma: Complete leading order results," *JHEP*, vol. 0112, p. 009, 2001.

[32] A. Adare *et al.*, "Enhanced production of direct photons in Au+Au collisions at $\sqrt{s_{NN}} = 200$ GeV and implications for the initial temperature," *Phys.Rev.Lett.*, vol. 104, p. 132301, 2010.

[33] R. Chatterjee, E. S. Frodermann, U. W. Heinz, and D. K. Srivastava, "Elliptic flow of thermal photons in relativistic nuclear collisions," *Phys.Rev.Lett.*, vol. 96, p. 202302, 2006.

[34] C. Gale, "Photon Production in Hot and Dense Strongly Interacting Matter," *Landolt-Bornstein*, vol. 23, p. 445, 2010.

[35] C. Gale, "Electromagnetic radiation in heavy ion collisions: Progress and puzzles," *Nucl.Phys.*, vol. A910-911, pp. 147–154, 2013.

[36] M. Dion, J.-F. Paquet, B. Schenke, C. Young, S. Jeon, *et al.*, "Viscous photons in relativistic heavy ion collisions," *Phys.Rev.*, vol. C84, p. 064901, 2011.

[37] R. Chatterjee, H. Holopainen, I. Helenius, T. Renk, and K. J. Eskola, "Elliptic flow of thermal photons from event-by-event hydrodynamic model," *Phys.Rev.*, vol. C88, p. 034901, 2013.

[38] C. Shen, U. W. Heinz, J.-F. Paquet, I. Kozlov, and C. Gale, "Anisotropic flow of thermal photons as a quark-gluon plasma viscometer," *Phys.Rev.*, vol. C91, no. 2, p. 024908, 2015.

[39] H. van Hees, M. He, and R. Rapp, "Pseudo-Critical Enhancement of Thermal Photons in Relativistic Heavy-Ion Collisions," *Nucl.Phys.*, vol. A933, pp. 256–271, 2015.

[40] O. Linnyk, V. Konchakovski, W. Cassing, and E. Bratkovskaya, "Photon elliptic flow in relativistic heavy-ion collisions: hadronic versus partonic sources," *Phys.Rev.*, vol. C88, p. 034904, 2013.

[41] K. Tuchin, "Particle production in strong electromagnetic fields in relativistic heavy-ion collisions," *Adv.High Energy Phys.*, vol. 2013, p. 490495, 2013.

[42] J. Collins, *Foundations of perturbative QCD*, vol. 32. Cambridge University Press, 2011.

[43] E. V. Shuryak, "High-energy collisions of strongly deformed nuclei: An Old idea with a new twist," *Phys.Rev.*, vol. C61, p. 034905, 2000.

[44] E. Abbas *et al.*, "Centrality dependence of the pseudorapidity density distribution for charged particles in Pb-Pb collisions at $\sqrt{s_{\rm NN}} = 2.76$ TeV," *Phys.Lett.*, vol. B726, pp. 610–622, 2013.

[45] I. Bearden *et al.*, "Charged meson rapidity distributions in central Au+Au collisions at $\sqrt{s_{NN}} = 200$ GeV," *Phys.Rev.Lett.*, vol. 94, p. 162301, 2005.

[46] J. Bjorken, "Highly Relativistic Nucleus-Nucleus Collisions: The Central Rapidity Region," *Phys.Rev.*, vol. D27, pp. 140–151, 1983.

[47] S. S. Gubser, "Symmetry constraints on generalizations of Bjorken flow," *Phys.Rev.*, vol. D82, p. 085027, 2010.

[48] H. Marrochio, J. Noronha, G. S. Denicol, M. Luzum, S. Jeon, *et al.*, "Solutions of Conformal Israel-Stewart Relativistic Viscous Fluid Dynamics," *Phys.Rev.*, vol. C91, no. 1, p. 014903, 2015.

[49] J. Stachel, A. Andronic, P. Braun-Munzinger, and K. Redlich, "Confronting LHC data with the statistical hadronization model," *J.Phys.Conf.Ser.*, vol. 509, p. 012019, 2014.

[50] B. Abelev *et al.*, "Centrality dependence of π, K, p production in Pb-Pb collisions at $\sqrt{s_{NN}} = 2.76$ TeV," *Phys.Rev.*, vol. C88, p. 044910, 2013.

[51] G. Aad *et al.*, "Measurement of the centrality and pseudorapidity dependence of the integrated elliptic flow in lead-lead collisions at $\sqrt{s_{\rm NN}} = 2.76$ TeV with the ATLAS detector," *Eur.Phys.J.*, vol. C74, no. 8, p. 2982, 2014.

[52] S. Chatrchyan *et al.*, "Measurement of higher-order harmonic azimuthal anisotropy in PbPb collisions at $\sqrt{s_{NN}} = 2.76$ TeV," *Phys.Rev.*, vol. C89, no. 4, p. 044906, 2014.

[53] A. Bilandzic, R. Snellings, and S. Voloshin, "Flow analysis with cumulants: Direct calculations," *Phys.Rev.*, vol. C83, p. 044913, 2011.

[54] M. Luzum and H. Petersen, "Initial State Fluctuations and Final State Correlations in Relativistic Heavy-Ion Collisions," *J.Phys.*, vol. G41, p. 063102, 2014.

[55] P. Stankus, "Direct photon production in relativistic heavy-ion collisions," *Ann.Rev.Nucl.Part.Sci.*, vol. 55, pp. 517–554, 2005.

[56] C. Shen, J. F. Paquet, G. Denicol, S. Jeon, and C. Gale, "Thermal photon radiation in high multiplicity p+Pb collisions at the Large Hadron Collider," 2015.

[57] S. Turbide, C. Gale, S. Jeon, and G. D. Moore, "Energy loss of leading hadrons and direct photon production in evolving quark-gluon plasma," *Phys.Rev.*, vol. C72, p. 014906, 2005.

[58] S. Turbide, C. Gale, E. Frodermann, and U. Heinz, "Electromagnetic radiation from nuclear collisions at RHIC energies," *Phys.Rev.*, vol. C77, p. 024909, 2008.

[59] G.-Y. Qin, J. Ruppert, S. Turbide, C. Gale, C. Nonaka, *et al.*, "Radiative jet energy loss in a three-dimensional hydrodynamical medium and high pT azimuthal asymmetry of pi0 suppression at mid and forward rapidity in Au+Au collisions at $\sqrt{s_{NN}}$=200 GeV," *Phys.Rev.*, vol. C76, p. 064907, 2007.

[60] F. Arleo, "Quenching of hadron and photon spectra in heavy-ion collisions from RHIC to LHC," *J.Phys.*, vol. G38, p. 124017, 2011.

[61] G. Basar, D. Kharzeev, and V. Skokov, "Conformal anomaly as a source of soft photons in heavy ion collisions," *Phys.Rev.Lett.*, vol. 109, p. 202303, 2012.

[62] L. McLerran and B. Schenke, "The Glasma, Photons and the Implications of Anisotropy," *Nucl.Phys.*, vol. A929, p. 71, 2014.

[63] L. Landau and E. Lifshitz, *Fluid Mechanics*. Pergamon Press, 1959.

[64] S. Jeon and U. Heinz, "Introduction to Hydrodynamics," 2015. [arXiv:1503.03931].

[65] G. Denicol, "Kinetic foundations of relativistic dissipative fluid dynamics," *J.Phys.*, vol. G41, no. 12, p. 124004, 2014.

[66] G. Denicol, H. Niemi, E. Molnár, and D. Rischke, "Derivation of transient relativistic fluid dynamics from the Boltzmann equation," *Phys.Rev.*, vol. D85, no. 3, p. 114047, 2012.

[67] W. Hiscock and L. Lindblom, "Stability and causality in dissipative relativistic fluids," *Annals Phys.*, vol. 151, pp. 466–496, 1983.

[68] E. Molnár, H. Niemi, G. Denicol, and D. Rischke, "Relative importance of second-order terms in relativistic dissipative fluid dynamics," *Phys.Rev.*, vol. D89, no. 7, p. 074010, 2014.

[69] G. Denicol, S. Jeon, and C. Gale, "Transport Coefficients of Bulk Viscous Pressure in the 14-moment approximation," *Phys.Rev.*, vol. C90, no. 2, p. 024912, 2014.

[70] B. Schenke, S. Jeon, and C. Gale, "(3+1)D hydrodynamic simulation of relativistic heavy-ion collisions," *Phys.Rev.*, vol. C82, p. 014903, 2010.

[71] A. Kurganov and E. Tadmor, "New high-resolution central schemes for nonlinear conservation laws and convection–diffusion equations," *Journal of Computational Physics*, vol. 160, no. 1, pp. 241–282, 2000.

[72] J. L. Albacete and C. Marquet, "Gluon saturation and initial conditions for relativistic heavy ion collisions," *Prog.Part.Nucl.Phys.*, vol. 76, pp. 1–42, 2014.

[73] L. D. McLerran and R. Venugopalan, "Computing quark and gluon distribution functions for very large nuclei," *Phys.Rev.*, vol. D49, pp. 2233–2241, 1994.

[74] B. Schenke, P. Tribedy, and R. Venugopalan, "Fluctuating Glasma initial conditions and flow in heavy ion collisions," *Phys.Rev.Lett.*, vol. 108, p. 252301, 2012.

[75] B. Schenke, P. Tribedy, and R. Venugopalan, "Event-by-event gluon multiplicity, energy density, and eccentricities in ultrarelativistic heavy-ion collisions," *Phys.Rev.*, vol. C86, p. 034908, 2012.

[76] T. Epelbaum and F. Gelis, "Pressure isotropization in high energy heavy ion collisions," *Phys.Rev.Lett.*, vol. 111, p. 232301, 2013.

[77] P. Huovinen and P. Petreczky, "QCD Equation of State and Hadron Resonance Gas," *Nucl.Phys.*, vol. A837, pp. 26–53, 2010.

[78] D. H. Rischke, "Fluid dynamics for relativistic nuclear collisions," *Lect.Notes Phys.*, vol. 516, p. 21, 1999.

[79] P. Huovinen and H. Petersen, "Particlization in hybrid models," *Eur.Phys.J.*, vol. A48, p. 171, 2012.

[80] P. Huovinen and D. Molnár, "The Applicability of causal dissipative hydrodynamics to relativistic heavy ion collisions," *Phys.Rev.*, vol. C79, p. 014906, 2009.

[81] H. Niemi and G. Denicol, "How large is the Knudsen number reached in fluid dynamical simulations of ultrarelativistic heavy ion collisions?," 2014.

[82] F. Cooper and G. Frye, "Comment on the Single Particle Distribution in the Hydrodynamic and Statistical Thermodynamic Models of Multiparticle Production," *Phys.Rev.*, vol. D10, p. 186, 1974.

[83] R. Fries and C. Nonaka, "Evaluating Results from the Relativistic Heavy Ion Collider with Perturbative QCD and Hydrodynamics," *Prog.Part.Nucl.Phys.*, vol. 66, pp. 607–660, 2011.

[84] G. Denicol. private communication. To be published.

[85] S. Bass, M. Belkacem, M. Bleicher, M. Brandstetter, L. Bravina, *et al.*, "Microscopic models for ultrarelativistic heavy ion collisions," *Prog.Part.Nucl.Phys.*, vol. 41, pp. 255–369, 1998.

[86] M. Bleicher, E. Zabrodin, C. Spieles, S. Bass, C. Ernst, *et al.*, "Relativistic hadron hadron collisions in the ultrarelativistic quantum molecular dynamics model," *J.Phys.*, vol. G25, pp. 1859–1896, 1999.

[87] H. Petersen, J. Steinheimer, G. Burau, M. Bleicher, and H. Stocker, "A Fully Integrated Transport Approach to Heavy Ion Reactions with an Intermediate Hydrodynamic Stage," *Phys.Rev.*, vol. C78, p. 044901, 2008.

[88] G. Denicol, T. Kodama, T. Koide, and P. Mota, "Effect of bulk viscosity on Elliptic Flow near QCD phase transition," *Phys.Rev.*, vol. C80, p. 064901, 2009.

[89] J. Noronha-Hostler, J. Noronha, and C. Greiner, "Transport Coefficients of Hadronic Matter near T(c)," *Phys.Rev.Lett.*, vol. 103, p. 172302, 2009.

[90] F. Karsch, D. Kharzeev, and K. Tuchin, "Universal properties of bulk viscosity near the QCD phase transition," *Phys.Lett.*, vol. B663, pp. 217–221, 2008.

[91] K. Aamodt *et al.*, "Higher harmonic anisotropic flow measurements of charged particles in Pb-Pb collisions at $\sqrt{s_{NN}}$=2.76 TeV," *Phys.Rev.Lett.*, vol. 107, p. 032301, 2011.

[92] S. Chatrchyan *et al.*, "Measurement of the elliptic anisotropy of charged particles produced in PbPb collisions at $\sqrt{s_{NN}}$=2.76 TeV," *Phys.Rev.*, vol. C87, no. 1, p. 014902, 2013.

[93] B. Abelev *et al.*, "Systematic Measurements of Identified Particle Spectra in pp, d^+ Au and Au+Au Collisions from STAR," *Phys.Rev.*, vol. C79, p. 034909, 2009.

[94] J. Adams *et al.*, "Azimuthal anisotropy in Au+Au collisions at $\sqrt{s_{NN}}$ = 200-GeV," *Phys.Rev.*, vol. C72, p. 014904, 2005.

[95] L. Adamczyk *et al.*, "Third Harmonic Flow of Charged Particles in Au+Au Collisions at $\sqrt{s_{NN}}$ = 200 GeV," *Phys.Rev.*, vol. C88, no. 1, p. 014904, 2013.

[96] S. Adler *et al.*, "Identified charged particle spectra and yields in Au+Au collisions at $\sqrt{s_{NN}}$ = 200 GeV," *Phys.Rev.*, vol. C69, p. 034909, 2004.

[97] B. Abelev *et al.*, "Identified baryon and meson distributions at large transverse momenta from Au+Au collisions at $\sqrt{s_{NN}}$ = 200 GeV," *Phys.Rev.Lett.*, vol. 97, p. 152301, 2006.

[98] D. Lohner, *Anisotropic flow of direct photons in Pb-Pb collisions at 2.76 TeV per nucleon.* PhD thesis, University of Heidelberg, 2013.

[99] B. Bannier, *Systematic studies of soft direct photon production in Au+Au collisions at* $\sqrt{s_{NN}}$*=200GeV.* PhD thesis, Stony Brook University, 2014.

[100] P. Aurenche, R. Baier, M. Fontannaz, and D. Schiff, "Prompt Photon Production at Large p(T) Scheme Invariant QCD Predictions and Comparison with Experiment," *Nucl.Phys.*, vol. B297, p. 661, 1988.

[101] F. Aversa, P. Chiappetta, M. Greco, and J. Guillet, "QCD Corrections to Parton-Parton Scattering Processes," *Nucl.Phys.*, vol. B327, p. 105, 1989.

[102] P. Aurenche, M. Fontannaz, J.-P. Guillet, E. Pilon, and M. Werlen, "A New critical study of photon production in hadronic collisions," *Phys.Rev.*, vol. D73, p. 094007, 2006.

[103] P. Aurenche, F. Aversa, R. Baier, T. Binoth, L. Bourhis, P. Chiappetta, M. Fontannaz, M. Greco, J. Guillet, G. Heinrich, E. Pilon, D. Schiff, and M. Werlen, "INCNLO v1.4," 2002. `http://lapth.cnrs.fr/PHOX_FAMILY/readme_inc.html`.

[104] M. Whalley, D. Bourilkov, and R. Group, "The Les Houches accord PDFs (LHAPDF) and LHAGLUE," 2005.

[105] D. Stump, J. Huston, J. Pumplin, W.-K. Tung, H. Lai, *et al.*, "Inclusive jet production, parton distributions, and the search for new physics," *JHEP*, vol. 0310, p. 046, 2003.

[106] L. Bourhis, M. Fontannaz, and J. Guillet, "Quarks and gluon fragmentation functions into photons," *Eur.Phys.J.*, vol. C2, pp. 529–537, 1998.

[107] K. Eskola, H. Paukkunen, and C. Salgado, "EPS09: A New Generation of NLO and LO Nuclear Parton Distribution Functions," *JHEP*, vol. 0904, p. 065, 2009.

[108] F. Arleo, K. J. Eskola, H. Paukkunen, and C. A. Salgado, "Inclusive prompt photon production in nuclear collisions at RHIC and LHC," *JHEP*, vol. 1104, p. 055, 2011.

[109] J. Ghiglieri, J. Hong, A. Kurkela, E. Lu, G. D. Moore, *et al.*, "Next-to-leading order thermal photon production in a weakly coupled quark-gluon plasma," *JHEP*, vol. 1305, p. 010, 2013.

[110] S. Caron-Huot, P. Kovtun, G. D. Moore, A. Starinets, and L. G. Yaffe, "Photon and dilepton production in supersymmetric Yang-Mills plasma," *JHEP*, vol. 12, p. 015, 2006.

[111] C. Gale, Y. Hidaka, S. Jeon, S. Lin, J.-F. Paquet, *et al.*, "Production and Elliptic Flow of Dileptons and Photons in a Matrix Model of the Quark-Gluon Plasma," *Phys.Rev.Lett.*, vol. 114, p. 072301, 2015.

[112] S. Turbide, R. Rapp, and C. Gale, "Hadronic production of thermal photons," *Phys.Rev.*, vol. C69, p. 014903, 2004.

[113] W. Liu and R. Rapp, "Low-energy thermal photons from meson-meson bremsstrahlung," *Nucl.Phys.*, vol. A796, pp. 101–121, 2007.

[114] M. Heffernan, P. Hohler, and R. Rapp, "Universal Parametrization of Thermal Photon Rates in Hadronic Matter," *Phys.Rev.*, vol. C91, no. 2, p. 027902, 2015.

[115] K. Dusling and I. Zahed, "Thermal photons from heavy ion collisions: A spectral function approach," *Phys.Rev.*, vol. C82, p. 054909, 2010.

[116] J. Serreau, "Out-of-equilibrium electromagnetic radiation," *JHEP*, vol. 0405, p. 078, 2004.

[117] R. Baier, M. Dirks, K. Redlich, and D. Schiff, "Thermal photon production rate from nonequilibrium quantum field theory," *Phys.Rev.*, vol. D56, pp. 2548–2554, 1997.

[118] J. I. Kapusta and C. Gale, *Finite-temperature field theory: Principles and applications*. Cambridge University Press, 2006.

[119] E. Braaten and R. D. Pisarski, "Soft Amplitudes in Hot Gauge Theories: A General Analysis," *Nucl.Phys.*, vol. B337, p. 569, 1990.

[120] B. Schenke and M. Strickland, "Photon production from an anisotropic quark-gluon plasma," *Phys.Rev.*, vol. D76, p. 025023, 2007.

[121] S. Mrowczynski and M. H. Thoma, "Hard loop approach to anisotropic systems," *Phys.Rev.*, vol. D62, p. 036011, 2000.

[122] M. E. Carrington, D.-f. Hou, and M. H. Thoma, "Equilibrium and nonequilibrium hard thermal loop resummation in the real time formalism," *Eur.Phys.J.*, vol. C7, pp. 347–354, 1999.

[123] B. Schenke, *Collective Phenomena in the Non-Equilibrium Quark-Gluon Plasma*. PhD thesis, Johann Wolfgang Goethe-Univ., 2008.

[124] C.-Y. Wong, *Introduction to high-energy heavy-ion collisions*. World scientific, 1994.

[125] K. Dusling, "Photons as a viscometer of heavy ion collisions," *Nucl.Phys.*, vol. A839, pp. 70–77, 2010.

[126] J. I. Kapusta, P. Lichard, and D. Seibert, "High-energy photons from quark - gluon plasma versus hot hadronic gas," *Phys.Rev.*, vol. D44, pp. 2774–2788, 1991.

[127] S. Turbide, *Electromagnetic radiation from matter under extreme conditions*. PhD thesis, McGill University (Canada), 2006.

[128] M. Dion, "Thermal photons and their role in probing the dynamics of heavy ion collisions," Master's thesis, McGill University (Canada), 2011.

[129] C. Shen. private communication.

[130] K. M. Burke *et al.*, "Extracting the jet transport coefficient from jet quenching in high-energy heavy-ion collisions," *Phys.Rev.*, vol. C90, no. 1, p. 014909, 2014.

[131] S. Endres, H. van Hees, J. Weil, and M. Bleicher, "Coarse-graining approach for dilepton production at energies available at the CERN Super Proton Synchrotron," *Phys.Rev.*, vol. C91, no. 5, p. 054911, 2015.

[132] S. Endres, H. van Hees, J. Weil, and M. Bleicher, "Dilepton production and reaction dynamics in heavy-ion collisions at SIS energies from coarse-grained transport simulations," *Phys. Rev.*, vol. C92, no. 1, p. 014911, 2015.

[133] P. Huovinen, M. Belkacem, P. Ellis, and J. I. Kapusta, "Dileptons and photons from coarse grained microscopic dynamics and hydrodynamics compared to experimental data," *Phys.Rev.*, vol. C66, p. 014903, 2002.

[134] R. Chatterjee, D. K. Srivastava, and T. Renk, "Triangular flow of thermal photons from an event-by-event hydrodynamic model for 2.76A TeV Pb+Pb collisions at LHC," 2014.

[135] D. Lohner, "Measurement of Direct-Photon Elliptic Flow in Pb-Pb Collisions at $\sqrt{s_{NN}} = 2.76$ TeV," *J.Phys.Conf.Ser.*, vol. 446, p. 012028, 2013.

[136] B. Bannier, "Systematic studies of the centrality dependence of soft photon production in Au + Au collision with PHENIX," *Nucl.Phys.*, vol. A931, pp. 1189–1193, 2014.